Texas A&M University
Mechanical Engineering Department
Turbomachinery Laboratory
Tribology Group

METAL MESH FOIL BEARINGS: PREDICTION AND MEASUREMENT OF STATIC AND DYNAMIC PERFORMANCE CHARACTERISTICS

Research Progress Report to the TAMU Turbomachinery Research Consortium

TRC-B&C-02-2013

by

Thomas Abraham Chirathadam
Research Assistant

Luis San Andrés
Mast-Childs Tribology Professor
Principal Investigator

May 2013

METAL MESH FOIL BEARINGS: OPERATION AT HIGH TEMPERATURES

TRC Project TEES # 32513/1519 FB (Year III)

ABSTRACT

Gas bearings in oil-free micro-turbomachinery for process gas applications and for power generation (< 400 kW) must offer adequate load capacity and thermal stability, reliable rotordynamic performance at high speeds and temperatures, low power losses and minimal maintenance costs. The metal mesh foil bearing (MMFB) is a promising foil bearing technology offering inexpensive manufacturing cost, large inherent material energy dissipation mechanism, and custom-tailored stiffness and damping properties. This report presents predictions and measurements of the dynamic forced performance of various high speed and high temperature MMFBs.

MMFB forced performance depends mainly on its elastic support structure, consisting of arcuate metal mesh pads and a smooth top foil. The analysis models the top foil as a 2D finite element (FE) shell supported uniformly by a metal mesh under-layer. The solution of the structural FE model coupled with a gas film model, governed by the Reynolds equation, delivers the pressure distribution over the top foil and thus the load reaction. A perturbation analysis further renders the dynamic stiffness and damping coefficients for the bearing. The static and dynamic performance predictions are validated against limited published experimental data.

A one-to-one comparison of the static and dynamic forced performance characteristics of a MMFB against a Generation I bump foil bearing (BFB) of similar size, with a slenderness ratio L/D=1.04, showcases the comparative performance of MMFB against a commercially available gas foil bearing design. The measurements of rotor lift-off speed and drag friction at start-up and airborne conditions are conducted for rotor speeds up to 70 krpm and under identical specific loads (W/LD =0.06 to 0.26 bar). The dynamic force coefficients of the bearings are estimated, in a 'floating bearing' type test rig, while floating atop a journal spinning to speeds as high as 50 krpm and with controlled static loads (22 N) applied in the vertical direction. The parameter identification is conducted in the frequency range of 200-400 Hz first, and then up to 600 Hz using higher load capacity shakers.

A finite element rotordynamic program (XLTRC^2) models a hollow rotor and two MMFBs supporting it and predict the synchronous rotor response for known imbalances. The predictions agree well with the ambient temperature rotor response measurements. Extensive rotor response measurements and rotor and bearing temperature measurements, with a coil heater warming up to 200 ºC and placed inside the hollow rotor, reveal the importance of adequate thermal management.

The database of high speed high temperature performance measurements and the development of a predictive tool will aid in the design and deployment of MMFBs in commercial high-speed turbomachinery. The work presented in the report is a cornerstone for future analytical developments and further testing of practical MMFBs.

NOMENCLATURE

A_{44}, A_{55}	Coefficients of transverse shear strains for elastic top foil [N/m]
$a_{\underline{X}(t)}$, $a_{\underline{Y}(t)}$	Bearing accelerations, $\underline{X}$ and $\underline{Y}$ directions [m/s^2]
$\overline{A}_{\underline{X}(\omega)}, \overline{A}_{\underline{Y}(\omega)}$	DFT of $\underline{X},\underline{Y}$ bearing accelerations [m/s^2]
$C_{\alpha\beta}$,C	Damping coefficients; $\alpha, \beta = X, Y$ [N·s/m]
c	Radial clearance [m]
$\overline{D}$	Empirical load coefficient [Ns/m^3]
D	Bearing inner diameter [m]
D_{Bi}	Bearing cartridge inner diameter [m]
D_{Bo}	Bearing cartridge outer diameter [m]
D_{ij}	Rigidity coefficients for elastic top foil [N/m]
D_{MMi}	Copper mesh inner diameter [m]
D_{MMo}	Copper mesh outer diameter [m]
D_O, D_I	Rotor outer and inner diameter [m]
D_W	Wire diameter [m]
E	Top foil elastic modulus [Pa] or [N/ m^2]
E_{disp}	Area of mechanical hysteresis loop [m^2]
E_V, E_M	Energy dissipated (viscous and hysteretic) [J]
e_X, e_Y	Journal eccentricity component [m], $e = \sqrt{e_X^2 + e_Y^2}$
f	T/WR. Drag or friction coefficient [-]
F_0	Force [N]
F_{ij}, i,j=$\underline{X},\underline{Y}$	DFT amplitude of forces [N]
F_o	Force applied at lowest frequency [N]
F_X, F_Y	Perturbed forces [N]
ΔF	Time rate of change of applied force [N/s]
G	Eddy current sensor gain [m/V]

$\{H_{\alpha\beta}\}_{\alpha\beta=X,Y}$	$K_{\alpha\beta}+j\omega C_{\alpha\beta}$. Bearing impedances [N/m],
h	Gas film thickness [m]
h_t	Shell thickness [m]
I_T	Moment of inertia [kg m^2]
i	Imaginary unit, $\sqrt{-1}$
K_{eff}	Effective stiffness coefficient [N/m]
K_L, K_S	Structural stiffnesses [N/m]
K_m	Metal mesh stiffness per unit area [N/m^3]
$\{K_{S\beta}\}_{\beta=\underline{X},\underline{Y}}$	Support structure stiffness coefficients [N/m]
k_t	Shear correction coefficient (=5/6) in a shear deformable plate model
$\{K_a\}_{\alpha=0,1,2,3}$	Coefficients of stiffness polynomial
$K_{\alpha\beta}$,K	Stiffness coefficients; $\alpha,\beta = X,Y$ [N/m]
L	Bearing axial length[m]
L_T	Torque arm length [m]
l	Half rotor length [m]
l_x	Pad circumferential length, $R(\theta_t-\theta_l)$ [m]
M_B	Bearing mass [kg]
M_R	Rotor mass [kg]
M, M_x, M_y, M_{yx}	Bending moment on top foil/unit length [N]
$\{M_{S\beta}\}_{\beta=\underline{X},\underline{Y}}$	Estimated test system masses [kg]
m_e	Unbalance mass [kg]
N	Rotor speed [rpm]
N_{rev}	Number of revolutions [s^{-1}]
P	$=W/LD$. Pressure or load per unit area [N/m^2]
P'	$=T\omega/LD$. Specific drag power [W/m^2]
P_W	Shear drag power [W]
p	Hydrodynamic pressure in gas film [Pa]

p_a	Ambient pressure [Pa]
P_0	Equilibrium pressure [Pa]
Q, Q_x, Q_y	Shear forces per unit length [N/m]
R	Rotor radius [m]
R_B	Bearing radius [m]
r	Radius for location of imbalance masses [m]
r_s	Bearing static displacement [m]
S	Sommerfeld number, $S = \left(\frac{R_B}{c}\right)^2 \frac{\mu N_{rev}}{P}$
Sn	Stribeck Number, $\mu\Omega / (W / LD)$
T	Drag torque [Nm]
T_{duct}	Duct air temperature [ºC]
$T_{FE,DE}$	Rotor free and drive end temperatures [ºC]
T_S	Heater set temperature [ºC]
T_i, i=1-8	Bearing cartridge temperature [ºC]
t	Time [s]
T_f	Top (thin) foil thickness [m]
U_{par}	Uncertainty, *par* is any parameter
u	Imbalance displacement [m]
u_e	$m_e\, r/M_R$, Imbalance displacement [μm]
V_X, V_Y	Rotor velocity [m/s]
W	Applied load [N]
$\overline{w}_{i=1,2,3}$	Weight functions in finite element formulation
$w_{(t)}$	Top foil transverse deflection [m]
w_X, w_Y	Perturbed top foil deflections [m]
X, Y and $\underline{X}, \underline{Y}$	Inertial (fixed) coordinate systems [m]
X_0, Y_0	Journal displacements [m]
$\underline{X}_{(t)}, \underline{Y}_{(t)}$	Bearing absolute displacements [m]

$\underline{X}_X$, $\underline{Y}_Y$	Bearing displacements [m]
x,y	Coordinate system on top foil surface [m]
$x'_{(t)}, y'_{(t)}$	Bearing displacements relative to journal [m]
$\overline{x}_{(\omega)}, \overline{y}_{(\omega)}$	*DFT* of bearing $\underline{X},\underline{Y}$ displacements relative to journal [m]
Z	Complex impedance [N/m]
γ	Structural damping loss factor [-]
ζ	Viscous damping ratio [-]
θ	Top foil angular coordinate [rad]
$\theta_l,\ \theta_t$	Top foil leading and trailing edge angles [rad]
Λ_g	Bearing speed number, $\Lambda_g = 6\mu\Omega R_B L / p_a c^2$
μ	Fluid viscosity [Pa-s]
ν	Poisson's ratio [-]
ζ	Damping ratio [-]
τ	Shear stress [N/m^2]
Φ	Journal attitude angle, $\tan^{-1}(e_X / e_Y)$ [rad]
φ	Angle of rotation from $\underline{X}$ to X axes
ϕ_x, ϕ_y	Angular displacements of top foil
ψ, ψ^1, ψ^2	Interpolation functions in FE analysis of top foil
Ω	$(\pi/30)N$, Rotor angular velocity [rad/sec]
Ω^e	Volume of a finite element
Ω_s	Threshold speed of instability [rad/sec]
Γ^e	Boundary of a finite element
ω	Excitation frequency [rad/s]
ω_n	Natural frequency [rad/s]
ω_S	Whirl frequency [rad/s]
ω_o	Low frequency excitation [rad/s]

Matrices and Vectors

F	$\{F_X, F_Y\}^T$ Lateral reaction force vector [N]
H	$\mathbf{K} + i\,\omega\,\mathbf{C}$. Matrix of impedances [N/m]
$\mathbf{F}^G$	Generalized force vector
K,C,M	Stiffness, damping and inertia matrices
$\mathbf{K}_L$	Lower triangular stiffness matrix
$\mathbf{K}^G$	FE global nodal stiffness matrix
P	Coordinate transformation matrix
$\mathbf{U}^G$	Generalized displacement vector
z	$\{x_{(t)}, y_{(t)}\}^T$. Bearing displacement vector, time domain [m]

Acronyms

BFB	Bump type foil bearing
DFT	Discrete Fourier transform operator
FE	Finite element
GFB	Gas foil bearing
MMFB	Metal mesh foil bearing
RBS	Rotor bearing system

TABLE OF CONTENTS

Page

Page

LIST OF FIGURES

FIGURE Page

FIGURE Page

FIGURE Page

FIGURE Page

FIGURE Page

FIGURE Page

LIST OF TABLES

1. INTRODUCTION

Advanced micro-turbomachinery (< 400 kW) requires cost-effective and reliable rotor support systems for efficient high speed operation at high temperature conditions, and in the presence of caustic process fluids [1, 2]. Automotive and aerospace applications require rugged gas bearings that are tolerant to misalignment and shock loads. Although conventional oil-lubricated bearings have a high load carrying capacity, large viscous drag losses at high rotor speeds and poor performance at high temperature [3] limit their use in specific applications. The burgeoning demand for hybrid/electric vehicles, auxiliary power units, high speed flywheel energy storage devices, and other systems that aim to reduce green house emissions and offering a low carbon foot print stimulates the growing interest in gas foil bearing technology.

Gas foil bearings (GFB) are traditionally used in micro-turbomachinery as they support high speed rotors on a thin film generated by the hydrodynamic viscous pumping of the ambient gas into the wedge shaped space between the spinning rotor and the bearing inner surface. Typically, a GFB consist of a smooth arcuate metal top foil and an elastic underspring support layer beneath it, both wrapped inside a solid cartridge. One end of the top foil is firmly affixed to the inner surface of the bearing cartridge.

GFBs offer other benefits such as reducing the number of components and system overall weight, lessening dependence on contaminated engine oil, and extending maintenance intervals. In addition to the removal of restrictions on *DN* life, i.e., diameter (*D)* in mm x rotational speed (*N)* in revolution/minute, and temperature limits typical for rolling element bearings, compliant surface or foil gas bearings also aid to increase efficiency by offering reduced drag power losses when operating airborne.

The metal mesh foil bearing (MMFB) [4] is a recent entrant in the gas foil bearing category with the promise of inexpensive manufacturing cost, large inherent material energy dissipation mechanism, and custom-tailored stiffness and damping properties enabling its ready scalability. Figure 1 depicts an isometric view of a MMFB and Figure

2 shows an exploded view of the bearing components. The bearing consists of a rigid steel cartridge with a compressed metal mesh pad and top foil wrapped inside. As the rotor spins within the MMFB, a thin gas film is generated that separates the surfaces in relative motion. The self-acting bearings, however, requires coatings on the top foil surface to reduce dry-sliding friction forces, and resulting drag torque and power loss, during start-up and shut-down processes. Ceramic powder or polymer based foil coatings and chrome-plated shafts are commonly used in the industry for long service life performance [5]. The rotor operating speed, the structural stiffness of the support elastic structure in the bearing [6], and the applied coatings are the major factors affecting the load carrying capacity of a foil bearing.

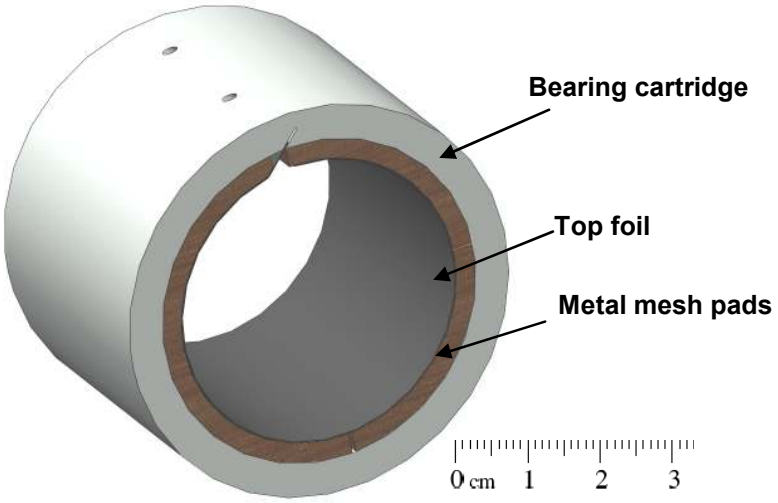

Fig. 1 View of a radial metal mesh foil bearing

Metal mesh, traditionally used as a vibration isolator [7] in gas turbine engines, operates satisfactorily in cryogenic temperatures as well as in high temperature environments [8]. Empirical design equations [9] render the structural force coefficients, stiffness K and equivalent viscous damping C, of a metal mesh damper ring as nonlinear functions of the displacement amplitude, excitation frequency, and radial interference.

The design equations [9], however, require of prior experimentation to determine an equivalent Young's modulus of the formed metal mesh ring.

San Andrés *et al*. [4] report constructing the first prototype of a MMFB (L=D=28.00 mm) with a metal mesh ring made of 0.3 mm Copper wire and compactness of 20 %. With the test bearing installed on a shaft with a slight preload, static load versus bearing deflection measurements display a cubic nonlinearity with large material hysteresis indicating significant mechanical energy dissipation. Identified structural stiffness and viscous damping coefficients decrease with increasing motion amplitudes, similarly as in metal mesh dampers [9]. On the other hand, with increasing excitation frequency, the bearing structural stiffness grows while the viscous damping coefficient rapidly decreases. A structural loss factor (material damping), not a viscous damping type, best describes the mechanical energy dissipation of metal meshes. The experiments reveal a loss factor (γ) ~ 0.7, higher than that in bump-type foil bearings, for example see Ref. [10]. In Ref. [4], the authors note that the metal mesh ring, with a large thickness of ~ 7 mm, undergoes significant sag or creep, resulting in the reduction of the magnitude of the structural force coefficients, upon operation and after multiple dismantling and re-assembly processes.

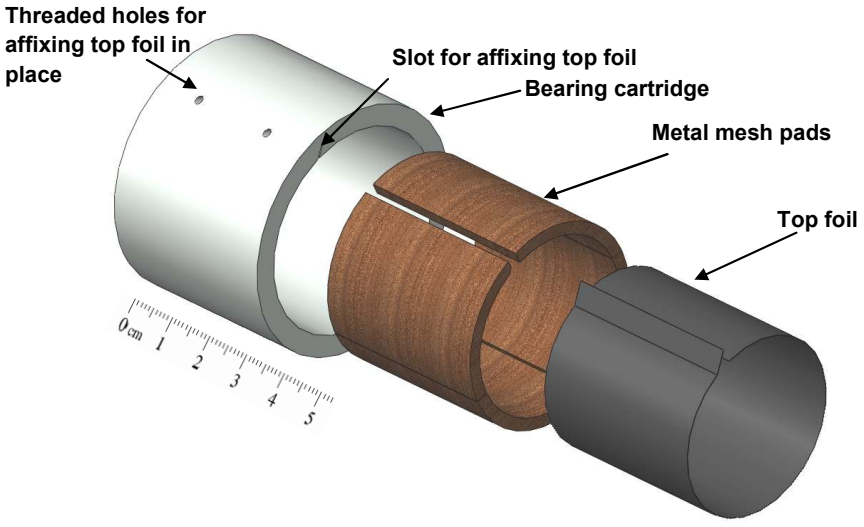

Fig. 2 Exploded view of the MMFB assembly

San Andrés *et al.* [11] demonstrate the readiness of the novel bearing technology by measuring the MMFB break-away torque, rotor lift off and touchdown speeds during multiple start up and shutdown tests. Later, San Andrés *et al.* [12] extend the work reporting measured bearing load capacity and drag torque for rotor speeds up to 60 krpm. During airborne operation, i.e., with a gas film separating the rotating journal from the bearing, the friction coefficient is two orders of magnitude smaller than the dry-friction coefficient during operation at start up (and shut down) where dry-friction sliding is present.

The bearing dynamic force coefficients play a significant role in the rotordynamic behavior of high-speed turbomachinery. Developing experimentally validated analytical tools for predicting bearing rotordynamic force coefficients is critical for the wide deployment of the MMFB technology. The present work fills this void by developing an accurate and efficient MMFB prediction model.

This report aims to provide guidelines for the design, manufacturing and application of MMFBs in high speed, high temperature applications. Section 2 discusses prior work on the experimental measurements of the foil bearing static and dynamic performance characteristics. Appendix A gives the details of the manufacturing procedure for a MMFB. Section 3 details a two dimensional finite element (FE) model of the top foil and metal mesh support structure. A computational analysis couples the FE model representing the bearing structure to a gas film model governed by Reynolds equations to predict the static and dynamic performance of a MMFB. To validate the analysis, section 4 presents the comparison of predictions against measured MMFB static and dynamic performance characteristics.

In order for a MMFB to be a commercially viable product, it must demonstrate performance comparable to existing GFB designs. Sections 5 and 6 compare the static and dynamic performance characteristics of similar sized MMFB and a generation I bump type foil bearing (BFB). Section 6 further advances the estimation of the dynamic force coefficients of a MMFB to a high frequency range (300 Hz - 600 Hz). These experimental results demonstrate that the MMFB has sufficient load carrying capacity,

and stiffness and damping properties to find application in commercial micro-turbomachinery.

In Section 7, a rotordynamic analysis (XLTRC$^{2®}$) software models a test rotor supported on two MMFBs, and predicts the rotor synchronous response amplitude and phase. Micro-turbomachinery applications, such as an automotive turbocharger for instance, require of rotor supports that can withstand high operating temperatures. Section 8 presents the measurements of the rotor response as well as rotor and bearing temperatures for various operating speeds in a test rig containing a heat source warming a hollow rotor.

Summarizing the findings in the report, Section 9 provides a set of guidelines to aid in the design of a MMFB and its use.

2. LITERATURE REVIEW*

This section reviews prior work on the measurements of gas foil bearing (GFB) static and dynamic performance characteristics. The bearing load capacity and drag power loss, the rotor lift-off speed, and the rotordynamic force coefficients influence the static and dynamic forced performance of a GFB. The compliance of the elastic structure and the top foil surface conditions largely affect these parameters. Recently, DellaCorte *et al.* [5] publish the design and fabrication procedures for generation I and II bump type foil bearings. The authors detail the mechanical operations and heat treatment procedures for manufacturing compliant foil (bump foil) and smooth top foil from a sheet of metal. Inspite of such efforts, the design and manufacturing of advanced GFBs, for instance a generation III GFB, as well as the composition of high temperature solid lubricants for the top foil and shaft surfaces still remain proprietary information shielded away from the public.

2.1 Foil Bearing Performance Characteristics

DellaCorte and Valco [13] reviews the experimental data in prior art and develops a 'Rule of Thumb' (ROT) model relating the empirical load capacity coefficient ($\bar{D}$) to the bearing geometry, the rotor speed, and the measured bearing load. The ROT model is described as $W = \bar{D}$ x (LD) x (DN) where $\bar{D}$ is an empirical load coefficient, (L x D) is the bearing projected area, and N is the rotor speed in krpm. $\bar{D}$, ranging from 0.1 to 1.5, serves to classify various foil bearing designs in terms of their load carrying capacity, defined as the maximum static load that the bearing supports while the rotor spins at constant speed and steady-state conditions. For instance, a generation III BFB has $\bar{D}$=1.0-1.5 nearly five times larger than $\bar{D}$=0.1-0.3 for a generation I bearing. The ROT formula is only intended to guide in the initial bearing sizing and selection process, and it ignores important factors such as ambient pressure and gas density [14],

* Part of this section is reprinted with permission from "Metal Mesh Foil Bearing: Effect of Motion Amplitude, Rotor Speed, Static Load, and Excitation Frequency on Force Coefficients" by San Andrés, L., and Chirathadam, T.A.,2011, ASME J. Eng. Gas Turbines Power, **133**(12), p.122503, Copyright [2011] by ASME.

operating temperature [15,16], surface condition of the top foil [12], and assembly pre-load [17].

The design of the compliant foil structure influences the bearing load capacity significantly. In a generation I GFB a uniform bump foil strip is used, while a generation II GFB employs a bump foil strip with staggered structural properties. The bump foil structural modifications aim to maintain a minimum gas film thickness over the entire top foil surface and reduce the leakage of air across the edges of the top foil while supporting larger loads. Advanced generation III GFBs use multiple bump foils arranged in a complex fashion along the bearing axial and circumferential directions.

Heshmat [18], in 1994, presents the load capacity measurements and static load-deflection characteristics of a generation II bump foil bearing, of 31 mm length and 35 mm diameter. The bearing with bump foils of axially varying stiffness supports a load of 727.8 N, i.e., a load carrying capacity of 673.5 kPa (97.7 psi), at the highest speed of 132 krpm. The author reports two fold improvement in load capacity compared to a generation I bearing. With increasing applied static load, the ensuing bearing deflections are highly nonlinear, and evidencing a large hysteresis loop indicative of large mechanical energy dissipation ability. The author presents the bearing deflections as eccentricity ratios >1, with geometric a clearance[1] as the reference, and find structural nonlinearity with increasing static loads. These bearings require custom tailoring for specific applications, especially in terms of the bump geometry and stiffness gradient in circumferential direction, and need extensive experimental verification before installation into a new application.

DellaCorte [19] builds a test rig for measuring the drag torque and load capacity of gas foil bearings for speeds up to 70,000 rpm and operating at ambient temperatures as high as 700 ºC. The author selects not to coat the top foil surface while coating the journal surface with thick solid lubricant composite material. This selection maintains the journal surface as the solid lubricant reservoir while the whole top foil acts as the

[1] The clearance in foil bearing is not directly measurable since most times there is a preload when the rotor is at rest. Hence, the representation of the rotor displacement as eccentricity ratio is often misleading.

sacrificial wear surface. The torque measurements indicate that, beyond the lift-off rotor speed, the bearing drag torque increases with increasing rotor speed and applied static load. The trend in the variation in load capacity with temperature is not clear. Importantly, the author notes that at room temperature operation, the wear is much larger than that at elevated temperature and with applied loads. This is so since the PS304 coating, a plasma sprayed composite coating of nickel-chrome bonded chrome oxide along with silver and barium-fluoride/calcium fluoride additive, is engineered to perform better at elevated temperatures.

Rudloff *et al*. [20] also report measuring the drag torque in a generation I bump type foil bearing, $L=D$=38.1mm, for speeds up to 40 krpm. The bearing housing made of two concentric rings separated by needle bearings aids in the error free measurement of the bearing drag torque while desired static loads are applied. For static loads of 10-50 N (W/LD = 6.8 kPa– 34.4 kPa), the rotor lift off speeds range from 2,750 rpm to 5,000 rpm. The drag torque increases nearly linearly with respect to the increasing static loads for the entire test speed range of 15.6 krpm to 35.4 krpm.

Conlon *et al.* [21] measure the steady state and dynamic performance characteristics of a large GFB, $L=D$= 70 mm, for speeds up to 60 krpm. The test facility is capable of applying maximum static and dynamic loads of 3500 N and 450 N using pneumatic cylinders and electro-dynamic shakers, respectively. The paper presents the bearing eccentricity as a function of rotor speed and static load, and shows the nonlinear stiffness characteristics of the bump foil structure. However, unlike other bearing performance measurements [19], the rotor speed appears not to affect the measured drag torque in this large diameter bearing. Conlon *et al.* [22] further compare the steady state performance of two GFBs of identical dimensions, $L=D$= 70 mm. During the load capacity tests applying static loads from 200 N to 700 N (W/LD= 40.8 kPa -142.9 kPa), and with the rotor speed varying from 10 to 40 krpm, a generation II bearing shows a frictional torque smaller in magnitude for the same rotor speed and static load. While the static structural stiffnesses are smaller for a generation II bearing, the dynamic load tests display higher stiffness for the generation II bearing compared to generation I

bearing. The authors ascribe this feature to the high nonlinearity in the stiffness of the bump foil structure, especially for the generation II bearing that has an axially varying stiffness distribution.

DellaCorte *et al.* [23] present an experimentally obtained gas foil bearing performance map, resembling a Stribeck curve for bearing friction coefficient, showing the bearing specific power loss[2] versus modified Sommerfeld number[3]. The load carrying capacity, from the performance map, and the thermal and shaft strength limits must be considered during the design stage for safe bearing operation limits. Radil and DellaCorte [24] further extend the work in Ref. [23] and present a three dimensional performance map for power loss in a generation III foil bearing, 35 mm in diameter and 27 mm in length, as a function of applied load (max. 109 N or 115.3 kPa in specific load) and shaft speed (max. 55 krpm). The authors recommend constructing 3D performance maps for every bearing to aid in the bearing sizing and selection process, especially to avoid excessive thermal gradients that could lead to failure.

Bruckner *et al.* [25] propose an analytical approach for developing a foil bearing operating map. The semi-empirical performance map could evidence a feasible range of operation using as few parameters as the load capacity coefficient, preload, and dry sliding friction coefficient. Due to the low viscosity of gases, a considerably large rotor speed is required to generate a fluid film and pressure field sufficient to lift a rotor for airborne operation. For low speeds or extremely large loads, the GFB operation is characterized by a large dry friction coefficient. However, once airborne, the gas film Couette shear stress dominates the source of drag torque and the drag friction drop by almost two orders of magnitude.

San Andrés *et al.* [11, 12] measure the bearing break-away torque and airborne drag torque, and rotor lift off and touchdown speeds in a MMFB, L=D=28 mm, for rotor

---

[2] Specific power loss [W/m^2] is defined by the authors as the frictional heat generated per unit bearing projected area

[3] Sommerfeld number or bearing characteristic number is defined as $S = \left(\frac{R_B}{c}\right)^2 \frac{\mu N_{rev}}{P}$ where R_B is the bearing inner radius, c is the radial clearance, μ is the viscosity of the fluid, N_{rev} is the speed in rev/s, and $P = W/LD$ is the load per projected bearing area.

speeds up to 60 krpm. The airborne operation friction coefficient $f \sim 0.01$, $f = T/(LR)$, is nearly two orders of magnitude smaller than the dry-friction coefficient during operation at start up (and shut down) where dry-friction sliding is the dominant resistance force to rotor motion. The experiments show that the presence of a solid lubricant (coating) reduces the friction, ~ 25 % lesser, during the initial dry sliding contact operation. The authors further present power loss versus rotor speed up to 60 krpm [26] for various static loads for the same test bearing in a similar fashion as that reported by Radil and DellaCorte [24].

Lee *et al*.[27] construct metal mesh foil bearings, 50 mm long and 60.18 mm in diameter, incorporating three metal mesh pads, 3.3 mm thick, beneath a top foil. The geometrical radial clearance is 0.18 mm. Three different test bearings are manufactured by using metal mesh pads made of copper wires, 0.15 mm in diameter, compressed to compactness of 13%, 23% and 32%. Static load versus bearing deflection measurements show a bearing stiffness and material loss factor increasing with metal mesh density. In comparison to a similar sized bump type foil bearing, the metal mesh foil bearings show a larger area enclosed by the load versus deflection hysteresis loop, indicating larger mechanical energy dissipation. Further, measurements of the bearing center line during static loading, with the shaft spinning at 30 krpm, demonstrate small (hydrodynamic) cross-coupled force effects.

Bruckner and Puleo [14] study the effect of ambient pressure and temperature on the load capacity of a bump type foil bearing, 35 mm in diameter and 27 mm in length, and with an uncoated Inconel X-750 top foil. The test shaft is coated with a proprietary coating (PS304) and ground finished. The load capacity measurements conducted for atmospheric pressures of 0.1 to 2.53 bar and for rotor speeds from 3 to 21 krpm, while the temperature varies from 25 to 500 °C, show an increasing load capacity with increasing ambient pressures and decreasing temperatures. Although gas viscosity increases with increasing temperature, the load capacity surprisingly decreases. The authors attribute this phenomenon to the softening of the support structure at elevated temperatures. The load capacity of the bearing abruptly drops due to the low gas density

and the gas rarefaction effect for pressures below 0.5 bar. The test results point towards the possibility of the failure of foil bearings while operating in low atmospheric pressure at extremely high altitudes. Characterization of the bearing load capacity and power loss while operating with different gases is crucial for the deployment of foil bearings operating with process gases other than air. Bruckner [28] presents measured power losses for a generation III foil bearing, for speeds up to 42 krpm, for pressures up to 40 bar, displaying the increase in power loss with increasing operating pressures for Nitrogen and CO_2. However, with the system operating in a Helium atmosphere, the pressure variation has only negligible effect on the power loss in the entire speed range of 10 to 42 krpm. The experiments indicate the effect of higher molecular weight lubricants on the power loss at high speeds.

Experimental and analytical development work over the past four decades has made tremendous progress in the load capacity, predictable rotordynamic force coefficients and dry lubricant technology. DellaCorte and Bruckner [29] review and summarize the current state of art of oil-free bearing technologies, and voice the concerns regarding the bearing scalability and suggest hybrid bearings as a possible solution for mitigating certain limitations. Typically, an increase in rotor speed or gas viscosity results in higher film thickness. But, the rotor surface velocities are restricted by the structural material strength limits, and maximum 'exit rim speed' in compressors, for instance. The major issues with a very thin gas film operation, in highly loaded regimes, are the increased shear rate and viscous losses, and resulting localized heating. The foil distortion due to thermal heating can give rise to rupture of films, possibly resulting in eventual bearing failure. The authors state that instead of load capacity, shaft dynamic loads and bearing stiffness and damping could become the limiting factors to scale foil bearings for heavier rotors. Note that, in a rotor bearing assembly with small clearances, dimensional control in manufacturing, surface roughness, and rotor-bearing alignment are also limiting factors.

2.2 Bearing Force Coefficients

A majority of archival publications report the structural force coefficients of foil bearings; especially bump type FBs. There are only a few publications reporting the experimental identification of rotordynamic force coefficients [30], representing the combined effect of the bearing structure and the hydrodynamic gas film generated between the journal and the top foil. See Ref. [31] for an exhaustive review of the past works on bump type gas foil bearings. San Andrés *et al.* [4] report the experimental identification of MMFB structural parameters and give a detailed review of the prior work on experimental identification and prediction of metal mesh damper structural parameters.

DellaCorte [32] develops a rule-of-thumb (ROT) formula for representing the foil bearing stiffness and damping coefficients deduced from the prior art. The foil bearing direct stiffness (K) and damping coefficients(C) range as $K \sim$ 2500-7500 (L x D) lb/in^3 and C~0.1-10 (L x D) lb-s/in^3, respectively, where (L x D) is the projected area of the bearing. The simple formula aids in the feasibility study of a GFB, while not taking into account the effects of excitation frequency, motion amplitude, applied load and rotational speed on the bearing dynamic force coefficients.

Howard [33] and Howard *et al.* [34] describe a test rig for measurement of load capacity and torque in gas foil bearings operating at high temperatures (max. 538 °C). While conducting the static load capacity measurements, a steady-state bearing stiffness is estimated from small bearing displacements due to an incrementally varying static load. The foil bearing stiffness drops, by a factor of two, as the operating temperature increases from ambient to 538 °C as the foil underspring material loses strength with increasing temperature. In general, the bearing[4] equivalent stiffness increases with increasing applied load, but decreases with increasing rotor speed to 30 krpm. Cross-coupled force effects are ignored. Later, Howard *et al.* [35] deliver impulse loads on a test foil bearing and record the ensuing bearing motion that decays as time elapses. Damping follows from the decay rate of the rotor peak amplitudes, i.e., the estimation of

[4] The parameter derived from single input (force)-single output(displacement)

the logarithmic decrement. At a high temperature (538 °C) and for a low impact load (11.2 N), the viscous damping mechanism is dominant with little dry friction losses. However, larger impact loads excite large bearing motions and enable more energy dissipation from dry-friction damping, thus leading to a higher equivalent viscous damping coefficient; i.e. a faster motion amplitude decay.

Lee *et al*. [36] are the first to report a full set of stiffness (**K**) and damping (**C**) force coefficients for a test GFB (L=D=38.1 mm) from measurements of impact loads and ensuing bearing displacements. The test bearing floats atop a rotor spinning to a top speed of 30 krpm and under a static load of 50 N (W/LD=0.34 bar). The identified parameters are regarded as frequency-independent. Transfer functions from the impact loads show an under damped (ζ~8 %–6 %) system with a natural frequency at 80 Hz and with significant hydrodynamic cross-coupling. The test bearing direct and cross-coupled stiffnesses are nearly constant with increasing rotor speed; while the direct and cross-coupled damping coefficients decrease in magnitude. The test force coefficients show peculiar drops at the lowest speed (10 krpm). Cross-coupled stiffnesses are ~ 1/3 of the direct stiffnesses, while cross-coupled damping force coefficients are relatively small when compared to the direct damping force coefficients. Predicted bearing direct stiffnesses, derived from a model coupling the foil underspring structure to the gas film, do not agree well with the experimental force coefficients. The paper does not provide enough information on the bearing tested (geometry, materials, etc) to attempt comparisons with other available predictive tools.

Kim and San Andrés [37] compare measured imbalance responses obtained in a rigid rotor supported on generation II GFBs (D= L=38.1 mm), for cylindrical and shim-preloaded bearing configurations, against predicted rotordynamic responses using foil bearing force coefficients obtained with a computational model integrating the top foil and the bump strip layer in series with the hydrodynamically generated gas film. The measured rotor motion data serves to identify effective (synchronous rotor speed) GFB reduced stiffness and damping coefficients. The good agreement of the measured imbalance responses to the predicted ones validates the predictive computational tool.

Conlon *et al.* [21] present force coefficients for a test GFB over a range of excitation frequencies (to 300 Hz) and three rotor speeds (0, 15, 20 and 25 krpm). The test rig, similar in conception to the original rig of Glienicke [38] and constructed nearly identical to the rig of Childs and Hale [39], employs a floating bearing mounted on a rigid rotating shaft (max. speed of 30 krpm) that is supported on stiff ball bearings. A pair of orthogonally mounted shakers deliver loads onto the test element (L=D=70 mm). A frequency domain identification method, using power spectral density functions [40] to reduce data scattering, leads to an impedance matrix from which bearing stiffness and damping coefficients are extracted. The tests show that both stiffness and damping coefficients are strong functions of the motion amplitude, excitation frequency and applied static load (max. 400 N). The experiments show that the shaft speed has no effect on the rotordynamic force coefficients of the test bearing. However, in comparison to the structural parameters, a spinning rotor reduces the test element stiffness and damping coefficients, both decreasing rapidly with excitation frequency. Notorious dips in the direct stiffnesses are left unexplained. As expected, the bearing stiffness and damping coefficients increase mildly with increasing static load; again showing conspicuous dips at a frequency of 200 Hz. A follow up paper [22] comparing the dynamic forced performance of two foil bearings, generations I and II, shows the strong dependency of the bearings' force coefficients on the excitation frequency and a lesser influence of the rotational speed. In general, a generation II bearing offers significantly more damping and stiffness than a generation I albeit with a more pronounced nonlinear behavior.

San Andrés and Chirathadam [26] employ unidirectional impact load tests to identify the direct and cross-coupled rotor dynamic force coefficients of a lightly loaded MMFB, floating on a test journal spinning at 50 krpm (833 Hz). Near centered operation is assumed, thus leading to K_{XX}=K_{YY} and K_{XY}= -K_{YX}, for example. The test bearing force coefficients obtained with no journal rotation and with rotor spinning at 50 krpm (833 Hz) are similar in magnitude and trend over the excitation frequency range [10-200 Hz]. The results show the minute hydrodynamic gas film does not affect

significantly the bearing structural force coefficients. Recall that, when the much stiffer air film acts in series with the underspring structure, the overall stiffness is due to the latter. Bearing motions, recorded during rotor speed coast down tests, are complex in character with distinctive subsynchronous whirl frequencies of large amplitude. The subsynchronous whirl motions may be due to the MMFB stiffness hardening characteristics.

Rudloff *et al.* [20] estimate experimentally the frequency-dependent force coefficients of a 38.1 mm diameter generation I foil bearing. The test rig comprises of a floating bearing excited by orthogonally positioned shakers, as in Ref. [39]. For small static loads up to 50 N (W/LD = 34.4 kPa), the test results indicate that the stiffness and damping coefficients are not affected by rotational speed, max. 30 krpm (600 Hz), but display intricate non-linear frequency dependent patterns. Large amplitude dynamic loads at high excitation frequencies produce larger than expected bearing displacements, and the estimated force coefficients also display an erratic variation. The authors recommend proper nonlinear characterization of foil bearings to understand their performance and to enable accurate design procedures.

Arora *et al.* [41] identify the rotordynamic force coefficients of a gas foil bearing (L=65 mm and D = 50.8 mm), using the inverse Eigen sensitivity method [42]. The parameter identification algorithm use eigenvalues, eigenvectors, and damping ratios obtained from the modal analysis of measured frequency response functions. The damping ratio, estimated using the half-power bandwidth method in the frequency domain, along with the identified stiffness aids in computing the viscous damping coefficient. The authors, however, do not publish details on the foil bearing geometry and materials rendering impossible any comparison of the presented bearing coefficients to those available in the open literature. The test bearing, with a static structural stiffness of 1.4 x 10^6 N/m displays rotordynamic stiffness of ~0.3 x 10^6 N/m at rotor speeds as high as 60 krpm, thus evidencing a large drop in bearing stiffness once the journal is airborne. However, once airborne, the bearing stiffness gradually increases with rotor speed. The identified damping coefficients are quite high, ~500 Ns/m at 35 krpm.

San Andrés and Chirathadam [30] estimate the dynamic force coefficients of a metal mesh foil bearing, 36.5 mm in diameter and 38.0 mm in length, and study the effect of motion amplitudes, rotor speed, static load, and excitation frequency. Two orthogonally positioned shakers excite the test bearing floating on a ball bearing supported test journal. The force coefficients without shaft rotation are larger than that with rotation. However, a variation in rotor speed from 40 -50 krpm causes no appreciable differences in the direct stiffness and damping coefficient magnitudes. The direct dynamic force coefficients, as well as the structural force coefficients, decrease in magnitude with increasing rotor motion amplitudes from 20 μm to 30 μm. The cross-coupled stiffness coefficients, although small in magnitude, increase with increasing dynamic load and motion amplitudes. The direct stiffness coefficients increase with increasing frequency (200-400 Hz), while the direct damping coefficients remain fairly constant. The applied static loads (22 N and 36 N) do not appear to affect the force coefficients. Importantly, the estimated loss factor *(γ)* remains nearly a constant, $\gamma \sim 1$, in the test frequency range of 200-400 Hz, for all the test cases.

The static and dynamic forced performance of GFBs is heavily influenced by the characteristics of the elastic substructure beneath the top foil. Hence, future studies should focus on the proper characterization of the bearing underspring structure. Also, the formulation of analytical models to predict the MMFB performance to a reasonable degree of accuracy is of utmost importance before the bearings can be implemented in high speed applications.

3. ANALYSIS OF METAL MESH FOIL BEARING

3.1 Introduction

This section presents the physical and numerical modeling of a MMFB. The current model couples a finite element (FE) model representing the top foil and underspring structure and the Reynolds equation governing the generation of gas film pressure. The solution of the governing equations for various operating conditions of applied load and rotor speed is used to obtain the bearing static and dynamic forced performance characteristics. The metal mesh layer, modeled as a uniformly distributed stiffness beneath the top foil elements, defines the bearing structural stiffness. The damping in the bearing is due to material hysteresis and dry-friction losses. A loss factor (γ) represents the bearing ability to dissipate mechanical energy.

3.2 Description of Metal Mesh Foil Bearing

Figure 3 depicts a schematic representation of a metal mesh foil bearing (MMFB). The MMFB comprises of a bearing cartridge, compressed metal mesh pad (or ring), and a smooth top foil. One end of the top foil is affixed inside a narrow slot in the bearing cartridge. The journal spin direction is from the top foil free end towards the fixed end. Appendix A describes in detail the manufacturing procedure for MMFBs. The metal mesh layer can be manufactured as an annular ring [4], a single arcuate pad [30], or multiple pads [27]. The metal mesh stiffness and its mechanical energy dissipation ability depend on the metal mesh compactness, defined as the ratio of metal mesh mass to the product of the mesh volume and the metal material density [4].

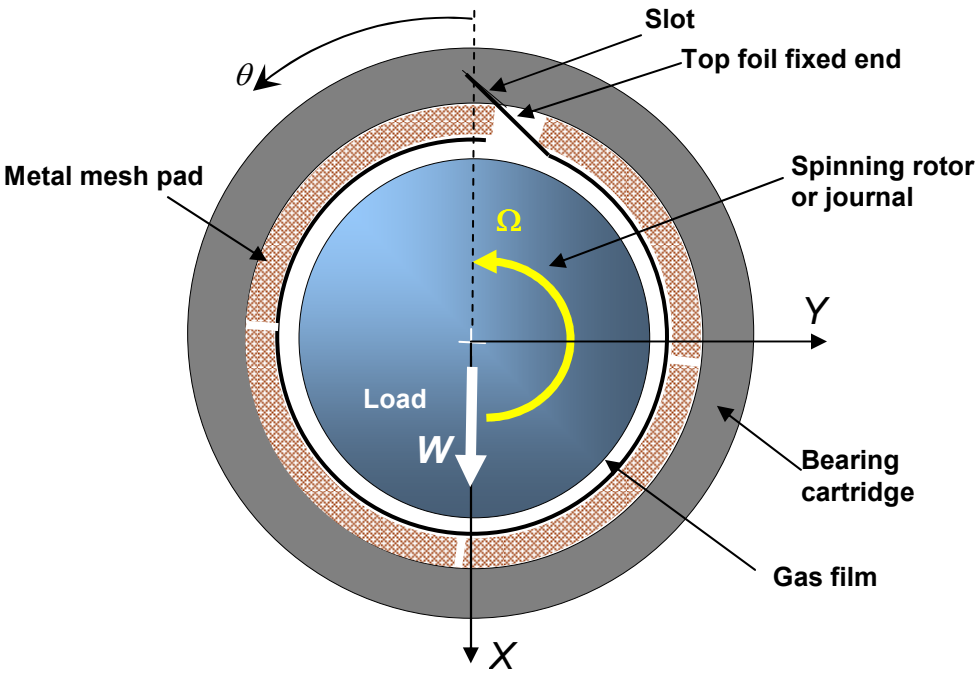

Fig. 3 Schematic representation of a metal mesh foil bearing

3.3 Modeling of a Metal Mesh Foil Bearing

3.3.1 Hydrodynamic Gas Film Model

Figure 4 shows a section of the bearing and rotor with relevant nomenclature. The top foil arcuate length (l_x) extends from the leading edge (θ_l) to its trailing edge (θ_t). During operation, due to an applied load W, the journal displaces (e_X, e_Y) eccentrically along the X and Y directions. The attitude angle Φ denotes the angle of the eccentricity vector relative to the vertical axis X. Also, the metal mesh layer deflects w due to the hydrodynamic pressure (p-p_a) acting on the top foil surface.

Thus, the film thickness (h) at angle θ combines the bearing radial clearance (c)[5], the rotor eccentricity (e_X, e_Y), and the metal mesh deflection (w).

$$h = c + e_{X(t)}\cos\theta + e_{Y(t)}\sin\theta + w_{(t)} \tag{1}$$

[5] The bearing radial clearance is usually obtained from a static load-displacement measurement and not directly from the bearing geometry.

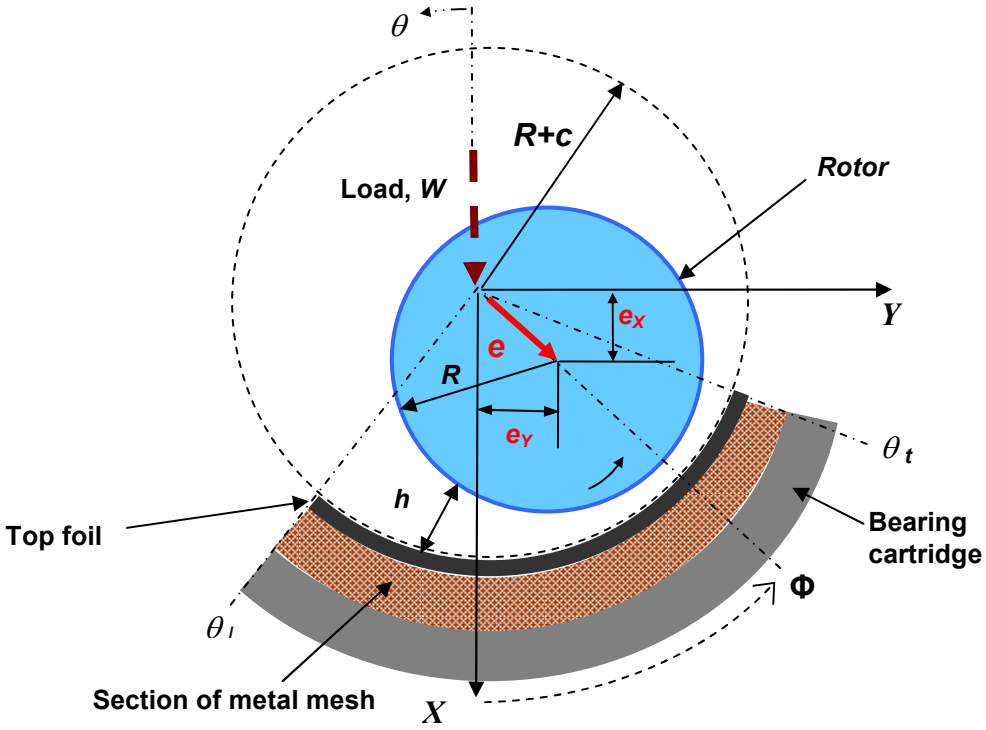

Fig. 4 Section of metal mesh foil bearing and journal, and coordinate system for analysis

The Reynolds equation for an isothermal, isoviscous ideal gas governs the generation of gas pressure, p, in the thin film region and relates pressure, p, the film thickness, h, viscosity, μ, rotor speed, Ω, and journal radius, R [36].

$$\frac{\partial}{\partial x}\left(ph^3 \frac{\partial p}{\partial x}\right)+\frac{\partial}{\partial y}\left(ph^3 \frac{\partial p}{\partial y}\right)=6\mu\Omega R\frac{\partial (ph)}{\partial x}+12\mu\frac{\partial (ph)}{\partial t}, \tag{2}$$

where $x=R\theta$, y are the circumferential and axial coordinates on the top foil surface.

The top foil deflection field (w), a function of the gas pressure difference (p-p_a), is computed simultaneously using the finite element method as detailed below.

3.3.2 Finite Element Modeling of Top Foil and Metal Mesh Underspring Support

The foil bearing prediction models available in the open literature range from simple models with the underlying elastic structure as discrete sets of uniform stiffnesses [43] to involved models integrating the top foil, to elaborately detailed bump type foil structures [44]. The metal mesh bearing consists of a "uniformly distributed"

metal mesh layer beneath the top foil. Hence, the top foil is modeled as a two-dimensional shell supported[6] on an elastic material of uniform stiffness per unit area, K_m. For dynamic analysis, a complex stiffness per unit area $K_m(1+i\gamma)$ is used to incorporate the effect of material hysteresis.

Figure 5 shows the finite element discretization of the unwrapped top foil. The top foil is considered as a two dimensional shell supported uniformly by the underlying metal mesh layer. The present model considers one or more identical metal mesh pads wrapped around the bearing housing. Also, it is assumed that there is no space between the pads after their assembly inside the bearing cartridge.

Note that in some MMFB designs, the top foil is bent and inserted into a thin slot in the bearing cartridge. For small loads, the deflection of the top foil is easily found by modeling it as a cantilever beam. For generality, the FE model ignores the top foil bent.

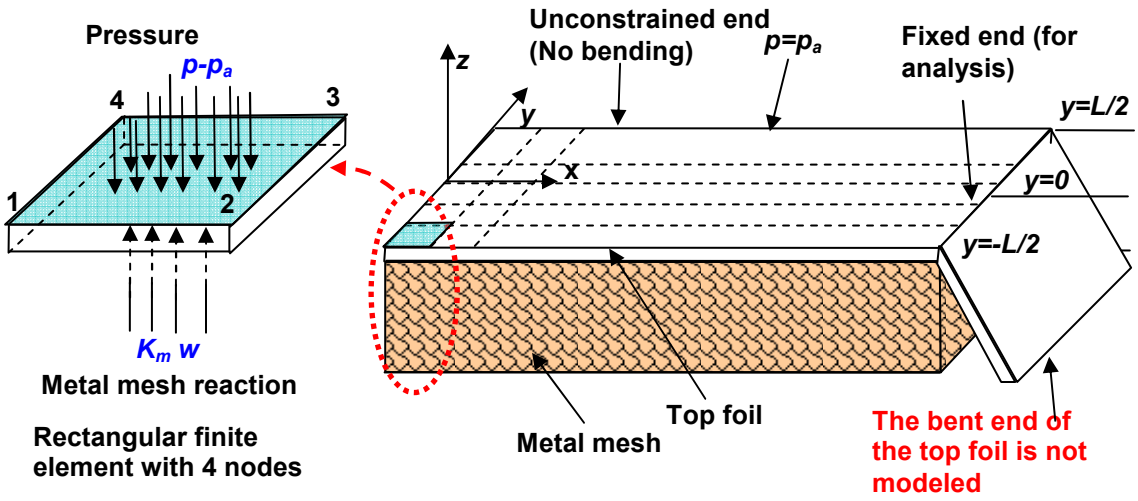

Fig. 5 Finite element discretization of an unwrapped top foil and noted boundary conditions

[6] The analysis models the top foil as always in contact with the metal mesh. However, for bearing designs where the top foil is fitted in a thin slot inside the bearing cartridge and if a small clearance exists, the applied load initially pushes the top foil towards the metal mesh structure. For small applied loads, the top foil alone may provide the reaction force to the applied load.

Figure 6 shows the shear forces (Q) and bending moments (M) per unit element length on the rectangular shell element representing a section of the top foil (curvature effects are neglected). Due to the external gas pressure difference, p-p_a, where p_a is ambient pressure, the top foil deflects (w) and the underlying metal mesh layer produces a reaction force per unit area, (K_m x w). Note that the membrane stresses, or in-plane stresses, are negligible as three ends of the top foil are free [45]. Also, the gas pressure acts normal to the top foil surface.

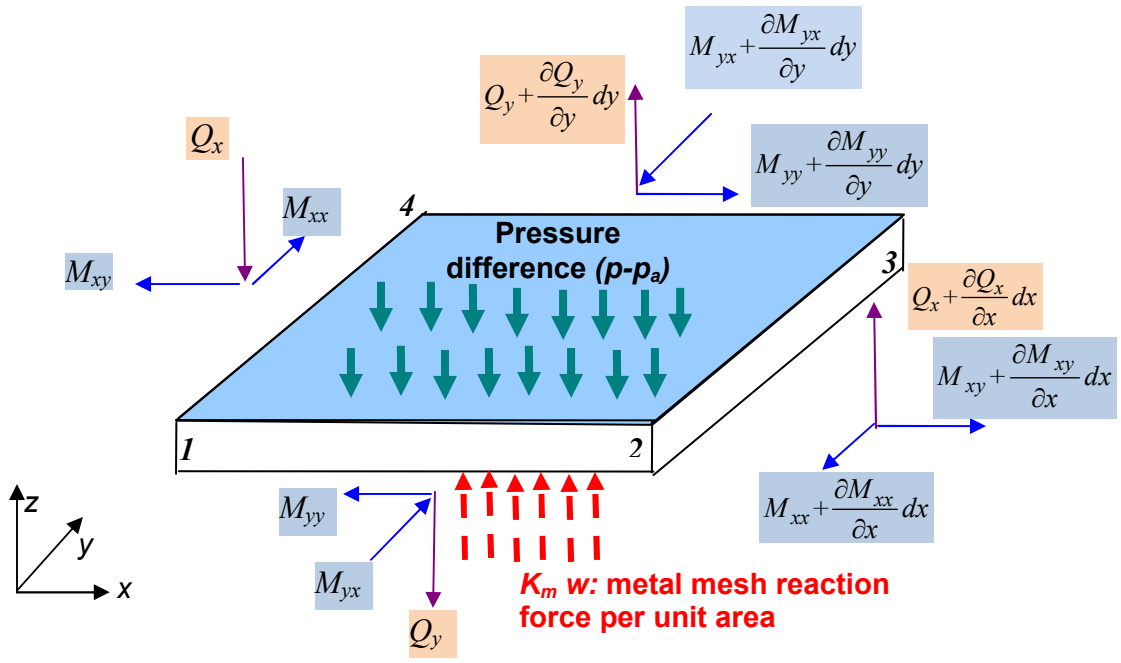

Fig. 6 Resultant bending moments (*M*) and shear stresses (*Q*) in a rectangular finite element in the domain of the plate finite element

According to first-order shear deformation theory [46], the steady state field equations for the deflection of the top foil element are

$$\frac{\partial Q_x}{\partial x}+\frac{\partial Q_y}{\partial y}-(p-p_a)+K_m w=0\,;\quad \frac{\partial M_x}{\partial x}+\frac{\partial M_{yx}}{\partial y}-Q_x=0\,;\quad \frac{\partial M_{yx}}{\partial x}+\frac{\partial M_y}{\partial y}-Q_y=0 \qquad (3)$$

where the shear forces, Q_x and Q_y, are functions of derivatives of the bending moments, M_x, M_y and M_{yx}, which in-turn are related to the derivatives of the transverse deflection (w), and rotation angles (ϕ_x, ϕ_y) [46].

In the FE method, the primary variables $\left(w, \phi_x, \phi_y\right)$ are expressed in terms of interpolation functions and the variable values at the element nodes.

$$\begin{aligned} w(x,y) &= \sum_{j=1}^{n=4} w_j \psi_j^1(x,y) \\ \phi_x(x,y) &= \sum_{j=1}^{n=4} \left(\phi_x\right)_j \psi_j^2(x,y) \\ \phi_y(x,y) &= \sum_{j=1}^{n=4} \left(\phi_y\right)_j \psi_j^2(x,y) \end{aligned} \tag{4}$$

The FE analysis develops weighted-integral formulations with weight functions $\overline{w}_{i=1,2,3}$, by integrating Eqns. (3) over the domain of the element Ω^e enclosed in a boundary Γ^e,

$$\begin{aligned} &\int_{\Omega^e} \overline{w}_1 \left(\frac{\partial Q_x}{\partial x} + \frac{\partial Q_y}{\partial y} - (p - p_a) + K_m\, w \right) = 0 \\ &\int_{\Omega^e} \overline{w}_2 \left(\frac{\partial M_x}{\partial x} + \frac{\partial M_{yx}}{\partial y} - Q_x \right) = 0 \\ &\int_{\Omega^e} \overline{w}_3 \left(\frac{\partial M_{yx}}{\partial x} + \frac{\partial M_y}{\partial y} - Q_y \right) = 0 \end{aligned} \tag{5}$$

The shear forces and moments are expressed as [46]

$$\begin{aligned} Q_x = A_{55}\left(\phi_x + \frac{\partial w}{\partial x}\right); Q_y = A_{44}\left(\phi_y + \frac{\partial w}{\partial y}\right) \\ M_x = D_{11}\frac{\partial \phi_x}{\partial x} + D_{12}\frac{\partial \phi_y}{\partial y}; M_y = D_{12}\frac{\partial \phi_x}{\partial x} + D_{22}\frac{\partial \phi_y}{\partial y}; M_{xy} = D_{66}\left(\frac{\partial \phi_x}{\partial y} + \frac{\partial \phi_y}{\partial x}\right) \end{aligned} \tag{6}$$

where D_{ij} are the plate rigidities and A_{44} and A_{55} are the coefficients of transverse shear strain terms.

$$D_{11}=\frac{E_1 h_t^3}{12\left(1-\nu_{13}\nu_{31}\right)} \quad ; \quad D_{33}=\frac{E_3 h_t^3}{12\left(1-\nu_{13}\nu_{31}\right)} \quad ; \quad D_{13}=\frac{\nu_{13} E_3 h_t^3}{12\left(1-\nu_{13}\nu_{31}\right)}$$

$$D_{66}=\frac{E_{13} h_t^3}{24\left(1-\nu_{13}\right)} \quad ; \quad A_{44}=k_t\frac{E_{32} h_t}{2\left(1-\nu_{32}\right)} \quad ; \quad A_{55}=k_t\frac{E_{12} h_t}{2\left(1-\nu_{12}\right)}$$

where h_t, E_{ij}, $\nu_{ij,\ i,j=1,2,3}$ are the shell thickness, anisotropic elastic moduli and Poisson ratios, respectively. A shear correction coefficient k_t (=5/6) compensates for the discrepancy between the distribution of transverse shear stresses of the first-order theory and the actual distribution [46].

Thus Eqn. (5) becomes

$$\begin{aligned}
&\int_{\Omega^e}\left\{A_{55}\left(\frac{\partial\overline{w}_1}{\partial x}\phi_x+\frac{\partial\overline{w}_1}{\partial x}\frac{\partial w}{\partial x}\right)+A_{44}\left(\frac{\partial\overline{w}_1}{\partial y}\phi_y+\frac{\partial\overline{w}_1}{\partial y}\frac{\partial w}{\partial y}\right)+K_m\overline{w}_1 w+\left(p-p_a\right)\overline{w}_1\right\}dxdy\\
&-\oint_{\Gamma^e}\left(Q_x n_x+Q_y n_y\right)\overline{w}_1 ds=0\\
&\int_{\Omega^e}\left\{D_{11}\frac{\partial\overline{w}_2}{\partial x}\frac{\partial\phi_x}{\partial x}+D_{12}\frac{\partial\overline{w}_2}{\partial x}\frac{\partial\phi_y}{\partial y}+D_{66}\left(\frac{\partial\overline{w}_2}{\partial y}\frac{\partial\phi_x}{\partial y}+\frac{\partial\overline{w}_2}{\partial y}\frac{\partial\phi_y}{\partial x}\right)+A_{55}\overline{w}_2\left(\phi_x+\frac{\partial w}{\partial x}\right)\right\}dxdy\\
&-\oint_{\Gamma^e}\left(M_x n_x^2+M_y n_y^2+2M_{xy}n_x n_y\right)\overline{w}_2 ds=0\\
&\int_{\Omega^e}\left\{D_{12}\frac{\partial\overline{w}_3}{\partial y}\frac{\partial\phi_x}{\partial x}+D_{22}\frac{\partial\overline{w}_3}{\partial y}\frac{\partial\phi_y}{\partial y}+D_{66}\left(\frac{\partial\overline{w}_3}{\partial x}\frac{\partial\phi_y}{\partial y}+\frac{\partial\overline{w}_3}{\partial x}\frac{\partial\phi_y}{\partial x}\right)+A_{44}\overline{w}_3\left(\phi_y+\frac{\partial w}{\partial y}\right)\right\}dxdy\\
&-\oint_{\Gamma^e}\left((M_y-M_x)n_x n_y+M_{xy}(n_x^2-n_y^2)n_y^2\right)\overline{w}_3 ds=0
\end{aligned} \tag{7}$$

The interpolation functions for the primary variables are a natural selection for weight functions ($\overline{w}_{i=1,2,3}$). However, for thin plates, the transverse shear strains introduce a numerical problem known as 'shear locking' [46], where the generalized displacement calculations become erroneous. In order to avoid this issue, Reddy [46] recommends using equal interpolation function, i.e., $\psi_j=\psi_j^1=\psi_j^2$, for the primary variables. Now, the shear energy terms associated with the transverse shear strains must be evaluated using reduced integration, i.e., using a polynomial of a lesser order. Eqns. (7) expressed in matrix form gives the finite element model.

$$\begin{bmatrix} [K^{11}] & [K^{12}] & [K^{13}] \\ & [K^{22}] & [K^{23}] \\ \text{symmetric} & & [K^{33}] \end{bmatrix} \begin{Bmatrix} \{w\} \\ \{\phi_x\} \\ \{\phi_y\} \end{Bmatrix} = \begin{Bmatrix} \{F^1\} \\ \{F^2\} \\ \{F^3\} \end{Bmatrix} \text{ or } \mathbf{K^e U^e = F^e} \tag{8}$$

where,

$$k_{ij}^{11} = \int_{\Omega^e} \left(A_{55} \frac{\partial \psi_i}{\partial x} \frac{\partial \psi_j}{\partial x} + A_{44} \frac{\partial \psi_i}{\partial y} \frac{\partial \psi_j}{\partial y} \right) dxdy + K_m \int_{\Omega^e} \psi_i \psi_j dxdy$$

$$k_{ij}^{12} = \int_{\Omega^e} \left(A_{55} \frac{\partial \psi_i}{\partial x} \psi_j \right) dxdy$$

$$k_{ij}^{13} = \int_{\Omega^e} \left(A_{44} \frac{\partial \psi_i}{\partial y} \psi_j \right) dxdy$$

$$k_{ij}^{22} = \int_{\Omega^e} \left(D_{11} \frac{\partial \psi_i}{\partial x} \frac{\partial \psi_j}{\partial x} + D_{66} \frac{\partial \psi_i}{\partial y} \frac{\partial \psi_j}{\partial y} + A_{55} \psi_i \psi_j \right) dxdy$$

$$k_{ij}^{23} = \int_{\Omega^e} \left(D_{12} \frac{\partial \psi_i}{\partial x} \frac{\partial \psi_j}{\partial y} + D_{66} \frac{\partial \psi_i}{\partial y} \frac{\partial \psi_j}{\partial x} \right) dxdy \tag{9}$$

$$k_{ij}^{33} = \int_{\Omega^e} \left(D_{66} \frac{\partial \psi_i}{\partial x} \frac{\partial \psi_j}{\partial x} + D_{22} \frac{\partial \psi_i}{\partial y} \frac{\partial \psi_j}{\partial y} + A_{44} \psi_i \psi_j \right) dxdy$$

$$F_i^1 = \int_{\Omega^e} -(p - p_a) \psi_i dxdy + \oint_{\Gamma^e} \left(Q_x n_x + Q_y n_y \right) \psi_i ds \text{; } n_x, n_y \text{ are direction cosines}$$

$$F_i^2 = \oint_{\Gamma^e} \left(M_x n_x^2 + M_y n_y^2 + 2M_{xy} n_x n_y \right) \psi_i ds$$

$$F_i^3 = \oint_{\Gamma^e} \left((M_y - M_x) n_x n_y + M_{xy} (n_x^2 - n_y^2) n_y^2 \right) \psi_i ds$$

Assembling the finite element equations for all the elements, the obtained global system of equations relates the global stiffness matrix, $\mathbf{K}^G$, generalized displacement vector, $\mathbf{U}^G$, and the generalized force vector containing the gas pressure difference acting on each node, $\mathbf{F}^G$ for *n* elements.

$$\mathbf{K}^G \ \mathbf{U}^G = \mathbf{F}^G \tag{10}$$

where,

$$\mathbf{K}^{\mathrm{G}} = \begin{bmatrix} \mathbf{K}^{\mathbf{1}} & & & \\ & \square & & \\ & & \square & \\ & & & \underline{\mathbf{K}^{n}} \end{bmatrix}, \mathbf{U}^{\mathrm{G}} = \begin{bmatrix} \{\mathbf{U}^{\mathbf{1}}\} \\ \{\mathbf{U}^{2}\} \\ .. \\ \{\mathbf{U}^{n}\} \end{bmatrix} \quad \mathbf{F}^{\mathrm{G}} = \begin{bmatrix} \{\mathbf{F}^{\mathbf{1}}\} \\ \{\mathbf{F}^{2}\} \\ .. \\ \{\mathbf{F}^{n}\} \end{bmatrix} \tag{11}$$

At the top foil fixed end, the deflection w=0 and the rotation angles $\phi_x = \phi_y$=0. Since there is no bending moments acting on the top foil, the moment terms in the generalized force vector is zero. Thus, the only input required to solve the displacement vector is the force acting on the top foil due to gas pressure. Further, the generalized displacement vector is rearranged as $\mathbf{U}^{G} = \begin{bmatrix} w_1 & \ldots & w_n; & \phi_{x1} & \ldots & \phi_{x_n}; & \phi_{y1} & \ldots & \phi_{y_n} \end{bmatrix}^{T}$ and the reduced Eqn (10) becomes

$$\underline{\mathbf{K}}^{\mathrm{G}}\ \underline{\mathbf{U}}^{\mathrm{G}} = \underline{\mathbf{F}}^{\mathrm{G}} \tag{12}$$

Decomposing the positive definite stiffness matrix $\underline{\mathbf{K}}^{\mathrm{G}}$ as the product of a lower triangular matrix $\mathbf{K_L}$ and its conjugate transpose, using Cholesky procedure [47], improves the efficiency of the numerical scheme used for finding the transverse deflections of the top foil.

$$\underline{\mathbf{K}}^{\mathrm{G}} = \mathbf{K_L}\ \mathbf{K_L}^{\mathbf{T}} \tag{13}$$

Further, a two-step procedure of forward and backward substitution finds the top foil deflections. Note that the foil bearing deflections are computed after solving Reynolds equation iteratively for the fluid film hydrodynamic pressure. Later, the top foil deflections alone are selectively extracted from the generalized displacement vector.

$$\begin{aligned} \mathbf{K_L}\ \mathbf{Y} &= \underline{\mathbf{F}}^{\mathrm{G}} \\ \mathbf{K_L}^{\mathbf{T}}\ \underline{\mathbf{U}}^{\mathrm{G}} &= \underline{\mathbf{F}}^{\mathrm{G}} \end{aligned} \tag{14}$$

3.3.3 Perturbation Analysis

Consider small amplitude motions $(\Delta e_X, \Delta e_Y)$ of the journal center and with frequency (ω) about an equilibrium position (e_{X_0}, e_{Y_0}), Then, the journal center displacements equal

$$e_X = e_{X_0} + \Delta e_X e^{i\omega t}, \qquad e_Y = e_{Y_0} + \Delta e_Y e^{i\omega t} \tag{15}$$

The pressure, p, and top foil deflection, $w=f(p-p_a)$, due to the journal center kinematics in Eqn. (15), consist of the superposition of their zeroth and first order fields

$$p = p_0 + \left(\Delta e_X p_X + \Delta e_Y p_Y\right) e^{i\omega t}$$

$$w = w(p_0) + \left[\left(\frac{\partial w}{\partial p}\right)_{p=p_0} p_X\right] \Delta e_X e^{i\omega t} + \left[\left(\frac{\partial w}{\partial p}\right)_{p=p_0} p_Y\right] \Delta e_Y e^{i\omega t} \tag{16}$$

Or, in compact form, $w = w_0 + \left(w_X \Delta e_X + w_Y \Delta e_Y\right) e^{i\omega t}$

where, $w_0 = w(p_0), w_X = \left[\left(\frac{\partial w}{\partial p}\right)_{p=p_0} p_X\right], w_Y = \left[\left(\frac{\partial w}{\partial p}\right)_{p=p_0} p_Y\right]$

p_0 and $w(p_0)$ are the equilibrium pressure and top foil deflection, respectively. Substituting eqn. (16) in to Eqn. (1), the perturbed film thickness is

$$h = h_0 + \left(\Delta e_X \cos\theta + \Delta e_Y \sin\theta\right) e^{i\omega t} + \left(\Delta e_X w_X + \Delta e_Y w_Y\right) e^{i\omega t} \tag{17}$$

where $h_0 = c + e_{X_0} \cos\theta + e_{Y_0} \sin\theta + w(p_0)$.

3.3.4 Zeroth and First Order Equations

Substituting Eqns. (16) and (17) in Eqn. (2) delivers zeroth and first-order equations for the equilibrium and perturbed pressure fields, respectively. Higher order terms are neglected. The zeroth order equation for the equilibrium pressure p_0 is

$$\frac{\partial}{\partial x}\left(p_0 {h_0}^3 \frac{\partial p_0}{\partial x}\right) + \frac{\partial}{\partial y}\left(p_0 {h_0}^3 \frac{\partial p_0}{\partial y}\right) = 6\mu\Omega R \frac{\partial\left(p_0 h_0\right)}{\partial x} \tag{18}$$

The first order equations for the perturbed pressures $p_{j=X,Y}$ are

$$\frac{\partial}{\partial x}\left(p_0 {h_0}^3 \frac{\partial p_X}{\partial x} + {h_0}^3 p_X \frac{\partial p_0}{\partial x} + 3 p_0 {h_0}^2 w_X \frac{\partial p_0}{\partial x} \right)$$
$$+\frac{\partial}{\partial y}\left(p_0 {h_0}^3 \frac{\partial p_X}{\partial y} + {h_0}^3 p_X \frac{\partial p_0}{\partial y} + 3 p_0 {h_0}^2 w_X \frac{\partial p_0}{\partial y} \right)$$
$$+\frac{\partial}{\partial x}\left(3 p_0 {h_0}^2 \cos\theta \frac{\partial p_0}{\partial x} \right)+\frac{\partial}{\partial y}\left(3 p_0 {h_0}^2 \cos\theta \frac{\partial p_0}{\partial y} \right)$$
$$= 6\mu\Omega R \frac{\partial}{\partial x}\left(p_0 \cos\theta + p_0 w_X + h_0 p_X \right) + 12 i\omega\mu \left(p_0 \cos\theta + p_0 w_X + h_0 p_X \right)$$

and (19)

$$\frac{\partial}{\partial x}\left(p_0 {h_0}^3 \frac{\partial p_Y}{\partial x} + p_Y {h_0}^3 \frac{\partial p_0}{\partial x} + 3 p_0 {h_0}^2 w_Y \frac{\partial p_0}{\partial x} \right)$$
$$+\frac{\partial}{\partial y}\left(p_0 {h_0}^3 \frac{\partial p_Y}{\partial y} + {h_0}^3 p_Y \frac{\partial p_0}{\partial y} + 3 p_0 {h_0}^2 w_Y \frac{\partial p_0}{\partial y} \right)$$
$$+\frac{\partial}{\partial x}\left(3 p_0 {h_0}^2 \sin\theta \frac{\partial p_0}{\partial x} \right)+\frac{\partial}{\partial y}\left(3 p_0 {h_0}^2 \sin\theta \frac{\partial p_0}{\partial y} \right)$$
$$= 6\mu\Omega R \frac{\partial}{\partial x}\left(p_0 \sin\theta + p_0 w_Y + h_0 p_Y \right) + 12 i\omega\mu \left(p_0 \sin\theta + p_0 w_Y + h_0 p_Y \right)$$

Recall that $w_X = \left[\left(\frac{\partial w}{\partial p} \right)_{p=p_0} p_X \right], w_Y = \left[\left(\frac{\partial w}{\partial p} \right)_{p=p_0} p_Y \right]$

As the pressure field is symmetric about the bearing mid-span, only one half of the bearing is modeled. At the boundaries, where the top foil end is free, the pressure equals ambient pressure $(p = p_a)$. Hence, the perturbed pressures at the free ends of the top foil are zero; $p_X = p_Y = 0$.

A control volume scheme with an exact flow advection model [48] is employed to numerically solve the partial differential Eqns. (18, 19). Once the pressure field solutions are obtained, the forces acting on the top foil are readily obtained by integrating the pressure over the top foil surface. The components of the bearing reaction force are

$$\begin{pmatrix} F_X \\ F_Y \end{pmatrix} = \int_0^L \int_{\theta_l}^{\theta_t} \left(p - p_a \right) \begin{bmatrix} \cos\theta \\ \sin\theta \end{bmatrix} R d\theta dy \tag{20}$$

The integration of the viscous shear stress, $\tau = \frac{h}{2}\frac{\partial p}{R\partial\theta} + \frac{\mu R\Omega}{h}$ delivers the bearing drag torque (T) as

$$T = \int_0^L \int_{\theta_l}^{\theta_t} \left[\frac{h}{2}\frac{\partial p}{Rd\theta} + \frac{\mu R\Omega}{h} \right] Rd\theta dy \tag{21}$$

The integration of the perturbed pressure components over the top foil surface delivers the dynamic force coefficients, i.e., the 4 x 4 matrices **K** and **C**, as follows

$$\mathbf{K} + i\omega\mathbf{C} = \begin{bmatrix} K_{XX} + i\omega C_{XX} & K_{XY} + i\omega C_{XY} \\ K_{YX} + i\omega C_{YX} & K_{YY} + i\omega C_{YY} \end{bmatrix} = -\int_0^L \int_{\theta_l}^{\theta_t} \begin{bmatrix} p_X \cos\theta & p_Y \cos\theta \\ p_X \sin\theta & p_Y \sin\theta \end{bmatrix} Rd\theta dy \tag{22}$$

4. COMPARISON OF PREDICTIONS TO PUBLISHED TEST DATA

This section presents the comparison of predictions with measured static and dynamic performance characteristics in a test MMFB. Predictions of MMFB performance are compared with measurements reported in Refs. [12, 26, 30].

4.1. Bearing Performance Characteristics

San Andrés *et al*. [12] and San Andrés and Chirathadam [26] present the drag torque, power loss, and airborne friction factor in a MMFB (with $L = D$ =28 mm) measured during rotor startup and shutdown cycles. Table 1 shows the nominal dimensions and specifications of the test bearing.

Table 1. Nominal dimensions and specifications for the MMFB (*L*=*D*=28.0 mm)[12]

Parameter name and physical dimension	
Bearing cartridge outer diameter, D_{Bo}	58.15 mm
Bearing cartridge inner diameter, D_{Bi}	42.10 mm
Bearing axial length, L	28.00 mm
Rotor radius, R	14.00 mm
Metal mesh outer diameter, D_{MMo}	42.10 mm
Metal mesh inner diameter, D_{MMi}	28.30 mm
Metal mesh thickness	6.90 mm
Metal mesh density (%)[7]	20
Top foil thickness, T_f	0.127 mm
Top foil elastic modulus, E	214 Gpa
Wire diameter, D_W	0.30 mm
Bearing mass (cartridge + mesh + foil), M_B	0.318 kg
Nominal radial clearance[8] , c	~ 20 μm
Metal mesh stiffness, K_m	2.8 GN/m^3

[7] Manufacturers define the density of metal mesh as the ratio of the ring mass to its volume times the metal material density.

[8] The radial clearance in a metal mesh foil bearing is usually found from static load versus deflection tests. In this test bearing, an approximate structural stiffness value, corresponding to the applied load acting on the bearing, and a nominal clearance value of ~ 20 μm is chosen such that the predicted deflections stay within the mechanical hysteresis curve.

The maximum bearing speed number, $\Lambda_g = 6\mu\Omega R_B L / p_a c^2$ is ~28 where μ=1.87 x 10^{-5} Pa.s is the viscosity of air at ambient pressure p_a=101.4 kPa and temperature 27 ºC, Ω=60 krpm is the maximum rotor speed, R_B is the bearing inner radius (~rotor radius R) and c the nominal clearance[9] =20 μm. Ref. [4] presents the static load-deflection measurements, from which a structural stiffness per unit area K_m = 2.8 GN/m^3 is found. Figure 7 shows the predicted and measured [4] bearing structural deflections for increasing static loads. Subsequent pull and push loads evidence a large hysteresis loop.

The analysis models the metal mesh pad as an elastic structure with a uniform stiffness. However, in reality, the application of a force on the metal mesh causes the bending of its many wires, slipping of wires at intersections, and even localized plastic deformations [9]. During this process, only some of the energy is stored as strain energy and the rest will be lost. Hence, when the force is removed, the compressed wires do not go back to its original position, and result in a hysteresis loop displaying characteristic non-linear stiffness during a push-pull load cycle. While a loss factor is included in the model for capturing the effect of hysteretic material damping, the consideration of a uniform stiffness for the elastic structure does not fully capture the nonlinearity in the metal mesh stiffness. Nota that the metal mesh stiffness (K_m = 2.8 GN/m^3 x LD) has a magnitude that lies between the estimated stiffnesses from the loading and unloading curves (K_m = 1.6 - 3.1 GN/m^3 x L x D), in Ref. [4], and hence the predicted deflections fall within the hysteresis loop and not along any one of the curves.

For the bearing detailed in Table 1, San Andrés *et al*. [12] present measurements of shear drag torque (T) for operation with rotor speeds (Ω) to 60 krpm and specific loads (W/LD) up to 45.7 kPa. A derived drag friction factor $f = T/(WR)$ is reported in Ref. [12]. Presently, Figure 8 depicts the predicted (hydrodynamic regime only) and measured drag friction factors (f) versus Stribeck number, $Sn = \mu\Omega/(W/LD)$, for measurements with applied static loads up to 35.8 N (W/LD= 45.7 kPa). Presently, μ=1.87 x 10^{-5} Pa.s is the viscosity of air at pressure 101.4 kPa and temperature 27 ºC. The data evidences the μdependency of the friction coefficients on specific load and rotor speed during the hydrodynamic regime.

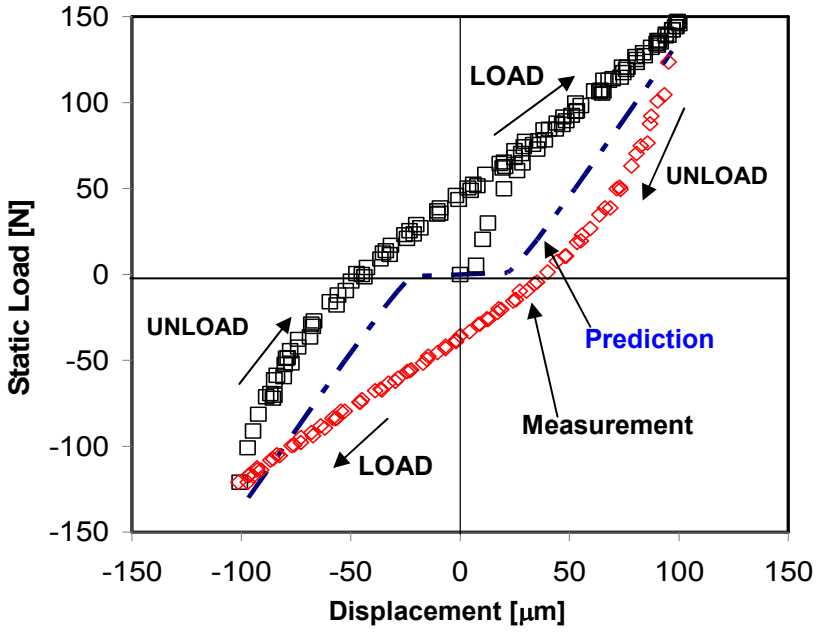

Fig. 7 Measured [4] and predicted bearing applied static load versus bearing displacement

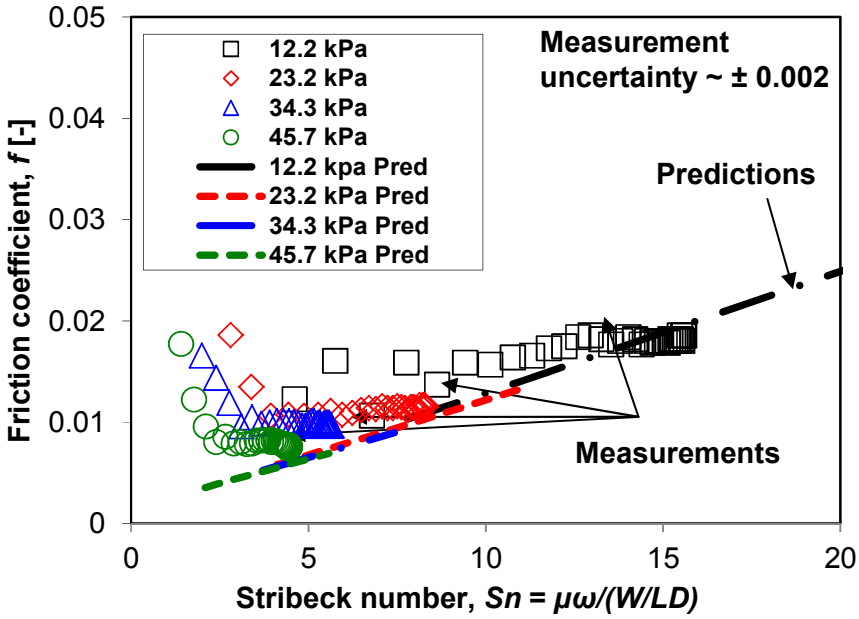

Fig. 8 Measured [12] and predicted bearing friction factor versus Stribeck number. Measurements during rotor speed up. Static specific loads noted in kPa

The measured airborne friction factor f agrees well with the predictions for all applied loads. For a Stribeck number < 5, corresponding to rotor speeds < 20 krpm, the measurements display the characteristics of operation under a mixed lubrication regime. Note that the predictive code shows friction factors only for the full film hydrodynamic lubrication regime, and not for either a mixed lubrication or dry sliding conditions. The predicted drag friction coefficient, valid only for airborne operation, is proportional to the sliding speed and lubricant viscosity, as stated by Petrov's law [49].

The minimum film thickness determines the bearing load carrying capacity [50]. Once the minimum film thickness becomes too small, smaller than the rotor or bearing surface roughness, the bearing begins to show immediate wear, noise and heat. These events most likely will lead to bearing seizure and failure. Figure 9 displays the predicted gas minimum film thickness (dimensionless with respect to the nominal clearance) versus applied specific load for various rotor speeds. The minimum film thickness decreases with an increase in static load and a decrease in rotor speed.

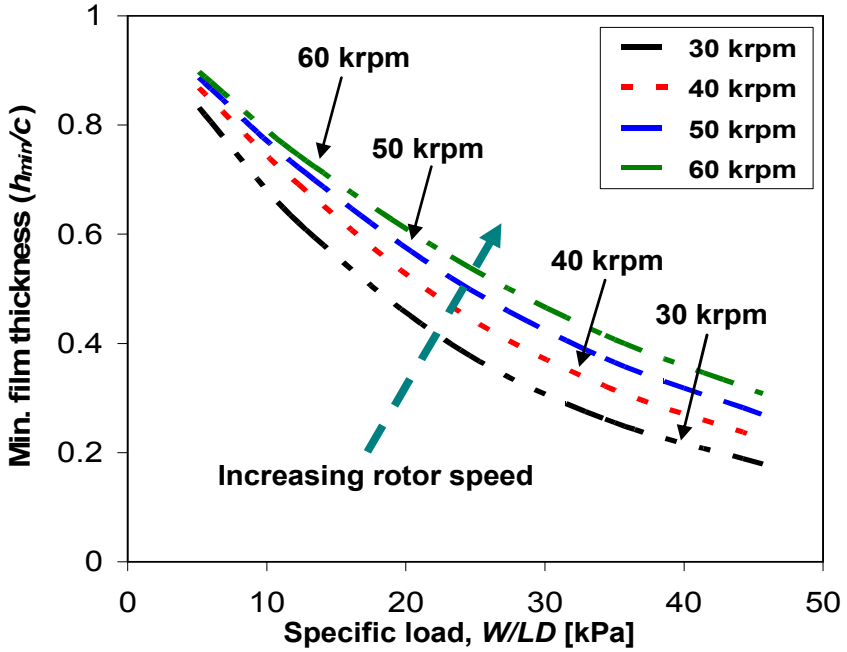

Fig. 9 Predicted minimum (dimensionless) film thickness versus specific load for increasing rotor speeds. (c = 20 μm)

Figure 10 shows (a) the journal eccentricity versus specific load for increasing rotor speeds and (b) the journal center displacements along the X and Y directions. Recall that the applied load is along the X direction, vertically downwards. In a rigid surface bearing, at high load and a low rotor speed, the journal eccentricity will approach the bearing clearance. However, as the MMFB is soft, unlike a rigid bearing, the journal eccentricity exceeds the nominal clearance at large applied loads. For small loads, and rotor speed in the 30 krpm - 60 krpm range, the journal is within the bearing clearance circle.

Figure 11 shows the journal attitude angle (Φ) decreasing with increasing specific load. The attitude angle is small (< 90°) for the specific load range and rotor speeds (30-60 krpm). For specific loads from 5 kPa to 45 kPa, the MMFB attitude angle varies from ~35° to ~ 15 °. Recall that, in a rigid bearing and with an incompressible fluid [50], the attitude angle is heavily dependent on the applied load and the rotor speed. Also, in a rigid bearing, for high rotor speeds and low loads, the eccentricity vector is orthogonal to the applied load, a probable cause for rotor instability at sufficiently high rotor speeds. Conversely, as Figure 10(b) shows, even for a high speed of 60 krpm and low applied load of 5 kPa, the eccentricity vector ($\Phi \sim 45°$) is not orthogonal to the applied load. In a cylindrical gas bearing [51], the attitude angle is not as large as that for an incompressible fluid bearing, and decreases ($\Phi \sim 0°$).

Appendix C displays the effect of increasing the metal mesh structural stiffness (K_m) on various bearing performance characteristics. The minimum film thickness and load carrying capacity increase with increasing K_m, i.e., while reducing the bearing compliance. The bearing design must aim for an optimum performance with tradeoff between compliance and load carrying capacity. For any specific load, the journal eccentricity decreases with as increasing K_m. The journal eccentricity is fairly linear with respect to the applied load as the metal mesh structure is rather soft. For soft metal mesh structural stiffnesses (1-2 GN/m^3), the top foil deflections and journal eccentricity are very similar. However, for increasing K_m (3 GN/m^3 to 4 GN/m^3) the film thickness

also reduces, and thus the journal eccentricity exceeds the amount of structural deflection.

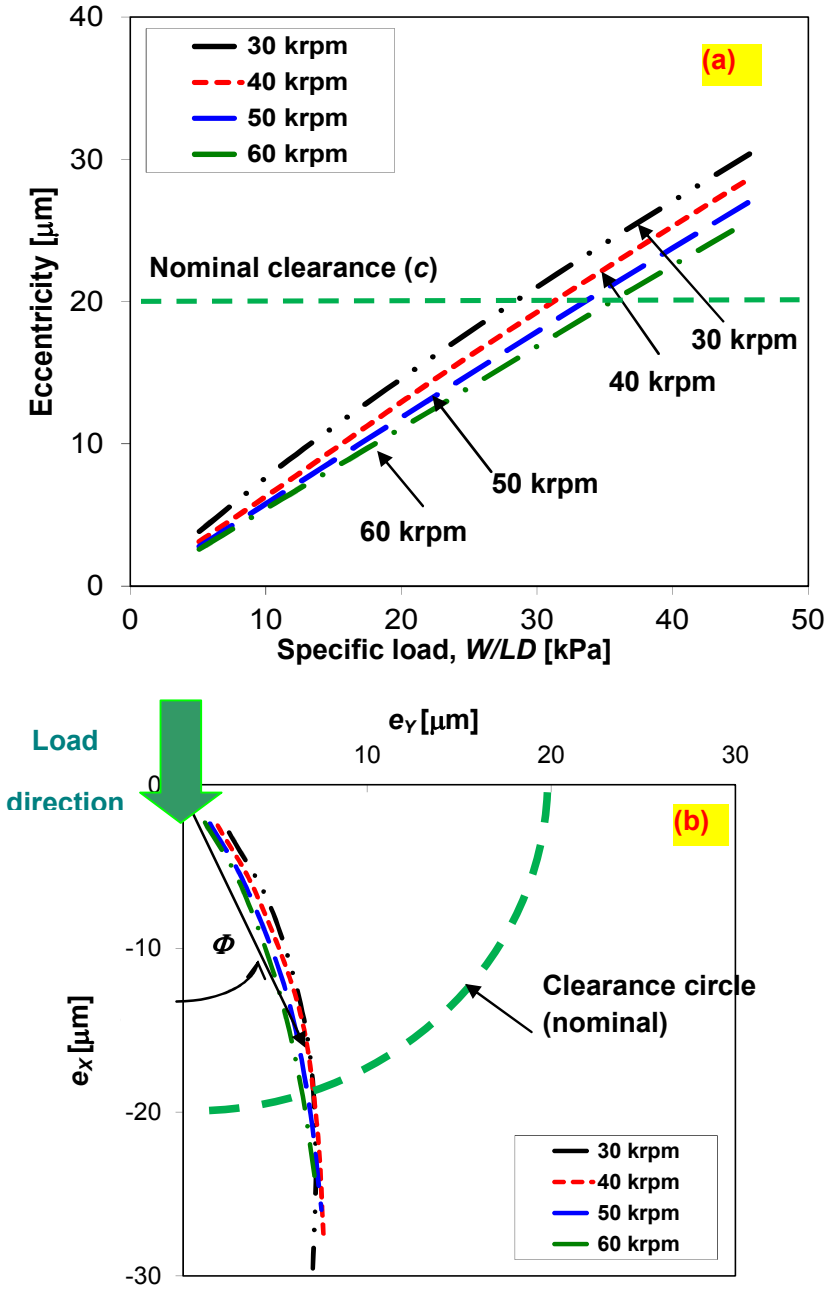

Fig. 10 Predicted journal eccentricity versus specific load and increasing rotor speeds (nominal *c* = 20 μm. (a) Eccentricity versus specific load and b) journal center displacements along *X* and *Y* directions

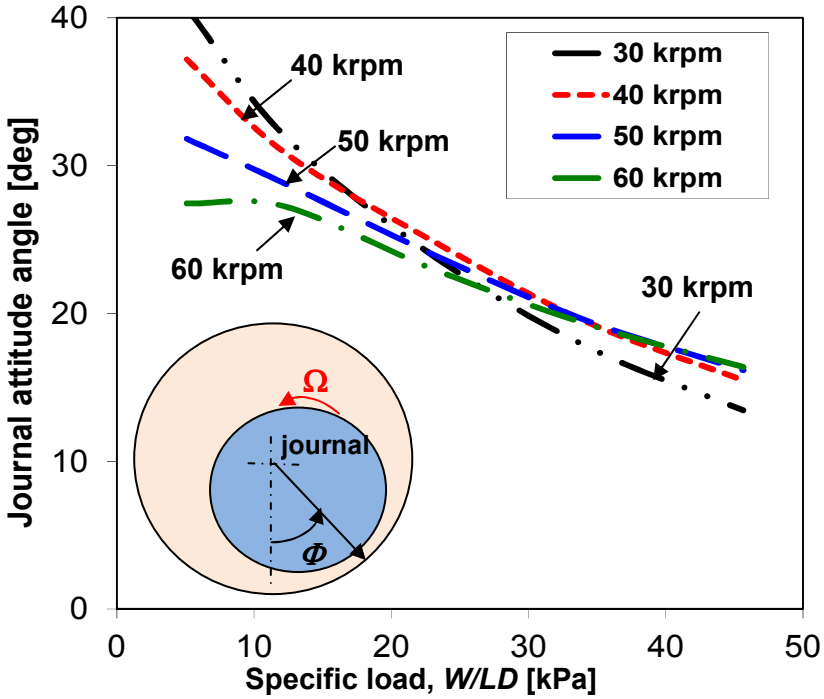

Fig. 11 Predicted journal attitude angle versus specific load for increasing rotor speeds

Appendix C also shows that the attitude angle increases with increasing K_m. Clearly, for increasing metal mesh compactness, the bearing behavior tends towards that of a rigid surface cylindrical bearing. Recall that Refs. [9, 27] report that metal mesh structural stiffness increases with increasing mesh compactness.

4.2. Bearing stiffness and damping coefficients

San Andrés and Chirathadam [30] identify the frequency dependent force coefficients of a MMFB, L = 38.0 mm and D = 36.5 mm, for various excitation amplitudes, static loads and rotor speeds. The experiments reveal that the bearing stiffness and damping slightly decrease with an increase in excitation amplitude. Prior experiments with metal mesh dampers also show similar results [9]. However, note that all compressed mesh rings do not display this behavior. For example, Ref. [52] reports that a Ni-Ti mesh, a shape memory alloy, shows the opposite trend, i.e., damping increasing with excitation amplitude.

Table 2 shows the nominal dimensions and specifications of the test bearing. The structural design of the present MMFB is different from that described in section 4.1 (Table 1). While the prior MMFB has an arcuate foil affixed within a thick metal mesh ring, the top foil in the current bearing is affixed directly to the bearing cartridge.

The analysis, as in the experimental procedure, takes the journal spinning at 50 krpm and performs forced excitation at frequencies in the 200-400 Hz range. See Appendix D for the load versus deflection measurements recorded at various rotor speeds. From static load deflection tests and dynamic load tests with the rotor at rest, a structural stiffness per unit area K_m = 0.8 GN/m^3 and loss factor γ =1.0 (in the frequency range of 200-400 Hz) are obtained. These parameters are used in the analysis to predict the MMFB dynamic performance.

Table 2. Nominal dimensions and specifications for the MMFB (*L*=38.0 mm, *D*=36.5 mm) [30]

Parameter name and physical dimension	Magnitude
Bearing cartridge outer diameter, D_{Bo}	63.57 ± 0.02 mm
Bearing cartridge inner diameter, D_{Bi}	42.07 ± 0.02 mm
Bearing inner diameter, D	36.60 mm
Bearing axial length, L	38.0 mm
Copper mesh outer diameter, D_{MMo}	42.07 ± 0.02 mm
mesh inner diameter, D_{MMi}	36.74 ± 0.02 mm
Copper mesh thickness	2.67 mm
Copper mesh density	20 %
Wire diameter, D_W	0.30 mm
Top foil thickness, T_f	0.12 mm
Top foil elastic modulus, E	214 GPa
Estimated[9] radial clearance, c	~ 75 μm
Metal mesh stiffness, K_m (determined from load-deflection tests)	0.8 GN/m^3

[9] Estimated from static load versus deflection measurements conducted with the bearing.

Figure 12 depicts the measured and predicted static load versus deflection for the metal mesh foil bearing. As the bearing has a ~75μm clearance, for small applied loads (< 20 N) the journal engages only the top foil. The fixed end of the top foil, as depicted in Figure 12 inset, acts as a cantilever beam and resists the applied force. However, with increasing loads (> 20 N), the top foil bends, touches and presses against the metal mesh structure. For further increasing loads, the top foil and the metal mesh structure remain in contact. Thus, the predictions consist of two segments, (i) only the top foil resisting the load, and (ii) the top foil and the metal mesh acting together. Since the metal mesh structure is stiffer than the top foil alone, it offers the dominant resistance to the applied load (for loads > 20 N). The predictions agree well with the measurements.

Figure 13 depicts the MMFB dynamic stiffness coefficients versus excitation frequency. The graph on the left shows the coefficients estimated from the experiments [30], while the graph on the right shows the predicted force coefficients.

A static load of 22 N, i.e., *W/LD*= 0.16 bar (2.32 psi), acts along the vertical *X*-direction. During the experiments, a sine-sweep excitation force of varying amplitude is applied on the bearing to excite bearing displacements of nearly constant amplitude, ~ 20 μm, over the entire excitation frequency range, 200 to 400 Hz. In the tests, the dynamic loads act along two orthogonal directions, each 45^o away from the vertical direction. Note that a coordinate transformation[10] is employed to obtain the test bearing coefficients along the *X* and *Y* directions displayed in Figure 13.

The predicted and measured direct stiffness coefficient along the *X* direction, K_{XX}, is ~ 0.5 MN/m. The test identified direct dynamic stiffnesses are comparable to the predictions in the 250-350 Hz range. In general, the cross-coupled coefficients, K_{YX} and K_{XY}, are much smaller than the direct stiffness values.

10

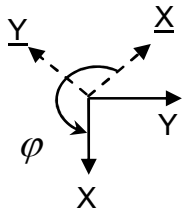

For example, the stiffness matrix **K** valid for the *X,Y* coordinate system is of the form $\mathbf{K}=\mathbf{P}\underline{\mathbf{K}}\mathbf{P}^{\mathbf{T}}$, where the coordinate transformation matrix $\mathbf{P} = \begin{bmatrix} \cos(\varphi) & \sin(\varphi) \\ -\sin(\varphi) & \cos(\varphi) \end{bmatrix}$

where φ is the angle from the $\underline{X}$ axis to the *X* axis.

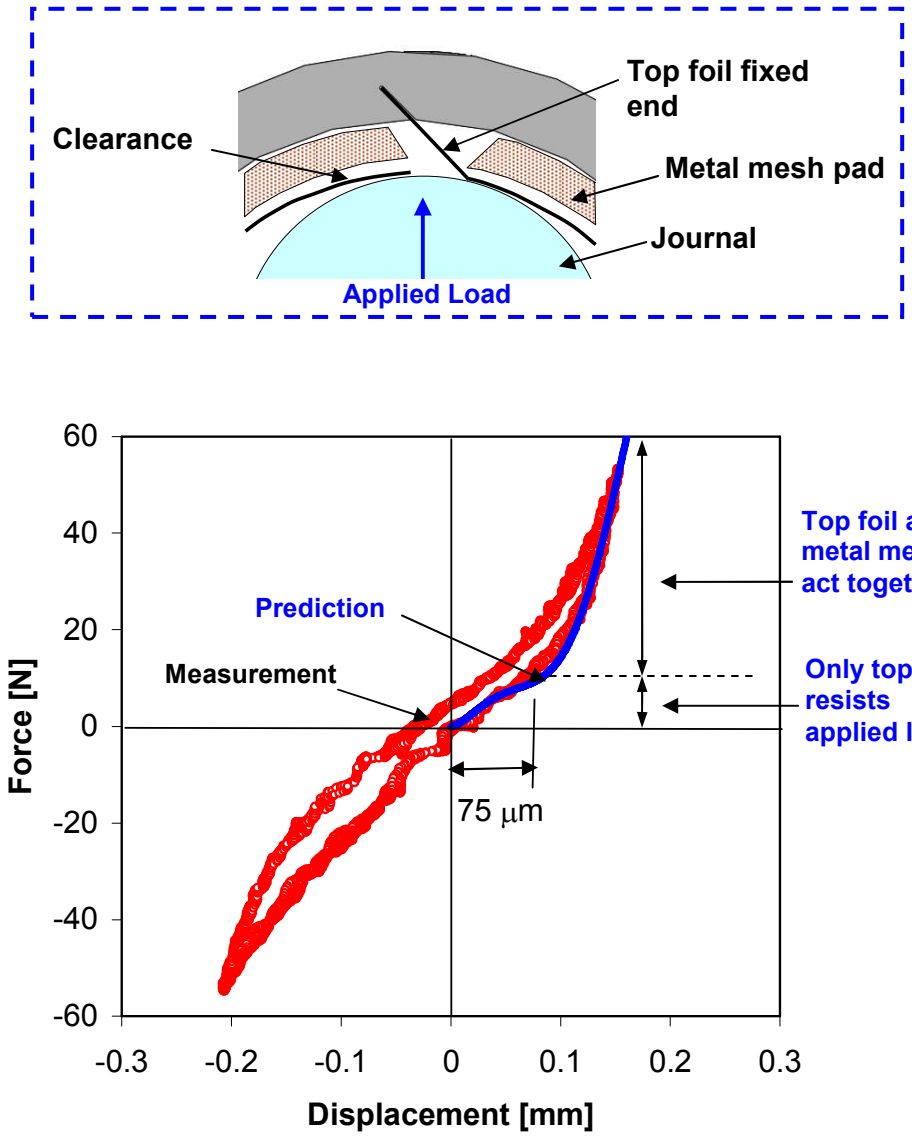

Fig. 12 Measured and predicted bearing deflection versus applied static load. Predictions at zero speed (structural deflection) comprises of two segments; (top foil deflection) and (metal mesh + top foil) deflection. Bearing from Ref. [30]. Inset shows a schematic view of the MMFB near the top foil fixed end

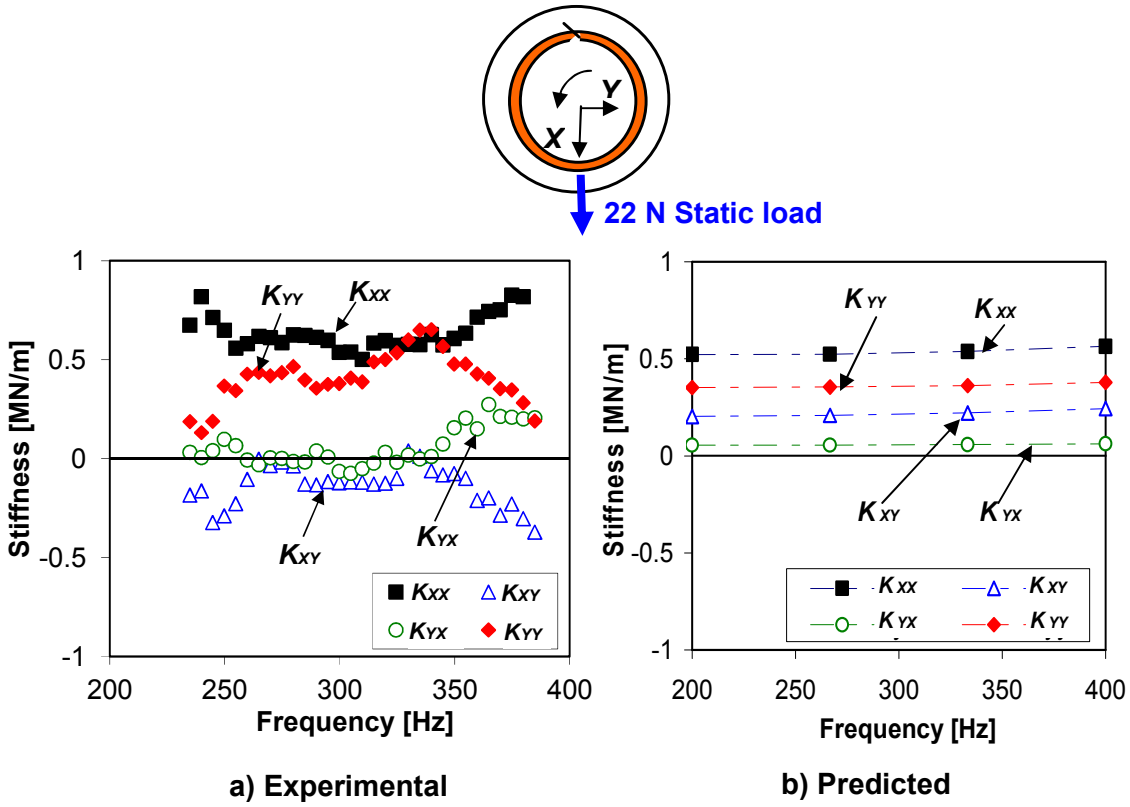

Fig. 13 MMFB a) experimental [30] and b) predicted dynamic stiffness coefficients versus frequency. Static load: 22 N vertically downwards. Loss factor γ=1. Rotor speed of 50 krpm (833 Hz)

Figure 14 depicts the MMFB damping coefficients versus excitation frequency. The graph on the left shows the coefficients estimated from the experiments [30] and the graph on the right shows the predicted force coefficients.

The estimated loss factor (γ) equals 0.9, 1.0, 1.1 and 1.2 at 200 Hz, 267 Hz, 333 Hz, and 400 Hz, respectively, showing a gradual increase with frequency. At each frequency, the predictions use the corresponding loss factors. The predictions show direct damping coefficients slightly decaying with frequency. However, the experiment damping coefficient C_{YY} is ~250 Ns/m, while C_{XX} increase from ~ 250 Ns/m to ~ 400 Ns/m, in the frequency range of 250 to 400 Hz. The predicted cross-coupled damping coefficients, C_{XY} and C_{YX}, show lower magnitudes than the direct damping coefficient

C_{XX}. Both measured and predicted cross-coupled damping coefficients are small in magnitude (< 100 Ns/m). Clearly, the model under predicts the test bearing damping coefficients. Recall that the analysis perturbs (by an infinitesimal amount) the rotor about the equilibrium position. However, in reality, the applied dynamic forces are as high as 100 N in the time domain and ~ 15 N in the frequency domain [30]. The large amplitude dynamic forces exerted in the experiments, as compared to a static load of 22 N, is responsible for the large increase in damping; thus then, the notable discrepancy between the measurements and predictions. At a low frequency of 200 Hz, where the dynamic loads are relatively small, the predictions show damping magnitudes comparable to the measurement values.

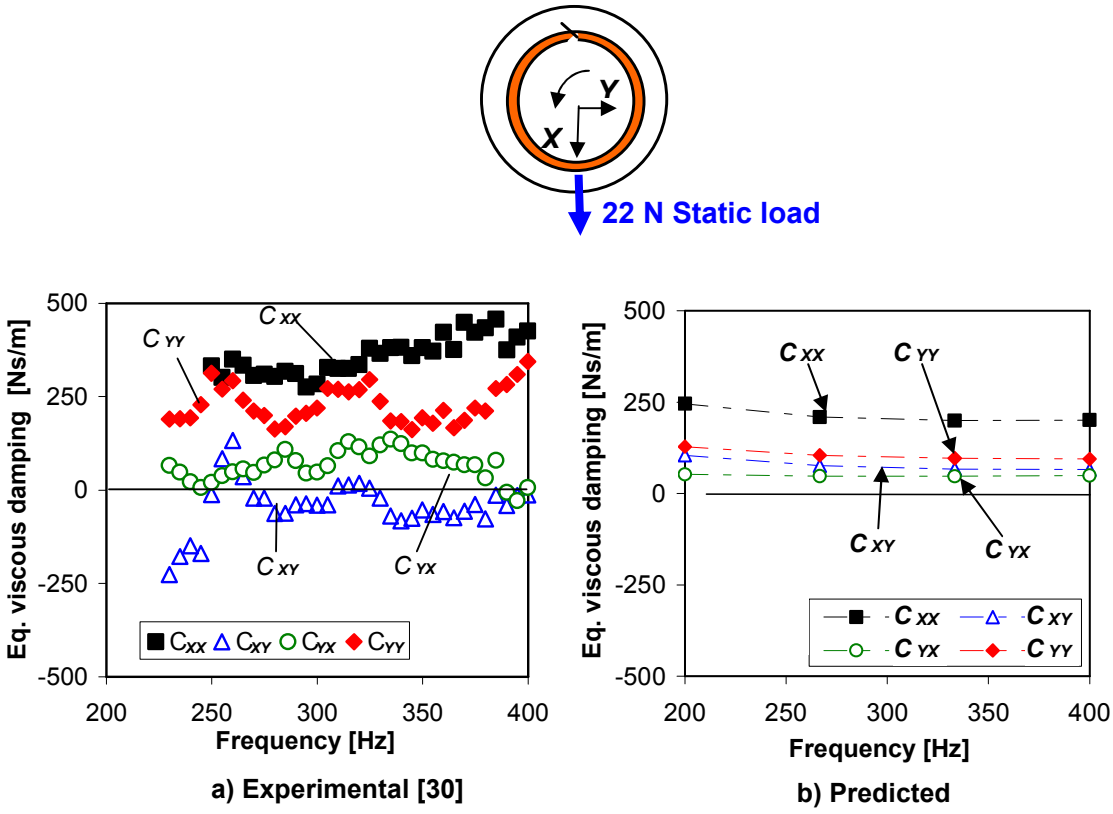

Fig. 14 MMFB: a) Experimental [30] and b) predicted dynamic equivalent viscous damping coefficients versus frequency. Static load: 22 N vertically downwards. Loss factor =1. Rotor speed of 50 krpm (833 Hz)

4.3 Conclusions

In this section, predictions of MMFB static performance characteristics and dynamic force coefficients are compared against limited published experimental data for two MMFBs, of dimensions L=D=28mm and L=38.0 and D=36.5 mm, respectively. The bearing structural stiffness and the nominal assembly clearances are estimated from static load-deflection measurements.

Predicted and measured airborne friction factors $f \sim 0.01$ to 0.02 for Stribeck number varying from 2 to 15, for the L=D=28 mm MMFB, are in good agreement. The predictions show that the minimum film thickness and journal attitude angle decreases with increasing applied load and decreasing structural stiffness. In one of the bearing designs, the top foil is affixed firmly to the bearing cartridge. The load deflection curve for this bearing indicates that the top foil stiffness affects the bearing load deflection characteristics, particularly for small applied loads.

The bearing linearized stiffness and viscous damping coefficients, in Ref. [30], are compared against predictions. The measured and predicted bearing direct stiffnesses show fairly comparable magnitudes for excitations in the 250-350 Hz range. In general, the difference between the measured and predicted direct stiffness coefficient K_{XX} is less than 10%, while that for K_{YY} is less than 20%. The cross-coupled stiffness coefficients are lower (< 40%) than the direct coefficients. The predicted direct damping coefficients show magnitudes smaller than that from the measurements. The estimated direct damping coefficients show a gradual increase with frequency. The cross-coupled damping coefficient magnitudes, for both predictions and measurements, are small < 100 Ns/m. The predicted direct damping coefficient C_{XX} is only 50% of the estimated experimental magnitude at the highest frequency of 400 Hz. At the lowest test frequency of 200 Hz, the predictions are within 10% of the estimated test values.

The predictions are compared against limited test data available from only two test bearings. For a more thorough validation of the predictive code, more test data corresponding to various different operating conditions is required.

5. COMPARISON OF PERFORMANCE CHARACTERISTICS OF A METAL MESH FOIL BEARING AND A BUMP TYPE FOIL BEARING*

5.1 Introduction

This section presents the structural performance characteristics of a MMFB and a similar sized generation I bump type foil bearing (BFB). Section 6 presents the experimental dynamic force coefficients. The measurement of the static performance characteristics such as the structural deflection, bearing drag torque, and power loss in the two bearings helps to compare vis-à-vis the two bearing types. From the start-up and shut-down rotor speed tests, rotor lift-off speeds for bearing airborne operation, drag power, and sliding friction coefficient are also estimated for both the bearings.

5.2 The Test Bearings: a Metal Mesh Foil Bearing and a Bump Type Foil Bearing

Figure 15 shows depictions of a metal mesh foil bearing (MMFB) and a generation I bump type foil bearing (BFB), both of similar size. Table 3 shows the nominal dimensions and specifications of the two test bearings. San Andrés *et al*. [4] constructed the first prototype of a MMFB (L=D=28.0 mm) using a 20% compact Copper mesh ring, made of 0.3 mm diameter wires. The test MMFB [30], as depicted in Figure 1, is manufactured in-house by assembling a bearing cartridge, compressed metal mesh pad, and a smooth top foil coated with an expendable MoS_2 layer. The top foil in the BFB[11] is identical in material and top foil thickness as that in the MMFB. The top foils are manufactured by wrapping 0.12 mm steel strips (Chrome-Nickel alloy, Rockwell 40/45) around a hot coil (~ 450 °C) and heat treated for 4 hours; and later left to cool at ambient temperature (~21 °C). After the heat treatment, the top foil loses its shiny metallic surface luster. The inner surface is brushed clean before a sacrificial coating of MoS_2 is sprayed. After drying, the coating is ~ 5 μm in thickness.

---

* Part of this section is reprinted with permission from "A Metal Mesh Foil Bearing and a Bump-Type Foil Bearing: Comparison of Performance for Two Similar Size Gas Bearings" by San Andrés, L., and Chirathadam, T.A., 2012, ASME J.Eng. Gas Turbines Power, **134** (10), p. 102501, Copyright [2012] by ASME.

[11] Donated by Korea Institute of Science and Technology (KIST), South Korea

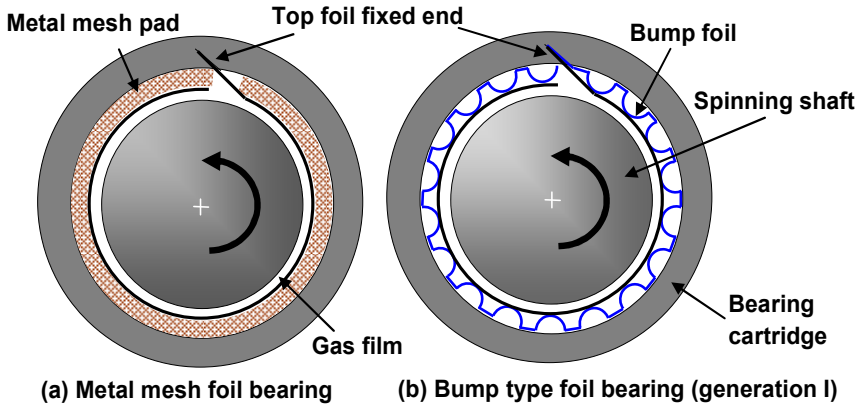

Fig. 15 Schematic representations of (a) MMFB and (b) BFB (not to scale)

Table 3. Nominal dimensions and specifications for the test MMFB and BFB

Parameter & physical dimension	**MMFB**	**BFB**
Cartridge outer diameter, D_{Bo}	63.57±0.02 mm	50.80 ± 0.02 mm
"" inner diameter, D_{Bi}	42.07±0.02 mm	37.95±0.02 mm
Bearing diameter, D	36.50 mm	36.61 mm
Bearing axial length, L	38.00 mm	38.10 mm
No of bumps	-	26 - steel
Bump pitch	-	4.3 mm
Bump length	-	2.1 mm
Bump height	-	0.54 mm
Copper mesh outer diameter, D_{MMo}	42.07±0.02 mm	-
Copper mesh inner diameter, D_{MMi}	36.74±0.02 mm	-
Copper mesh density	20 %	-
Wire diameter, D_W	0.30 mm	-
Top foil (steel) thickness, T_f	0.12 mm	0.12 mm
Top foil elastic modulus, E	214 GPa	214 GPa
Shaft outer diameter for static load-deflection tests	36.62 mm	36.62 mm
Journal outer diameter for rotordynamic tests	36.50 mm	36.50 mm
Ad-hoc bearing diametric clearance	0.150 mm	0.110 mm

The metal mesh pad is manufactured by stacking up several layers of copper gauze[12] and compressing under high load in a hydraulic press for several hours. The compression load is incrementally adjusted to obtain the desired metal mesh thickness. This is so since the metal mesh pad slightly expands upon the removal of the compression load, necessitating several rounds of load-application for obtaining the desired thickness. The compressed metal mesh pad is rolled inside the bearing cartridge. One end of the top foil is inserted in a thin slot on the inner surface of the bearing cartridge to complete the MMFB assembly.

5.3 The Bearings' Static Structural Stiffness and Loss Factor

Static-load deflection measurements were conducted for the test MMFB and BFB to estimate the bearing static structural stiffness and loss factor. Figure 16 depicts the schematic representation of a test bearing (MMFB or BFB) mounted on a rigid shaft, 36.62 mm in diameter, and affixed rigidly at both ends in a lathe such that no shaft deflection occurs during the loading process. The motion of the lathe tool holder applies unidirectional static loads on the test bearing and measured by a load cell attached between the lathe tool holder and the bearing housing. See Refs. [4, 53] for a detailed description of the test procedure.

An eddy current sensor affixed to the bearing measure the relative bearing displacement (x) with respect to the rigid stationary shaft and along the direction of load (F) application. Two bearing orientations are considered: one with the load applied 45° away from the top foil fixed end, and the other 90° away. Three cycles of push and pull loads are applied on the test bearings and bearing displacements recorded. The force (F) and ensuing displacement (x) relate best through a third order polynomial,

$$F = K_0 + K_1 x + K_2 x^2 + K_3 x^3 \tag{23}$$

where $\{K_a\}_{\alpha=0,1,2,3}$ are constants determined from the test data. The bearing structural stiffness is

$$K_S = \frac{\partial F}{\partial x} = K_1 + 2K_2 x + 3K_3 x^2 \tag{24}$$

[12] Commercially available in the form of copper gauze/copper cloth.

Figure 17 displays the MMFB static load (F) and nonlinear structural stiffness (K_S) versus displacement (x) for two bearing orientations**.** The static deflection curve, as well as the mechanical hysteresis loop and the derived stiffness are nearly the same for loads applied along the two directions. Note that the MMFB has a uniform stiffness along its circumference because the metal mesh layer is uniform in thickness. The hysteresis loop does not show any nominal-clearance region. Note that K_S~0.1 MN/m for small displacements (x ~ -0.1 mm).

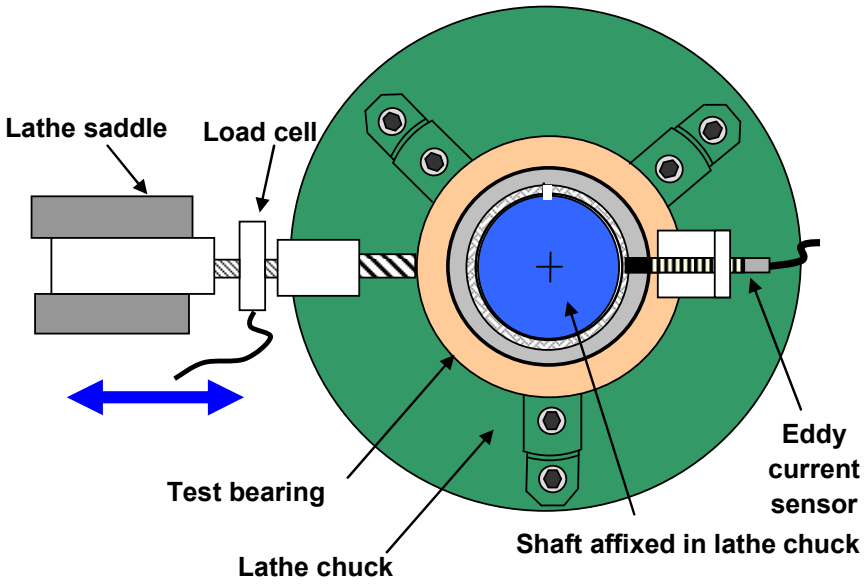

Fig. 16 Schematic view (not to scale) of test bearing mounted on a rigid shaft affixed in the lathe chuck

Figure 18 depicts similar results for the BFB, i.e. load and stiffness versus deflection. In opposition to the measurements with the MMFB, the BFB displays differing load-deflection characteristics for the two bearing orientations. The difference is due to the variation in bump stiffness distribution, in particular those near the fixed top foil end with respect to the direction of load application [53]. For a load applied 90° away from the top foil fixed end, the bearing hysteresis loop shows a nominal clearance region for small bearing displacements. However, for a load applied at 45° away, the

test results do not evidence a clearance or gap. Note that for the two load orientations K_S~0 MN/m and 0.05 MN/m at x~0 mm.

The hysteresis loop aids in the prediction of the bearing structural damping or loss factor γ, defined as [27]

$$\gamma = \frac{\Delta E_{disp}}{\pi K_L r_s^2} = \frac{1}{\pi K_L r_s^2} \oint F\, dx \tag{25}$$

where ΔE_{disp}, the area inside the hysteresis loop, is a direct measure of the mechanical energy dissipated in a cycle of loading. Above, r_s is the maximum static displacement and K_L is a linear stiffness estimated from the maximum load and bearing deflection. Figure 19 highlights the area of the hysteresis loop (ΔE_{disp}) and the linear stiffness (K_L) for a test with the MMFB.

Table 4 presents for both bearings the loss factor estimated from measurements with two load orientations. In general, γ for the MMFB is ~ 2 to 3 times that of the BFB. This result is evident since the BFB load-deflection curves show narrow mechanical hysteresis loops, see Figure 18. Notice also the similarity in linear structural stiffness (K_L) for both bearings.

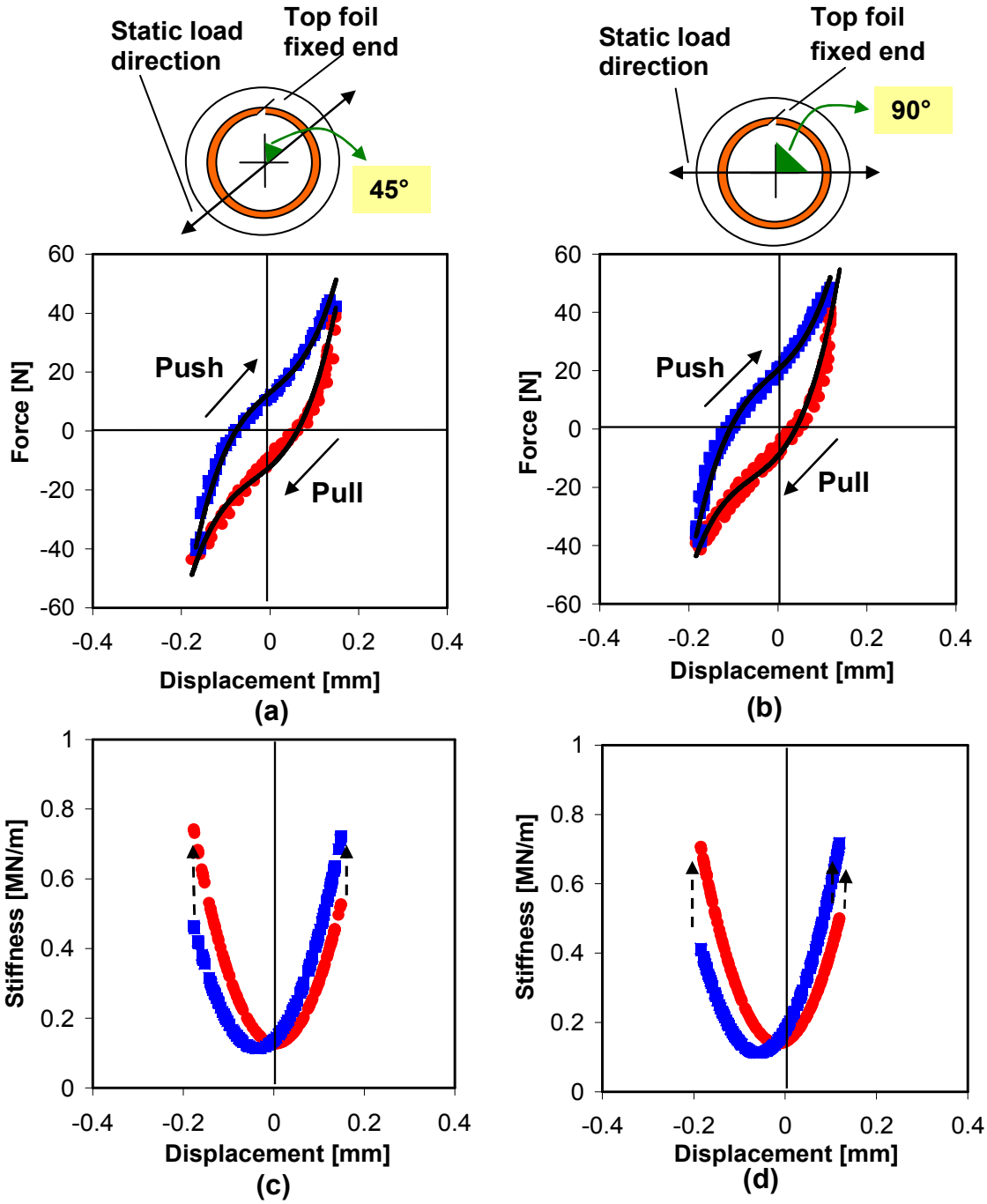

Fig. 17 MMFB applied static load and structural stiffness vs. displacement for loads applied along (a, c) 45° and (b, d) 90° from the top foil fixed end

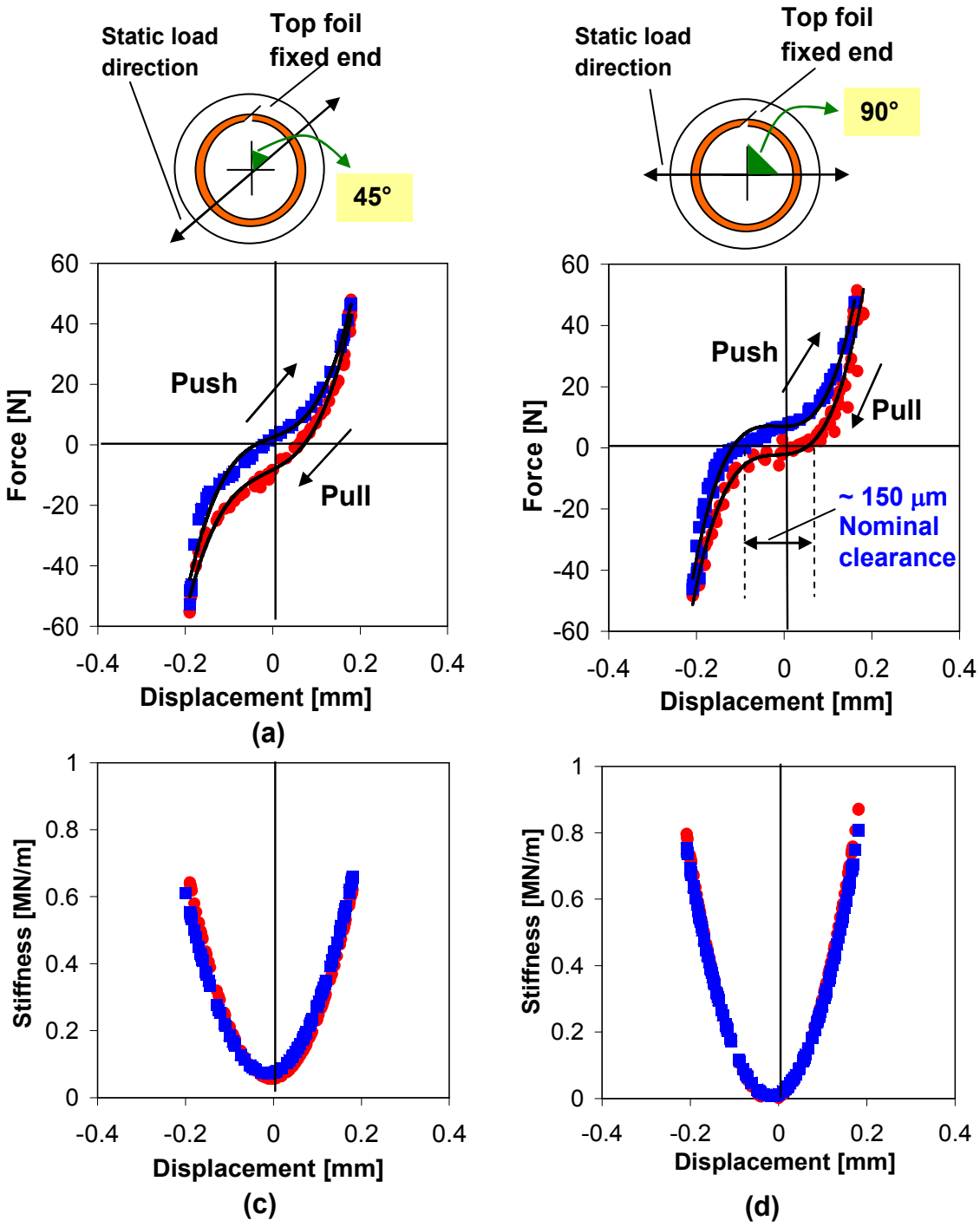

Fig. 18 BFB applied static load and structural stiffness vs. displacement for loads applied along (a, c) 45° and (b, d) 90° from the top foil fixed end

Table 4. Loss factor (γ) for MMFB and BFB estimated from static load-deflection measurements

Bearing type	Load direction	Stiffness, K_L [MN/m]	Max. static displacement, r [mm]	Estimated loss factor, γ
MMFB	45º	0.27	0.163	0.27
	90º	0.29	0.148	0.34
BFB	45º	0.26	0.184	0.12
	90º	0.25	0.187	0.13

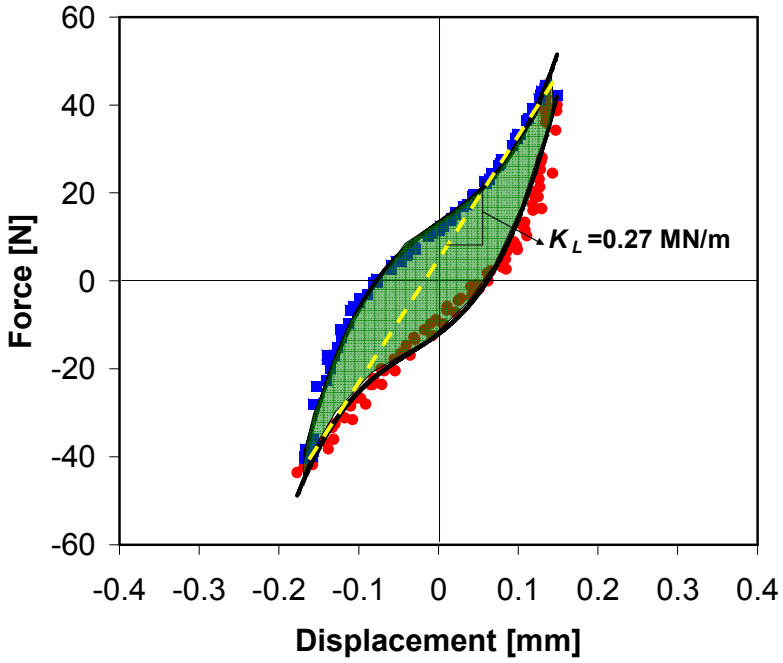

Fig. 19 Mechanical hysteresis loop and structural linear stiffness (K_L) from load-displacement measurements in a MMFB. Load applied along 45° from the top foil fixed end

5.4 The Bearings' Drag Torque, Friction Factor, and Lift-Off Speed

San Andrés *et al.* [12] report drag torque measurements for a MMFB (L/D=1) on a turbocharger driven test rig. The current work follows a similar experimental procedure

but for the method of application of static load. Figure 20 depicts the schematic view of a test bearing mounted on the turbocharger-driven rotordynamic test rig. The compressor impeller and volute of a small size commercial[13] turbocharger is removed, and a test journal, 36.50 mm in diameter, is press fitted on the exposed overhanging shaft stub. The test bearing floats on the journal once the shaft starts spinning. A torque arm attached to the bearing prevents the bearing cartridge rotation, and aids in the measurement of the bearing drag torque via the deflection of a calibrated spring. The static load is applied on the test bearing, in the vertical upward direction.

A string wraps around the test bearing cartridge and the outer race of a ball bearing. The inner race of the ball bearing is attached to a rigid frame, via a load cell and an ad-hoc device to vary load. Thus, due to the introduction of a ball bearing in-line with the application of the static load, even with a large applied load, no torque acts on the bearing and hence there is no hindrance to rotation. The arrangement facilitates seamless measurement of bearing drag torque. As the journal starts spinning, first the dry-sliding induced frictional torque and later the viscous drag torque is transmitted to the calibrated spring via the torque arm. An eddy current sensor measures the deflection of the calibrated spring and aids in the measurement of the bearing torque. A very soft elastic band applies a known preload on the spring and also prevents the axial motion of the test bearing on its journal.

The MMFB and BFB are similar in dimensions albeit with mass equal to 0.88 kg and 1.72 kg, respectively, due to difference in the bearing housing thicknesses. Hence, the applied static loads are adjusted so that the net applied vertical loads are the same on both the MMFB and the BFB. A net load (W) equals the applied load minus the bearing weight; W= 8.9 N, 17.8 N, 26.7 N and 35.6 N. Note that the applied loads per unit area are W/LD = 6.4 kN/m^2 (0.92 psi), 12.8 kN/m^2 (1.86 psi), 19.2 kN/m^2 (2.78 psi), and 26.3 kN/m^2 (3.81 psi).

During the experiments, oil is supplied continuously to the turbocharger to lubricate the ball bearings in the TC center housing. After the bearing is mounted on the test

[13] Honeywell Turbocharging Technologies donated the Garrett T25 turbocharger.

journal and the desired static load is applied, the air inlet valve to the TC is gradually opened. The valve is controlled to accelerate the journal speed to a maximum of 70 krpm, and then closed to decelerate the rotor to rest. The rotor speed and torque arm displacements are recorded for an elapsed time of 32 s.

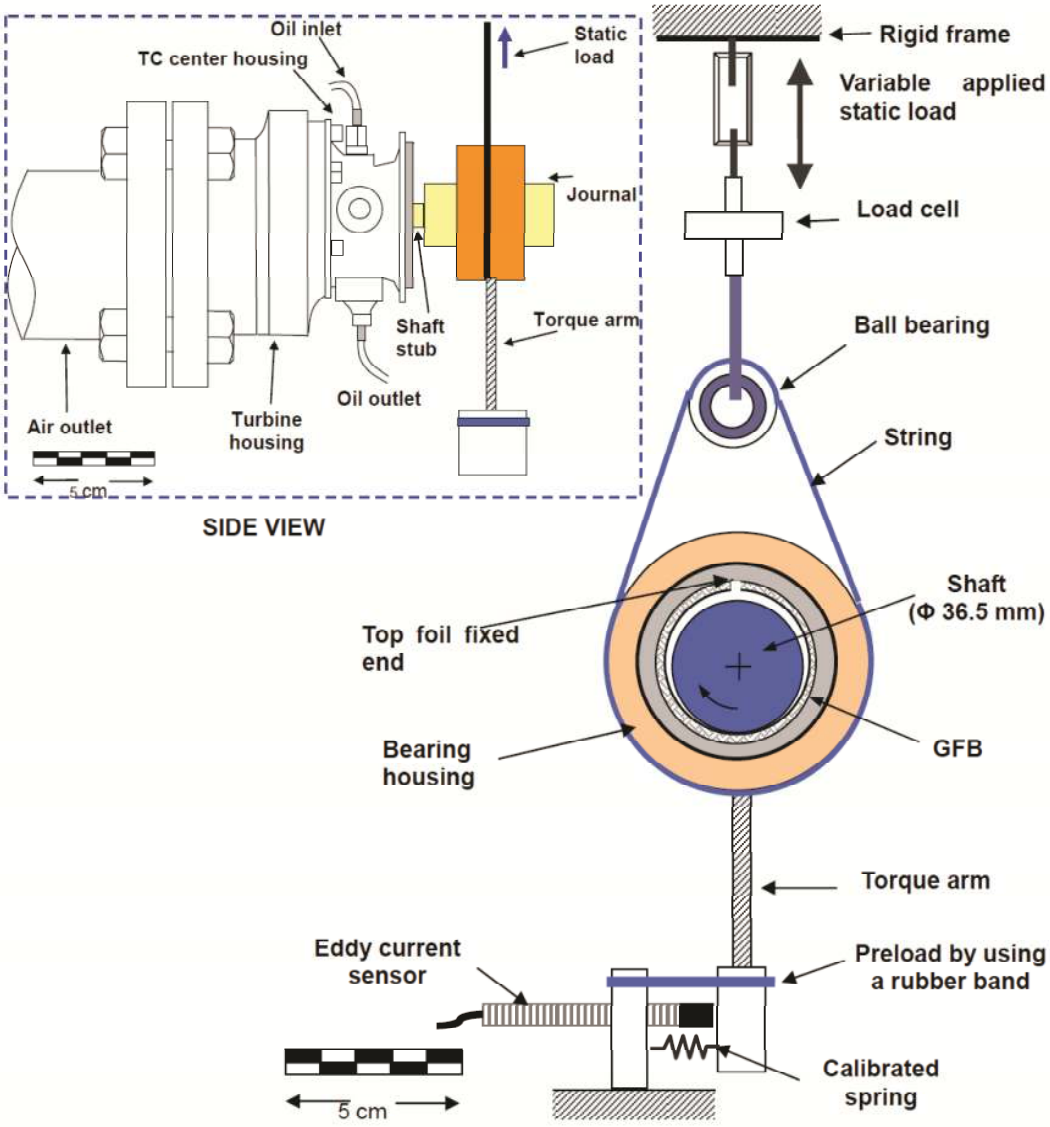

Fig. 20 Schematic view of a test bearing, rotating journal, and instrumentation for static (pull) load and drag torque measurements. Inset shows a side view of the test rig

Figure 21 depicts for both bearings the journal speed and the bearing drag torque versus time during one of the lift-off and shut down test cycles and with a net static load of 35.6 N (26.3 kN/m^2). As the rotor speeds towards a peak speed of ~70 krpm, the bearing lifts-off, first the MMFB at ~ 15 krpm and next the BFB at ~25 krpm, from the journal surface after going through the dry friction sliding and mixed lubrication regimes to become fully airborne. Rubbing of the top foil and the journal, soon after the journal starts spinning, gives rise to large start-up torques; ~ 350 N-mm for the MMFB and ~ 225 N-mm for the BFB.

The results shown in Figure 21 are typical of other load conditions and also for multiple start-up and shut down cycles. The uncertainty in the torque measurement is due to the uncertainties from the spring calibration, force gauge reading, torque arm and bearing weight measurements and voltmeter uncertainty. For a bearing drag torque equaling 20 N.mm when airborne, the maximum uncertainty is less than 2 N.mm.

Figure 22 shows the two bearings' drag torque (T) versus rotor speed (Ω) as measured during rotor start speed-up tests for increasing static loads, from 8.9 N (6.4 kN/m^2) to 35.6 N (26.3 kN/m^2). The MMFB shows a higher peak torque during start-up (also during shut-down) than the BFB; however the MMFB drag torque when airborne is smaller than that for the MMFB. Also, for the MMFB, the drag torques appears to be more or less constant (or slightly increasing) for rotor speeds from 20 to 70 krpm.

In Figure 22(b), note that the BFB drag torque gradually decreases with increasing rotor speed, giving an impression that the BFB is yet to lift. However, beyond a rotor speed of 50 krpm, the BFB drag torque is fairly constant. For both bearings, the peak torques at speed start-up and shut-down, as well as the airborne drag torque, increase with increasing static loads.

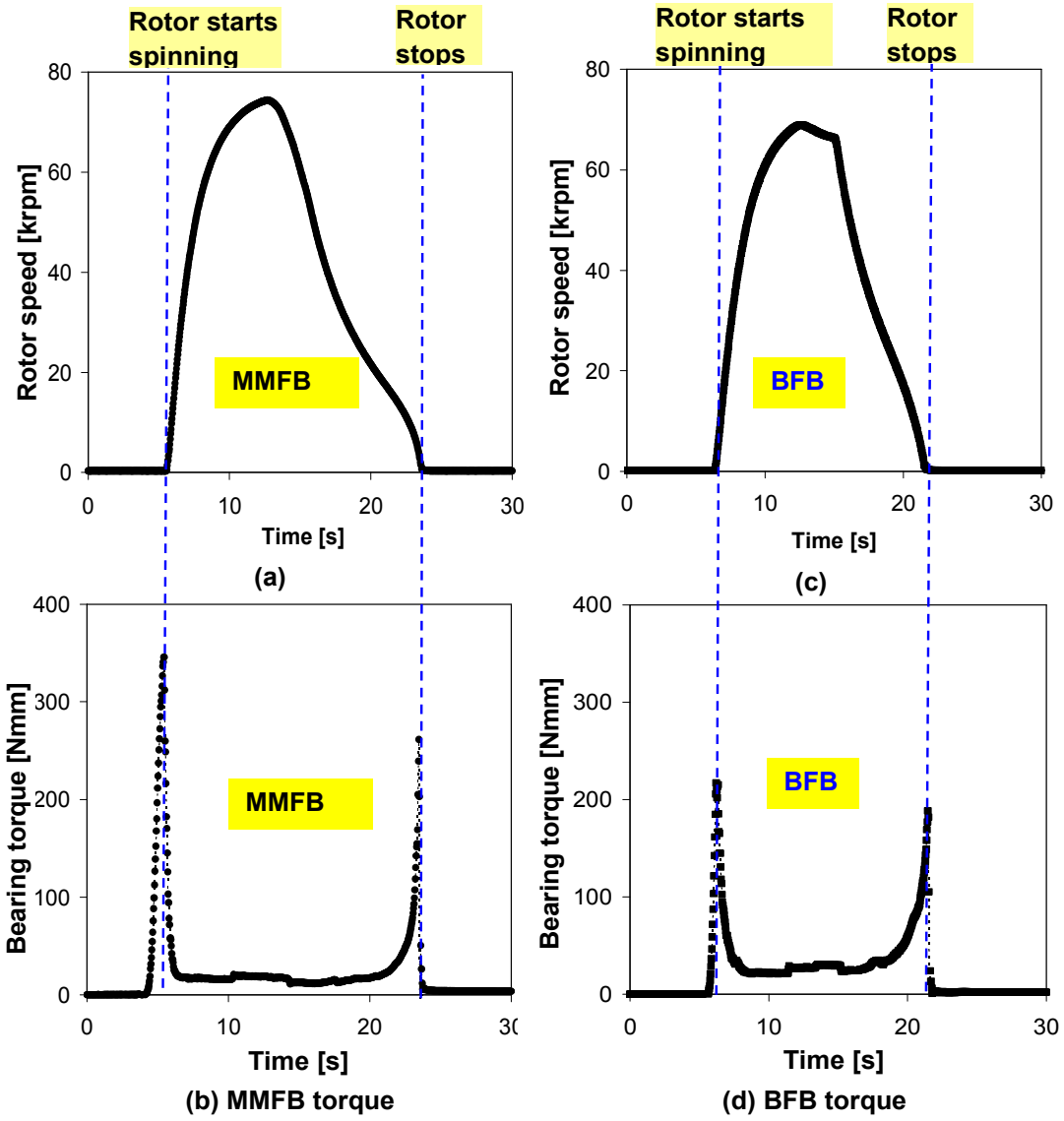

Fig. 21 Rotor speed (Ω) and bearing drag torque (*T*) versus elapsed time during a lift-off test cycle for operation with net static load *W*=35.6 N. Metal mesh foil bearing (a, b) and bump type foil bearing (c, d). Manual rotor speed-up to ~70 krpm and deceleration to rest

Figure 23 shows the drag friction coefficient $f = T/(RW)$ estimated using the test data depicted in Figure 22(a, b) for the MMFB and the BFB, respectively. Note the logarithmic scale on the vertical axes of the graphs. At start-up, when the rotor is in contact with the top foil surface (rub condition), f= 0.54 and 0.35 for the MMFB and

BFB, respectively. When airborne, f is a minute ~ 0.03 due to the generation of the air film separating the rotor from the top foil. In general, when operating airborne, the MMFB offers a lesser friction coefficient than the BFB. Note also that, once airborne, the friction factor for the MMFB decreases when the applied load increases; the opposite effects is apparent for the BFB.

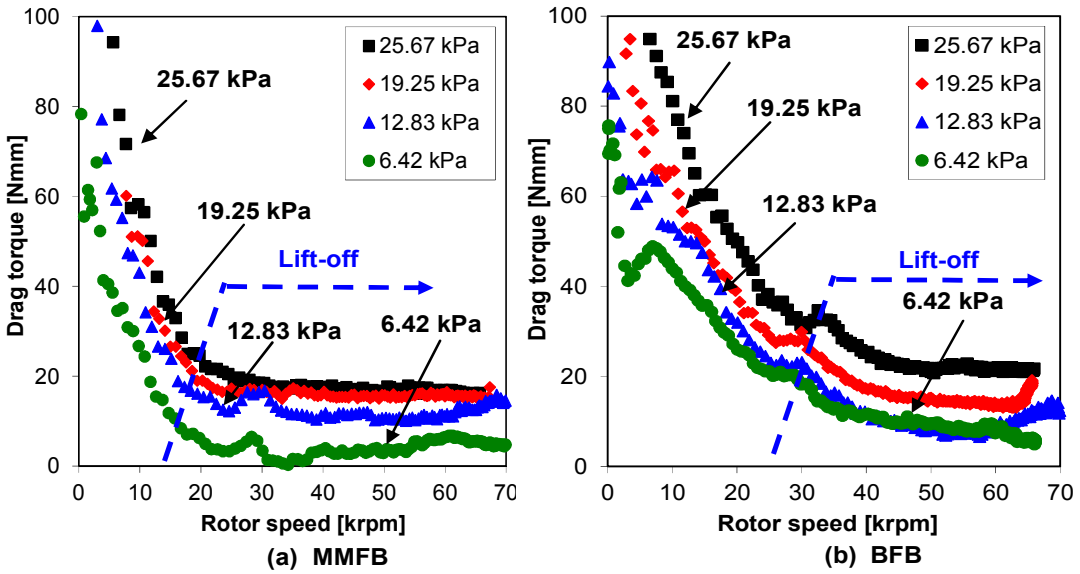

Fig. 22 Drag torque (*T*) for (a) MMFB and (b) BFB versus rotor speed (Ω) and for increasing specific static loads (*W/LD*) in kPa. Measurements during rotor speed-up tests. Rotor speed when bearing lifts-off noted

Figure 24 shows the specific drag power, $P' = P_W/LD$, where $P_W = (T \times \Omega)$ is the shear drag power. The graphs depict test results for the various applied static loads. When the bearings are airborne, the drag power is small due to the smallness of the friction coefficient, f ~ 0.03. The drag power increases as the static load increases; this effect being more pronounced for the BFB. The drag power for the MMFB, see Figure 24(a), displays an initial peak and an immediate dip that denotes bearing lift-off; the drag power later gradually increases with rotor speed. On the other hand, at low rotor speeds the drag power in the BFB does not show a clear reduction upon lift-off.

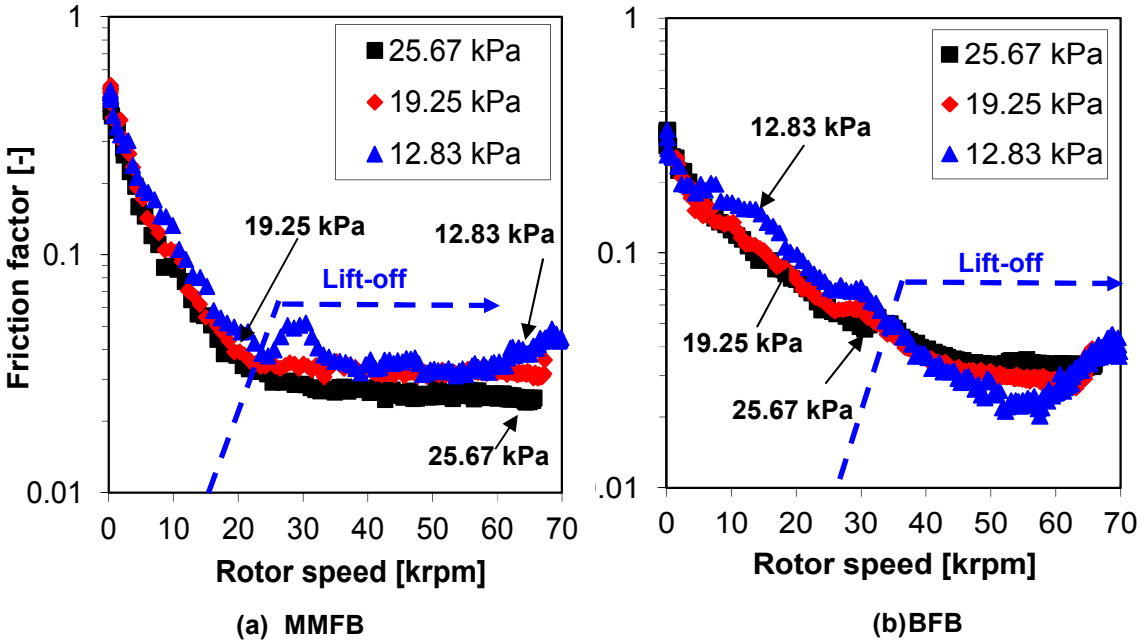

Fig. 23 Drag friction coefficient (*f*) for (a) MMFB and (b) BFB versus rotor speed (Ω) and increasing specific static loads (*W/LD*) in kPa. Test data for rotor speed-up tests

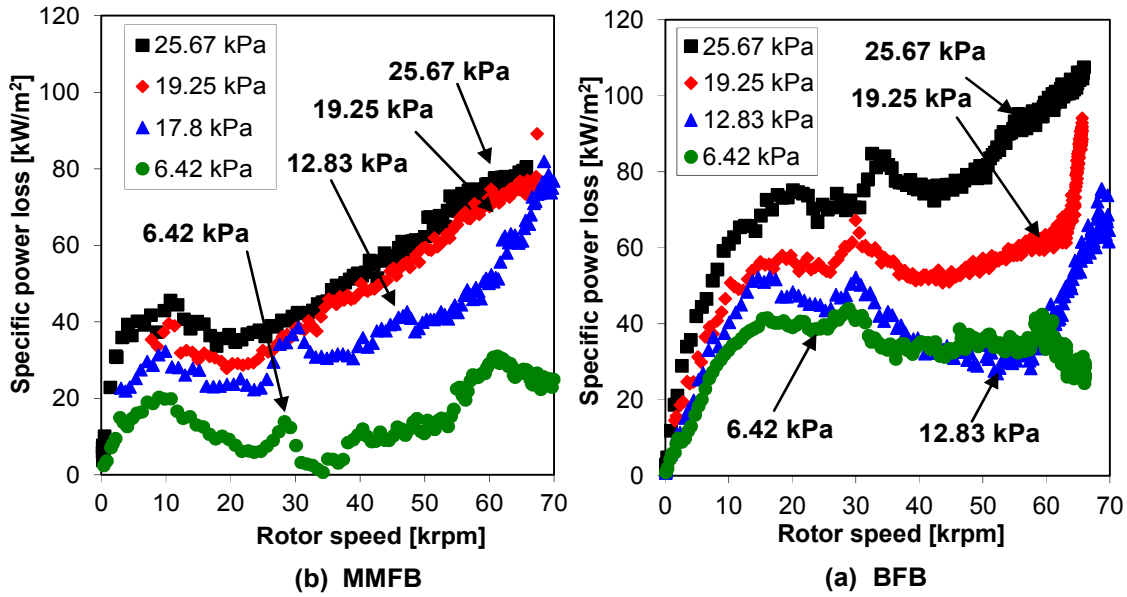

Fig. 24 Specific drag power (*P'*) for (a) MMFB and (b) BFB versus rotor speed (Ω) and for increasing specific static loads (*W/LD*) in kPa. Test data for rotor speed-up tests

Figure 25 presents the peak or maximum start-up torques for the MMFB and BFB during dry-sliding (i.e., with rotor contact) for increasing specific loads. The MMFB has a higher torque for all applied loads. Note that, once airborne, both bearings display similar drag torques at ~ 20 N-mm and with a friction coefficients f~0.03 for the largest applied load of 35.6 N. Note that prior experiments [12] with a smaller size MMFB show f as small as ~ 0.01 for operation with a rotor speed ~50 krpm.

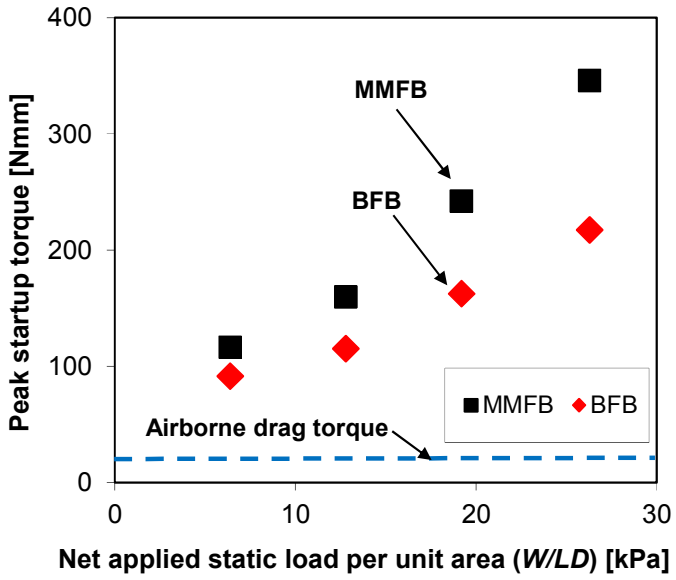

Fig. 25 Peak (maximum) start-up torque during dry-sliding condition versus specific load for both MMFB and BFB

5.5 Conclusions

This section presented comparisons of the static performance characteristics for a MMFB and a BFB, both similar in size. The parameters of importance include drag torque and lift-off speed, and bearing structural stiffness and loss factor. The static-load deflection measurements display similar non-linear variations in static structural stiffness with increasing loads for both bearings. Incidentally, the MMFB shows larger mechanical hysteresis loops that evidence structural loss factors two to three times

higher than those for the BFB. Drag torque measurements during shaft acceleration tests to a high speed (70 krpm) show that the MMFB lifts off at ~ 15 krpm while the BFB achieves airborne conditions at ~ 25 krpm. Before achieving lift-off, the MMFB shows a larger drag torque than the BFB. This regime is characterized by a dry-sliding condition. Once airborne, both bearings operate with little drag torque and showing a friction factor as low as ~0.03. Once airborne, the MMFB and GFB drag power increase with increasing rotor speed and applied static load. In general, when operating with a gas film, i.e., airborne, the MMFB displays slightly lower drag torque and power loss than the BFB. The MMFB and the BFB performance characteristics display similar trends, with the MMFB showing slightly lower drag torque and drag power loss, and an earlier lift-off speed.

[*]6. COMPARISON OF THE DYNAMIC FORCE COEFFICIENTS OF A METAL MESH FOIL BEARING AND A BUMP TYPE FOIL BEARING*

6.1 Introduction

The dynamic performance of a rotor-bearing system depends on the force coefficients of its support elements. Hence, the characterization of bearing dynamic force coefficients is important for the accurate prediction of the rotordynamic response in a high speed rotor-bearing system. This section presents the comparison of the stiffness and damping coefficients of a MMFB and a similar size BFB in the frequency range 200-400 Hz. Further, the identification of the MMFB dynamic force coefficients is extended to 600 Hz. In order to excite the test bearings at high frequencies, the test rig is modified by replacing the original electromagnetic shakers (max. 100 N dynamic load) with higher capacity shakers (max. 500 N).

6. 2 Description of Test Facility

Figure 26 shows a 'floating bearing' type rotordynamic test rig [30] for the identification of the frequency dependent dynamic force coefficients of gas bearings and for operation at varying rotor speeds while static load are applied along the vertical direction. A parameter identification procedure aids to identify the bearing dynamic stiffness and damping coefficients from sine-sweep dynamic loads exerted on the bearing along two orthogonal directions (*X*, *Y),* 45^{o} away from the vertical axis.. The electromagnetic shakers are controlled to produce dynamic loads producing bearing displacements of a certain amplitude at the specified frequency. Note that the amplitude of the dynamic loads exceeds the applied static load, in particular at high excitation frequencies. In the test rig, excitation loads are applied in the frequency range of 200-400 Hz.

[*] Part of this section is reprinted with permission from "Metal Mesh Foil Bearing: Effect of Motion Amplitude, Rotor Speed, Static Load, and Excitation Frequency on Force Coefficients" by San Andrés, L., and Chirathadam, T.A.,2011, ASME J. Eng. Gas Turbines Power, **133**(12), p.122503, Copyright[2011] by ASME.

Figure 27 displays a schematic view of the ball bearing supported turbocharger (TC), with the compressor and its casing removed, driving a shaft stub onto which a hollow journal is mounted. A test bearing slides atop the journal, of 36.5 mm in diameter and 55.0 mm in length. A squirrel-cage like structure supports the bearing with a low radial stiffness but high angular stiffness, thus reducing misalignment with respect to the rotor during dynamic loading. The cage stiffness is soft (~20 kN/m) enough not to affect significantly the dynamic parameters of the test bearing.

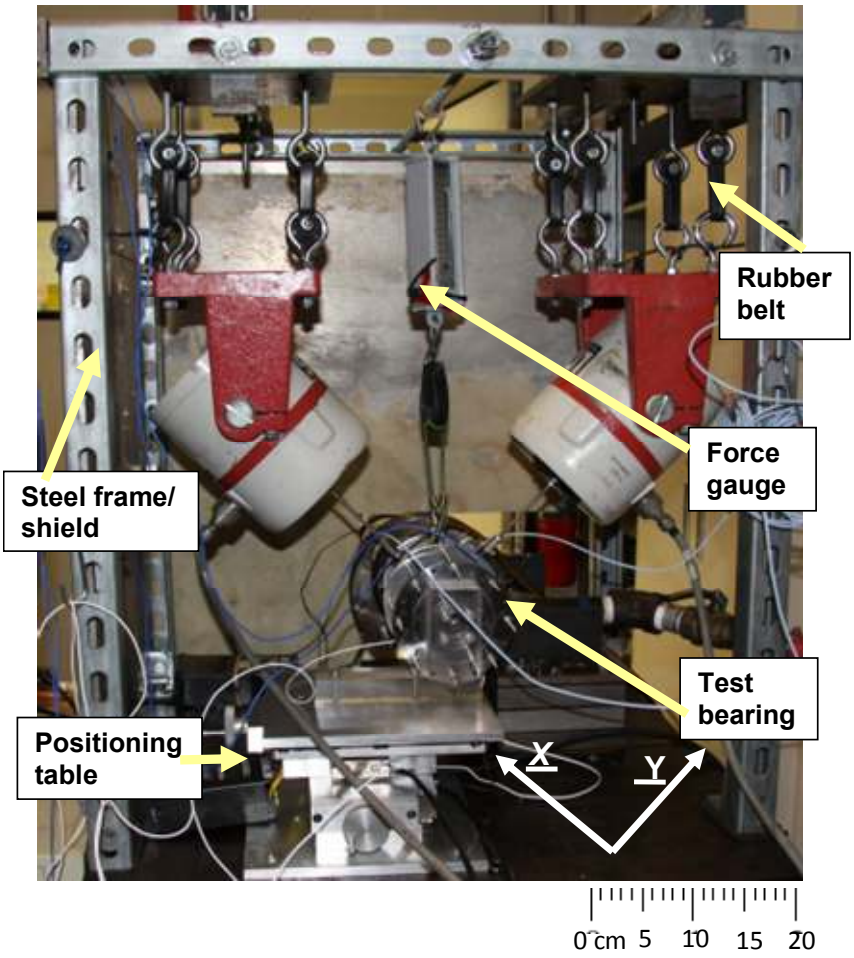

Fig. 26 Photograph of the gas bearing test rig for dynamic load excitations [30]

The squirrel cage is affixed to a turn knob controlled positioning table that can displace horizontally. This feature aids in the easy removal and mounting of the test bearing into the journal. Two eddy current sensors affixed to the bearing cartridge record the displacement of the bearing with respect to the rotating journal. Two accelerometers affixed on the bearing cartridge, at its midspan, record the absolute acceleration of the bearing along two orthogonal directions. Two electromagnetic shakers apply dynamic loads on the bearing, via stingers and force sensors. Static loads, measured with a force gauge, are applied in the vertically upward direction using strings tied onto a hook threaded at the bearing OD.

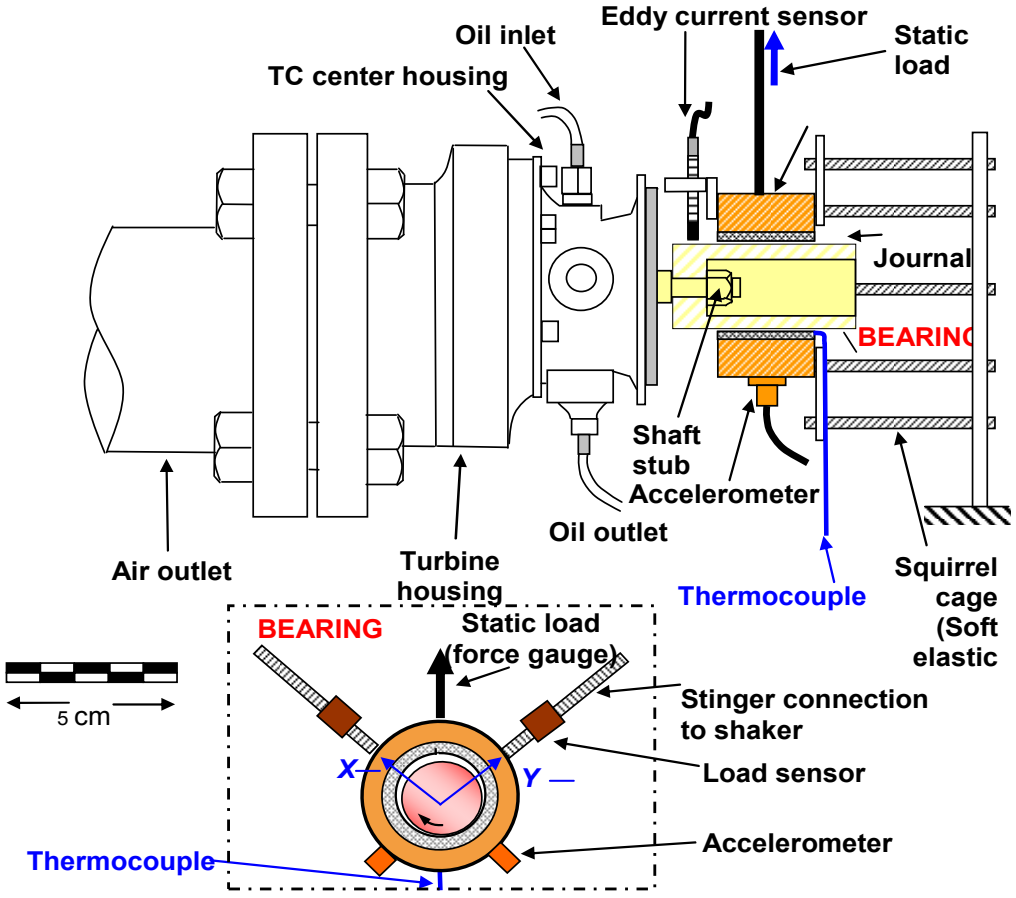

Fig. 27 Schematic view of a gas foil bearing mounted on shaft of turbocharger drive system. Inset shows two stingers for application of dynamic loads along two orthogonal directions [30]

The original set of shakers was not able to excite the bearings with sufficient motion amplitude at high frequencies. Recall that, with increasing excitation frequency, larger loads are required to generate the same motion amplitudes. Hence, for later tests, the test rig is modified with higher capacity shakers (max. 500 N). The ad-hoc loading mechanism, as depicted in Figure 28, is also improved for seamless application of the static load in the vertical direction. In the modified test rig, the test bearings are excited to a maximum frequency of 600 Hz.

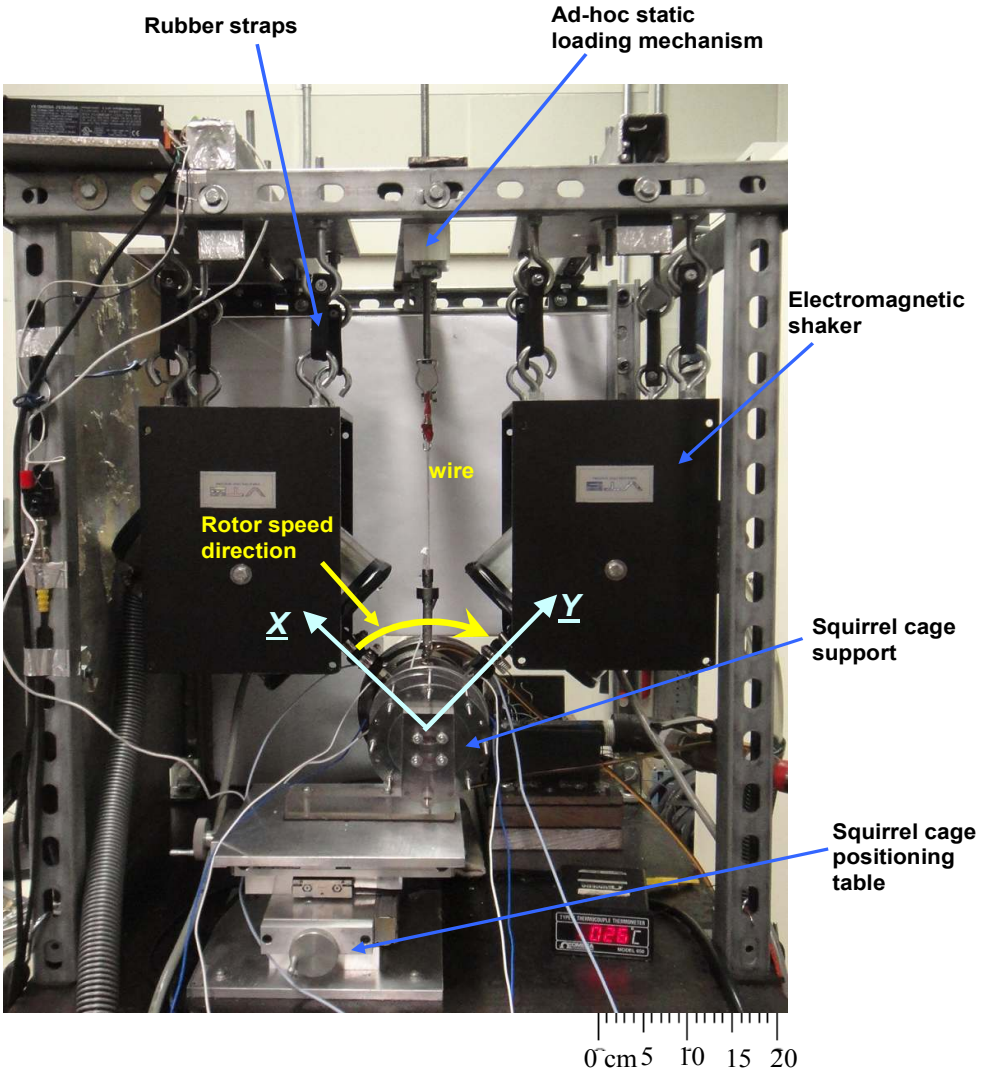

Fig. 28 Photograph of the rotordynamic test rig with high load capacity shakers. Maximum dynamic load of 500 N

6.3 Parameter Identification Procedure

The test rotor is balanced in place prior to conducting dynamic load measurements. The synchronous bearing displacements due to the spinning rotor are relatively small when compared to the forced displacements induced by the shaker loads. As the rotating shaft is rather flexible, the journal also moves when a dynamic load is applied on the bearing. Hence, for absolute bearing displacements ($\underline{X}$, $\underline{Y}$), the bearing displacements relative to the journal are $x' = \underline{X} - \underline{X}_J$ and $y' = \underline{Y} - \underline{Y}_J$.

External (shaker) loads, $F_{\underline{X}}$ and $F_{\underline{Y}}$, are exerted on the test bearing cartridge which displaces with absolute accelerations ($a_{\underline{X}}$, $a_{\underline{Y}}$), and displacements (x', y') relative to the journal. Prior to the experiments, a transfer function due to impact load tests allows the determination of the system effective masses ($M_{S_{\underline{X}}}$, $M_{S_{\underline{Y}}}$), cage structure stiffnesses $(K_S)_{\underline{X},\underline{Y}}$ and remnant damping stiffnesses $(C_S)_{\underline{X},\underline{Y}}$. The equations of motion (EOM) for the bearing cartridge are

$$\begin{pmatrix} M_{S_{\underline{X}}} a_{\underline{X}} \\ M_{S_{\underline{Y}}} a_{\underline{Y}} \end{pmatrix} + \begin{pmatrix} C_{S_{\underline{X}}} v_{\underline{X}} \\ C_{S_{\underline{Y}}} v_{\underline{Y}} \end{pmatrix} + \begin{pmatrix} K_{S_{\underline{X}}} \underline{X} \\ K_{S_{\underline{Y}}} \underline{Y} \end{pmatrix} + \begin{bmatrix} C_{\underline{X}\underline{X}} & C_{\underline{X}\underline{Y}} \\ C_{\underline{Y}\underline{X}} & C_{\underline{Y}\underline{Y}} \end{bmatrix} \begin{pmatrix} \dot{x}' \\ \dot{y}' \end{pmatrix} + \begin{bmatrix} K_{\underline{X}\underline{X}} & K_{\underline{X}\underline{Y}} \\ K_{\underline{Y}\underline{X}} & K_{\underline{Y}\underline{Y}} \end{bmatrix} \begin{pmatrix} x' \\ y' \end{pmatrix} = \begin{pmatrix} F_{\underline{X}} \\ F_{\underline{Y}} \end{pmatrix}$$

(26)

where $\left(K_{ij}, C_{ij}\right)_{i,j=\underline{X},\underline{Y}}$ are the bearing stiffness and damping force coefficients. Note $v_{\underline{X}} = \dot{\underline{X}}$ while $\dot{x}' = dx'/dt = v_{\underline{X}} - \dot{\underline{X}}_J$, for example.

The time domain forces and bearing motions are transformed into the frequency domain by applying the Discrete Fourier Transform (*DFT*). The applied forces, displacements, and accelerations become

$$\begin{bmatrix} \bar{F}_{\underline{X}(\omega)} \\ \bar{F}_{\underline{Y}(\omega)} \end{bmatrix} = DFT \begin{bmatrix} F_{\underline{X}(\omega)} \\ F_{\underline{Y}(\omega)} \end{bmatrix}; \begin{bmatrix} \bar{x}_{(\omega)} \\ \bar{y}_{(\omega)} \end{bmatrix} = DFT \begin{bmatrix} x'_{(t)} \\ y'_{(t)} \end{bmatrix}; \begin{bmatrix} \bar{A}_{\underline{X}(\omega)} \\ \bar{A}_{\underline{Y}(\omega)} \end{bmatrix} = DFT \begin{bmatrix} a_{\underline{X}(t)} \\ a_{\underline{Y}(t)} \end{bmatrix} \tag{27}$$

where ω is frequency. Recall that $DFT\left[\dot{x}'_{(t)}\right] = j\,\omega\,\bar{x}_{(\omega)}$, j=$\sqrt{-1}$, for example. Also note that

$$DFT\left[v_{\underline{X}(t)}\right]=\frac{a_{\underline{X}(\omega)}}{j\,\omega},\ DFT\left[\underline{X}_{(t)}\right]=-\frac{a_{\underline{X}(\omega)}}{\omega^2} \tag{28}$$

In the frequency domain, Eqn. (26) becomes

$$\begin{bmatrix} K_{\underline{X}\underline{X}}+j\omega C_{\underline{X}\underline{X}} & K_{\underline{X}\underline{Y}}+j\omega C_{\underline{X}\underline{Y}} \\ K_{\underline{Y}\underline{X}}+j\omega C_{\underline{Y}\underline{X}} & K_{\underline{Y}\underline{Y}}+j\omega C_{\underline{Y}\underline{Y}} \end{bmatrix}\begin{pmatrix} \bar{x}_{(\omega)} \\ \bar{y}_{(\omega)} \end{pmatrix}=\begin{pmatrix} \bar{G}_{\underline{X}(\omega)} \\ \bar{G}_{\underline{Y}(\omega)} \end{pmatrix}$$

$$=\begin{pmatrix} \bar{F}_{\underline{X}(\omega)} \\ \bar{F}_{\underline{Y}(\omega)} \end{pmatrix}-\begin{pmatrix} M_{S_{\underline{X}}}+C_{S_{\underline{X}}}/j\omega-K_{S_{\underline{X}}}/\omega^2 \\ M_{S_{\underline{Y}}}+C_{S_{\underline{Y}}}/j\omega-K_{S_{\underline{Y}}}/\omega^2 \end{pmatrix}\begin{pmatrix} \bar{A}_{\underline{X}(\omega)} \\ \bar{A}_{\underline{Y}(\omega)} \end{pmatrix} \tag{29}$$

Or in compact form,

$$\begin{bmatrix} H_{\underline{X}\underline{X}} & H_{\underline{X}\underline{Y}} \\ H_{\underline{Y}\underline{X}} & H_{\underline{Y}\underline{Y}} \end{bmatrix}\begin{pmatrix} \bar{x}_{(\omega)} \\ \bar{y}_{(\omega)} \end{pmatrix}=\begin{pmatrix} \bar{G}_{\underline{X}(\omega)} \\ \bar{G}_{\underline{Y}(\omega)} \end{pmatrix} \tag{30}$$

where $\mathbf{H}_{(\omega_k)}=\left(\mathbf{K}+j\,\omega_k\,\mathbf{C}\right)$ is the matrix of bearing impedances at discrete frequencies ω_κ. Two linearly independent forced excitations are required to identify the eight bearing force coefficients (four stiffnesses and four damping parameters). Hence, the system is sequentially excited along the $\underline{X}$ and $\underline{Y}$ directions, i.e., by applying loads of the form $\mathbf{F}^{\underline{X}}=\begin{pmatrix} F_{\underline{X}} & 0 \end{pmatrix}^T$ and $\mathbf{F}^{\underline{Y}}=\begin{pmatrix} 0 & F_{\underline{Y}} \end{pmatrix}^T$. The combined algebraic equations for the two sets of excitations are written as

$$\begin{bmatrix} H_{\underline{X}\underline{X}} & H_{\underline{X}\underline{Y}} \\ H_{\underline{Y}\underline{X}} & H_{\underline{Y}\underline{Y}} \end{bmatrix}\begin{bmatrix} \bar{x}^{\underline{X}} & \bar{x}^{\underline{Y}} \\ \bar{y}^{\underline{X}} & \bar{y}^{\underline{Y}} \end{bmatrix}=\begin{pmatrix} \bar{G}^{\underline{X}}_{\underline{X}} & \bar{G}^{\underline{Y}}_{\underline{X}} \\ \bar{G}^{\underline{X}}_{\underline{Y}} & \bar{G}^{\underline{Y}}_{\underline{Y}} \end{pmatrix}\Rightarrow\mathbf{H}\bar{\mathbf{z}}=\bar{\mathbf{G}} \tag{31}$$

At each frequency ω_κ, the bearing impedance coefficients are obtained from $\mathbf{H}_{(\omega_k)}=\bar{\mathbf{G}}_{(\omega_k)}\bar{\mathbf{z}}^{-1}_{(\omega_k)}$.

Lastly, the force coefficients are transformed to the (*X, Y*) coordinate system described in Figure 3 such that, by convention, one of the principal directions (*X*) is

parallel to the line of application of the static load. Recall that, for instance the stiffness matrix referred to the (*X, Y*) coordinate system equals $\mathbf{K}=\mathbf{P}\underline{\mathbf{K}}\mathbf{P}^{\mathbf{T}}$, where **P** is the coordinate transformation matrix.

Gas foil bearings are nonlinear with respect to motion amplitudes and excitation frequencies. Periodic loads of fixed amplitude produce bearing dynamic displacements that decrease in magnitude with frequency. This is so since more mechanical energy is required to generate similar motion amplitudes at higher frequencies. Hence, in order to maintain constant displacement amplitude, a controlled sine-sweep load of the following form is applied.

$$F_{(t)} = \left[F_o + \Delta F\, t\right] \sin\left[(\omega_o + \Delta\omega t)t\right] \tag{32}$$

where F_o is the magnitude of the applied force at the initial frequency of ω_O, and ΔF and $\Delta\omega$ are rates of increase in force and frequency, respectively. The changes in force (ΔF) and frequency ($\Delta\omega$) are based on the elapsed time for the measurement and the final force needed to keep the displacements magnitude nearly constant.

Figure 29 depicts a typical sine sweep load (300-600 Hz), applied along the $\underline{X}$ direction, versus time. The programmed data acquisition system generates ten consecutive excitation force signals of 0.2 s, and records 4,096 data samples of force, displacement, and bearing acceleration signals at a sampling rate of 20,480/second for each excitation waveform. The ten waveforms (40,960 data samples) are recorded and averaged in frequency domain.

Figure 30 shows the Discrete Fourier Transform (DFT) amplitudes of the dynamic forces versus frequency. Note that the amplitude of the forces in the frequency domain is much smaller than those in the time domain. During the tests, it is noticed that the amplitudes of dynamic force required to maintain identical displacement amplitudes along the $\underline{Y}$ direction are larger than that those along the $\underline{X}$ direction. This is due to the difference in bearing stiffness along the $\underline{Y}$ direction.

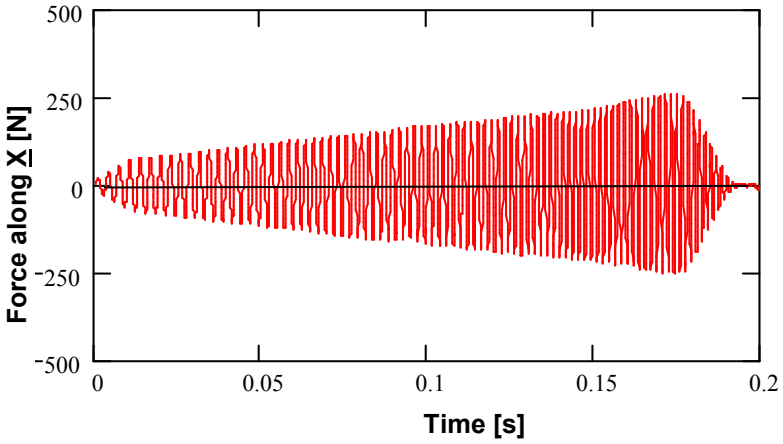

Fig. 29 Typical excitation force along *X* direction versus time. Sine sweep 300 - 600 Hz

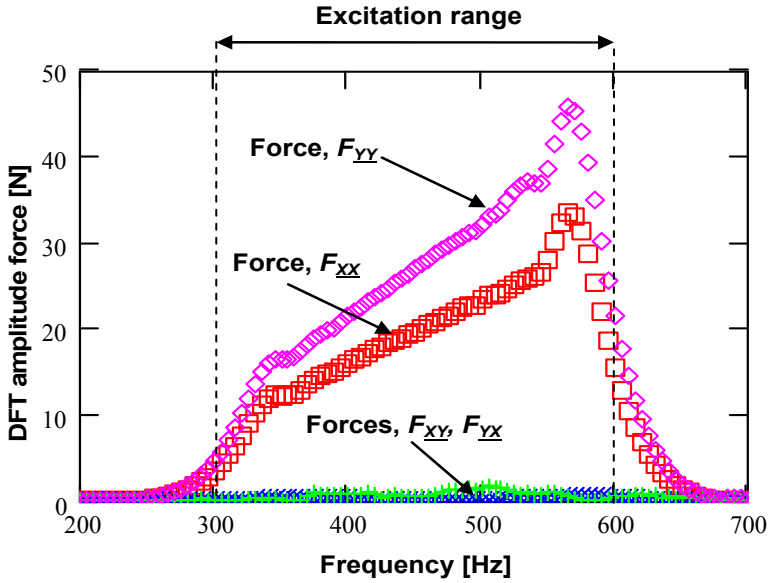

Fig. 30 DFT amplitudes of forces versus frequency. Sine sweep 300 - 600 Hz

Figure 31 displays the filtered bearing displacements relative to a journal, spinning at 50 krpm (833 Hz), along the *X* and *Y* directions while external loads are applied alternately from orthogonal directions. The bearing relative displacements along *X* and *Y*, for loads along the *X* and *Y* directions respectively, are maintained at ~20 μm. The

cross directional motions in Figure 31 (b) and 31(c) are due to the cross coupling stiffnesses in the bearing.

Figure 32 displays the corresponding DFT amplitudes of the bearing displacements relative to the spinning journal. The direct displacements ($X_{\underline{X}}$, $Y_{\underline{Y}}$) show nearly similar displacement amplitudes in the 300-600 Hz range. Recall that the dynamic loads are adjusted to obtain such an agreement in the displacement amplitudes. In the frequency domain, the DFT amplitudes of the bearing displacements are much smaller (~ 3 μm) than that in the time domain (~ 20 μm).

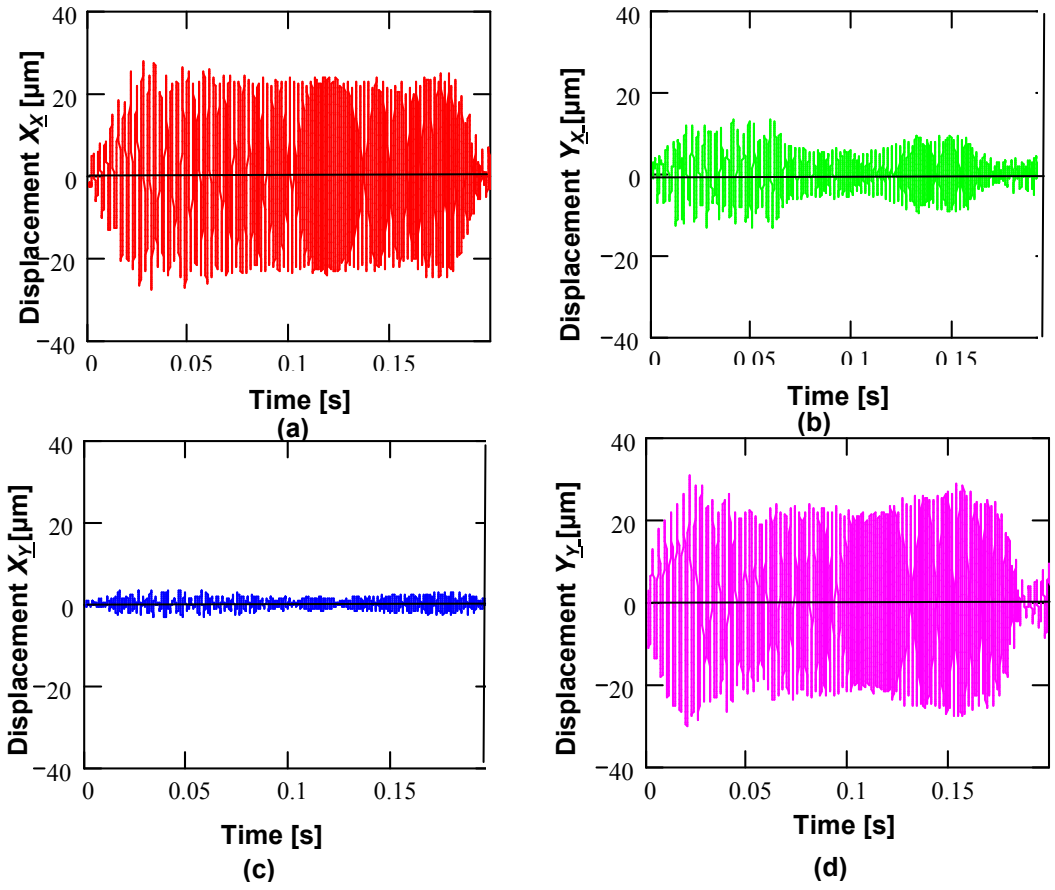

Fig. 31 Bearing relative displacements along *X* and *Y* directions for excitation forces along *X* (top) and *Y* (bottom) directions. Rotor speed ~ 50 krpm (833 Hz). Filtered signals. Applied static load of 22 N

Figure 33 shows the DFT amplitudes of the bearing cartridge absolute acceleration ($A_{ij,\ i,j=\underline{X},\underline{Y}}$) along the $\underline{X}$ and $\underline{Y}$ directions. The trend in the DFT amplitude of the acceleration with respect to increasing excitation frequency is similar to that of the applied dynamic forces. The direct accelerations along the $\underline{X}$ and $\underline{Y}$ directions are dissimilar since the magnitude of the dynamic loads along these directions are different. The cross-directional accelerations are nearly negligible. However, the bearing relative displacements in the cross-directions show non-negligible magnitudes. This is due to the motion of the flexible rotor within the bearing.

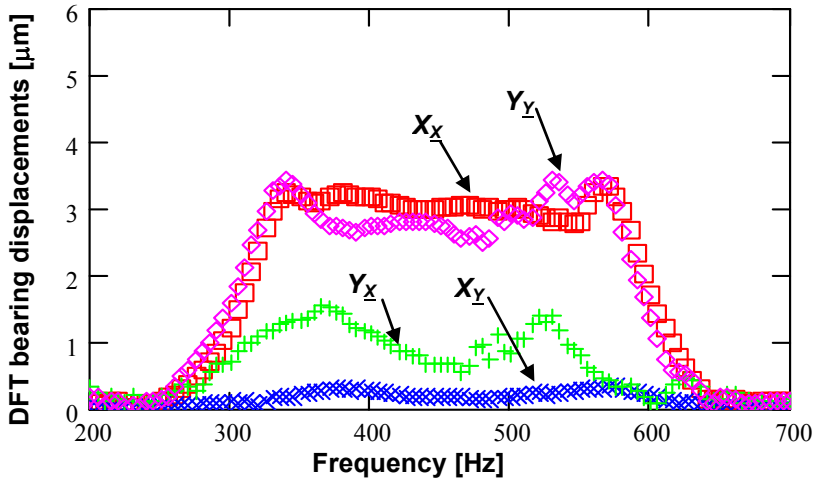

Fig. 32 DFT amplitudes of displacements versus frequency. Sine sweep 300-600 Hz

6. 4 Comparison of MMFB and BFB Dynamic Force Coefficients (200-400 Hz)

Figure 34 shows typical MMFB and BFB dynamic stiffness coefficients $(K_{\alpha\beta})_{\alpha\beta=X,Y}$ estimated from bearing motion amplitudes of ~25 μm and for excitation frequencies (ω) from 200 Hz to 400 Hz, while the bearing floats on a journal spinning at 50 krpm (833 Hz) and with a static load W=22 N (W/LD=0.16 bar).

Recall that the force coefficients are transformed from the $\underline{X}$, $\underline{Y}$ coordinate system (measurement axes 45° away from the vertical axis) to the X,Y coordinate system (vertical and horizontal planes).

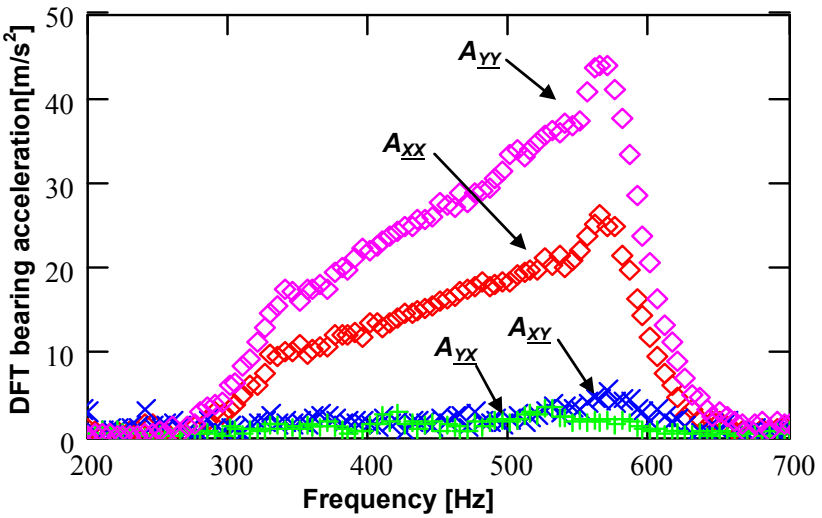

Fig. 33 DFT amplitudes of bearing accelerations versus frequency. Sine sweep 300-600 Hz

While the magnitude of the MMFB direct stiffness coefficients (K_{XX}, K_{YY}) are rather constant in the test frequency range, the BFB direct stiffness coefficients increase with increasing frequency. The cross-coupled stiffnesses (K_{XY}, K_{YX}) for both bearings are small in magnitude for most frequencies. At a low frequency of ~ 200 Hz, the BFB direct stiffness coefficient is ~ 1.5 times that of the MMFB. However, at ~ 400 Hz, the BFB direct stiffnesses are nearly 3 times larger than those in the MMFB.

Figure 35 displays the estimated viscous damping coefficients $(C_{\alpha\beta})_{\alpha\beta=X,Y}$ for both bearings. The direct damping coefficients (C_{XX}, C_{YY}) for the MMFB are somewhat constant for frequencies above 250 Hz albeit lesser than the coefficients for the BFB. For both the bearings, the cross-coupled coefficients, though small, vary slightly with excitation frequency.

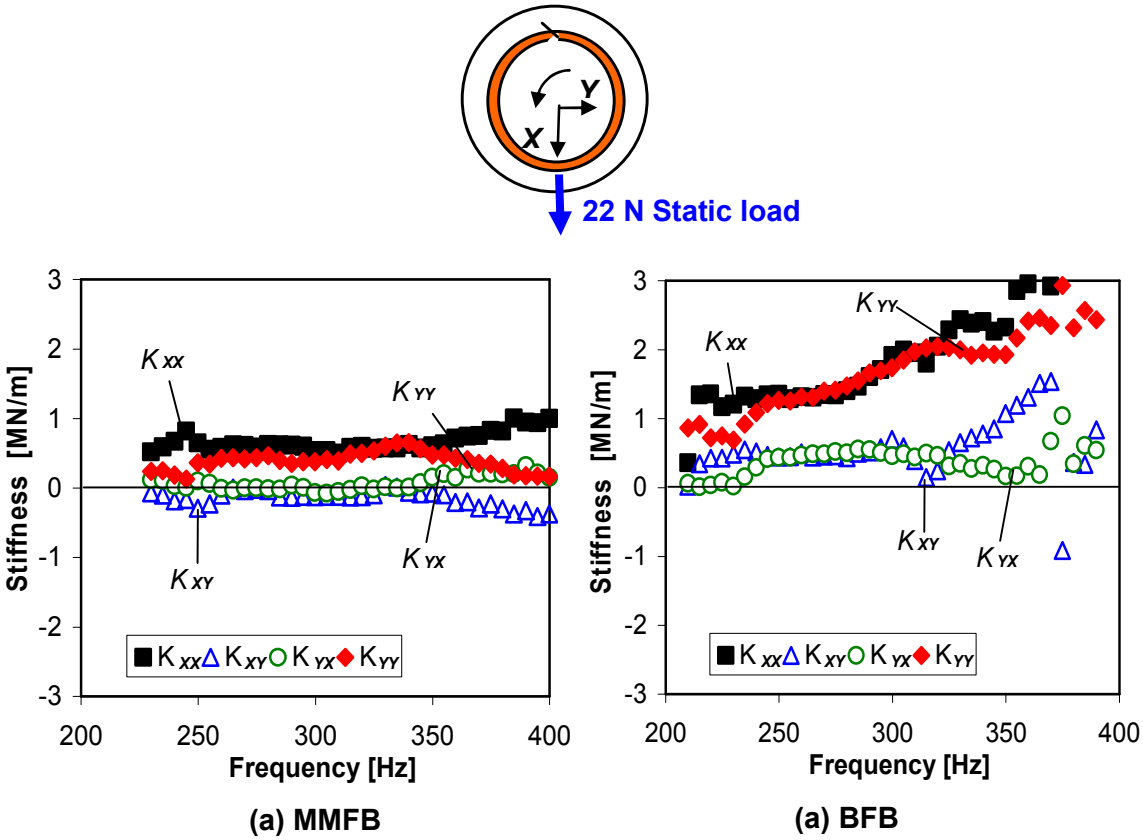

Fig. 34 Dynamic stiffness coefficients for (a) MMFB [30] and (b) BFB versus excitation frequency. Net applied static load *W*=22 N (*W/LD* =16 kPa). Rotor speed = 50 krpm (833 Hz)

6. 4.1 Estimation of Loss Factor

Metal mesh foil bearings dissipate mechanical energy through a mechanism best described by material or hysteretic damping, typically characterized by a loss factor (γ) [4]. Recall that for proportional structural damping,

$$\mathbf{C}\omega = \gamma \mathbf{K} \tag{33}$$

Over a full period of motion, $T=2\pi/\omega$, an estimation for a single γ follows from equating the energy dissipated by viscous damping (E_V) to the energy dissipated by material damping (E_M), i.e., from

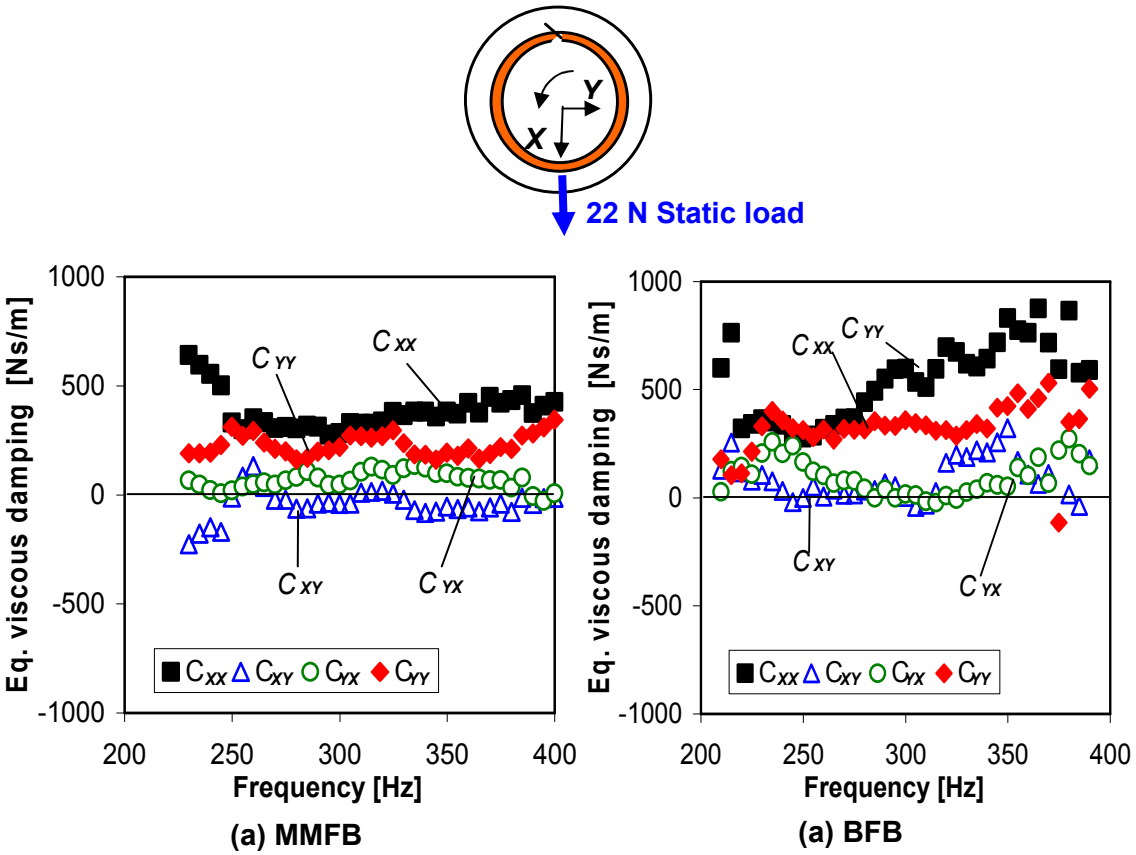

Fig. 35 Equivalent viscous damping coefficients for (a) MMFB [30] and (b) BFB versus excitation frequency. Net applied static load *W*=22 N (*W/LD* =16 kPa). Rotor speed = 50 krpm

$$E_V = \int_t^{t+T} \dot{\mathbf{z}}^{\mathrm{T}} \mathbf{C} \dot{\mathbf{z}}\, dt = E_M = \frac{\gamma}{\omega} \int_t^{t+T} \dot{\mathbf{z}}^{\mathrm{T}} \mathbf{K} \dot{\mathbf{z}}\, dt \tag{34}$$

it follows

$$\gamma = \omega \frac{\int_t^{t+T} \dot{\mathbf{z}}^{\mathrm{T}} \mathbf{C} \dot{\mathbf{z}}\, dt}{\int_t^{t+T} \dot{\mathbf{z}}^{\mathrm{T}} \mathbf{K} \dot{\mathbf{z}}\, dt} \tag{35}$$

Clearly, the formulation above is path dependent, i.e., depends on the motion history. For near circular orbits, Eq. (35) reduces to

$$\gamma = \frac{\omega\left(C_{XX} \left|V_X\right|^2 + C_{YY} \left|V_Y\right|^2 \right)}{K_{XX} \left|V_X\right|^2 + K_{YY} \left|V_Y\right|^2} \tag{36}$$

where (V_X,V_Y) are velocity components. For circular orbital motions, since $|V_X| = |V_Y|$, Eq. (36) reduces to

$$\gamma = \frac{\omega\left(C_{XX} + C_{YY} \right)}{K_{XX} + K_{YY}} \tag{37}$$

Figure 36 depicts the estimated loss factor for both bearings with the rotor at rest as well as while spinning at 50 krpm. San Andrés *et al.* [54] estimate structural loss factors for the same BFB from unidirectional single frequency load experiments and finds them ranging from 0.2-0.4 for frequencies from 100-200 Hz. The current test shows that the loss factor (γ) with shaft rotation is slightly higher than that without journal rotation. Importantly, the loss factor for the test MMFB is ~ 2 to 3 times that in the test BFB. Note that although the BFB has larger viscous damping coefficients it also has larger direct stiffness, and hence shows a lesser loss factor than the MMFB.

Presently, within the test frequency range, the force coefficients have a 5% or less uncertainty. Typical precision uncertainties for the measurement of force, acceleration and displacement are less than 2%, 1% and displacement 0.2%, respectively. Appendix B details the estimation of uncertainties for various parameters.

6.5 Estimation of MMFB Dynamic Force Coefficients over a High Frequency Range (300-600 Hz)

The earlier measurements correspond to sine-sweep dynamic loads with excitation frequencies ranging from 200 Hz to 400 Hz. More tests with the modified test rig, depicted in Figure 28, are conducted with excitation frequencies between 300 Hz and 600 Hz. Figure 37 shows the excitation forces along the $\underline{X}$ direction recorded from the two tests. The top graph shows the variation of the forces with time, and the bottom graphs depicts the DFT of the forces versus frequency. The DFT amplitudes of the forces show comparable magnitudes in the overlapping frequency range of 350-400 Hz. However, the magnitude of the force (~2N to 8 N) in the lowest range of 300 Hz-350 Hz

is much smaller than that from the low-frequency test (~8N to 10N). Hence, the estimated bearing parameters will evidence differences. Importantly enough, note the large magnitude of the forces in the frequency range from 400 Hz to 600 Hz required to displace the bearing a pre-selected (constant) amplitude.

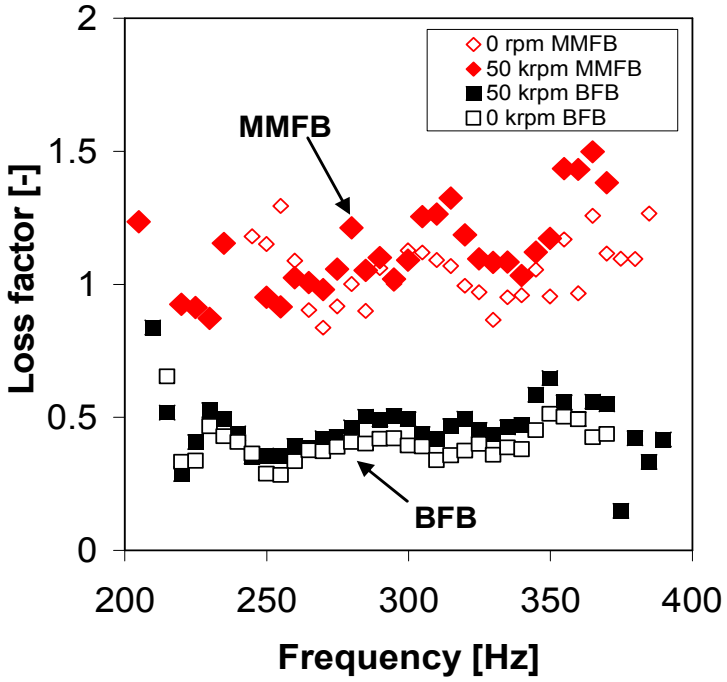

Fig. 36 Estimated loss factor (γ) for a MMFB [30] and a BFB versus excitation frequency. Net static load *W*=22 N (*W/LD*=16 kPa). Rotor at rest and spinning at 50 krpm (833 Hz)

Figure 38 depicts the MMFB stiffness and damping coefficients identified from the two tests. The data includes the earlier load measurements with frequencies from 200-400 Hz, and the current ones over an extended range of frequencies, 300 Hz to 600 Hz. The inset shows the excitation force along the $\underline{X}$ direction applied during the tests. The overlapped time domain data shows that the magnitude of the controlled force increases steadily with increasing excitation frequency.

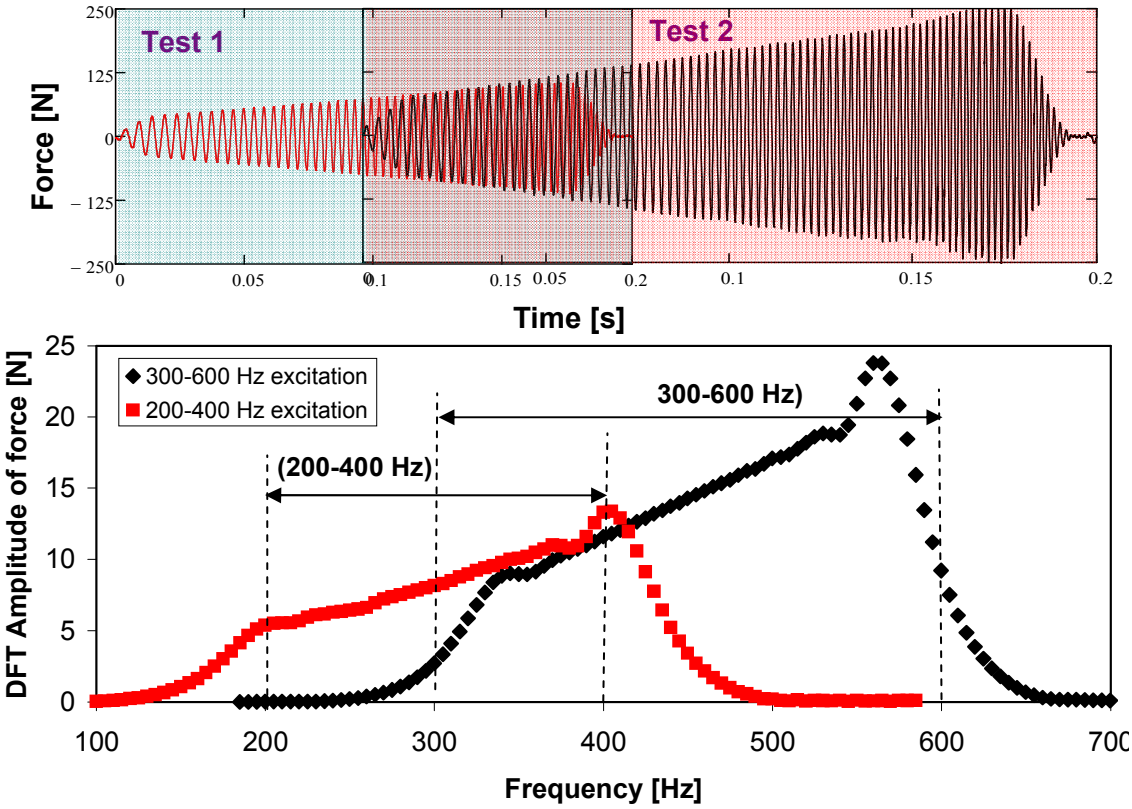

Fig. 37 Time traces and DFT amplitudes of excitation force along *X* direction from two experiments with excitation frequencies ranging from (i) 200-400 Hz [30] and (ii) 300-600 Hz

The measurements are conducted with the rotor at rest. In the frequency range of 300 Hz-400 Hz, the direct stiffness coefficients K_{XX} and K_{YY} from the two[14] tests are comparable. Both K_{XX} and K_{YY} gradually increase with frequency and have similar magnitudes. In the high frequency range, the cross coupled stiffness K_{XY} has large magnitude and increases with frequency. The direct damping coefficients (C_{XX}, C_{YY}) are ~ 400 Ns/m and show a gradual increasing tendency with frequency. The cross-coupled damping coefficients (C_{XY}, C_{YZ}) are much smaller than the direct damping coefficients.

[14] One test with sine-sweep loads with frequency ranging from 200 Hz to 400 Hz. The other test with loads applied with frequencies ranging from 300 Hz to 600 Hz.

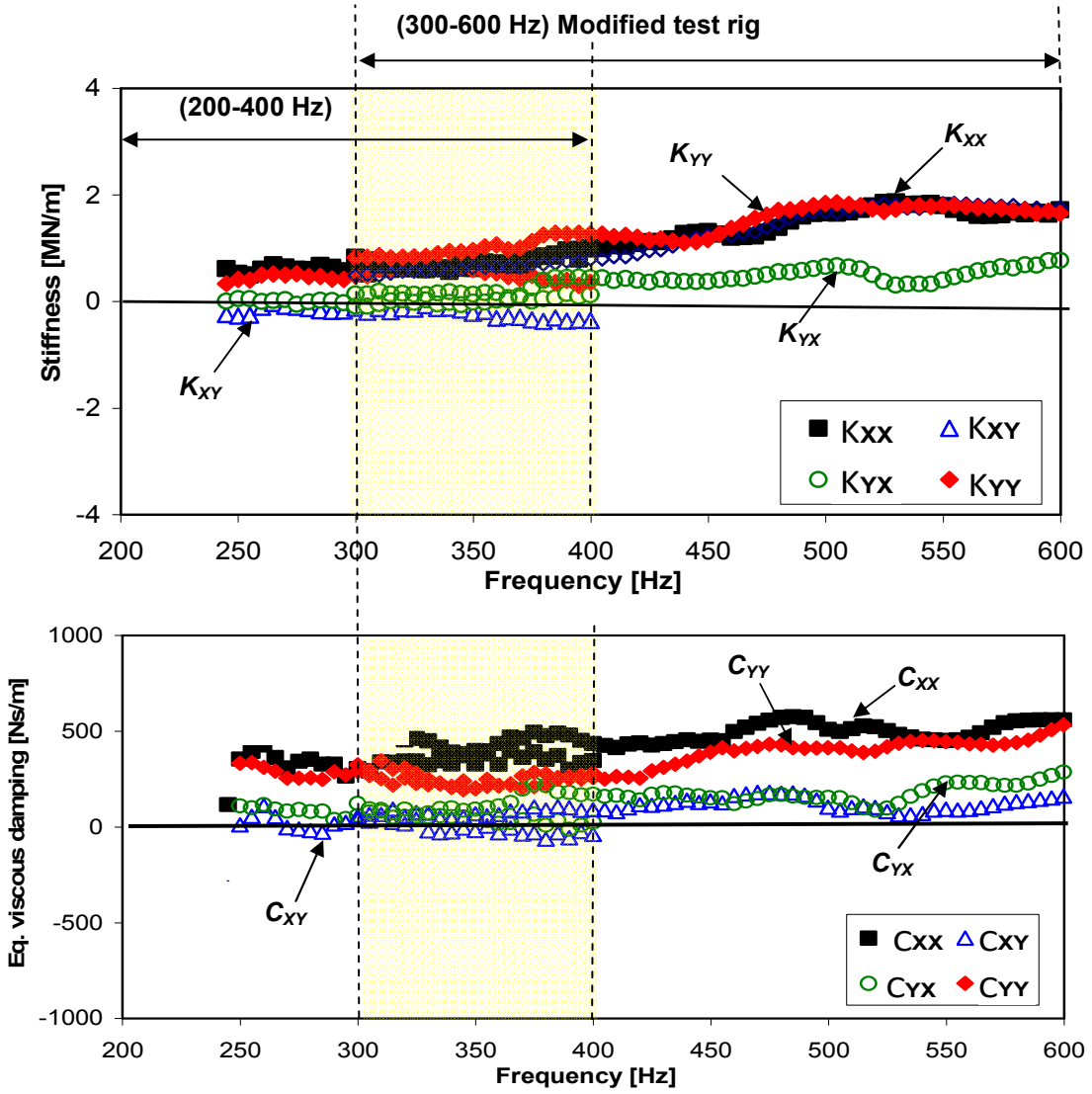

Fig. 38 Identified MMFB dynamic stiffness and damping versus frequency. Net applied static load of 22 N. Dynamic displacement amplitude ~ 20 μm. Rotor at rest. Test data overlaps two experiments with excitation frequencies ranging from (i) 200-400 Hz [30] and (ii) 300-600 Hz

Figure 39 shows the estimated MMFB stiffness and damping coefficients for tests with the journal spinning at 50 krpm. The stiffness coefficients have magnitudes similar to those from the tests with the rotor at rest. The direct viscous damping coefficient C_{XX} shows a slightly larger magnitude ~ 500 Ns/m over the entire test frequency range. In

general, the trend in the force coefficients is consistent in the 250-600 Hz test frequency range.

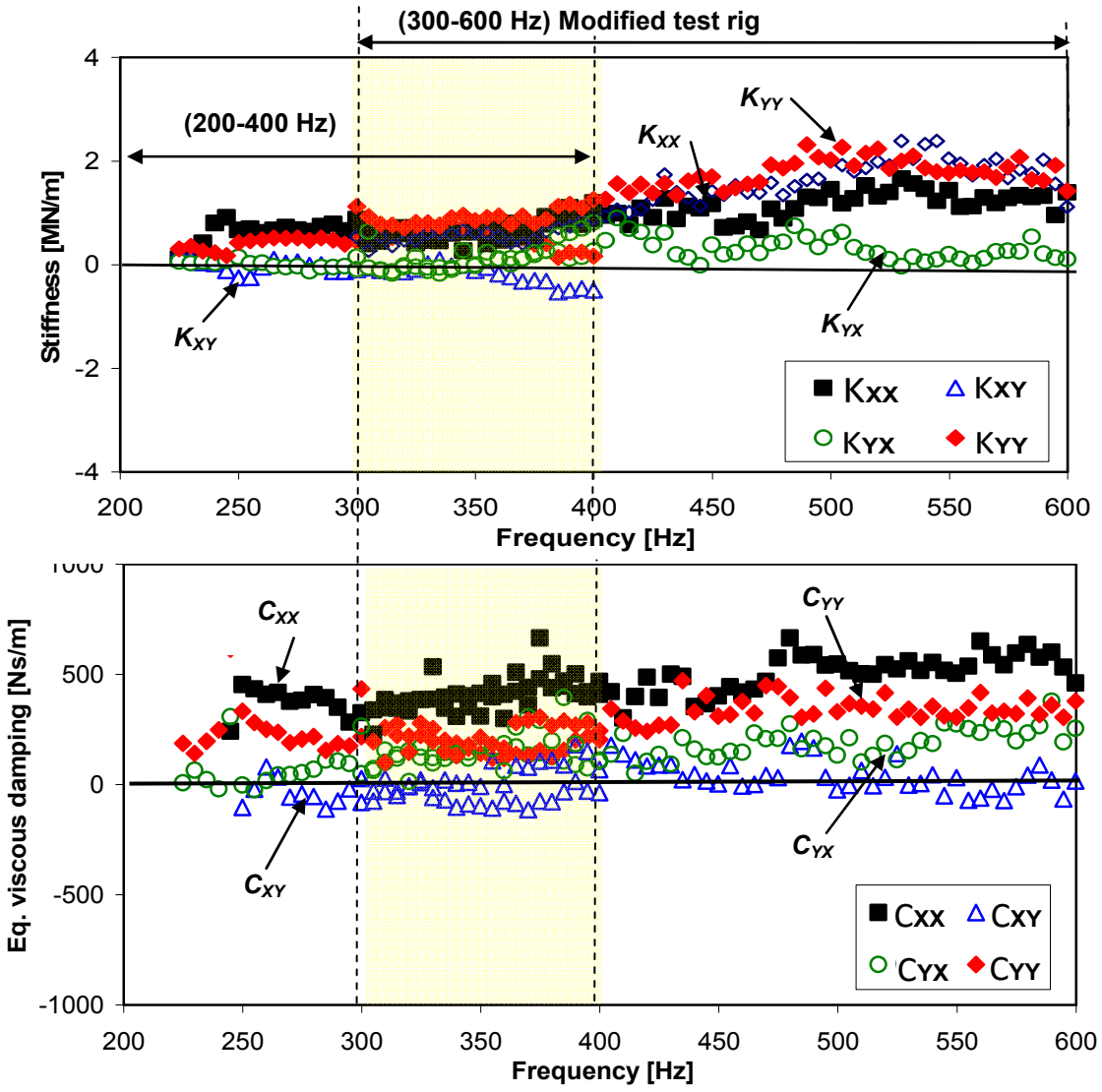

Fig. 39 Identified MMFB dynamic stiffness and damping versus frequency. Net applied static load of 22 N. Dynamic displacement amplitude ~ 30 μm. Rotor spinning at 50 krpm (833 Hz). Test data overlaps two experiments with excitation frequencies ranging from (i) 200-400 Hz [30] and (ii) 300-600 Hz

In the experimental work, for further comparisons and validation, a bump foil bearing (BFB) replaces the MMFB. Both bearings are similar in size (see Table 3). Next, the experiments were repeated for similar dynamic load conditions [30]. Figure 40 shows the estimated stiffness and damping coefficients for the bump foil bearing while the rotor is at rest. The direct stiffness and damping coefficients increase with increasing frequency. At high frequencies $K_{XX} > K_{YY.}$ However the direct damping coefficients show similar magnitudes and trend in the entire test frequency range.

The tests identifying the bump foil bearing force coefficients with a spinning rotor were discontinued as the bump foil geometry had changed after applying dynamic loads with too large amplitude. Note that the bump foils were not heat treated, thus resulting in their deformation upon application of large loads.

6.5.1 Effect of Rotor Speed on MMFB Dynamic Force Coefficients

Figure 41 depicts the identified MMFB dynamic stiffnesses $(K_{\alpha\beta})_{\alpha,\beta=X,Y}$ versus excitation frequency for operation at increasing rotor speeds (0 rpm, 40 krpm, and 50 krpm) and a net applied static load of 22 N along the vertical upward direction (W/LD = 16 kPa [2.3psi]). The bearing motion amplitudes are kept constant at~ 20 μm. With and without the journal rotation, the direct stiffness K_{XX} does not vary much in the test frequency range; however, K_{YY} increases with increasing frequency. Recall that for tests with motion amplitude maintained at ~ 30μm, both direct stiffnesses show comparable magnitudes. The dynamic force coefficients, with and without journal rotation, are comparable indicating the minimal influence from the stiff gas film at high rotor speeds. The cross-coupled stiffnesses (K_{XY} , K_{YX}), after their transformation to the X-Y coordinate system, show large magnitudes. Recall, however, that $(K_{XY} - K_{YX}) > 0$ is a net source of energy that may cause rotor-bearing instability. Presently, $(K_{XY} - K_{YX}) \sim 0$, for most frequencies; and thus not a significant factor for a potential instability.

Figure 42 shows the MMFB damping coefficients $(C_{\alpha\beta})_{\alpha,\beta=X,Y}$ versus frequency for operation at various journal speeds. The direct damping coefficients increase with frequency and display comparable magnitudes. The journal spin speed has little effect

on the damping coefficients. The cross-coupled damping coefficients have magnitudes smaller than the direct ones.

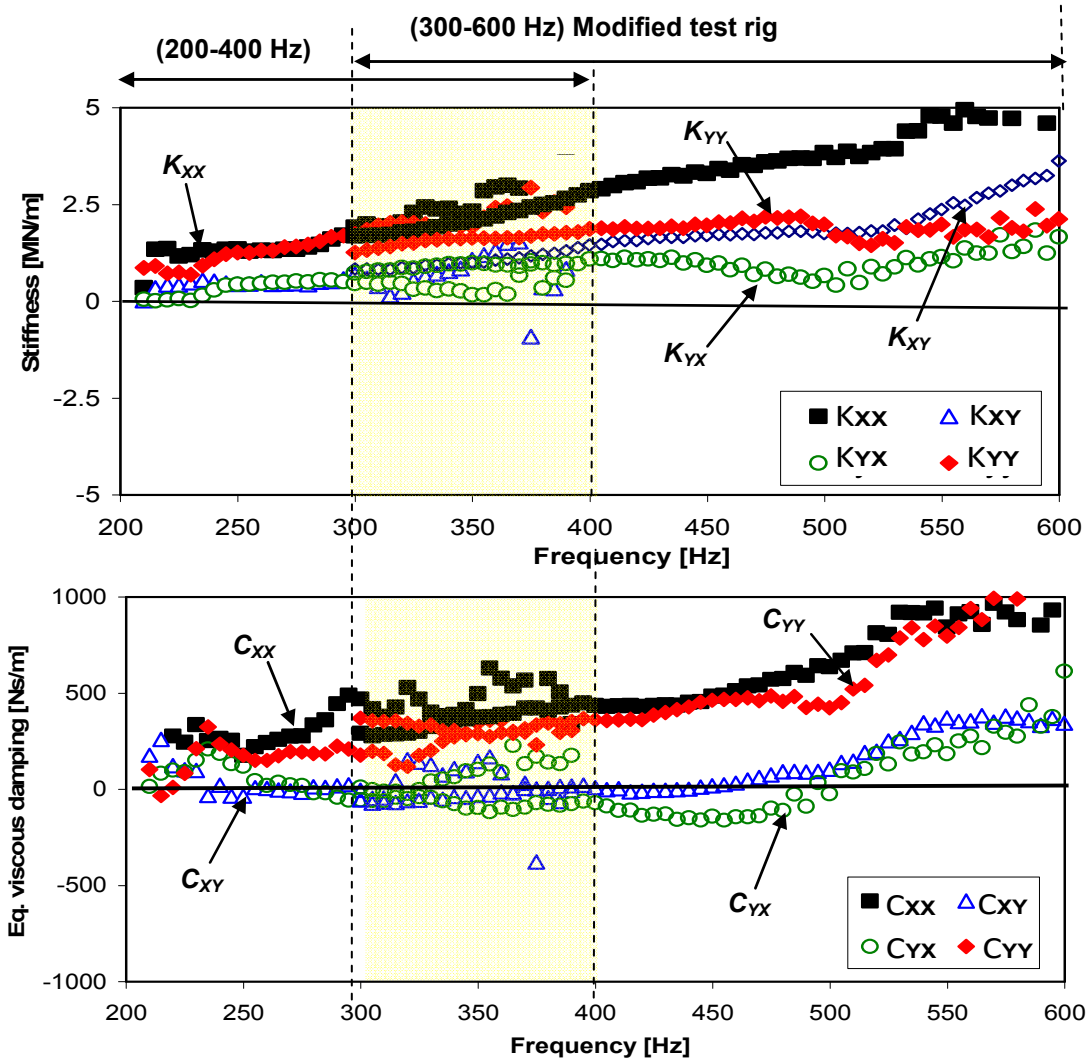

Fig. 40 Identified BFB dynamic stiffness and damping versus frequency. Net applied static load of 22 N. Dynamic displacement amplitude ~ 20 μm. Rotor at rest. Test data overlaps two experiments with excitation frequencies ranging from (i) 200-400 Hz [30] and (ii) 300-600 Hz

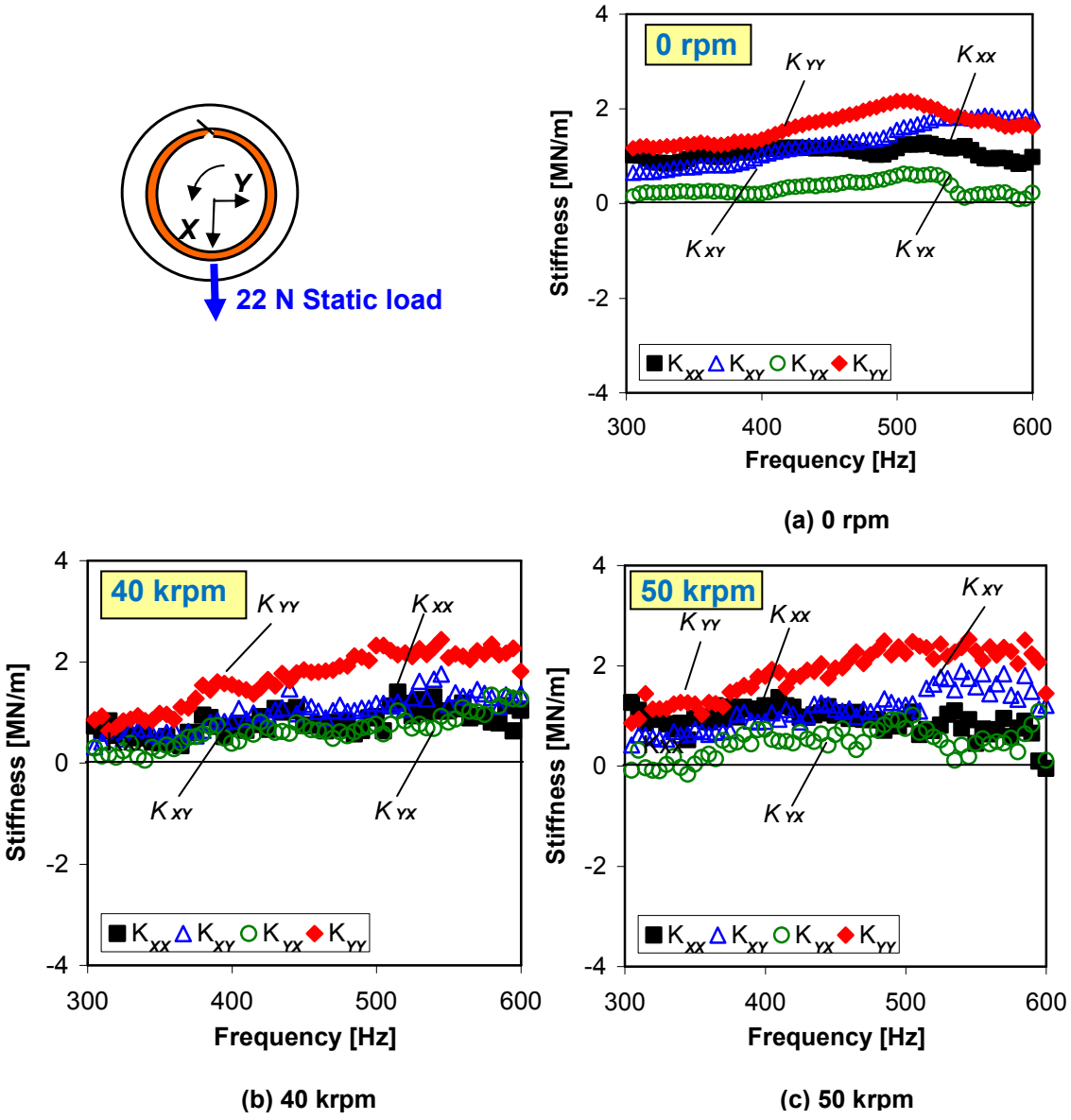

Fig. 41 Identified MMFB direct and cross coupled stiffnesses versus frequency. Net applied static load of 22 N. Dynamic displacement amplitude ~ 20 μm. Rotor speeds = (a) 0 rpm, (b) 40 krpm(667 Hz) , and (c) 50 krpm(833 Hz)

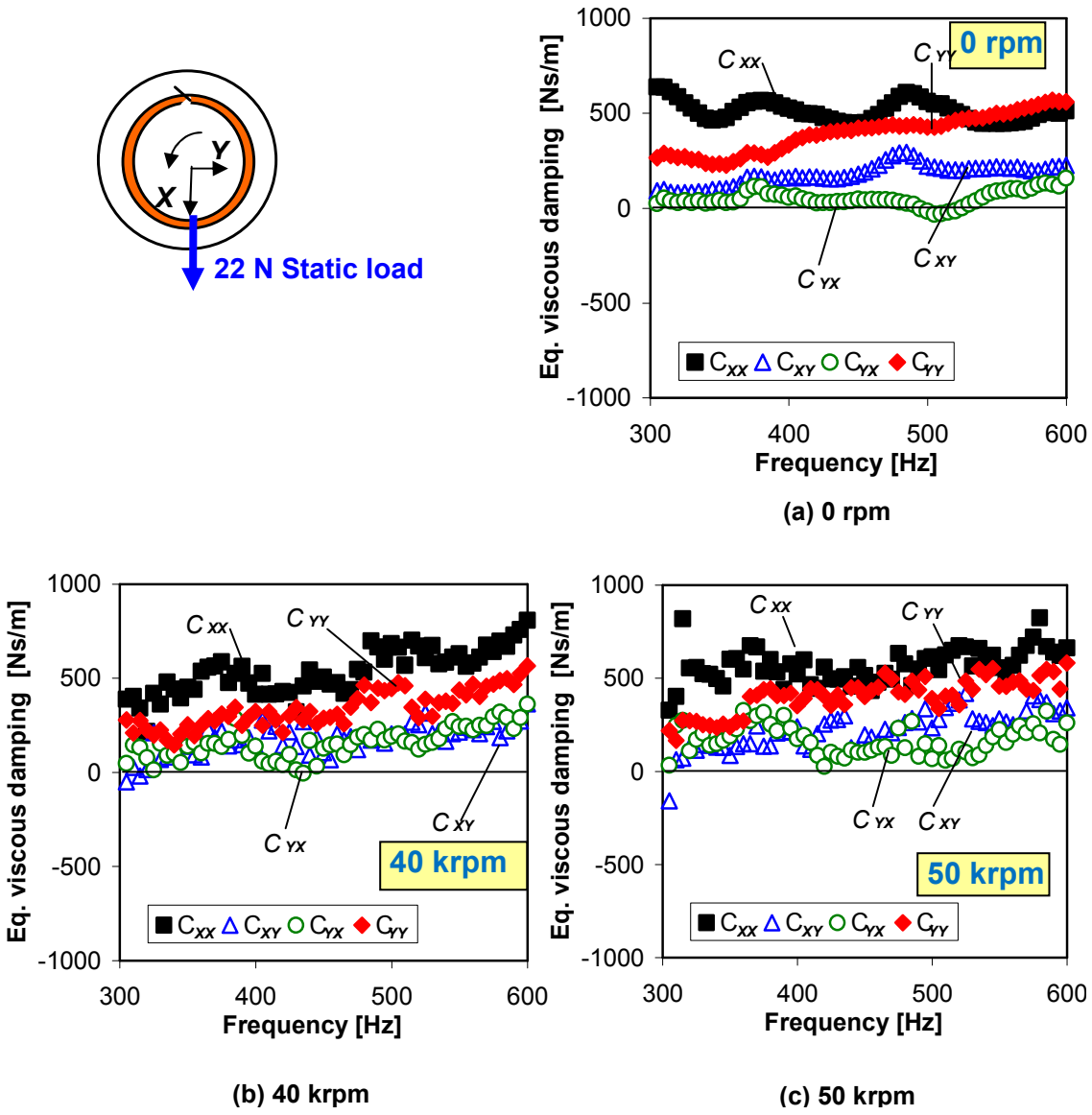

Fig. 42 Identified MMFB direct and cross coupled equivalent viscous damping coefficients versus frequency. Net applied static load of 22 N. Dynamic displacement amplitude ~ 20 μm. Rotor speeds = (a) 0 rpm, (b) 40 krpm(667 Hz) , and (c) 50 krpm(833 Hz)

6.5.2 Effect of Bearing Motion Amplitude on MMFB Dynamic Force Coefficients

The test MMFB is excited in the frequency range 300 Hz – 600 Hz while ensuring fairly constant motion amplitudes, first at ~20 μm and next at ~30 μm. The rotor was at

rest, and then spinning at 40 krpm and 50 krpm. As the identified force coefficients do not show any significant variation with journal speed, the following results are shown for operation at 50krpm (833 Hz) only.

Figures 43 and 44 depict the identified direct and cross-coupled stiffnesses and viscous damping coefficients for operation with a static load of 22 N (*W/LD* =16 kPa). For tests with motion amplitude of 20 μm, the direct stiffness (K_{XX}) does not change with frequency. However, for tests with motion amplitude of 30 μm, with slightly higher excitation forces, K_{XX} increases with frequency. The direct stiffness (K_{YY}) increases gradually with frequency for both tests. Recall that at the highest frequency of 600 Hz, dynamic loads as high as 250 N are applied (over a short time) to excite the bearings. The cross-coupled stiffnesses (K_{XY} , K_{YX}) show large magnitudes, but are of the same sign and hence do not promote large destabilizing forces, except for displacements at 0.030 mm.

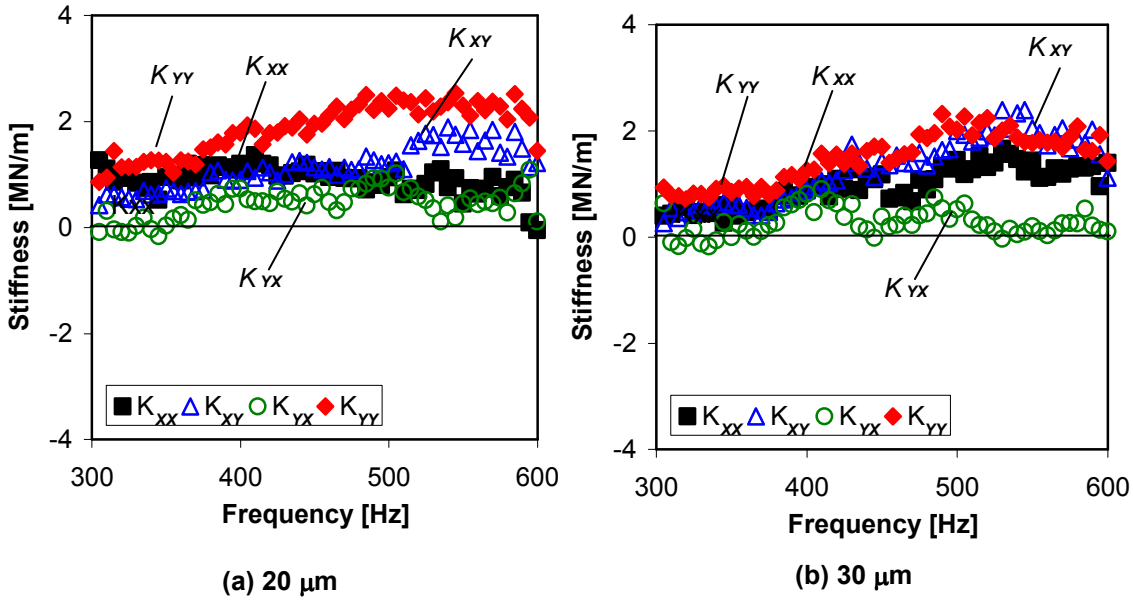

Fig. 43 Identified MMFB direct and cross coupled stiffnesses versus frequency. Bearing motion amplitudes of 20μm and 30μm. Net applied static load of 22 N. Rotor speed of 50 krpm (833 Hz)

The damping coefficients are mostly independent of the motion amplitudes, 20 μm or 30 μm. The direct damping coefficients show a very gradual increase with frequency.

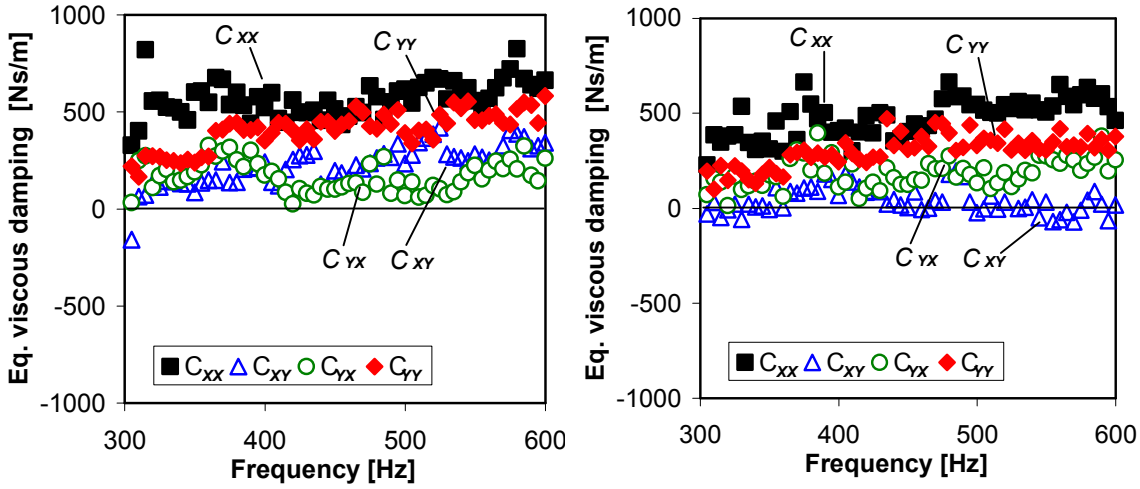

Fig. 44 Identified MMFB direct and cross coupled equivalent viscous damping coefficients versus frequency. Bearing motion amplitudes = 20μm and 30 μm. Net applied static load = 22 N. Rotor speed = 50 krpm (833 Hz)

Figure 45 shows the estimated MMFB loss factor (γ) versus excitation frequency determined for tests with bearing dynamic displacement amplitudes of 20 μm and 30 μm, respectively. The graphs show the loss factors estimated with the rotor at rest and while spinning at 40 krpm and 50 krpm. The estimated loss factors gradually increase with frequency but are independent of rotor speed. The loss factor (γ) increases from ~0.8 to 1.5 and ~0.8 to 1.2 for tests with displacement amplitudes of 20 μm and 30 μm, respectively.

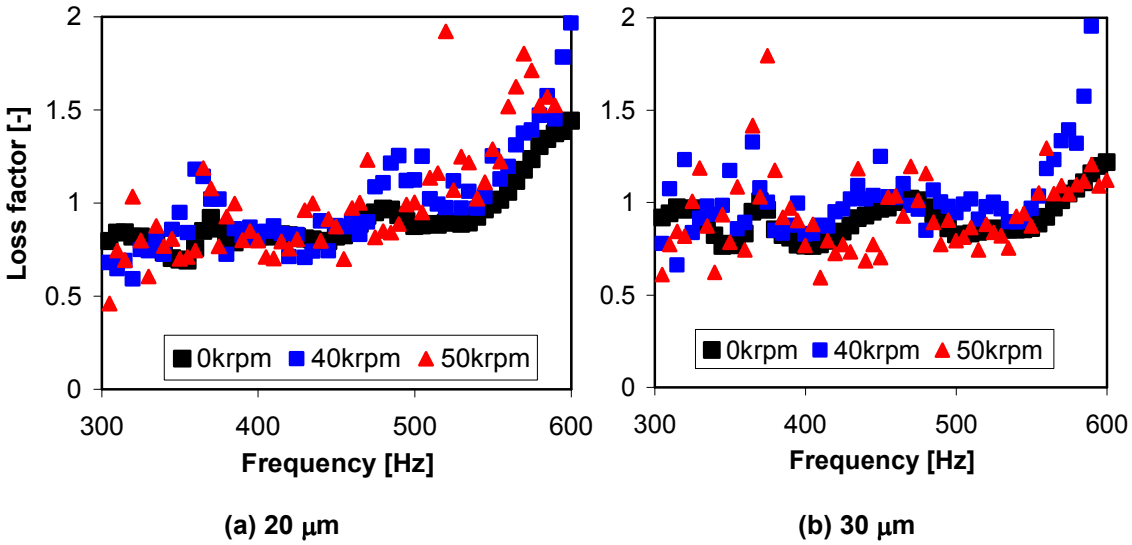

Fig. 45 Derived MMFB loss factor versus frequency. Dynamic displacement amplitude ~ 20 μm and ~ 30 μm . Rotor speeds = 0 rpm, 40 krpm (667 Hz), and 50 krpm (833 Hz). Net applied static loads of 22 N

6.6 Stability Analysis of a Simplified Rotor-Bearing System

For simplicity in the analysis, assume a point mass supported on a MMFB characterized by the dynamic force coefficients determined experimentally. Recall in the tests, for an operating speed of 50 krpm (833 Hz), the excitation whirl frequency (ω_S) ranged from 200 Hz to 600 Hz. The equation of motion in the frequency domain is

$$\begin{bmatrix} K_{\underline{XX}} - M_R\omega^2 + j\omega C_{\underline{XX}} & K_{\underline{XY}} + j\omega C_{\underline{XY}} \\ K_{\underline{YX}} + j\omega C_{\underline{YX}} & K_{\underline{YY}} - M_R\omega^2 + j\omega C_{\underline{YY}} \end{bmatrix} \begin{pmatrix} \bar{x}_{(\omega)} \\ \bar{y}_{(\omega)} \end{pmatrix} = \begin{pmatrix} 0 \\ 0 \end{pmatrix} \tag{38}$$

At the threshold speed of instability (Ω_S), the determinant of the matrix in Eqn. (38) must be zero. Introducing $H_{ij=\underline{XY}} = K_{ij} + i\omega C_{ij}$ and a complex term Z replacing $M_R\omega^2$, the solution of the determinant in Eqn. (38) delivers Z as [55]:

$$Z = \frac{1}{2}\left(H_{\underline{XX}} + H_{\underline{YY}}\right) - \sqrt{\frac{\left(H_{\underline{XX}} - H_{\underline{YY}}\right)^2}{4} + H_{\underline{XY}}H_{\underline{YX}}} \tag{39}$$

A solution exists only if the imaginary part of Z becomes zero while the real part is positive. Figure 46 presents the real and imaginary parts of Z versus the whirl frequency

ratio (ω_S/Ω_S) equaling whirl speed divided by rotor speed. Figure 46 shows that no valid solution is available, i.e., the imaginary part of $Z \neq 0$; and hence the system is stable in the whirl frequency range (200 Hz-600 Hz). Presently, the simple stability analysis merely certifies the experimental data.

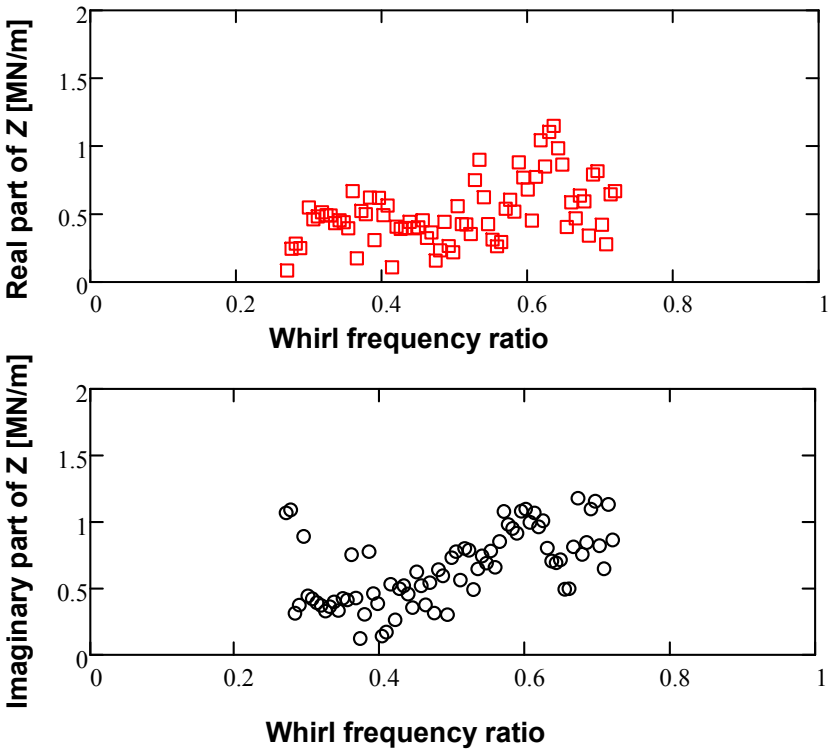

Fig. 46 Stability analysis of simple rotor-MMFB system. Real and imaginary parts of parameter *Z* versus whirl frequency ratio

Although sub-synchronous whirl motions were recorded for a smaller MMFB (L=D=28.0 mm) during rotor speed up tests [26], no sub-synchronous rotor motions are found with the current MMFB during the dynamic load tests while operating in the 40 krpm-60 krpm speed range. The sub-synchronous whirl motion reported in Ref. [26] are not due to a bearing hydrodynamic instability, but attributed to the nonlinear hardening stiffness typical of a MMFB.

6.7 Conclusions

This section presents the dynamic force coefficients of a test MMFB and a test BFB for various operating speeds and excitation amplitudes. Over a frequency excitation range of 200-400 Hz, the MMFB shows nearly constant direct stiffness coefficients while the BFB produce larger magnitudes, up to three times, and also increasing with frequency. The MMFB viscous damping coefficients vary little with frequency (200-400 Hz); but the BFB coefficients are larger and increase with frequency. The loss factor (γ), an indicator of the mechanical energy dissipation ability for foil bearings, in a MMFB (γ~1) is at least twice larger than that in the BFB (γ~0.4).

In the high frequency range (300-600 Hz), for small motion amplitudes of ~ 20 μm the MMFB direct stiffness along the *Y* direction shows larger magnitude than that along the *X* direction. However, for tests with larger controlled motion amplitude of ~30 μm, the direct stiffness coefficients show comparable magnitudes. With and without journal rotation, the direct damping coefficients increase with increasing frequency. Cross coupled damping coefficients, C_{XY} and C_{YX}, are small relative to the direct coefficients. The bearing coefficients do not vary noticeably at high speeds as the stiff gas film do not influence the overall bearing properties much. The material loss factor in MMFB γ is ~*0.8*-1.0 in most of the test frequency range (300 Hz-500 Hz) and is consistent with that measured in the low frequency range (200-400 Hz). But, at high frequencies ~600 Hz, the loss factor increases to ~1.5 and ~1.2 for tests with motion amplitudes of 20 μm and 30 μm, respectively.

A stability analysis for a simple mass-MMFB system shows that, in the frequency range where the force coefficients are available (200-600 Hz), the bearing is stable. This assertion applies to the test bearing only.

7. MEASUREMENTS AND PREDICTIONS OF THE ROTORDYNAMIC RESPONSE OF A HOLLOW ROTOR SUPPORTED ON TWO MMFBs

7.1 Introduction

The MMFB static and dynamic forced performance characteristics, presented in sections 5 and 6, suggest that MMFBs have favorable properties to reliably support high speed rotors. Next, it is important to predict accurately the rotordynamic response and stability of a rotor-MMFB system. Addressing this need, the current section presents the measurements and predictions of the dynamic response of a hollow rotor supported on two metal mesh foil bearings (MMFBs) and with increasing mass imbalances. A linear finite element structural analysis (XLTRC$^{2®}$), modeling the rotor supported on two bearings, predicts the rotor synchronous response, amplitude and phase. The computational analysis in section 3 predicts the MMFB stiffness and damping synchronous speed coefficients used in the rotordynamic analysis.

7.2 Description of Experimental Facility and Bearing

Figure 47 shows a sectioned 3D view of the test rig [56], with two metal mesh foil bearings supporting the rotor. The bearing span is ~103 mm. The test rig consists of a solid AISI 4140 steel block housing the test bearings, a high speed motor (max. 50 krpm) driving the rotor via a coupling, a cartridge heater, and instrumentation for recording rotor speed, rotor lateral displacements, and temperatures at various locations.

Dry high pressure air, from a shop compressor, is supplied to the enclosure inside the steel block at a set flow rate and which acts as a cooling flow to the test bearings. A thin ring (end cap) tightly holds the bearings in place, as depicted in Figure 48. The end cap is ~ 2 mm thick and has an inner diameter slightly smaller than the bearing OD (50.8 mm). A 15.9 mm diameter electric cartridge heater fits loosely inside the hollow rotor and heats the system[15] to a maximum temperature of 200º C. Two infrared

[15] A safety insulation shield, covering the entire test rig, is assembled during the high temperature measurements for operator safety.

thermometers (not shown in the figures) record the temperatures on the rotor surfaces near the bearings. See Ref. [56] for more details on high temperature measurements conducted in the test rig.

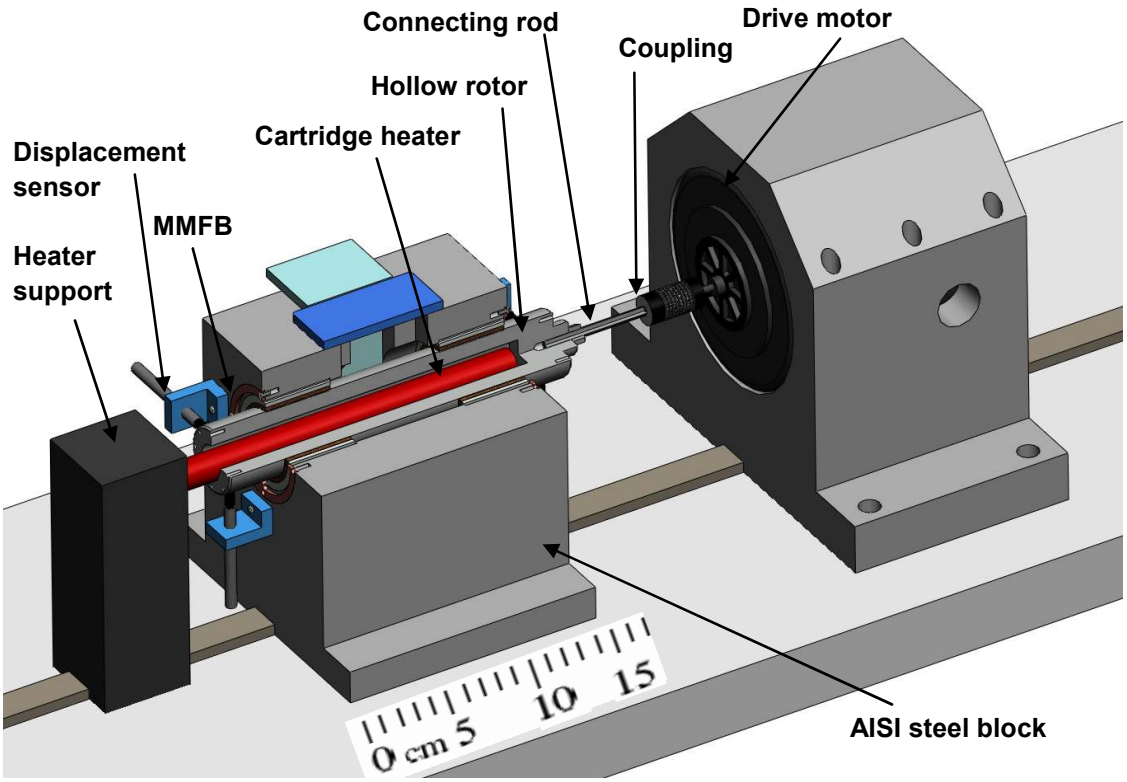

Fig. 47 Sectioned view of test rotor and bearings inside their housing

Figure 49 shows a view of the test MMFB consisting of a stainless steel bearing cartridge, four compressed copper mesh pads[16] ~2.6 mm thick, and a smooth pre-formed (hot rolled) alloy steel top foil, 0.120 mm in thickness. One end of the top foil slides to fit into a slot in the bearing cartridge. The metal mesh pads are manufactured by compressing weaves of thin copper wire into flat strips. The strips are later pressed

[16] Prior metal mesh foil bearings had a single ring shaped metal mesh pad [30]. However, for better dimensional control, the current MMFB consists of multiple arcuate pads.

under high pressure (~ 100 kN or higher) to curve them, and then inserted into the bearing cartridge. The top foil inner surface is spray coated with a thin layer (< 10 μm) of MoS_2 to reduce friction between the journal and top foil surface during rotor start-up and shut-down.

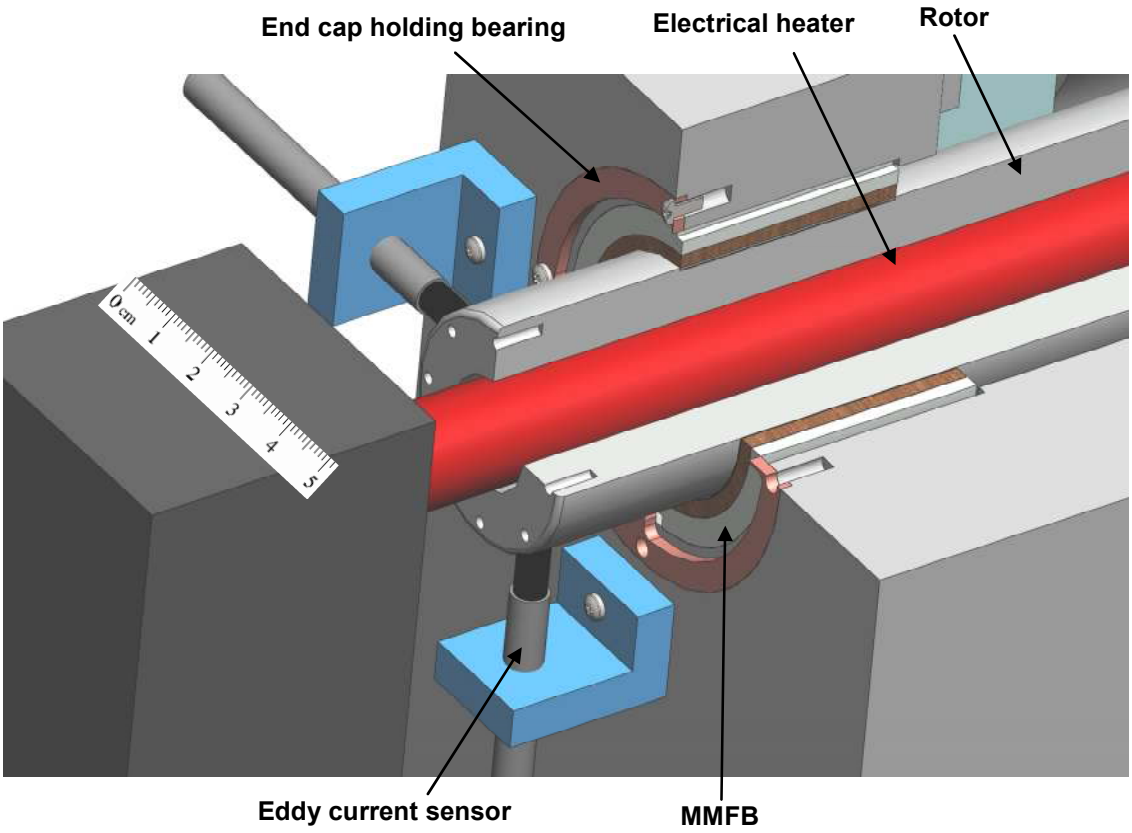

Fig. 48 Close-up view of rotor free end and cartridge heater

Table 5 lists the dimensions and specifications for the test bearing and test rotor[17]. As seen in Figure 49, four axial slots 90º apart, of depth 2mm and width 3mm, are machined on the OD the bearing cartridge. K type thermocouples cold-welded to the slots measure the cartridge OD temperature at its axial mid-span.

[17] Inconel rotor donated by Korea Institute of Science and Technology, KIST.

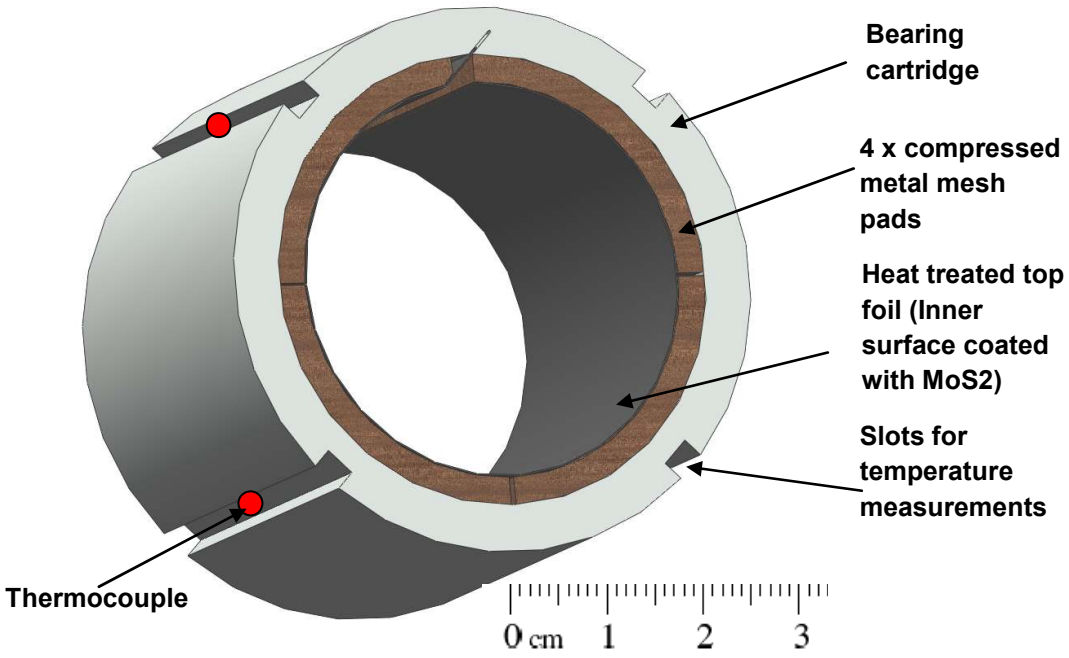

Fig. 49 Metal mesh foil bearing with four compressed mesh pads

The hollow Inconel rotor[18] is 200.66 mm long and weighs 1.360 kg (13.33 N), its outer diameter (D_o) = 36.51 mm and inner diameter (D_i) = 17.9 mm. At the rotor end face, eight equally spaced threaded holes, 13 mm deep, and at a radius of 15.5 mm permit the addition of imbalance masses. As the rotor center of mass[19] (excluding the connecting rod) is located 105.8 mm from the rotor free end, the bearings carry unequal fractions of the rotor weight; with 7.39 N (W/LD= 5.3 kPa) on the bearing on the drive end (DE) side, and 5.94 N (W/LD= 4.3 kPa) on the bearing on the free end (FE) side of the rotor.

[18] Donated by Korea Institute of Science and Technology (KIST).
[19] The c.g. of the combined rotor and the connecting rod is located 133.0 mm from the rotor free end, and applies 0.91 kg and 0.50 kg load at the rotor drive and free end bearings respectively.

Table 5. Nominal dimensions and specifications for rotor and MMFBs

Rotor	Inconel 718
Mass, M_R	1.36 kg
Length	200.66 mm
Inner diameter, D_I	17.90 mm
Outer diameter, D_O	36.51 mm
Rotor diameter at bearings	36.51 ± 0.01 mm
Bearing span	103 mm
Bearings	
Cartridge outer diameter	50.80 mm
Cartridge inner diameter	42.00 ± 0.02
Inner diameter, D	36.58 ± 0.02 mm
Axial length, L	38.10 mm
Copper mesh pad thickness	2.6 mm
mesh density (compactness)	30 %
Wire diameter (mm)	0.30
Number of metal mesh pads	4
Top foil thickness, T_f	0.12 mm
Top foil (Chrome Nickel steel alloy)	Hardness Rockwell (40/45)
Top foil elastic modulus, E	214 GPa
Radial clearance based on geometry	0.035 mm

7.3 Effect of Imbalance Mass on Rotor Response

The rotordynamic measurements are conducted at room temperature (~ 22 ^{o}C) and with an air flow rate into the bearings maintained at ~ 160 L/min and with a supply gauge pressure of 1.9 bar (27.6 psig). The rotor response is recorded on the outboard of both bearings, along the horizontal and vertical directions. Inserted in the holes at the two end planes of the rotor, in-phase (0^{o}) and out-of-phase (180^{o}) imbalance masses equal to 240 mg correspond to imbalance off-center displacements (u) of 5.5 μm and 15 μm, respectively. Similarly, in-phase and out-of-phase imbalance masses of 360 mg give imbalance displacements (u)[20] of 8.2 μm and 22.6 μm, respectively. During the

[20] In-phase (0^{o}) imbalance masses (m_e) cause a rotor off-center displacement $u = 2 \times r\left(m_e / M_R\right)$. The imbalance mass is located at a radial distance of r=15.5 mm from the rotor axis, and M_R=1.36 kg is the rotor mass. The couple imbalance due to 180^{o} out-of-phase placed masses (m_e) produces a rotor end side

tests, the rotor accelerates at 600 rpm/s up to the highest rotor speed of 50 krpm (833 Hz) and then coasts down to rest. The motor does not actively control the rotor speed during the coast down process.

The remnant imbalance in the rotor, even after trim balancing in place, affects the rotor response. Hence, baseline response vectors are recorded and subtracted from the imbalance response vectors. Note that, the DAQ system does not record the baseline response and imbalance response at identical rotor speeds, and most of the time the number of vector elements are not equal either. A Mathcad ® program generates a re-sampled baseline response vector with elements equal to that of the measured imbalance response vector.

7.3.1 Rotor Response Predictions versus Measurements (at Room Temperature)

A linear finite element structural rotordynamic analysis (XLTRC^2 ®) predicts the response amplitude and phase of the rotor supported on the two MMFBs. The rotordynamic analysis uses the synchronous speed stiffness and damping coefficients of the MMFB and predicted by the MMFB analysis described in Section 3. Appendix F shows the predicted MMFB force coefficients.

Figure 50 depicts the finite element structural model of the test rotor and connecting rod, the added inertia and mass of the flexible coupling and the axial locations of the MMFBs. The imbalance masses are added at station 5 (rotor drive end) and station 16 (rotor free end) at a radius of 15.5 mm.

---

off-centered displacement $u = 2 \times r \times \left(m_e \, l^2 / I_T \right)$, where l is half the rotor length and I_T is the rotor transverse moment of inertia. These formulas apply to a simple 1DOF model (cylindrical and conical motions) of the rotor-bearing system.

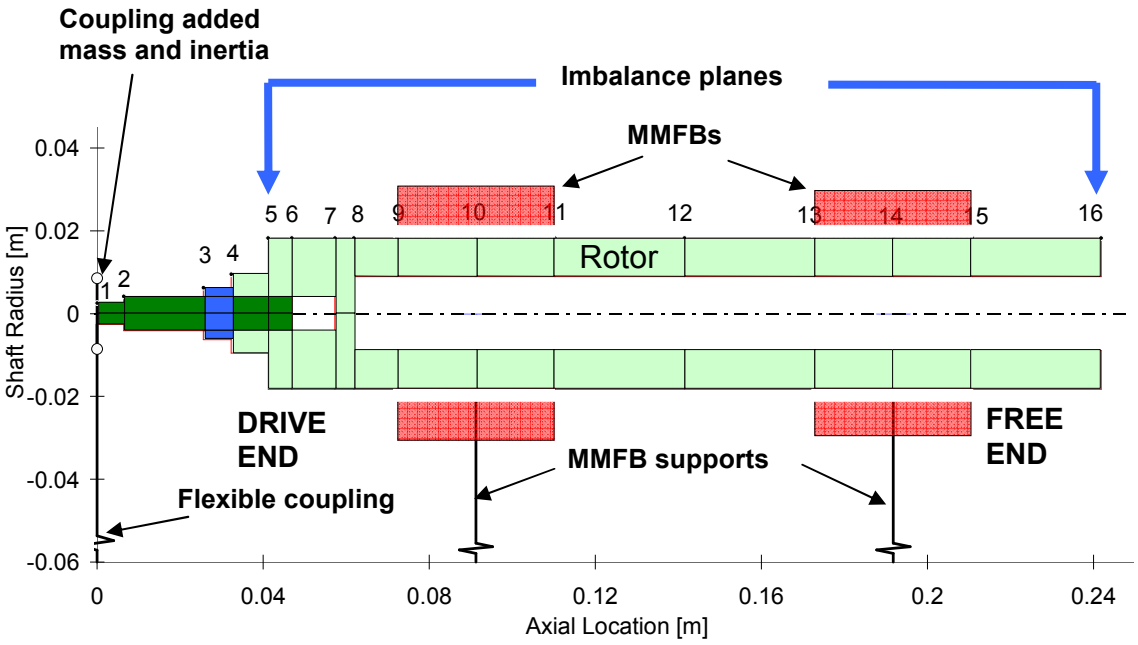

Fig. 50 Finite element structural model of test rotor supported on MMFBs. A flexible coupling connects the drive motor to the connecting rod affixed to the rotor

Figure 51 depicts the damped natural frequency map of the rotor bearing system for operation to 50 krpm, with insets showcasing two forward whirl mode shapes at 10 krpm. These mode shapes correspond to conical and ~cylindrical rigid body modes at ~ 6.3 krpm and ~ 7.8 krpm. Figure 52 depicts the viscous damping ratios, corresponding to the two forward whirl modes, decreasing with rotor speed. This behavior is typical of a foil bearing since damping arises from dry-friction and/or mechanical hysteresis effects. It is well known that the equivalent viscous damping in a GFB is inversely proportional to whirl frequency (ω or rotor speed), i.e., $C \sim \gamma/\omega$, where γ is the bearing loss factor, a measure of the mechanical energy dissipation characteristic to the bearing. Note also that the damping ratio for the conical mode is nearly zero at the top rotor speeds (> 40 krpm) and likely to result in rotor motions with subsynchronous whirl frequencies.

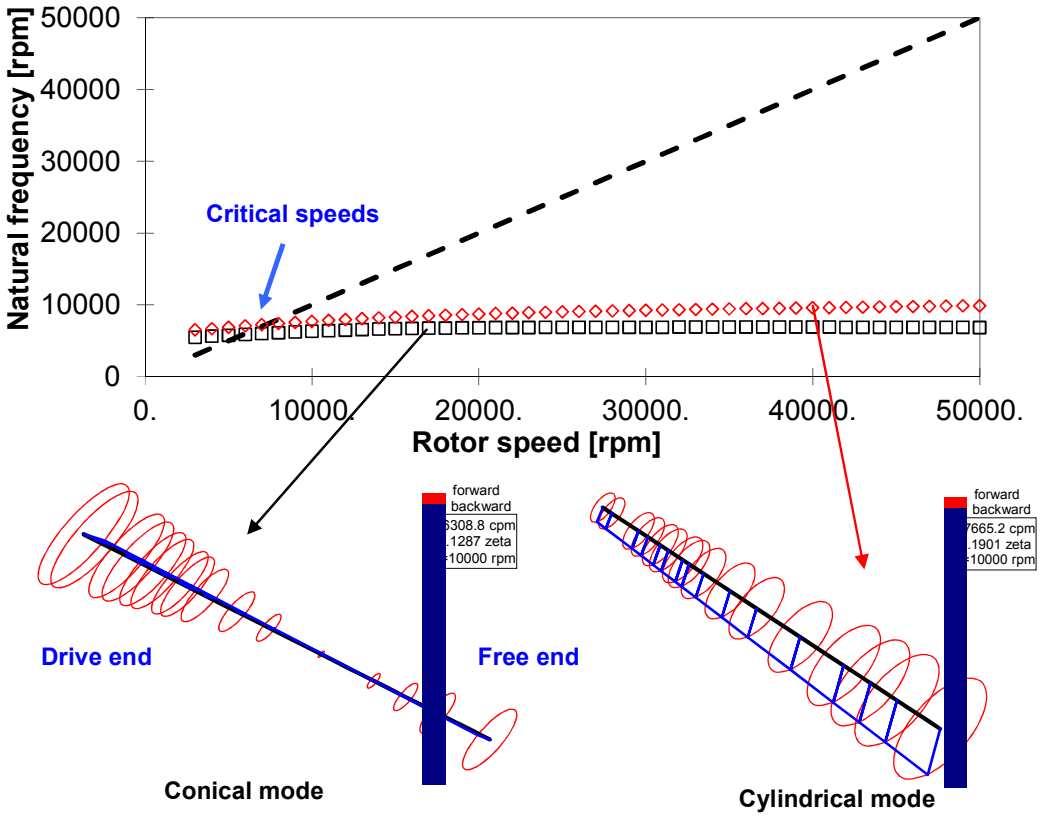

Fig. 51 Predicted damped natural frequency map for rotor-MMFB system. Insets show first two forward whirl mode shapes

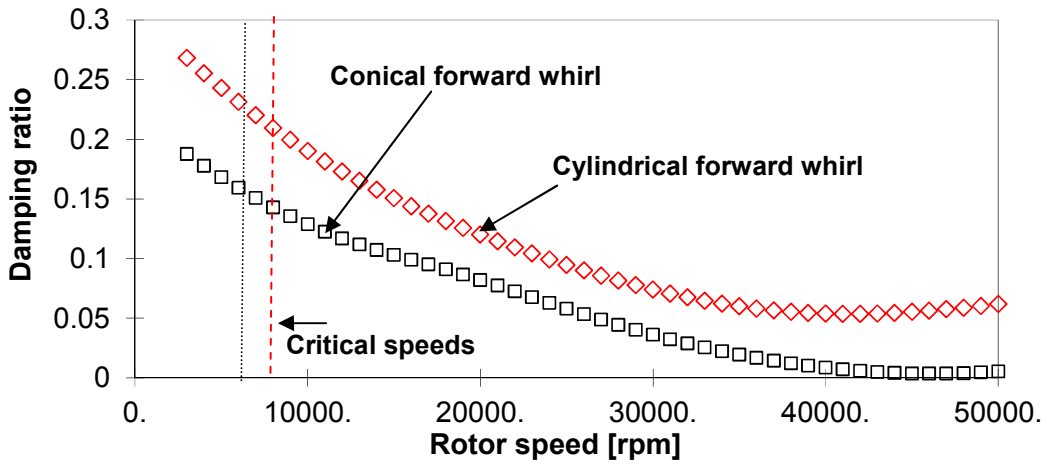

Fig. 52 Predicted damping ratios corresponding to natural frequencies in Fig. 51

Figure 53 shows the normalized[21] rotor response amplitude and phase angle measured at the rotor drive end, horizontal direction, for measurements with out-of-phase (180°) imbalances masses, 240 mg (u = 15 μm) and 360 mg (u = 22.6 μm). The normalized response amplitudes in the speed range from 10 krpm to 50 krpm show comparable magnitudes indicating that the system behaves linearly. At the critical speed, ~7 krpm , the peak normalized amplitude for the test with the largest imbalance (360 mg) is slightly larger than that for the 240 mg imbalance.

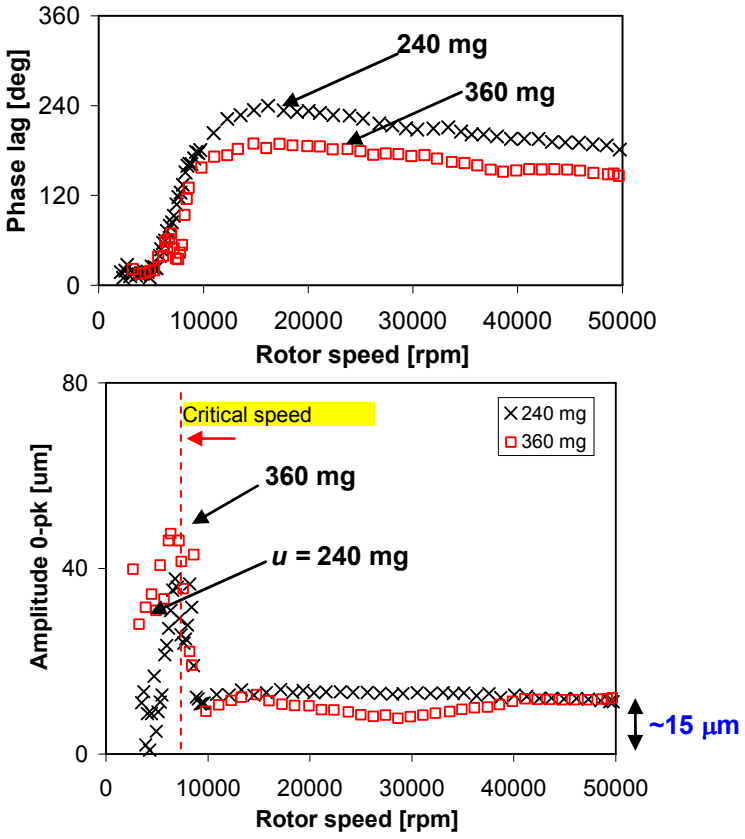

Fig. 53 Normalized rotor response amplitude and phase angle vs. shaft speed for out-of-phase imbalance masses: 240 mg and 360 mg. Measurements at rotor drive end horizontal direction during rotor ramp up (acceleration 600 rpm/s). Measurements show baseline subtraction

[21] The rotor response amplitude for u = 22.6 μm (m_e=360 mg)is normalized by multiplying its amplitude times the ratio of smallest imbalance mass to the current imbalance mass.

Figure 54 shows the predicted and measured rotor response- angle of phase lag and displacement amplitude- at the rotor drive, horizontal direction, obtained for two out-of-phase (180°) imbalance masses, 240 mg (u = 15 μm) and 360 mg (u = 22.6 μm). At high speeds, the synchronous response amplitude for the larger imbalance mass (360 mg) is proportionately larger than that with a 240 mg imbalance mass. The predictions, amplitude and phase, agree well with the measured displacements for the lowest imbalance (240 mg). However, for the larger mass of 360 mg, the measured peak response amplitude when traversing the critical speed is much larger than the prediction. The difference points out to the test MMFBs offering lesser damping than predicted.

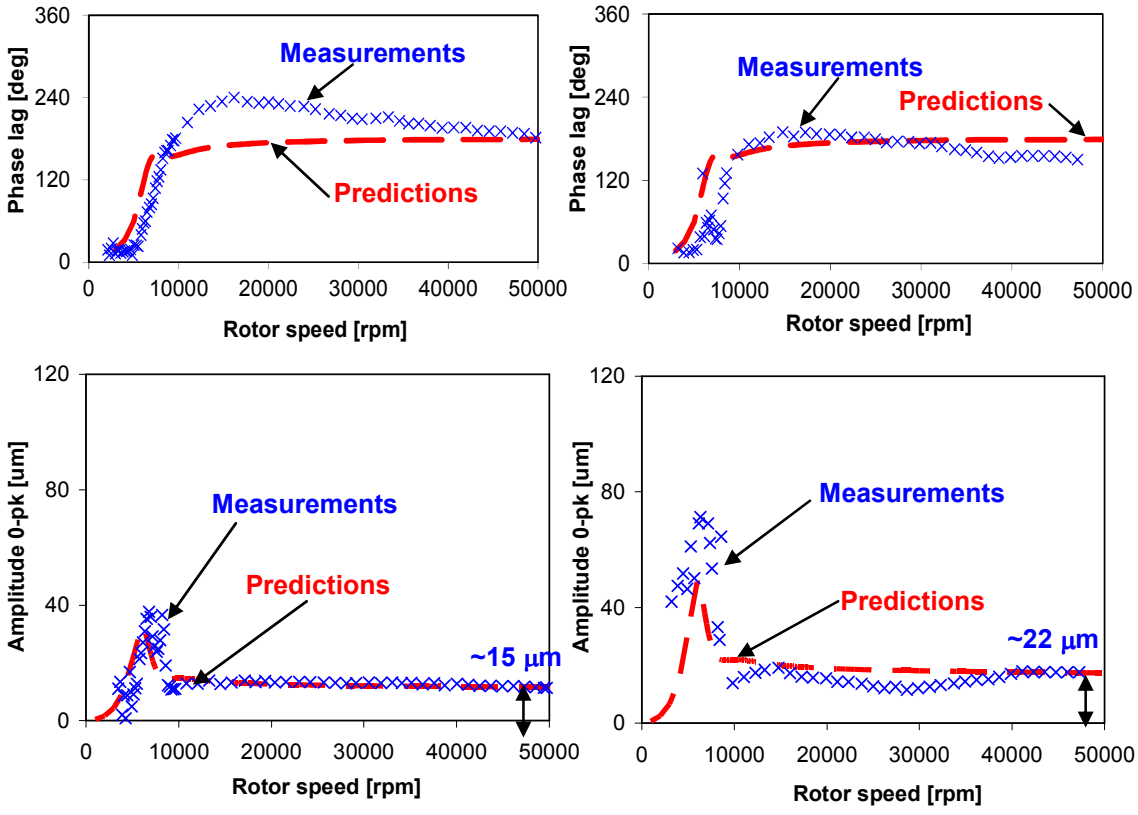

(a) 240 mg Out-of-phase (b) 360 mg Out-of-phase

Fig. 54 Measured and predicted rotor response amplitude and phase angle versus shaft speed for two out-of-phase imbalance masses (a) 240 mg and (b) 360 mg. Measurements at rotor drive end horizontal direction during rotor ramp up. Measurements show baseline subtraction

Figure 55 shows the predicted and measured rotor response, phase angle and amplitude, at the rotor free end, vertical direction, for (a) in-phase and (b) out-phase imbalance masses m_e= 360 mg, corresponding to imbalance displacements of u =8.2 μm and 22.6 μm, respectively.

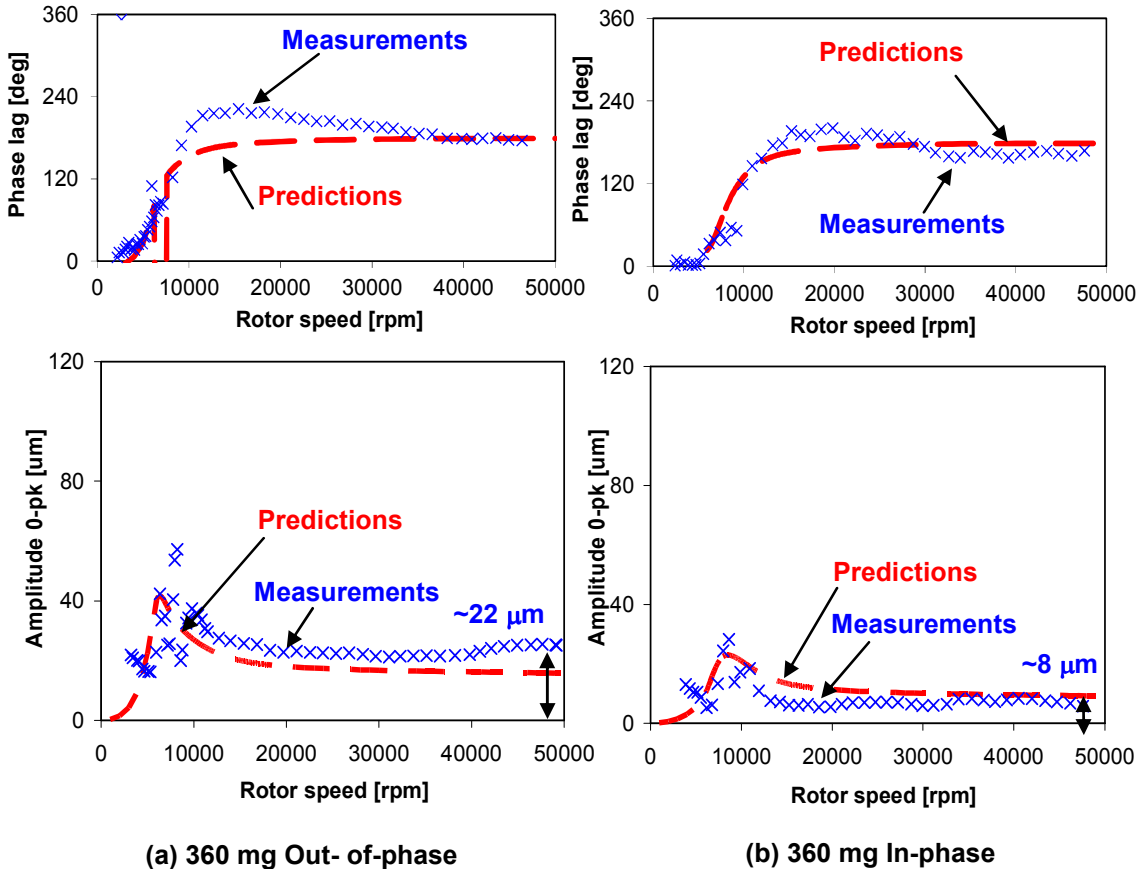

Fig. 55 Measured and predicted rotor response amplitude and phase angle versus shaft speed for (a) In-phase and (b) out-of-phase 360 mg imbalance masses. Measurements at rotor free end vertical direction during rotor ramp up. Measurements show baseline subtraction

The measurements show the effect of adding the same imbalance masses, first in-phase and next out-of-phase at the end planes. The predicted and measured peak response amplitudes are comparable. While the finite element model under-predicts the

response amplitudes for the tests with out-of-phase imbalance mass of 360 mg, the predictions and measurements agree well for the in-phase imbalance of 360 mg.

Figures 56 and 57 show waterfall plots of the recorded rotor responses at the rotor drive end (horizontal plane), for out-of-phase imbalance masses equaling 240 mg and 360 mg, respectively. The rotor acceleration is 600 rpm/s (10 Hz/s). The plots show large amplitudes of synchronous motion (1X) as the rotor traverses a critical speed. 2X and 3X vibration components are present, although are small in amplitude. No sub-synchronous whirl motions appear in the measurements even at the highest rotor speed (50 krpm), in spite of the little to null viscous damping in the bearings.

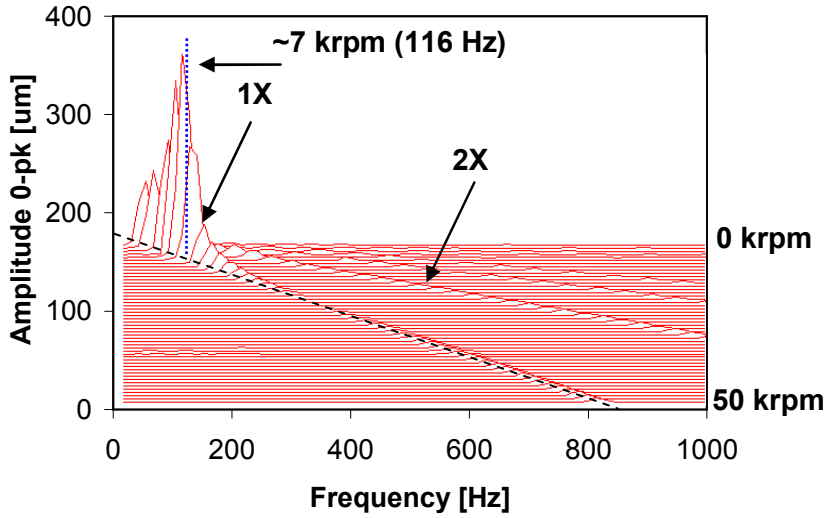

Fig. 56 Waterfall plot of rotor response at its drive end, horizontal plane, for out-of-phase imbalance mass of 240 mg. Rotor acceleration 600 rpm/s

Figure 58 depicts the waterfall plot of rotor response at its free end, vertical plane, for an in-phase imbalance mass of 360 mg. Again, the response is clean without any anomalies.

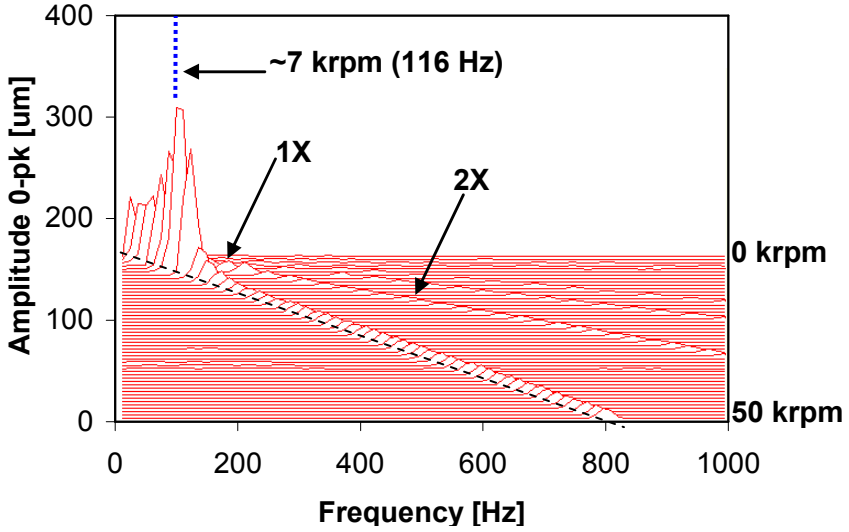

Fig. 57 Waterfall plot of rotor response at the rotor drive end, horizontal plane, for out-of-phase imbalance mass of 360 mg. Rotor acceleration 600 rpm/s

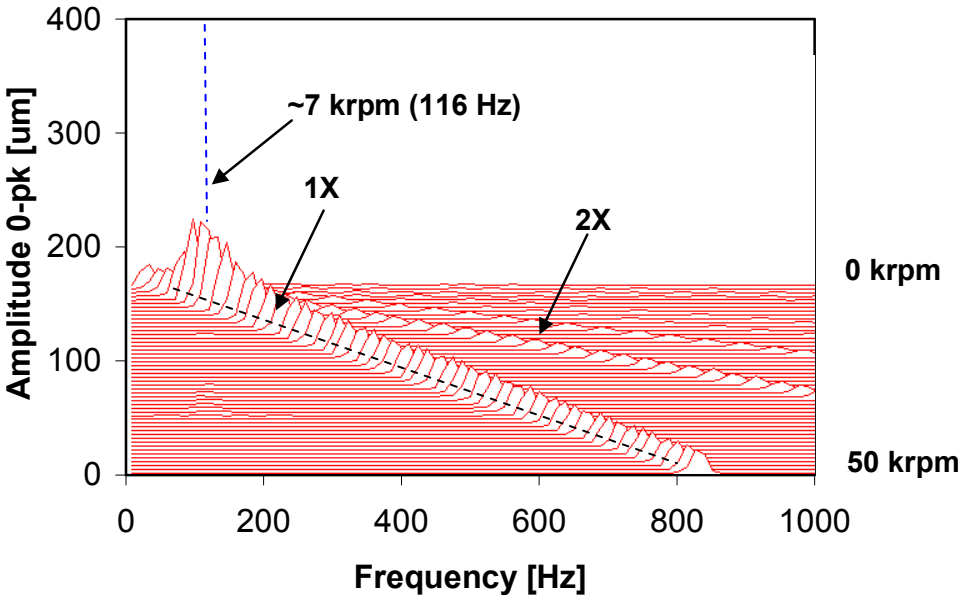

Fig. 58 Waterfall plot of rotor response at the rotor drive end, vertical plane, for in-phase imbalance mass of 360 mg. Rotor acceleration 600 rpm/s

7.4 Conclusions

This section presents the measurements and predictions of response for a hollow rotor supported on two MMFBs while accelerating to a maximum speed of 50 krpm. A finite element structural analysis of the rotor, with force coefficients predicted for the MMFB, predicts rotor responses for in-phase and out-of-phase imbalance masses, as in the tests. The normalized amplitudes of the recorded rotor responses show the system behaves linearly up to the maximum speed of 50 krpm. Waterfall plots show dominant synchronous responses; 2X and 3X motions are very small in amplitude. The predictions agree well with the recorded displacements albeit there are differences in the peak amplitudes when the rotor crosses its critical speeds; the test bearings show lesser damping than predictions indicate.

8. MEASUREMENTS OF HIGH TEMPERATURE ROTORDYNAMIC RESPONSE OF A HOLLOW ROTOR SUPPORTED ON TWO MMFBs

8.1 Introduction

High speed, high efficiency power generation micro-turbomachinery typically operates at elevated temperatures. The investigation of the performance of MMFBs operating at high temperatures, especially for an extended duration of time, is required before MMFBs can be implemented into such applications.

This section presents (i) the rotor and bearing temperature measurements for the rotor at rest and spinning at 30 krpm, 40 krpm, and 50 krpm and (ii) the dynamic response of the rotor while accelerating from rest to a maximum speed of 36 krpm. In the tests, the heater set temperature (T_s) is fixed at 22 ºC (room temperature), 100 ºC, 150 ºC, and 200 ºC.

8.2 Description of Test Setup

The bearing and rotor temperatures are measured at ten locations as depicted in Figure 59. T_1-T_4 and T_5-T_8 denote K-type thermocouples recording the temperatures at the bearing cartridge OD near the rotor free and drive ends, respectively. Infrared thermometers record the rotor surface temperatures at the free and drive ends, T_{FE} and T_{DE}, respectively. The cartridge heater heats the rotor non-uniformly along its length [56], with the rotor free end being substantially hotter than the drive end. The cooling air flow rate into the test bearings is maintained steady at ~ 160 L/min[22] with an inlet upstream pressure of 1.9 bar (27.6 psi) for all tests.

Note that, for tests with the heater turned off, although the ambient temperature is ~ 22 ºC, upon operation, for rotor speeds from 30 krpm to 50 krpm, the rotor temperature rises to a steady value; varying from ~ 32 ºC to 38 ºC at the rotor free end and from ~ 28 ºC to 33 ºC at the rotor drive end. Also, rotor spinning at 30 krpm, 40 krpm, and 50

[22] In prior tests [57] with two similar bump type foil bearings supporting the rotor, a cooling flow rate of ~160 L/min was found to adequately cool the rotor and the two bearing during high temperature tests, and hence this flow rate is chosen for the current tests. The flowmeter is calibrated by the manufacturer at 1 atmosphere and 21ºC. The uncertainty in the measured flow is ±1.5% of the full scale range (500 L/min).

krpm, requires 20s, 35s, and 55s, respectively, for reaching thermal equilibrium while the heater is turned off. Note that the viscous drag losses result in system temperature rise.

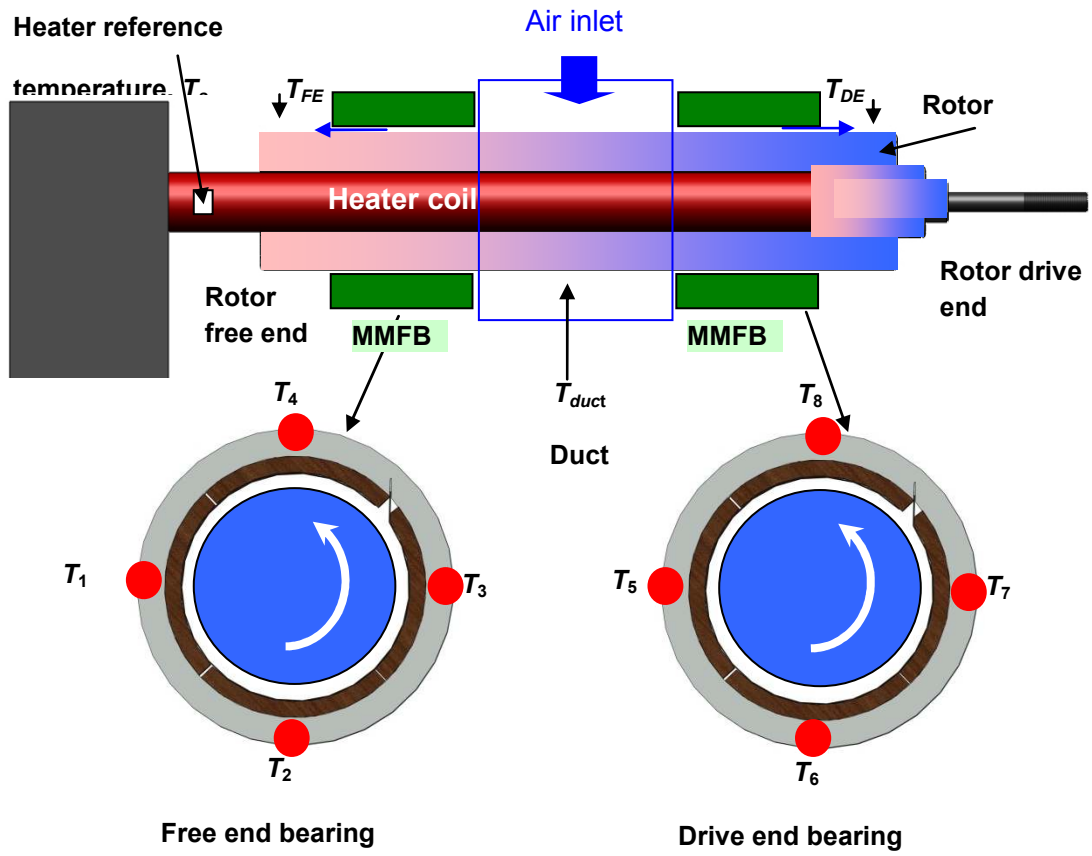

Fig. 59 Locations for measurements of temperatures on the rotor surface and the bearing cartridges

8.3 Temperature Rise of System Components versus Elapsed Time

Table 6 shows the various test cases, for increasing heater set temperatures (T_s = ~22 ºC (heater off), 100 ºC, 150 ºC, and 200 ºC) and for the rotor at rest and spinning at 30 krpm, 40 krpm, and 50 krpm. For test case #1, the rotor is at rest and the heater set temperature is increased, in steps of 50 ºC, up to 200 ºC, while recording the

temperatures continuously until the system reaches equilibrium for each set temperature. For test cases #2-4, at steady rotor speeds, the bearings and rotor temperatures are recorded until the system reaches equilibrium. The rotor and bearing temperatures are recorded every five minutes until the system reaches a thermal equilibrium[23]. The results show the temperature rise at each measuring location, i.e., the difference between the absolute temperature and the steady ambient temperature before commencement of the experiment.

Table 6. Test cases for various rotor speeds and heater set temperatures (T_s)

Test case #	Heater set Temperature, T_s [ºC]	Rotor speed [krpm]	Time [min]
1	~ 22 (Heater off) →100→150→200	0	135
2	~ 22 (Heater off) →100→150→200	30	145
3	~ 22 (Heater off) →100→150→200	40	150
4	~ 22 (Heater off) →100→150→200	50	230
			Overall : 11 hr

8.3.1 Temperature Measurements without Rotor Spinning

Figure 60 depicts, for test case # 1 (no rotor spinning), the temperature rise of the rotor free (T_{FE}) and drive (T_{DE}) ends, the bearing sleeves ($T_{1\text{-}8}$), and the duct air (T_{duct}) versus elapsed time while the rotor remains at rest. These measurements are later used to estimate the effect of rotor spinning on the temperature distribution in the bearings.

Since the electric heater heats non-uniformly the rotor along its axial length [56], the equilibrium temperatures at the rotor free and drive ends are dissimilar, with the rotor free end being hotter than the drive end. Note that the air flow cooling the coupling near the rotor drive end also cools the rotor drive end. With increasing heater set temperatures (up to 200 ºC), the difference between the equilibrium temperatures at the

[23] If any temperature fluctuation is less than 1 ºC within a 15 minute time period, the system is considered to be in thermal equilibrium.

rotor drive and free ends increases, resulting in a larger thermal gradient along the rotor length. The air temperature inside the enclosure (duct) of the steel block housing the bearings also increases with increasing heater set temperatures, and follow trends similar to that of the rotor surface temperatures.

T_1 to T_4 and T_5 to T_8 are the temperatures measured on the outer surface of the bearing cartridges at their mid-span. The temperatures around the bearing cartridge circumference are not identical, varying by a maximum of 4 ºC at the highest heater set temperature of 200 ºC. While the rotor surface temperature reaches thermal equilibrium quickly, the bearing cartridge outer surfaces require considerably longer time (typically > 30 min). However, the rate of increase in temperature after ~ 20 min is rather small. Hence, when the bearing temperatures do not increase more than 1 ºC in a 15 minute time period, the system is considered to be in thermal equilibrium and the heater set temperature increased to the next magnitude. The rate of increase in the temperature of the bearing cartridge is considerably lesser than that for the rotor. The steady cooling air flow and the heat loss by conduction to the steel block removes heat from the bearing. Although the temperature rise at the rotor free end is much higher than that at the rotor drive end, the two bearing cartridge temperatures are nearly identical.

8.3.2 Temperature Measurements with a Spinning Rotor

Figures 61, 62, and 63 depict the temperature rise on the rotor free end (T_{FE}) and drive end (T_{DE}), of the bearing sleeves (T_1-T_8), and the duct air (T_{duct}) versus elapsed time while the rotor spins at 30 krpm, 40 krpm, and 50 krpm respectively. The cooling flow into both bearings is at a rate of ~ 160 L/min. The trends in the variation of the temperature rise of the components, in general, follow patterns similar to those without rotor spinning. However, while spinning at 30 krpm - 50 krpm, even without the heater turned on, the temperatures on the rotor and the bearings slightly increase.

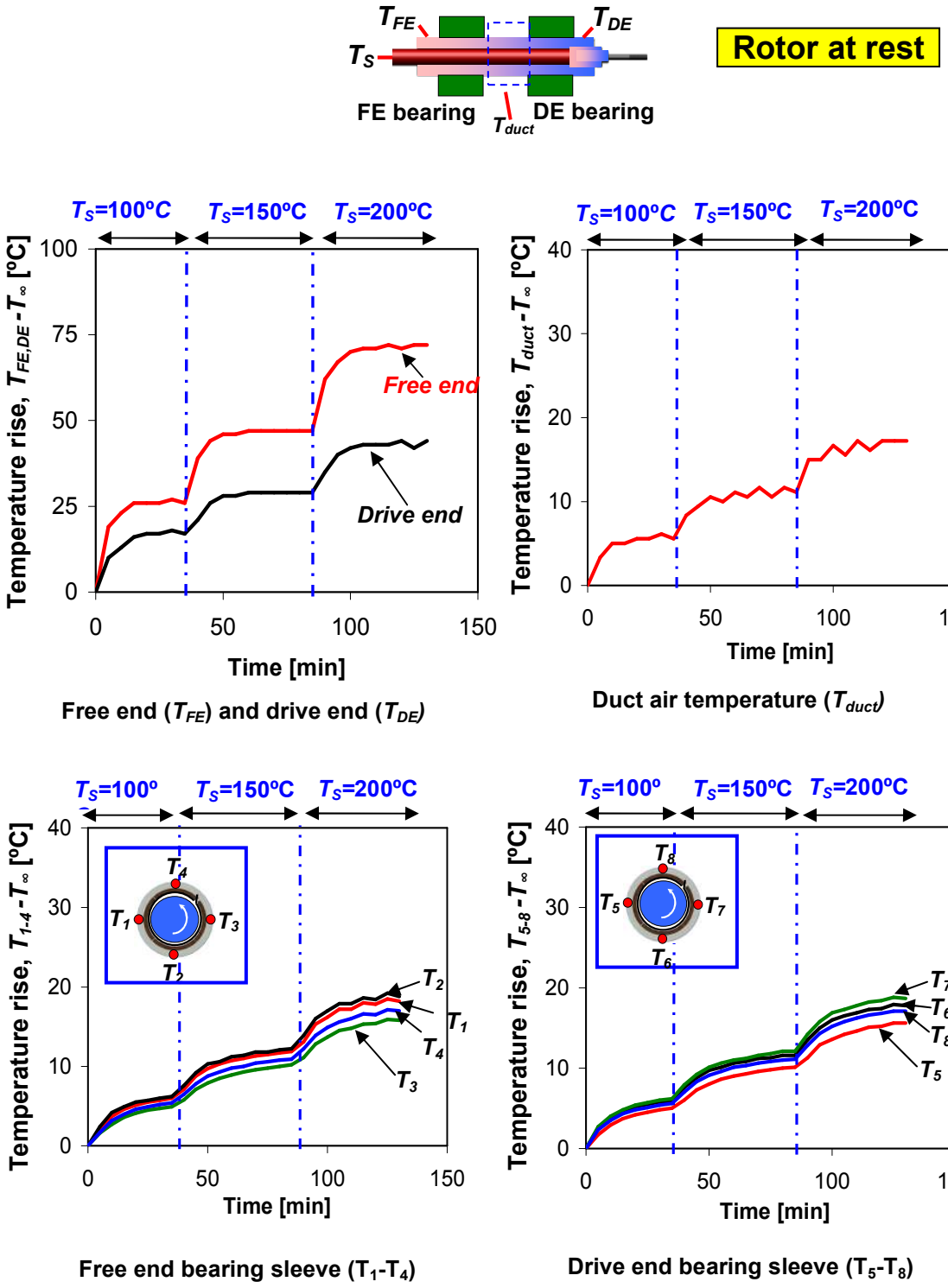

Fig. 60 No rotor spinning: Recorded test system component temperature rises versus elapsed time. Steady axial cooling flow into bearings at 160 L/min.

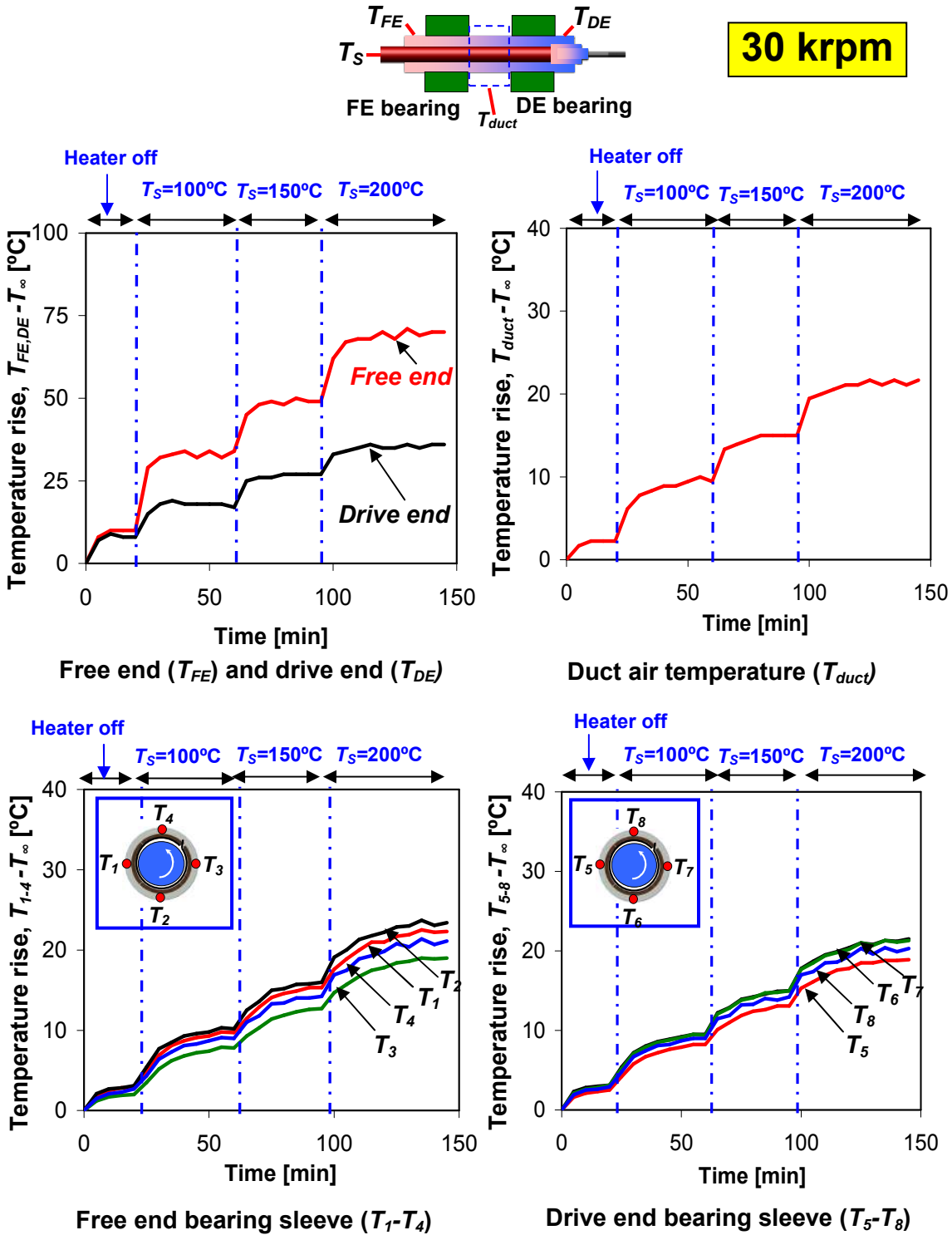

Fig. 61 Rotor spinning at 30 krpm: Recorded test system component temperature rises versus elapsed time. Steady axial cooling flow into bearings at 160 L/min.

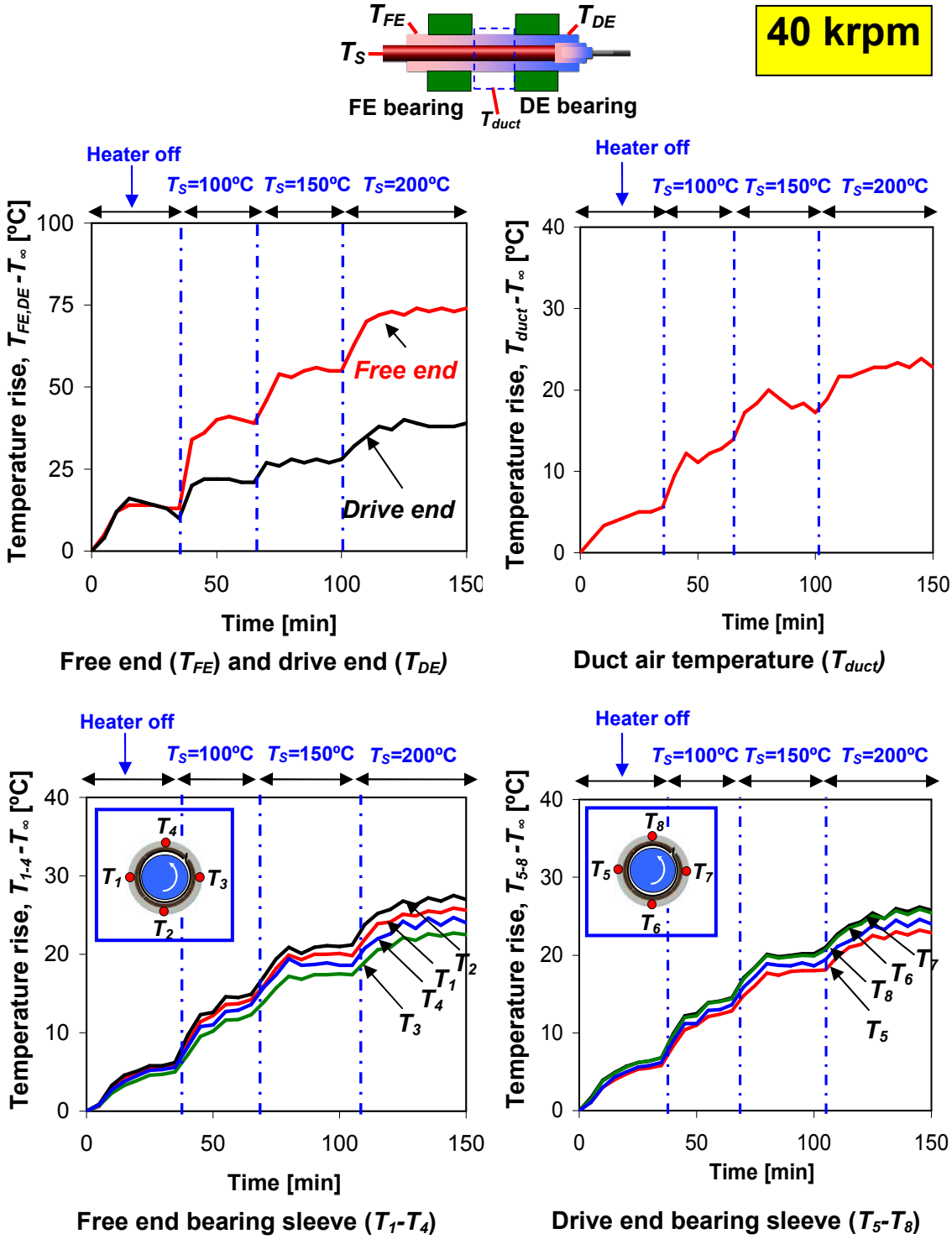

Fig. 62 Rotor spinning at 40 krpm: Recorded test system component temperature rises versus elapsed time. Steady axial cooling flow into bearings at 160 L/min.

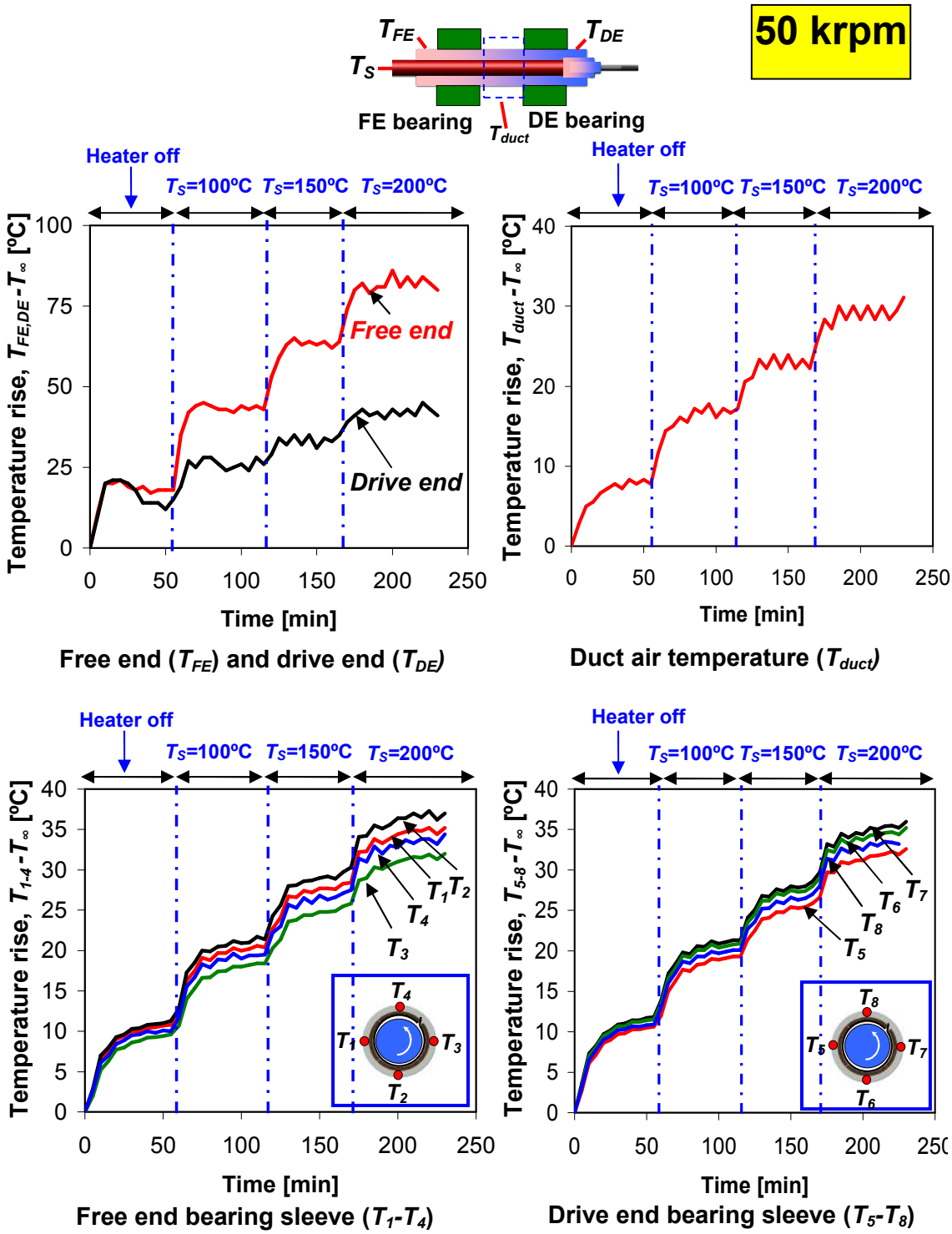

Fig. 63 Rotor spinning at 50 krpm: Recorded test system component temperature rises versus elapsed time. Steady axial cooling flow into bearings at 160 L/min.

Figure 64 shows the temperature rise on the rotor surface, (a) free end and (b) drive end, for various heater set temperatures and versus rotor speed. The rotor shows a marked axial temperature gradient, more pronounced as the heater temperature increases. The rotor free end temperature rise is higher than that at the drive end since the heater has a marked temperature differential along its axis, being hotter at the rotor free end. In general, the rotor OD temperature rises as the rotor speed increases. This effect is markedly linear, in particular when the heater is not active. Note that without spinning, the rotor contacts the bearings. As the rotor starts spinning, an air gap is formed between the top foil and the rotor that aids to 'cool' the rotor. This effect is noticeable only for the test with the highest heater set temperature of 200 ºC.

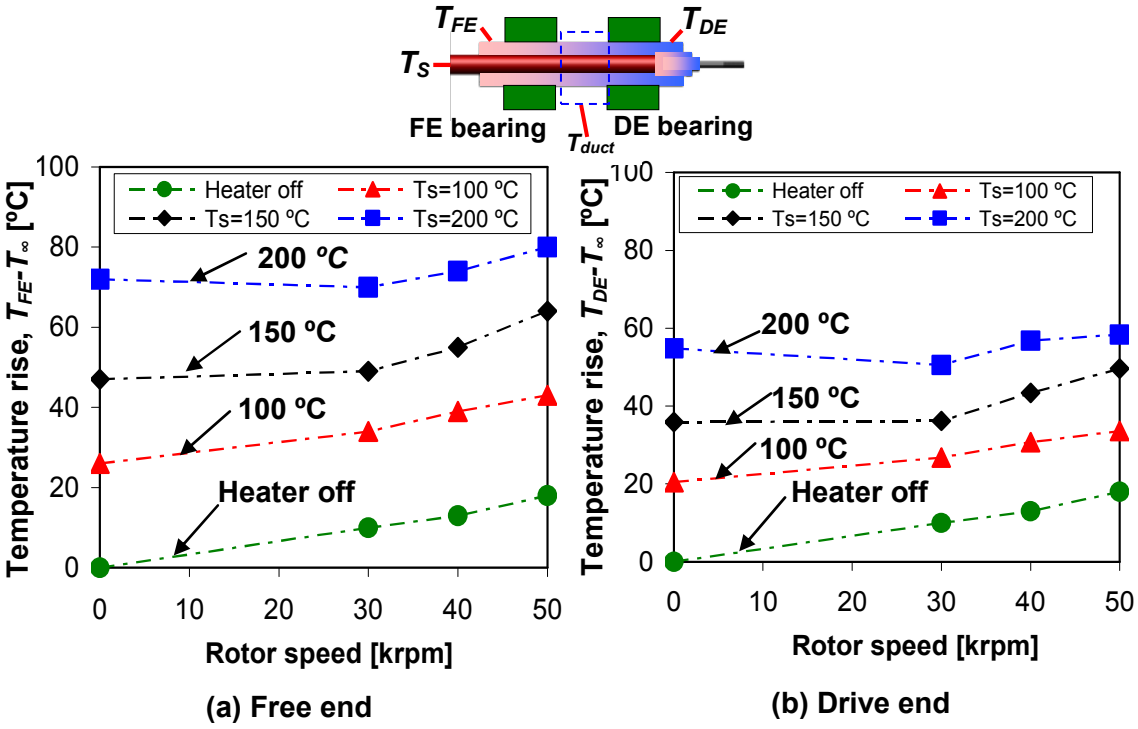

Fig. 64 Equilibrium temperatures rise at rotor OD surface, free and drive ends, versus rotor speed. Steady axial cooling flow into bearings at 160 L/min.

Figure 65 shows the rotor OD temperature rises (T_{FE} -T_{duct}) and (T_{DE} -T_{duct}) with respect to the duct air temperature (T_{duct}) versus rotor speed for various heater set temperatures. Recall that there is a distinct temperature gradient along the rotor when the heater is active. The rotor temperature rises at both ends are almost identical when the heater is turned off. With the heater set temperatures at T_s=100 ºC, 150 ºC, and 200 ºC, the rotor OD free end shows a much larger increase in temperature than the rotor drive end. In general, with increasing rotor speed, the temperature rises at either of the rotor ends.

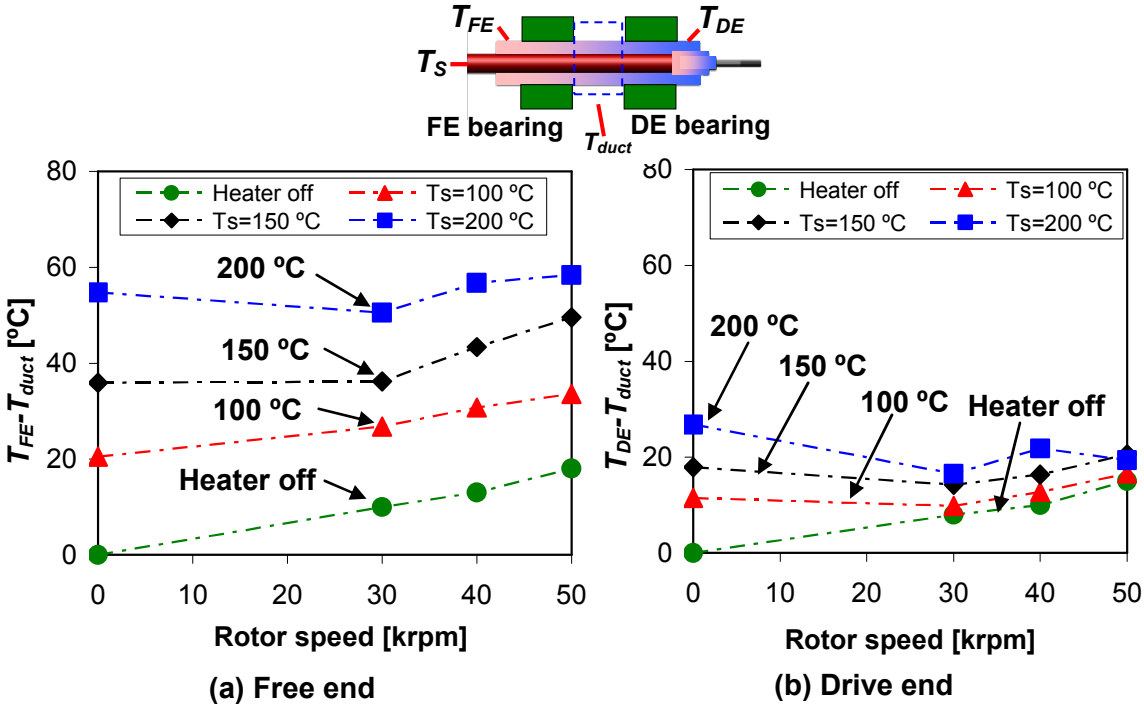

Fig. 65 Rotor temperature rise relative to the duct temperature, (T_{FE}-T_{duct}) and (T_{DE}-T_{duct}), at equilibrium versus rotor speed. Steady axial cooling flow into bearings at 160 L/min. (Note that T_{duct} increases with rotor speed)

Figure 66 depicts the bearings' OD average temperature rise ($T_{1\text{-}4}$ -T_∞, $T_{5\text{-}8}$ -T_∞) versus rotor speed and for increasing heater temperatures (T_s). Figure 67 depicts the same temperatures but relative to the duct temperature, i.e., ($T_{1\text{-}4}$ -T_{duct}) and ($T_{5\text{-}8}$ -T_{duct}).

Note that the vertical bars in each data point show the standard deviation of the four measured temperatures on a bearing cartridge. Even though there is a significant thermal gradient along the rotor axis (max. ~ 20 ºC between the two bearing locations for the highest heater set temperature), the temperature rises in the two bearings are nearly identical. The standard deviation of the temperatures around the bearing cartridge outer surface increases with increasing heater temperature. Thus, for a higher T_s, a more pronounced circumferential thermal gradient takes place around the bearing cartridge. With increasing rotor speed, from 30 krpm to 50 krpm, the bearing OD temperatures with respect to the duct temperature increase rapidly. That is, relative to the air inlet temperature, the bearings heat steadily and show a temperature rise growth proportional to rotor speed.

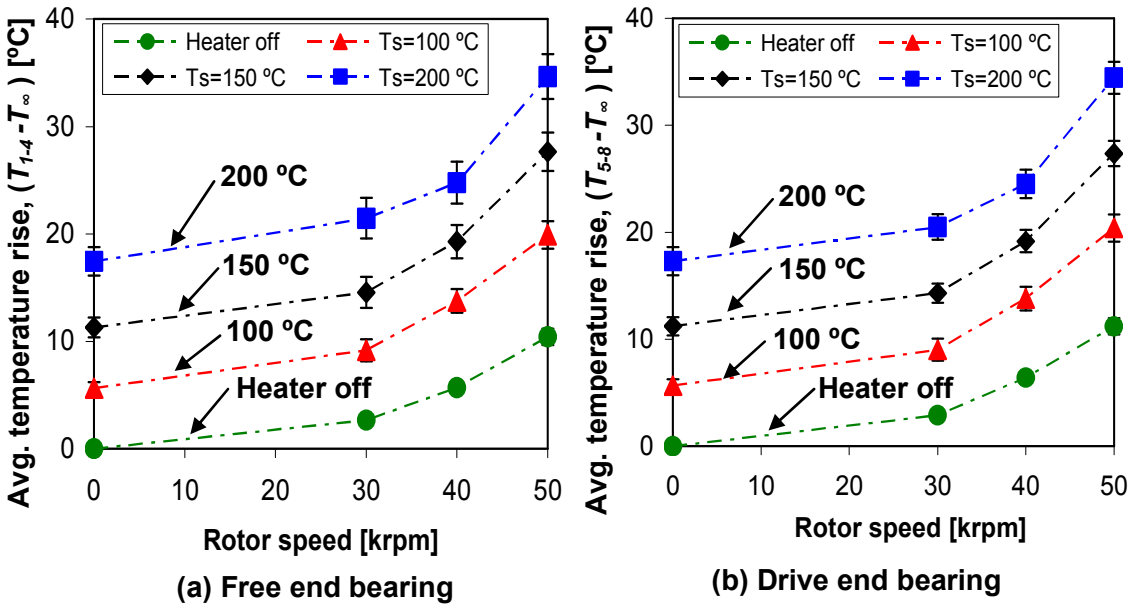

Fig. 66 Average bearing OD temperature rises (with std. deviation) versus rotor speed and increasing heater temperatures. Steady axial cooling flow into bearings at 160 L/min.

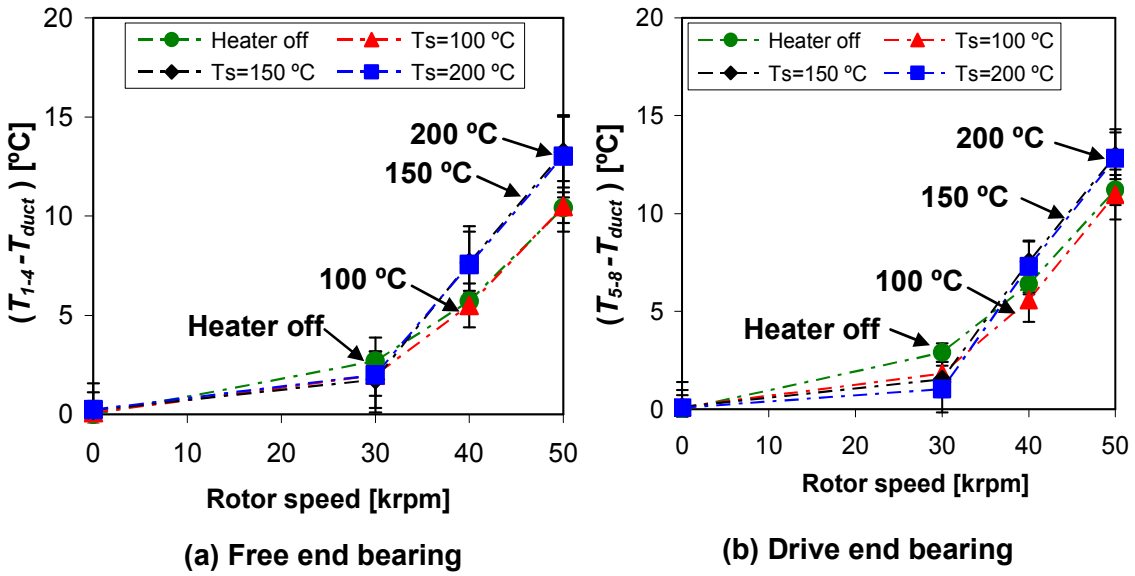

Fig. 67 Average bearing OD temperature rise with respect to duct temperature versus rotor speed and increasing heater temperatures. Steady axial cooling flow into bearings at 160 L/min.

8.4 Measurements of Rotor Response for Test Rig Operation at Various Heater Set Temperatures

The following measurements elucidate the effect of rotor temperature on the dynamic forced response of the rotor. The experiments are conducted with heater set temperatures (T_S) of 22 ºC (room temperature), 100 ºC, 150 ºC, and 200 ºC. Note that, with increasing rotor temperatures, the rotor and bearing geometry as well as the assembly clearances do change.

Once the bearings and the rotor are assembled and the rotor balanced in place, large imbalance masses of 240 mg and 360 mg are added at the two rotor end planes for various tests. Note that the baseline response due to remnant imbalance is not subtracted in the following results as baseline responses for the various operating temperatures are not identical. See section 6.3 for baseline subtracted rotor responses (room temperature). The rotor dynamic response is recorded while the rotor speeds up to 36 krpm (600 Hz) with an acceleration of 400 rpm/s (6.7 Hz/s). All experiments were conducted three times to establish the repeatability of the recorded rotor responses.

Once the electric heater is turned on, the operator waits for the system to reach a thermal equilibrium, and turns on the motor to spin the rotor to a maximum speed of 36 krpm[24] (600 Hz) and then the rotor is allowed to coast down to rest. The operator waits for the system to reach a thermal steady state once again before resuming a test. After three sets of identical tests, the heater set temperature is increased and the procedure repeated. The heater temperature fluctuates ± 5 ºC maximum while the heater control circuit turns the heater coil on/off intermittently to maintain the set temperature. However, the rotor and bearing cartridge OD temperatures remain fairly constant once a thermal steady state is achieved.

Table 7 lists the steady state temperatures on the rotor surfaces ($T_{FE,}$ T_{DE}) and at the four bearing OD locations. Figure 68 depicts the rotor surface temperatures ($T_{FE,}$ T_{DE}) versus heater set temperatures. The rotor free and drive end equilibrium temperatures show slight variations in the repeated tests; being more pronounced when the heater set temperature is at 200 ºC. These temperatures were measured before spinning the rotor. The operator waits for ~ 30 mins between tests to achieve a thermal equilibrium; however, the measurements reveal that the tests with the heater temperature at 200ºC were resumed slightly before reaching a thermal equilibrium. Note that this thermal equilibrium is lost instantly as soon as the rotor starts spinning. The rotor surface temperatures are much lower than the heater set temperatures. Also, the bearing cartridge temperatures are smaller than the rotor surface temperatures, and hence it is reasonable to assume that the metal mesh (and top foil) temperatures fall somewhere in between the rotor and bearing cartridge temperatures.

[24] High temperature measurements are conducted only up to a maximum speed of 36 krpm. Ambient temperature measurements are conducted to a maximum speed of 50 krpm.

Table 7 Measured bearing cartridge and rotor OD temperatures for increasing heater set temperatures (T_S)

Imbalance mass	Heater set temp. T_S °C	Rotor free end temp. T_{FE} °C	T_1- T_4 °C		Duct air, T_{duct} °C	Rotor drive end temp. T_{DE} °C	T_5- T_8 °C	
			Avg. bearing OD temp.	Std. dev.			Avg. bearing OD temp.	Std. dev.
240 mg	Heater off	25.5	25.5	0.0	22	25.5	25.5	0.0
	100	47±1	30.8	0.4	30	36±1	31.0	0.5
	150	63±1	35.5	0.7	33	46±1	35.7	0.7
	200	82±3	39.5	1.1	38	54±3	39.4	1.2
360 mg	Heater off	24	24.0	0.0	21	24	24.0	0.0
	100	46±1	28.7	0.5	27	32±2	28.6	0.5
	150	68	35.2	0.9	33	47±1	35.2	0.9
	200	92±1	41.5	1.4	37	62±1	41.3	1.3

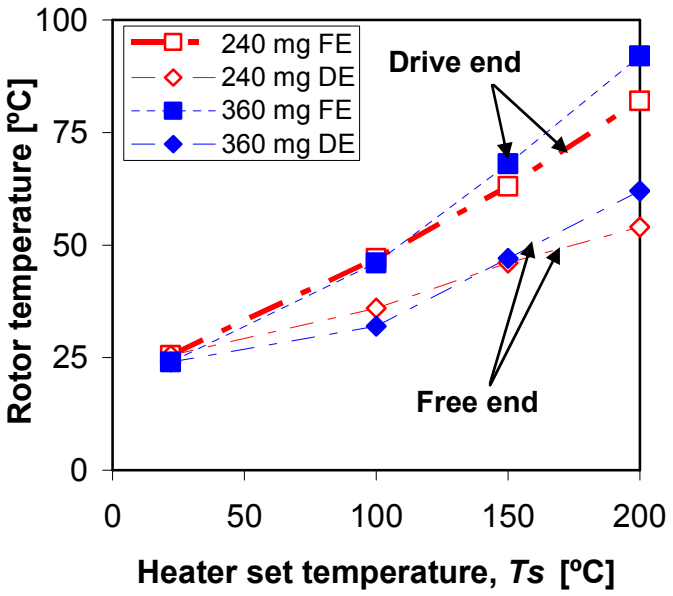

Fig. 68 Rotor OD free and drive end side temperatures immediately before conducting a rotor speed ramp-up test. Steady axial cooling flow into bearings at 160 L/min. Data from tests with 240mg (out-of-phase) and 360 mg (in-phase) imbalances

Note that the thermal equilibrium is lost instantly as soon as the rotor starts spinning. The rotor OD surface temperatures are much lower than the heater set temperatures. Also, the bearing cartridge temperatures are smaller than the rotor surface temperatures, and hence it is reasonable to assume that the metal mesh (and top foil) temperatures fall somewhere in between the rotor and bearing cartridge temperatures.

Figure 69 shows the amplitude and phase of rotor response, near the rotor free end bearing, during controlled rotor acceleration (400 rpm/s) and with out-of-phase imbalance masses (m_e=240 mg) attached at the rotor end planes. Note that the rotor has a remnant imbalance even after trim balancing. The inset table shows the corresponding rotor OD surface temperatures for each heater set temperature. The rotor amplitudes along the horizontal plane peak at ~ 7 krpm, while the vertical amplitudes peak at ~9 krpm. Rotor slow roll is compensated at ~ 2,300 rpm. The heater temperature has little influence on the recorded amplitude. Note from Table 7 that the bearings OD temperatures ($T_{1\text{-}4}$ and $T_{5\text{-}8}$) rise by only ~ 20 ºC for the highest T_s= 200 ºC. Thus, with the set cooling flow rate at 160 liter/min, the rotor and bearing do not heat too much

Figure 70 shows a typical waterfall plot of the rotor response amplitude at the free end, horizontal plane, for a test with the heater set temperature T_s= 200 ºC. The measurements evidence no sub-synchronous vibration amplitudes, while small amplitude 2X and 3X components are present over the entire speed range.

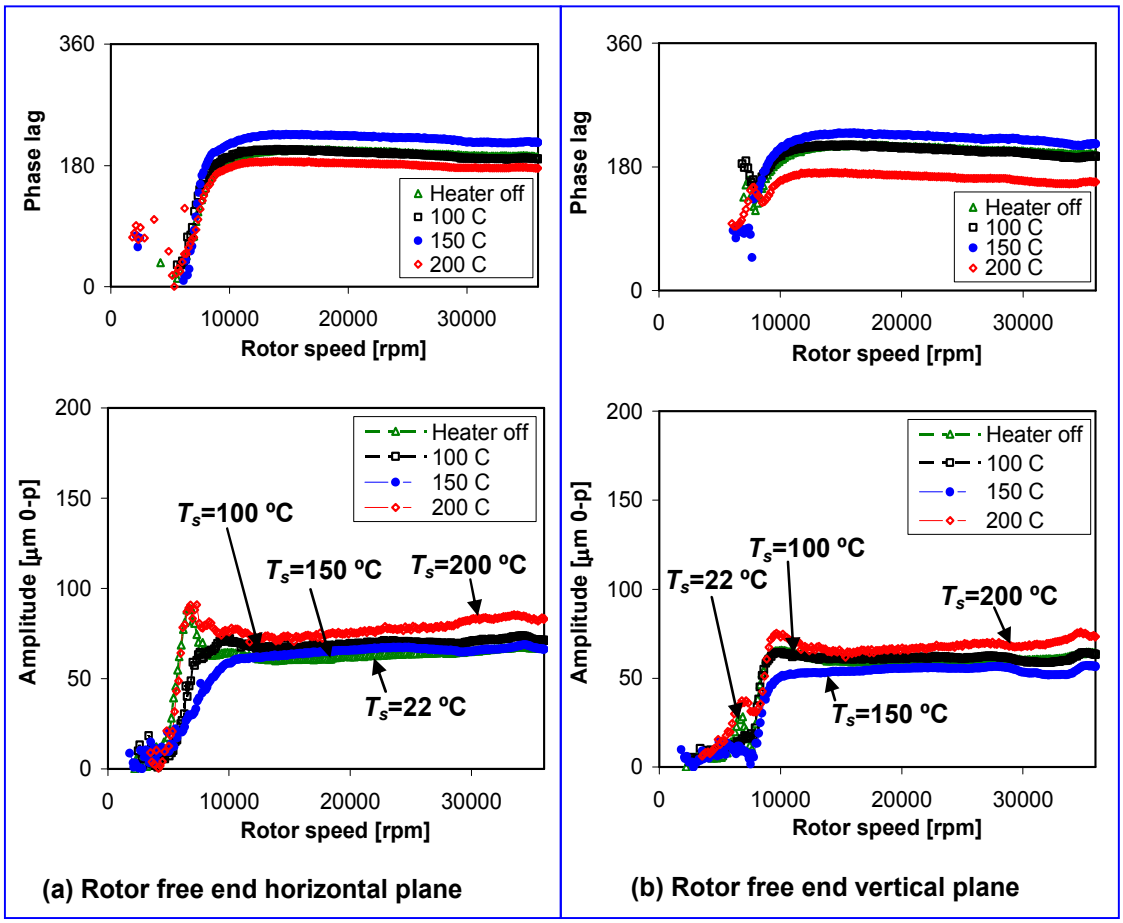

Heater set temp, T_s (ºC)	22	100	150	200
Rotor FE, T_{FE} (ºC)	26	47	63	82
Rotor DE, T_{DE} (ºC)	26	36	46	54

Fig. 69 Rotor synchronous response amplitude and phase versus shaft speed for out-of-phase imbalance masses = 240 mg. Measurements at rotor free end, (a) horizontal plane and (b) vertical plane. Rotor acceleration of 400 rpm/s. Cooling flow rate ~160 L/min. Inset table shows average rotor OD temperatures corresponding to each heater set temperature

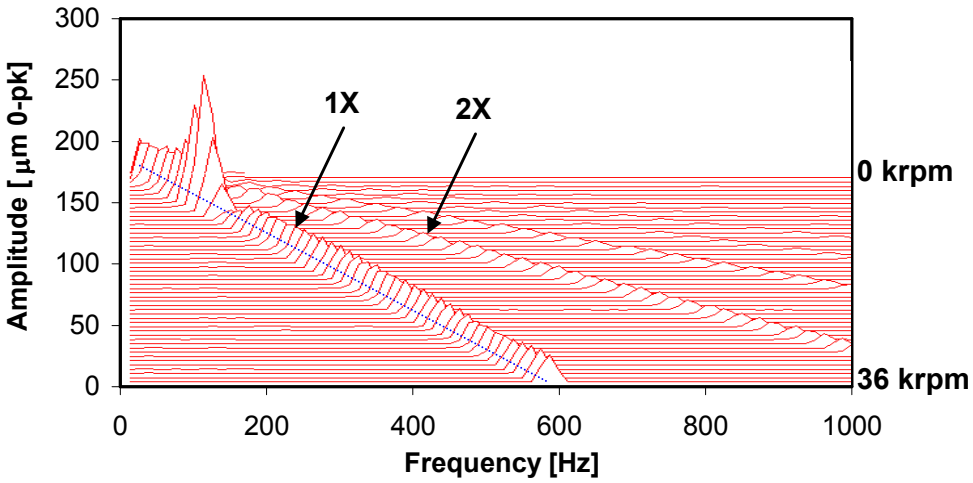

Fig. 70 Waterfall plot of rotor response at the rotor free end, horizontal plane, for out-of-phase imbalance masses = 240 mg. Rotor acceleration 400 rpm/s. Heater set temperature = 200 ºC. Cooling flow rate ~160 L/min.

In general, the rotor lateral displacements show only a single peak as it accelerates to the top speed of 36 krpm. A one DOF (degree of freedom) model may be used to estimate effective stiffness coefficients, K_{eff}, from the measured rotor radial displacements. The natural frequency (ω_n), corresponding to the phase angle of 90º and the fraction of the rotor mass (M_R) supported by the bearing readily provides an estimate of the effective stiffness as $K_{eff} = \omega_n^2 M_R$. Here, along the horizontal direction, ω_n ~ 732 rad/s (7 krpm), and along the vertical direction, ω_n ~ 942 rad/s (9 krpm).

The fraction of the weight of the rotor acting at the free end bearing is 0.58 kg (5.7 N). Thus, the effective bearing stiffness (K_{eff}) along the horizontal direction is ~0.31 MN/m and that along the vertical direction is ~ 0.51 MN/m.

Figure 71 shows the amplitude and phase of the rotor response, near the rotor drive end bearing. Out-of-phase imbalance masses equaling 240 mg are attached at the rotor end planes. The response at the rotor drive end shows that, along the horizontal direction, ω_n ~ 732 rad/s (7 krpm), and along the vertical direction, ω_n ~ 942 rad/s (9 krpm). The fraction of the rotor load acting at the drive end bearing is 0.75 kg. Thus, the

effective bearing stiffness (K_{eff}) along the horizontal direction is ~0.40 MN/m and that along the vertical direction is ~ 0.66 MN/m.

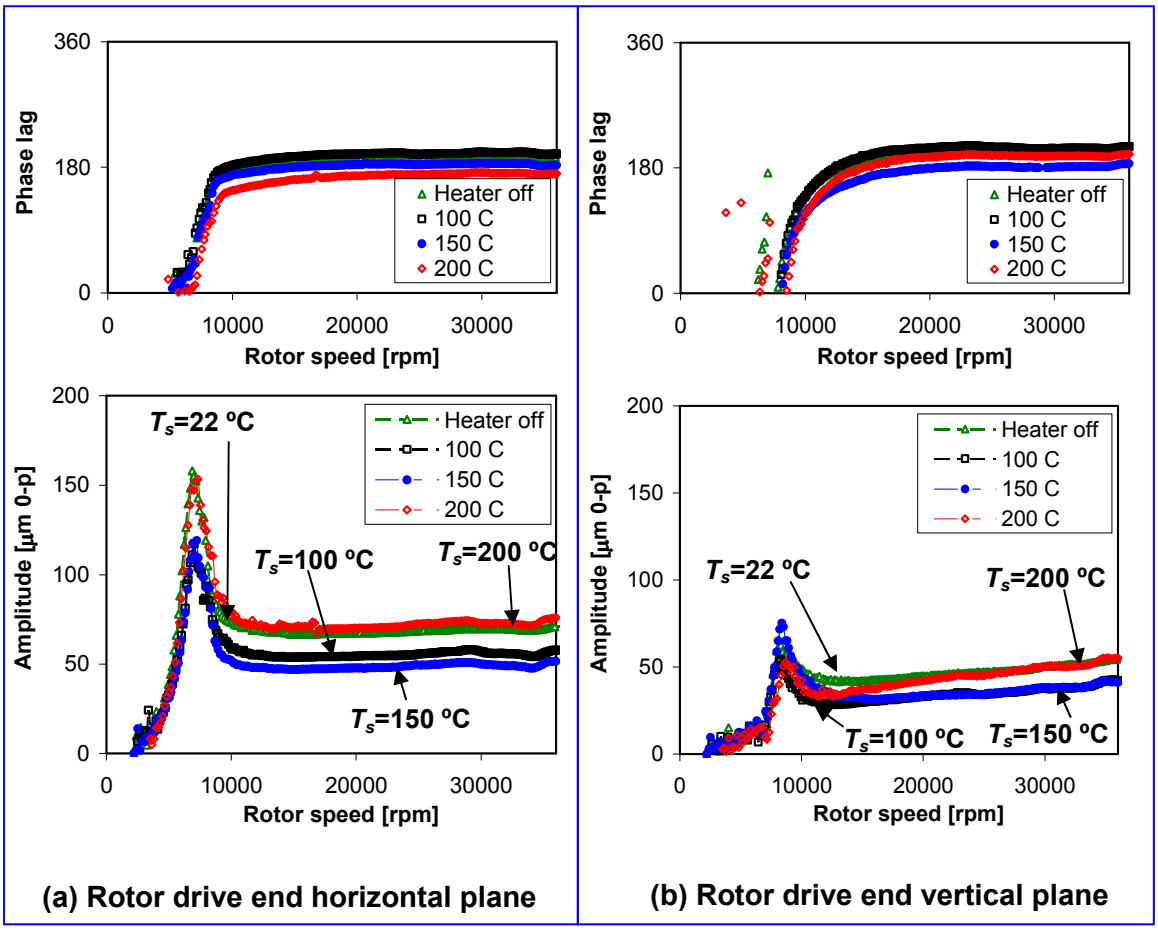

Heater set temp, T_s ºC	22	100	150	200
Rotor FE ºC	25	47	63	82
Rotor DE ºC	25	36	46	54

Fig. 71 Rotor synchronous response amplitude and phase versus shaft speed for out-of-phase imbalance masses = 240 mg. Measurements at rotor drive end (a) horizontal plane and (b) vertical plane. Rotor acceleration of 400 rpm/s. Cooling flow rate ~160 L/min. Inset table shows average rotor OD temperatures corresponding to each heater set temperature

Figures 72 and 73 depict the amplitudes (V & H) and phase angles of rotor response, near its free end and drive end, respectively, during a controlled speed ramp rate of 400 rpm/s and with in-phase imbalance masses equaling 360 mg attached at the rotor end planes. The rotor amplitude measurements for all temperatures are fairly comparable; except for the notorious dip at ~9krpm, in the rotor free end vertical displacements with the heater set temperature at 200 ºC.

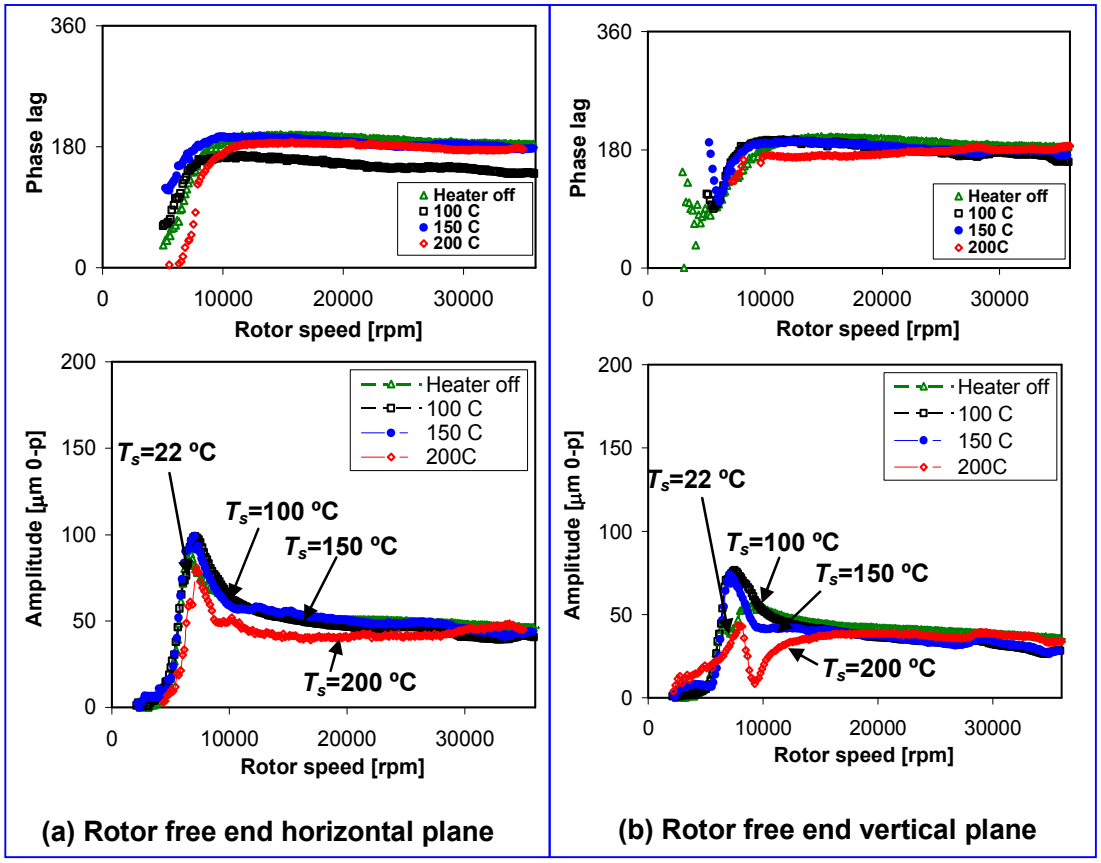

Heater set temp, T_s ºC	22	100	150	200
Rotor FE ºC	24	46	68	92
Rotor DE ºC	24	32	47	62

Fig. 72 Rotor synchronous response amplitude and phase versus shaft speed for in-phase imbalance masses = 360 mg. Measurements at rotor free end (a) horizontal plane and (b) vertical plane. Rotor acceleration of 400 rpm/s. Cooling flow rate ~160 L/min. Inset table shows average rotor OD temperatures corresponding to each heater set temperature

For the largest in-phase imbalance masses (360 mg), Figure 73 shows the amplitude and phase of motion at the drive end, vertical and horizontal planes. At room temperature (heater off) the rotor motions are the largest.

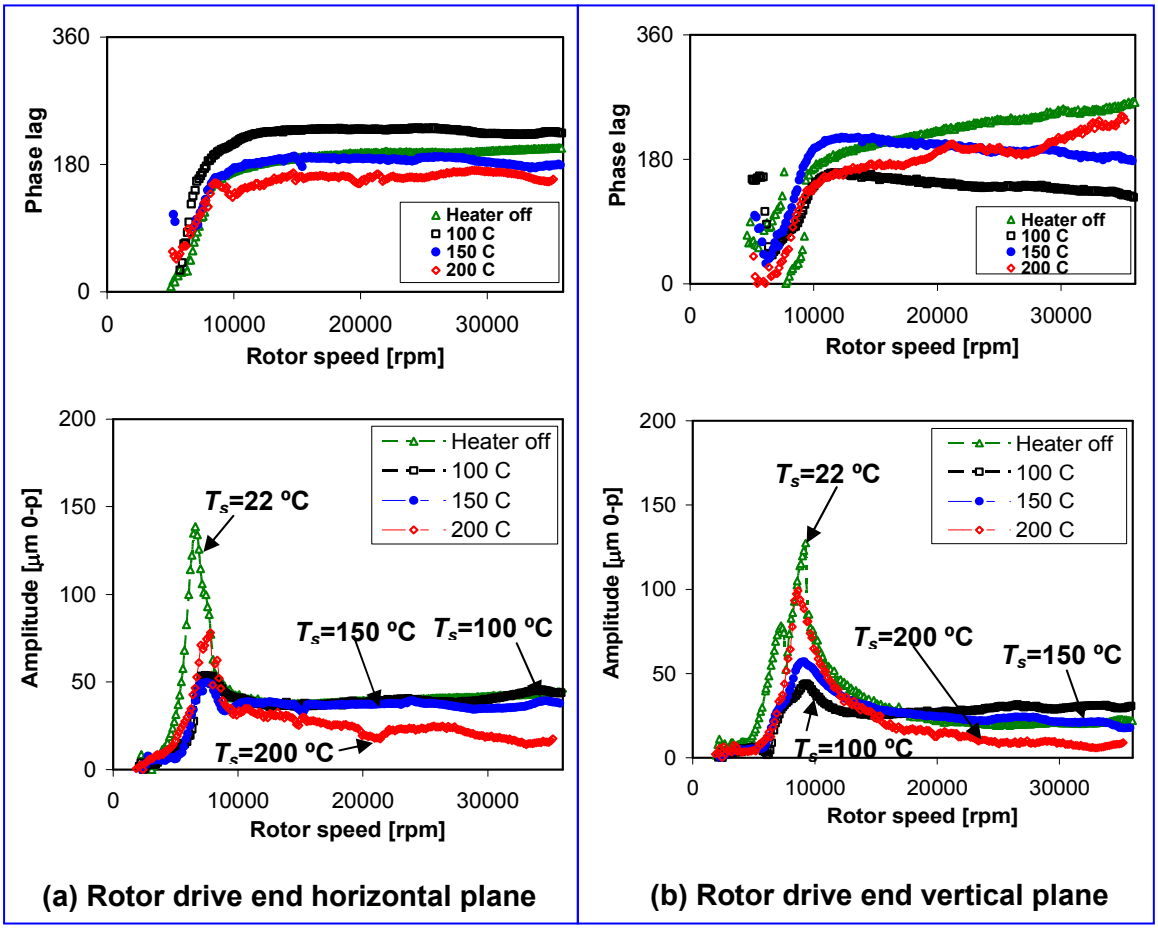

Heater set temp, T_s ºC	22	100	150	200
Rotor FE ºC	24	46	68	92
Rotor DE ºC	24	32	47	62

Fig. 73 Rotor synchronous response amplitude and phase versus shaft speed for in-phase imbalance masses = 360 mg. Measurements at rotor drive end (a) horizontal plane and (b) vertical plane. Rotor acceleration of 400 rpm/s. Cooling flow rate ~160 L/min. Inset table shows average rotor OD temperatures corresponding to each heater set temperature

The waterfall plot of rotor response, depicted in Figure 74, displays peak amplitudes at ~ 116 Hz (7 krpm) and small amplitude subsynchronous motion at ~150 Hz (9 krpm) as the rotor speeds up beyond its critical speed.

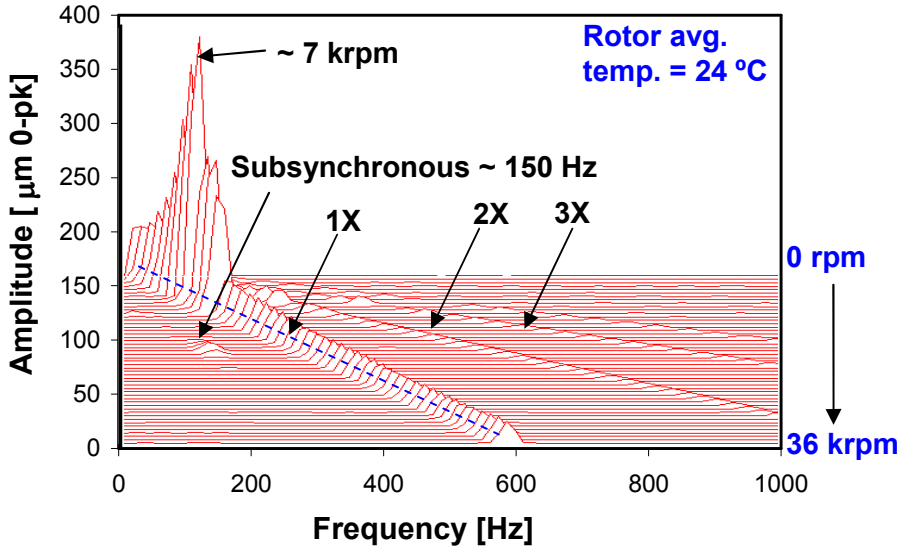

Fig. 74 Waterfall plot of rotor response at drive end, horizontal plane, with heater turned off (ambient temperature). Rotor acceleration 400 rpm/s. In-phase imbalance masses = 360 mg. Cooling flow rate ~160 L/min.

Figure 75 displays the waterfall plot of rotor response amplitude at the rotor drive end, vertical plane, with the heater (a) turned off and (b) with a set temperature of 200 °C. While the waterfall plots for the imbalance mass of 240 mg out-of-phase displayed no sub-synchronous amplitudes, the present waterfall for a larger imbalance mass of 360 mg in-phase shows sub-synchronous motion amplitudes at ~150 Hz. Again, for the highest heater set temperature of 200 °C, the sub-synchronous motion is more pronounced. The measurements also show 2X and 3X vibration components, albeit with a very small magnitude.

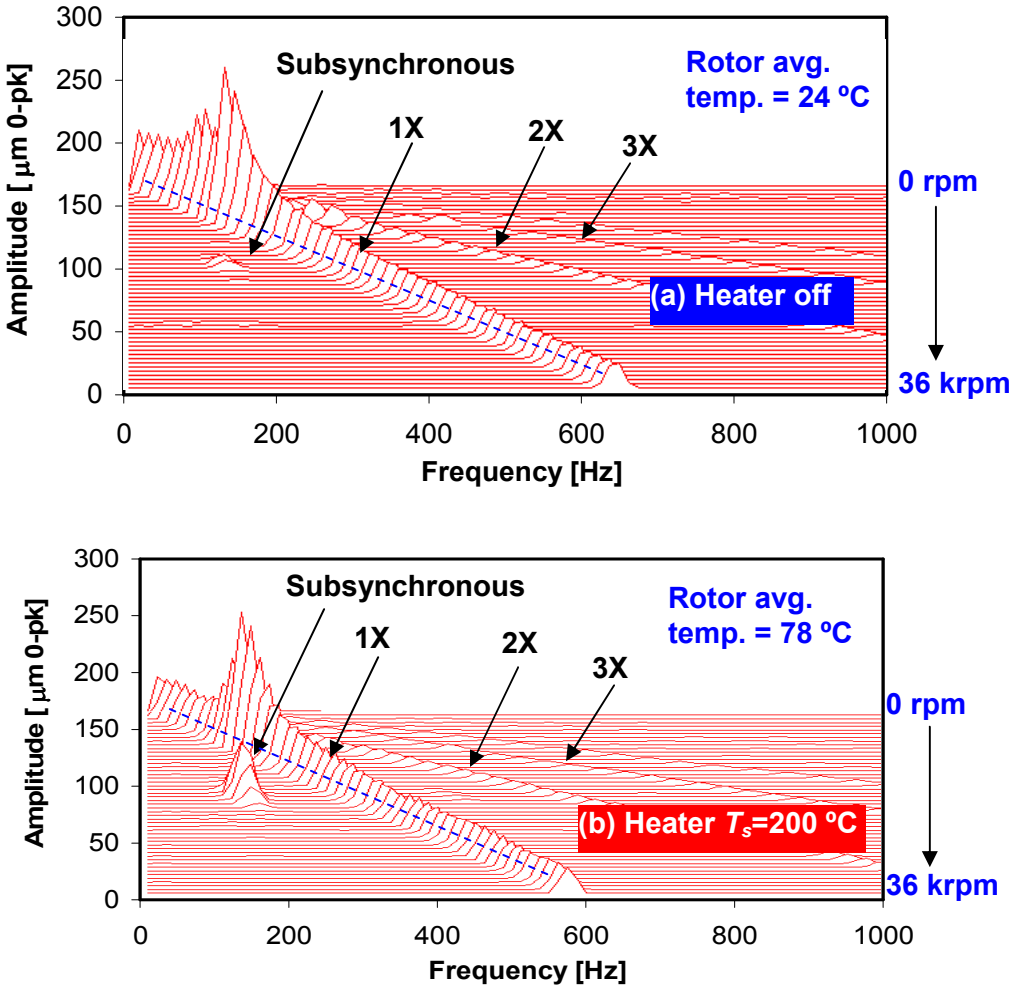

Fig. 75 Waterfall plot the rotor response at the rotor drive end, vertical plane, for (a) heater turned off, and (b) heater set temperature = 200 ºC. Rotor acceleration 400 rpm/s. In-phase imbalance masses = 360 mg. Cooling flow rate ~160 L/min.

8.5 Conclusions

This section presents the response of a hollow Inconel rotor supported on two metal mesh foil bearings while the heater is set at different temperatures (22 ºC, 100 ºC, 150 ºC, and 200 ºC). Note that, with the maximum heater set temperature of 200 ºC, the rotor average temperature is only 78 ºC. A steady cooling air flow at 160 L/min is supplied to the test bearings. The measurement of the rotor and bearing temperatures,

for an entire duration of 11 hours, evidence the gradual increase in temperature for the system components until reaching a thermal equilibrium.

In the tests with the heater set to a high temperature (max. 200 °C), the rotor and bearing OD temperatures increase by 70°C and 25°C, respectively. Most of the rotor vibration responses do not show a marked difference for operation under cold (ambient temperature) and hot rotor conditions. Note that a steady inlet air flow rate at ~ 160L/min cools the bearings continuously.

The rotor and bearings survived numerous start up-shutdown events, and steady speed operation for several hours, with added imbalance masses as large as 360 mg (u=22.6 μm) at 50 krpm speed and 200 °C heater temperature (~ max. 100 °C at the rotor OD). With an abundant cooling flow rate (160 LPM), the performance of the test bearings is not significantly affected by increasing rotor temperatures.

The effect of varying the strength of the air cooling flow rate was not investigated; prior research [56] shows that the cooling air supply is important for the safe operation of foil bearing supported rotors, particularly for operation at high temperatures.

9. MMFB DESIGN GUIDELINES

This section provides guidelines for designing a MMFB based on the knowledge gained from experiments and predictions presented in earlier sections. Refer to Appendix A for details on the MMFB manufacturing procedure. The important parameters of interest during the MMFB design are the bearing rotordynamic force coefficients and the load carrying capacity. The following guidelines will aid in the design and operation of MMFBs.

9.1 Load Carrying Capacity

1. Load carrying capacity increases with structural stiffness, a function of the metal mesh compactness, and increasing rotor speed. Although the structural stiffness slightly increases with preload, it also delays the lift-off speed.
2. Solid lubricant coatings are required for the top foil and the shaft surface to reduce lift-off speed and to increase the load carrying capacity. See Ref. [5] for details on top foil and rotor surface coatings.
3. Shaft-bearing misalignment decreases load carrying capacity. Also, severe misalignment damages the top foil edge due to its rubbing contact with the journal surface.
4. The attitude angle increases with increasing metal mesh structural stiffness. i.e., MMFB with highly compact metal meshes with act like rigid bearings.

9.2 Rotordynamic Force Coefficients

1. The metal mesh pad radius, thickness, and compactness affect its structural stiffness. See Ref. [9] for empirical equations providing the relationship of the metal mesh ring geometry to its structural force coefficients.
2. MMFB damping cannot be independently controlled, as the material damping and structural stiffness is related through a loss factor.
3. Copper meshes provide larger energy dissipation ability than steel meshes. However, metal mesh rings made of shape memory alloy materials, NiTi for

instance, show interesting characteristics, such as increased damping for larger motion amplitudes.

9.3 Thermal Management

1. Continuous cooling air supply is necessary for MMFBs operating in high temperature environment.

2. Preliminary design must incorporate the possible reduction in clearances while operating at elevated temperatures.

9.4 Maintenance Free Operation

1. Adequate top foil and journal coating is required for long maintenance-free operation of MMFB.

2. Metal mesh pads with higher compactness and smaller thickness show less sag and creep over time.

3. Providing a bearing end cap to axially constrain the metal mesh aids in maintaining the metal mesh geometry. In the absence of any bearing end cap, the metal mesh grows axially over time. This axial growth will increase the bearing radial clearance and decrease the metal mesh compactness, thus resulting in bearing stiffness reduction.

10. SUMMARY AND CONCLUSIONS

Metal mesh foil bearings (MMFB) are compliant surface gas bearings that adequately support micro-turbomachinery rotors at high operating speeds, extreme temperatures, and in corrosive environments. This report covers the (i) analysis to predict the MMFB static and dynamic forced performance; (ii) compares the performance of a MMFB and a generation I bump type foil bearing, both similar in size; (iii) details the manufacturing procedure for a commercially viable MMFB design; (iv) reports measurements and rotordynamic predictions of the response of a rotor supported on MMFBs, for various imbalance masses; (v) presents the measurements of the system component temperatures and rotor radial response for increasing rotor temperatures; and (vi) provides design guidelines for implementing MMFBs in high speed, high temperature micro-turbomachinery applications.

The major conclusions from this work are:

(i) Prediction of MMFB performance characteristics

a. The present work advances an analysis, coupling the finite element model of the top foil and a Reynolds equation governed gas film model, to predict the static and dynamic performance of a MMFB.

b. The model predictions are validated against limited published test data [12, 26, and 42]. For thorough validation, however, test data from several different bearings are required.

c. The predicted drag friction factor under a gas film operation regime is very small, $f \sim 0.03$, and agrees well with measurements at increasing rotor speeds and with increasing applied loads. The drag friction factor (f) is proportional to the Stribeck number.

d. At high loads, W/LD =30 kPa, predicted journal eccentricities will exceed the bearing nominal clearances (c=20 μm) as the metal mesh structure is rather soft (K_m=2.8 GN/m^3). The journal attitude angle, for

small loads and high speeds, are lesser than 90°. Also, the attitude angle increases with increasing metal mesh stiffness.

e. The predicted frequency dependent stiffness and damping characteristics show comparable magnitudes, but differ in their trends with respect to frequency, particularly the direct damping coefficients.

(ii) Comparison of MMFB and BFB performance characteristics

a. Static load deflection measurements show similar non-linear variations with increasing loads for both bearings. MMFB structural loss factor is ~ 2-3 times that of the BFB.

b. BFB and MMFB show similar drag torque, and lift-off characteristics. The airborne friction factor for the bearings is as low as ~0.03.

c. The dynamic force coefficients of MMFB and BFB show markedly dissimilar characteristics. The loss factor (γ) is an indicator of the mechanical energy dissipation ability for foil bearings. In a MMFB (γ) is at least twice larger than that in a first-generation BFB. The MMFB loss factor increases gradually with frequency from ($\gamma \sim 0.8$ -1.5 for 200 Hz-600 Hz). The loss factor is not sensitive to rotor speed or bearing motion amplitude.

d. The test results and analysis show the floating MMFB is rotordynamically stable over the range of excitation frequencies tested.

(iii) Measurements and Predictions of Rotordynamic Response of a Hollow Rotor Supported on two MMFBs

a. A finite element structural analysis of a rotor-bearing modeled in XLTRC^2© predicts the rotor response and amplitudes, for in-phase and out-of-phase imbalance masses of 240 mg and 360 mg at the rotor end planes, agreeing with the recorded baseline-subtracted rotor responses at high rotor speeds.

b. The normalized rotor responses for two different imbalance masses show linear rotor response characteristics.

(iv) Measurements of High Temperature Rotordynamic Response of a Hollow Rotor Supported on two MMFBs

a. Rotor responses are recorded with an electric heater, co-axially placed inside the hollow rotor, and set at different temperatures (100 °C, 150 °C, and 200 °C). The bearing and rotor temperatures increase with increasing heater temperatures and rotor speeds. The experiments show that cooling air supply is necessary for failsafe operation of MMFB supported rotors.

b. Most rotor dynamic responses do not show a marked difference for operation under cold (ambient temperature) and hot rotor conditions. Note that steady air flow rate at~ 160L/min cools the bearing and rotor continuously.

c. Recorded waterfall plots for a test with a large imbalance mass of 360 gm (in-phase) shows that the sub-synchronous vibration amplitudes near the bearing natural frequency increases with increasing rotor temperatures. In the majority of the operating speed range, however, the spectrums of rotor displacements show that only the synchronous response is dominant.

This report advances significant original contributions towards the physical modeling of the static and dynamic performance of metal mesh foil bearings. Importantly, the MMFB prediction tool and the database of high temperature, high speed rotordynamic measurements will aid in the advancement of this inexpensive bearing technology. However, further validation of the predictive tool against more experimental data from multiple bearings is necessary before it may be used effectively to further the design of MMFBs.

REFERENCES

[1] Valco, M.J. and DellaCorte, C., 2003, "Emerging Oil-Free Turbomachinery Technology for Military Propulsion and Power Applications," *Proc. ARMY Sciences Conf.*, Ft. Lauderdale, FL.

[2] Barnett, M.A., and Silver, A., 1970, "Application of Air Bearings to High-Speed Turbomachinery," SAE Paper No. 700720.

[3] Peng, Z.-C., and Khonsari, M.M., 2004, "Hydrodynamic Analysis of Compliant Foil Bearings with Compressible Air Flow," J.Tribol., **126**(3), pp. 542-546.

[4] San Andrés, L., Chirathadam, T.A., and Kim, T.H., 2010, "Measurement of Structural Stiffness and Damping Coefficients in a Metal Mesh Foil Bearing," ASME J. Eng. Gas Turbines Power, **132**(3), p. 032503.

[5] DellaCorte, C., Radil, K.C., Bruckner, R.J., and Howard, S.A., 2008, "Design, Fabrication, and Performance of Open Source Generation I and II Compliant Hydrodynamic Gas Foil Bearings," Tribol. Transactions, **51**, pp. 254-264.

[6] Kim, T.H., and San Andrés, L., 2006, "Limits for High Speed Operation of Gas Foil Bearings," ASME J.Tribol, **128**, pp. 670-673.

[7] Ao, H., Jiang, H., Wei, W., and Ulanov, A.M., 2006, "Study on the Damping Characteristics of MR Damper in Flexible Supporting of Turbo-Pump Rotor for Engine," *Proc. 1st Symposium on Systems Control in Aerospace and Astronautics*, Harbin, China, Jan. 19-21, pp. 618-622.

[8] Ertas, B.H., Al-Khateeb, E.M., and Vance, J.M., 2003, "Rotordynamic Bearing Dampers for Cryogenic Rocket Engine Turbopumps," AIAA J. Propul. Power, **119**(4), pp. 674-682.

[9] Choudhry, V., and Vance, J.M., 2005, "Design Equations for Wire Mesh Bearing Dampers in Turbomachinery," ASME Paper No. GT 2005-68641.

[10] Kim, T.H., Breedlove, A.W., and San Andrés, L., 2009, "Characterization of Foil Bearing Structure for Increasing Shaft Temperatures: Part I-Static Load Performance," ASME J.Tribol., **131**(4), p.041703.

[11] San Andrés, L., Kim, T.H., Ryu, K., Chirathadam, T. A., Jarrett, C., Hagen, K., Martinez, A., Rice, B., Niedbalski, N., Hung, W., and Johnson, M., " Gas Bearing Technology for Oil-Free Microturbomachinery – Research Experience for Undergraduate (REU) Program at Texas A&M University," ASME Paper No. GT2009-59920.

[12] San Andrés, L., Kim, T.H., Chirathadam, T.A., and Ryu, K., 2010, "Measurements of Drag Torque, Lift-Off Journal Speed and Temperature in a Metal Mesh Foil Bearing," ASME J. Eng. Gas Turbines Power, **132**(11), p. 112503.

[13] DellaCorte C, and Valco M., 2000, "Load Capacity Estimation of Foil Air Journal Bearing for Oil-Free Turbomachinery Applications," Tribol Trans., **43**(4). pp. 795–801.

[14] Bruckner, R.J., and Puleo, B.J., 2008, "Compliant Foil Journal Bearing Performance at Alternate Pressures and Temperatures," ASME Paper No. GT2008-50174.

[15] Howard, S.A., DellaCorte, C., Valco, M.J., Prahl, J.M., and Heshmat, H., 2001, "Steady-State Stiffness of Foil Air Journal Bearings at Elevated Temperatures," Tribol. Trans., **44**(3), pp. 489-493.

[16] Howard, S., DellaCorte C., Valco, M.J., Prahl, J.M., and Heshmat, H., 2001, "Dynamic Stiffness and Damping Characteristics of a High-Temperature Air Foil Journal Bearing," Tribol. Trans., **44**(4), pp. 657-663.

[17] Kim, T.H., and San Andrés, L., 2008, "Heavily Loaded Gas Foil Bearings: A Model Anchored to Test Data," ASME J. Eng. Gas Turbines Power, **130**, p.012504.

[18] Heshmat, H., 1994, "Advancements in the Performance of Aerodynamic Foil Journal Bearings: High Speed and Load Capacity," ASME J. Tribol., 116, pp. 287-295.

[19] DellaCorte, C., 1997, "A New Foil Air Bearing Test Rig for Use to 700 C and 70,000 rpm," NASA TM-107405.

[20] Rudloff, L., Arghir, M., Bonneau, O., and Matta, P, 2011, "Experimental Analyses of a First Generation Foil Bearing: Startup Torque and Dynamic Coefficients," ASME J. Eng. Gas Turbines Power, **133**, p. 092501.

[21] Conlon, M.J., Dadouche, A., Dmochowski, W.M., Payette, R., Bedard, J.-P, and Liko, B., 2009, "Experimental Evaluation of Foil Bearing Performance: Steady-State and Dynamic Results," ASME Paper No. GT2009-60186.

[22] Conlon, M.J., Dadouche, A., Dmochowski, W.D., and Bédar, J.-P., 2010, "A Comparison of the Steady-State and Dynamic Performance of First- and Second-Generation Foil Bearings," ASME Paper No. GT2010-23683.

[23] DellaCorte, C., Radil, K.C., Bruckner, R.J., and Howard, S.A., 2006, "A Preliminary Foil Gas Bearing Performance Map," NASA TM-2006-214343.

[24] Radil, K.C., and DellaCorte, C., 2009, "A Three-Dimensional Foil Bearing Performance Map Applied to Oil-Free Turbomachinery," NASA APRL-TR-4473.

[25] Bruckner R.J., DellaCorte, C., and Dykas B.D., 2006, "An Analytic Approach to the Foil Gas Bearing Performance Map," Paper No. IJTC2006-12364, *Proc. of STLE/ASME 2006 International Joint Tribology Conf.*, October 23–25, 2006 , San Antonio, Texas, USA.

[26] San Andrés, L., and Chirathadam, T. A., 2011, "Identification of Rotordynamic Force Coefficients of a Metal Mesh Foil Bearing using Impact Load Excitations," ASME J. Eng. Gas Turbines Power, **133**(11), p. 112501**.**

[27] Lee, Y-B., Kim, C.H., Kim, T.H., and Kim, T.Y., 2011, "Effects of Mesh Density on Static Load Performance of Metal Mesh Gas Foil Bearings," ASME Paper No. GT2011-46589.

[28] Bruckner, R.J., 2009, "Windage Power Loss in Gas Foil Bearings and the Power-Stator Clearance of High Speed Generators Operating in High Pressure Environments," ASME Paper No. GT2009-60118.

[29] DellaCorte, C., and Bruckner, R.J., 2010, "Remaining Technical Challenges and Future Plans for Oil-Free Turbomachinery," ASME Paper No. GT2010-22086.

[30] San Andrés, L., and Chirathadam, T. A., 2011, "Metal Mesh Foil Bearing: Effect of Motion Amplitude, Rotor Speed, Static Load, and Excitation Frequency on Force Coefficients," ASME J. Eng. Gas Turbines Power, **133**(12), p.122503.

[31] Kim, T.H., Breedlove, A.W., and San Andrés, L., 2009, "Characterization of Foil Bearing Structure for Increasing Shaft Temperatures: Part I-Static Load Performance," ASME J.Tribol., **131**(4), p.041703.

[32] DellaCorte, C., 2010, "Stiffness and Damping Coefficient Estimation of Compliant Surface Gas Bearings for Oil-Free Turbomachinery," *Proc. of STLE/ASME 2010 Int. J. Tribol. Conference*, Paper No. IJTC2010-41232. Oct. 17-20, San Francisco, CA.

[33] Howard, S.A., 1999, "Preliminary Development of Characterization Methods for Compliant Air Bearings," Tribol. Transactions, **42** (4), pp. 789-794.

[34] Howard, S.A., DellaCorte, C., Valco, M.J., Prahl, J.M., and Heshmat, H., 2001, "Steady-State Stiffness of Foil Air Journal Bearings at Elevated Temperatures," Tribol. Transactions, **44**(3), pp. 489-493.

[35] Howard, S., DellaCorte C., Valco, M.J., Prahl, J.M., and Heshmat, H., 2001, "Dynamic Stiffness and Damping Characteristics of a High-Temperature Air Foil Journal Bearing," Tribol. Transactions, **44**(4), pp. 657-663.

[36] Lee, Y.-B., Park, D.–J., and Kim, C.–H., 2006, "Numerical Analysis for Bump Foil Journal Bearing Considering Top Foil Effect and Experimental Investigation," Paper-ID 229, *7th IFToMM-Conference on Rotor Dynamics*, Vienna, Austria.

[37] Kim, T.H., and San Andrés, L., 2009, "Effect of Side Feed Pressurization on the Dynamic Performance of Gas Foil Bearings: A Model Anchored to Test Data," ASME J.Eng. Gas Turbines Power, **131**(1), p. 012501.

[38] Glienicke, J., 1967, "Experimental Investigation of the Stiffness and Damping Coefficients of Turbine Bearings and their Application to Instability Prediction," Proc. Inst. Mech. Eng., **181**(3B), pp. 116-129.

[39] Childs, D., and Hale, K., 1994, "A Test Apparatus and Facility to Identify the Rotordynamic Coefficients of High-Speed Hydrostatic Bearings," J. Tribol., **116**, pp. 337-344.

[40] Rouvas, C., Murphy, B. T., and Hale, R.K., 1992, "Bearing Parameter Identification Using Power Spectral Density Methods," *Proc. of the Fifth International Conference of Vibrations in Rotating Machinery*, Bath, England, pp. 297-303.

[41] Arora, V., Van der Hoogt, P.J.M., Aarts, R.G.K.M., and de Boer, A., 2010, " Identification of Dynamic Properties of Radial Air-Foil Bearings," Int. J. Mech Mater Des, **6**, pp. 305-318.

[42] Modak, S.V., Kundra, T.K., and Nakra, B.C., 2000, "Comparative Study of Model Updating Methods Using Simulated Experimental Data," Comput. Struct., **80**, pp. 437-447.

[43] Heshmat, H., Walowit, J. A., and Pinkus, O., 1983, "Analysis of Gas-Lubricated Foil Journal Bearings," ASME J. Lubr. Tech., **105**, pp. 647-655.

[44] Carpino M., Talmage, G., 2003, "A Fully Coupled Finite Element Formulation for Elastically Supported Foil Journal Bearings," STLE Tribol. Trans., **46**, pp. 560-565.

[45] Kim, T.H., 2007, "Analysis of Side End Pressurized Bump Type Gas Foil Bearings: A Model Anchored to Test Data," Ph.D Thesis, Texas A&M University, College Station, TX.

[46] Reddy, J. N., 1993, *An Introduction to the Finite Element Method*, McGraw Hill, Singapore, pp. 516-520.

[47] Press, W.H., Flannery, B.P., Teukolsky, S.A., and Vetterling, W.T., 2007, *Numerical Recipes in Fortran 77: The Art of Scientific Computing*, Cambridge University Press, New York.

[48] Faria, M., and San Andrés, L., 2000, "On the Numerical Modeling of High Speed Hydrodynamic Gas Bearing," ASME J. Tribol., **122**, pp. 124-130.

[49] Hamrock, B.J., Schmid, S.R., and Jacobson,B.O., 1994, *Fundamentals of Fluid Film Lubrication*, McGraw Hill, New York.

[50] San Andrés, L., and Chirathadam, T.A., 2012, "A Metal Mesh Foil Bearing and a Bump-Type Foil Bearing: Comparison of Performance for Two Similar Size Gas Bearings," ASME J.Eng. Gas Turbines Power, **134** (10), p. 102501.

[51] San Andrés, L., 2010, *Modern Lubrication Theory*, "Gas Film Lubrication," Notes 15, Texas A&M University Digital Libraries, http://repository.tamu.edu/handle/1969.1/93197 [accessed on 09-09-2012]

[52] Delgado, A., and Ertas, B., 2012, "Identification of Damping and Stiffness Coefficients of a Shape Memory Alloy Wire Mesh Damper," *Proc. 14th Int. Symposium on Transport Phenomena and Dynamics of Rotating Machinery*, ISROMAC-14, Feb. 27-Mar. 2, Honolulu, HI.

[53] Rubio, D., and San Andrés, L., 2006, "Bump-Type Foil Bearing Structural Stiffness: Experiments and Predictions," ASME J. Eng. Gas Turbines and Power, **128**(3), pp. 653-660.

[54] San Andrés, L., Camero, J., Muller, S., Chirathadam, T.A., and Ryu, K., 2010, "Measurements of Drag Torque, Lift Off Speed, and Structural Parameters in 1st

Generation Floating Gas Foil Bearing," *Proc. 8th IFToMM Int. Conf. on Rotordynamics*, Sept. 12-15, Seoul, Korea.

[55] Lund, J. W., 1968, "Calculation of Stiffness and Damping Properties of Gas Bearings," ASME J. Lubr. Tech., **90**, pp. 793-803.

[56] San Andrés, L., Kim, T.H., and Ryu, K., 2010, "Thermal Management and Rotordynamic Performance of a Hot Rotor-Gas Foil Bearings System: Part 1-Measurements," ASME Paper No. GT2010-22981.

[57] Ryu, K., 2011, "Effect of Cooling Flow on the Operation of a Hot Rotor-Gas Foil Bearing System," Ph.D Thesis, Texas A&M University, College Station, TX.

[58] Coleman, H.W., and Steele, G.W., 1998, *Experimentation and Uncertainty Analysis for Engineers*, John Wiley & Sons, New York.

[59] Pritz, T., 2004, "Frequency Power Law of Material Damping," J. Applied Acoustics, **65**, pp. 1027-1036.

APPENDIX A. MANUFACTURING OF METAL MESH FOIL BEARING

A metal mesh foil bearing (MMFB), as depicted in Figure A.1 comprises of three components, (a) a bearing cartridge, (b) one or more compressed metal mesh pads, and (c) a pre-formed top foil. This section describes the manufacturing procedure for the components of a MMFB.

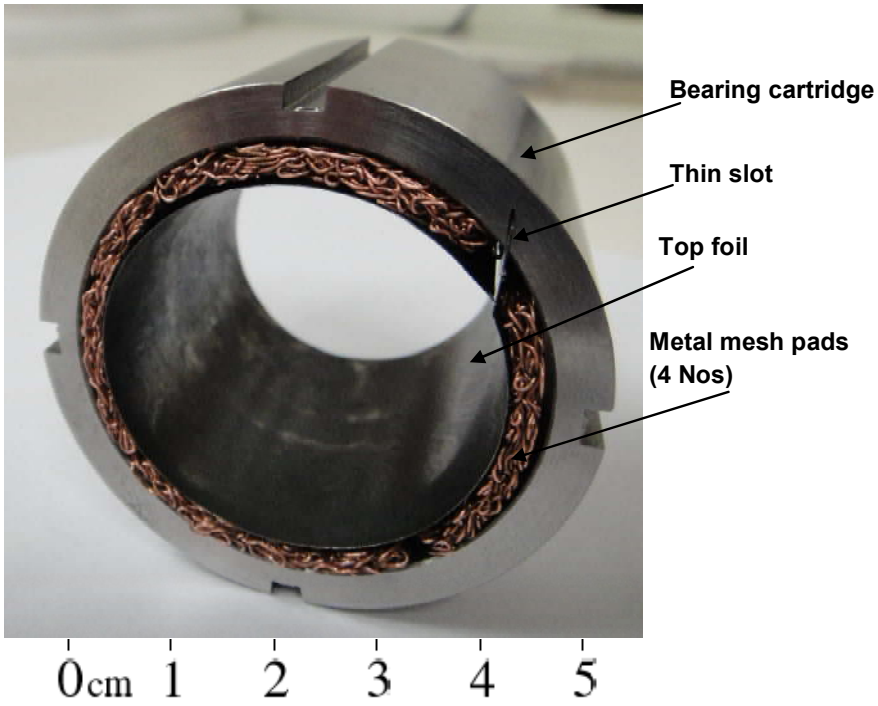

Fig. A.1 Metal mesh foil bearing with four metal mesh pads

A.1 Bearing Cartridge

The bearing cartridge is an annular cylindrical shell, typically made of stainless steel, and has a thin slot on the inner surface for affixing one of the top foil ends. The thin slot, machined using electrical discharge machining (EDM)' method, is wide

enough for top foil slide fit. Further, the top foil is secured in place using set screws threaded into the bearing cartridge from the outer surface. Figure A.2 illustrates the details of the slot on bearing cartridge and the dimensions for the test bearing reported in Section 6.

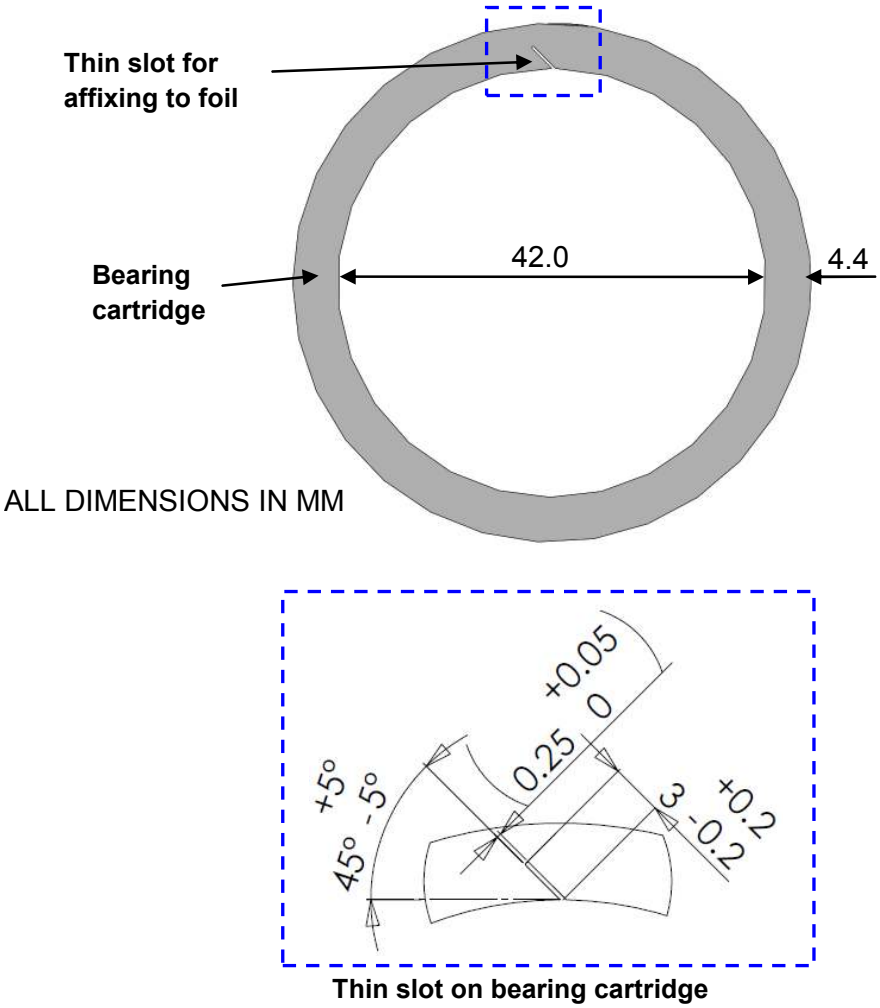

Fig. A.2 Bearing cartridge with a thin slot for affixing top foil. Inset shows the details of the thin slot

A.2 Top Foil

The top foil is a smooth curved metal strip that is heat treated for desirable properties. The top foil, depicted in Figure A.3, is manufactured from a hard cold Rolled steel strip of Chrome-Nickel alloy steel (Rockwell 40/45) of 120 μm thickness. The dimensions of the top foil are chosen according to the desired bearing inner diameter and axial length. As the cold rolled steel strip shows considerable resistance to deformation, annealing at high temperature is required to curve it into the desired diameter.

Fig. A.3 Top foil before assembly in a MMFB. The inner surface of the top foil coated with MoS_2

Figure A.4 shows a practical arrangement for heat treating the top foil. The apparatus consists of a steel strip wrapped around the cartridge of an electric heater and wrapped tightly with clamps. The top foil is heat treated ~ 450 º C for nearly two hours and then allowed to cool in room temperature condition. The top foil after cooling retains its arcuate shape, and has the desirable strength properties. Note that, prior

efforts to heat treat the top foil at temperatures as high as ~ 800 º C made the foils considerably brittle. One end of the top foil is slightly bent for easy installation in to the thin slot in the bearing cartridge. Although the top foil end may be bent before the heat treatment process, for proper clamping of the top foil to the heater coil, it is recommended to bend the end of the top foil later.

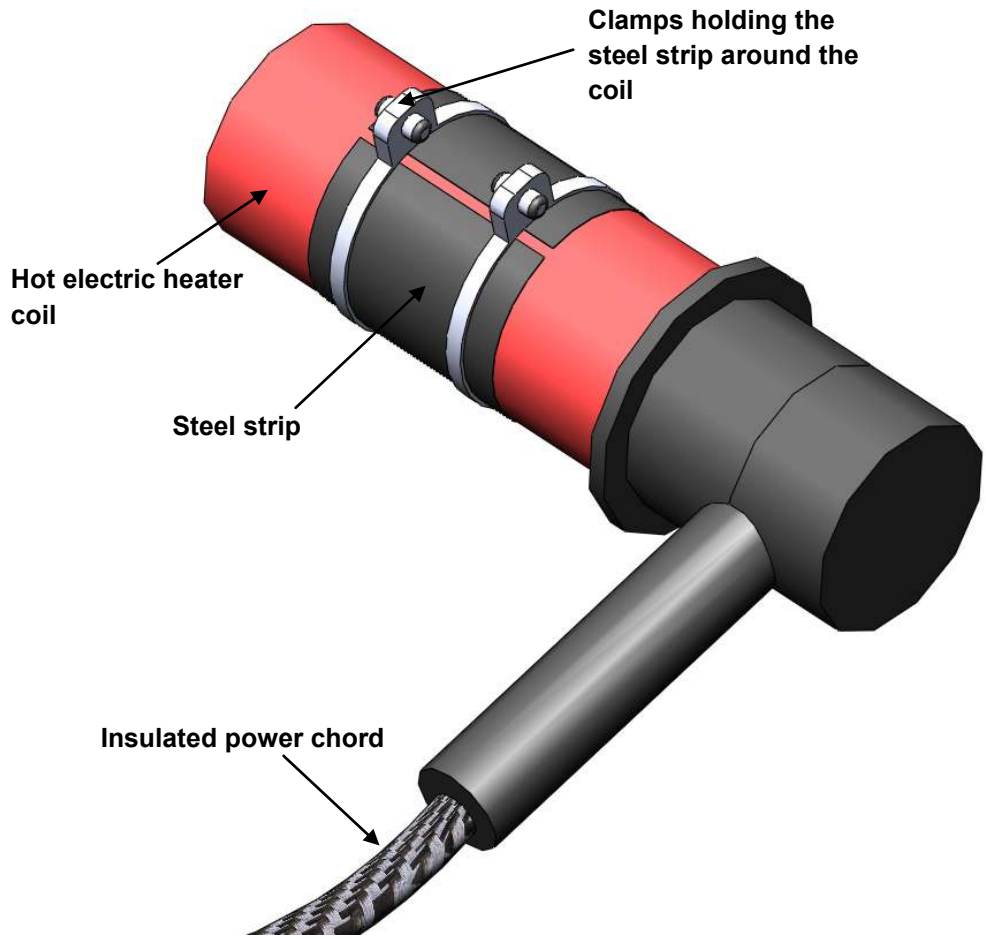

Fig. A.4 Heat treatment of the top foil wrapped around a hot heater cartridge

A.3 Metal Mesh Pad

The compressed metal mesh structure can be a ring [4], a single flat strip curved to fit in a bearing cartridge [12], or multiple pads arranged [31] along the bearing

circumferential direction. The latest MMFB design employs multiple mesh pads as they are easier to manufacture and provides better dimensional control. The following section describes the manufacture of metal mesh pads, each spanning 90 º arc width in a bearing. The metal mesh pad length equals the bearing axial length.

The metal mesh compactness (density) largely determines the bearing stiffness and damping. For instance, a 20 % compact metal mesh pad requires copper wires of total mass = (Volume of each pad) x (Density of copper) x (20/100). The required amount of copper wires (or copper gauze) is stacked inside an ad-hoc die made of plexi-glass, as depicted in Figure A.5, and compressed under large loads for extended amount of time. The ad-hoc die consists of a hydraulic press (not shown), a plexi-glass fixture, a metal plate equaling the desired size of the metal mesh pad, and copper wires (or gauze). Once the compression load is removed, the metal mesh slightly grows larger in thickness due to the memory effect. Hence, several iterations are required until the desired thickness is achieved.

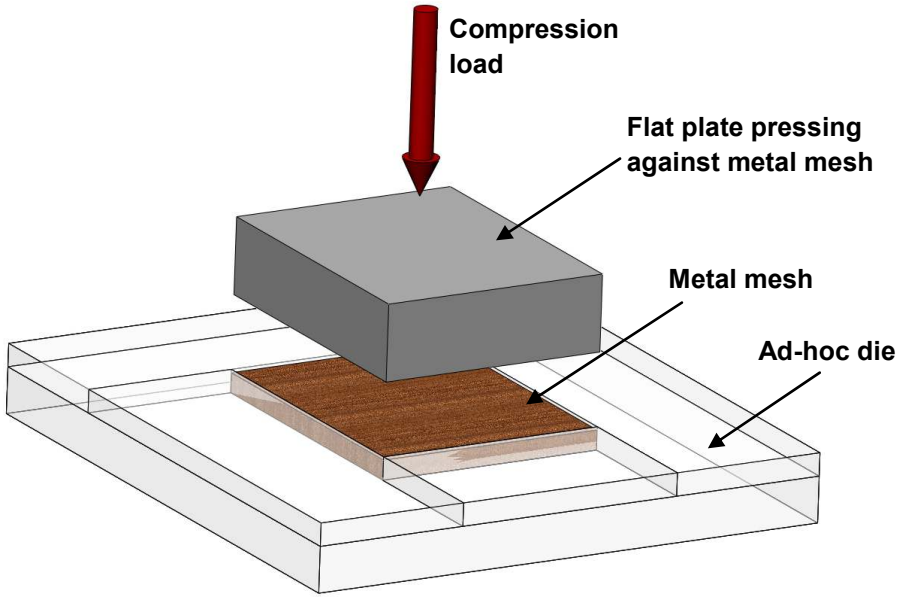

Fig. A.5 Compressing metal mesh gauze into a flat strip in an ad-hoc die

Figure A.6 shows the test setup to convert the flat metal mesh pads to an arcuate shape. The flat metal mesh pad, prepared in a die shown in Figure A.5, is placed inside a concave steel block, prepared using a hollow steel pipe of the required inner diameter. A steel cylinder with inner diameter equal to the desired metal mesh pad inner diameter is placed on top of the metal mesh pad. Then compression load is applied in a hydraulic press for several hours (typically 2-3 hours). Upon the removal of the load, the pad retains its arcuate shape.

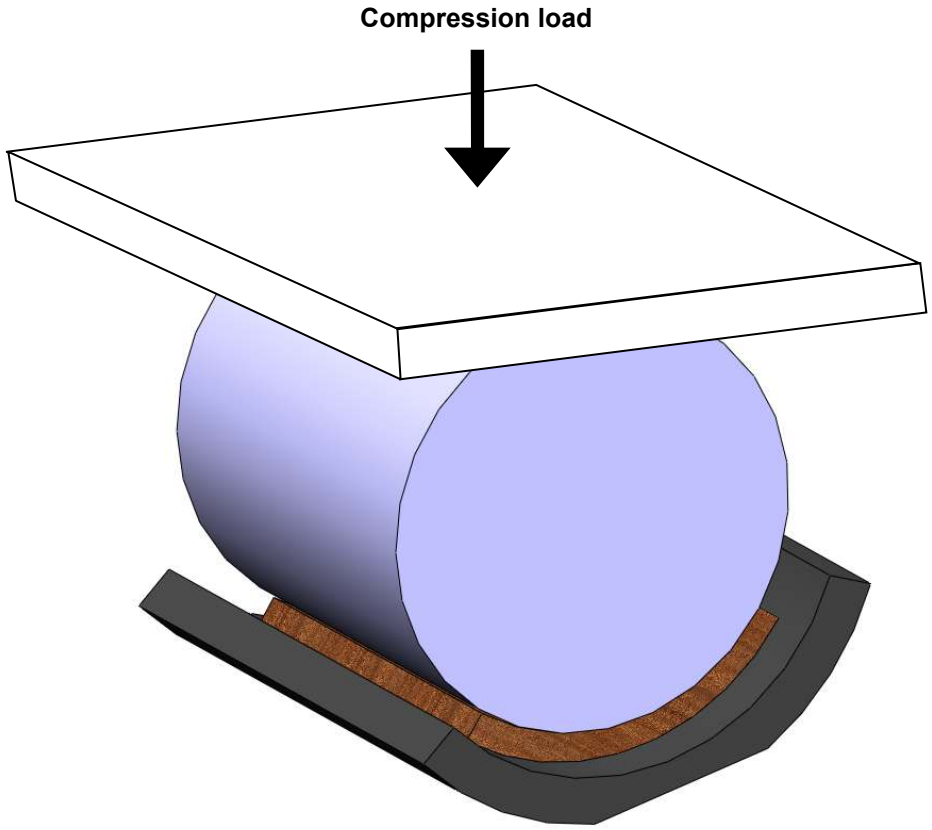

Fig. A.6 Compressing flat metal mesh strip into arcuate mesh pads

APPENDIX B. UNCERTAINTY ANALYSIS

Typical uncertainties associated with signal measurements are bias, precision, and random uncertainties. While bias uncertainties can be controlled and random uncertainties reduced by averaging, the precision uncertainties in the sensors cannot be nullified. The general equation for computing the uncertainty of parameters [58] propagated through a typical expression, $r = f(x_1, x_2, \ldots x_n s)$, is defined as

$$U_r = \sqrt{(\frac{\partial r}{\partial x_1} U_{x_1})^2 + (\frac{\partial r}{\partial x_1} U_{x_2})^2 + \ldots + (\frac{\partial r}{\partial x_n} U_{x_n})^2} \tag{B.1}$$

The data acquisition program is carefully controlled to acquire high precision voltage signals so as to avoid any measurement uncertainty arising from low resolution signals. Note that this is particularly important for eddy current sensor measurements. The eddy current sensor gain is calibrated using a positioning table digital readout (U_X= ± 0.0005 mm) and a voltmeter (U_v= ± 0.005 V). The eddy current proximity sensor gain follows the relationship

$$G = \frac{\Delta X}{\Delta V_{fit}} \tag{B.2}$$

where ΔX is the change in displacement for a change in voltage, $\Delta V_{fit.}$, resulting from a linear fit. The uncertainty of expression B.2, using equation B.1 becomes

$$(\frac{U_G}{G})^2 = (\frac{\partial G}{\partial X}\frac{U_X}{X})^2 + (\frac{\partial G}{\partial V_{fit}}\frac{U_{fit}}{G})^2 = (\frac{1}{\Delta X}\frac{U_X}{})^2 + (\frac{1}{\Delta V_{fit}}\frac{U_{V_{fit}}}{})^2 \tag{B.3}$$

where ΔD and ΔV_{fit} are the range of experimental values and $U_{V_{fit}}$ is computed from the uncertainty of the voltmeter and the uncertainty of the curve fit as described

$$U_{V_{fit}} = \sqrt{(U_{fit})^2 + (U_V)^2} \tag{B.4}$$

B.1 Torque Measurement

The bearing drag torque is measured using a calibrated spring, and follows the relationship

$$T = V\,G\,K\,L_T \tag{B.5}$$

where, T is the bearing torque, V the voltmeter reading, G the Eddy current sensor gain, K the spring constant, and L_T the torque arm length. The uncertainty propagated through expression B.5, is found using equation B.1

$$\left(\frac{U_T}{T}\right)^2 = \left(\frac{U_V}{V}\right)^2 + \left(\frac{U_G}{G}\right)^2 + \left(\frac{U_K}{K}\right)^2 + \left(\frac{U_{L_T}}{L_T}\right)^2 \tag{B.6}$$

Here, the spring constant is calibrated using a positioning table digital readout (U_X = ±0.0005 mm) and a force gauge (U_f = ± 0.2 N).

B.2 Bearing Parameter Identification

The uncertainties in the bearing force coefficients are due to the instrumentation uncertainty associated with the measurements of relative bearing displacements, bearing cartridge acceleration, and shaker force. Eqn. (25) in Section 5 describe the relationship of the bearing impedances $H_{\alpha\beta} = K_{\alpha\beta} + j\omega C_{\alpha\beta}\ ;\alpha,\beta = X,Y$ to the measured signals. For an excitation load along X direction, the equation becomes

$$H_{XX}\bar{x}^X + H_{XY}\bar{y}^X = \bar{G}_X^X = \bar{F}_X^X - \left(M_{S_X} + {C_{S_X}}/{j\omega} - {K_{S_X}}/{\omega^2}\right)\bar{A}_X^X \tag{B.7}$$

Here, note that the direct and cross coupled impedances are not independent of each other. Assuming that the fractional uncertainties of the two terms on the LHS of Eqn. (B.7) are nearly equal, the uncertainty in the impedance H_{XX} is found using Eqn. B.1 as

$$\left(\frac{U_{H_{XX}}}{H_{XX}}\right)^2 = \frac{1}{\sqrt{2}}\sqrt{\left(\frac{U_{G_X^X}}{G_X^X}\right)^2 + \left(\frac{U_{\bar{x}^X}}{\bar{x}^X}\right)^2} \tag{B.8}$$

Here, $\left(\frac{U_F}{F}\right)$ < 0.02 (2 % linearity), $\left(\frac{U_{A_X}}{A_X} = \frac{U_{A_Y}}{A_Y}\right)$ < 0.01 (1 % linearity), $\left(\frac{U_\omega}{\omega}\right)$ < 0.05 for frequencies >50 Hz. The uncertainties associated with the squirrel cage stiffness, damping and estimated mass are computed beforehand.

APPENDIX C. EFFECT OF STRUCTURAL STIFFNESS ON MMFB CHARACTERISTICS

This section presents the effect of the metal mesh stiffness (K_m) on MMFB film thickness, structural deflection, eccentricity, and attitude angle for increasing applied loads. The following predictions are for a MMFB with L=D=28.0 mm and nominal clearance c=20 μm. Table 1 in the main text shows other specifications, while Table C.1 below lists specific operating parameters. Metal mesh pads of density (compactness) 20% to 30% typically have structural stiffness per unit area less than 4 GN/m^3 [27].

Table C.1 Operating conditions and parameters

Parameters	Values
Ambient pressure	1.014 bar
Ambient temperature	27 °C
Viscosity of air	0.0187 cPoise
Density	1.22 kg/m^3
Rotor speed	40 krpm
Top foil elastic modulus	214 GPa
Top foil (chrome nickel steel alloy) hardness	40/45 Rockwell

The minimum film thickness, as depicted in Figure C.1, gradually increases with increasing metal mesh structural stiffness and decreases rapidly with increasing applied load. Thus, a stiffer MMFB displays higher load carrying capacity. The eccentricity ratio, as depicted in Figure C.2, increases beyond the (nominal) clearance for higher specific loads as the MMFB is rather soft. With increasing metal mesh stiffness, the journal eccentricity decreases. Figure C.3 shows the journal attitude angle versus applied load for various structural stiffnesses. The attitude angle increases with increasing structural stiffness and decreases with increasing applied load. MMFB with very high compactness metal mesh will show characteristics similar to a rigid journal bearing. Figure C.4 shows that the MMFB deflection increases with decreasing

structural stiffness. In the range of applied loads (up to 40 N), the structural deflection varies fairly linearly with load.

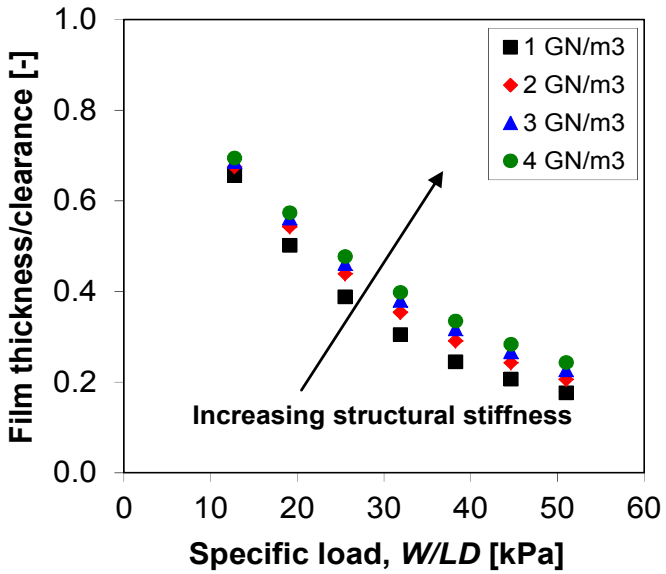

Fig. C.1 Example MMFB: Effect of increasing structural stiffness and specific load on the (dimensionless) minimum film thickness. Rotor speed of 40 krpm

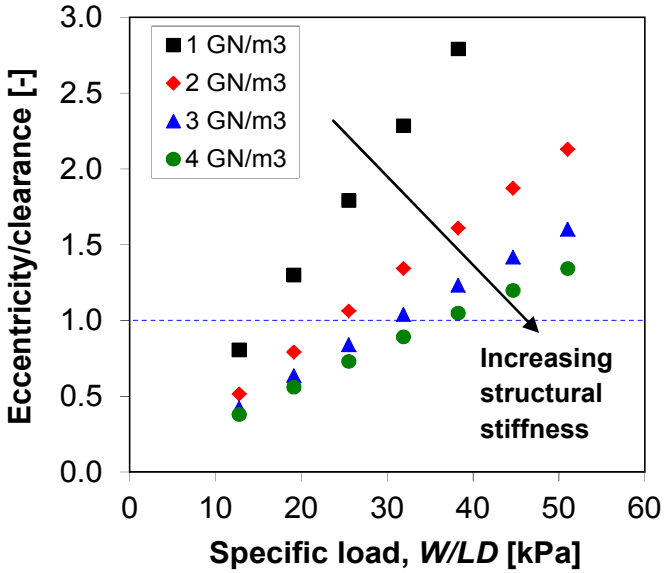

Fig. C.2 Example MMFB: Effect of increasing structural stiffness and specific load on the dimensionless eccentricity. Rotor speed of 40 krpm

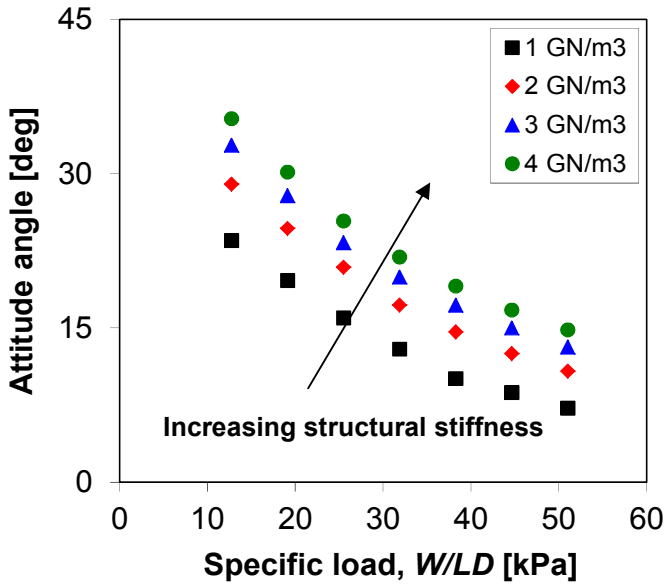

Fig. C.3 Example MMFB: Effect of increasing structural stiffness and specific load on journal attitude angle. Rotor speed of 40 krpm

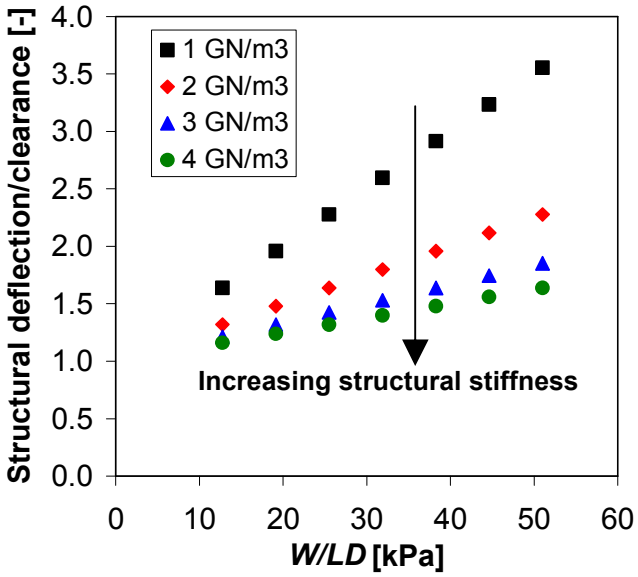

Fig. C.4 Example MMFB: Effect of increasing structural stiffness and specific load on (dimensionless) structural deflection. Rotor speed of 40 krpm

Figures C.5 and C.6 show the stiffness and damping coefficients (synchronous with rotor speed) versus specific load, respectively, for increasing structural stiffnesses per unit area (K_m). The rotor speed is 40 krpm. In general, with increasing metal mesh structural stiffness, i.e., with increasing mesh density, the stiffness and damping coefficients increase in magnitude. The direct stiffness and damping coefficients also increase gradually with increasing specific load. For the direct damping orthogonal to the load direction, its magnitude decreases with specific load up to 40 kPa and then flattens out.

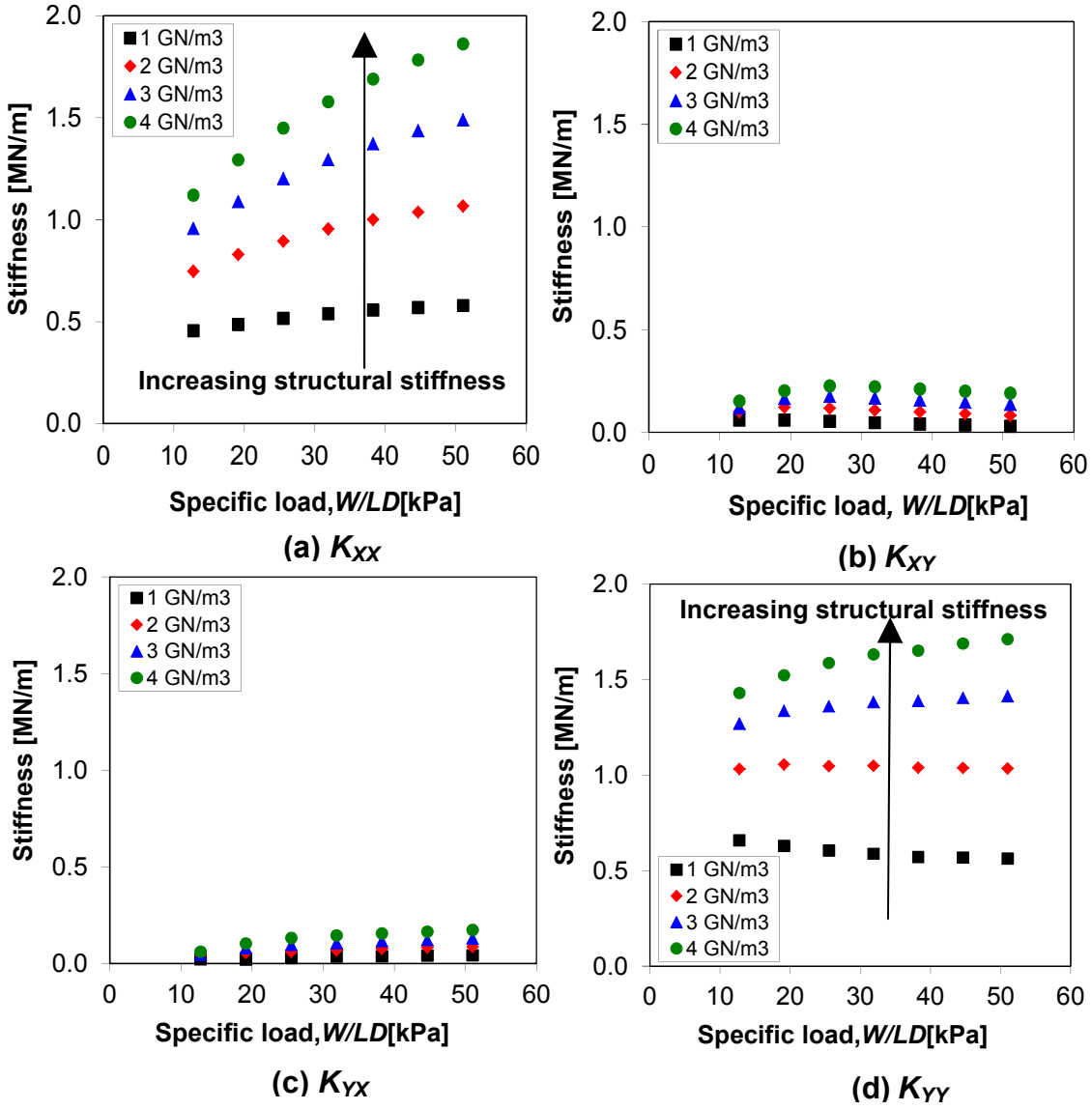

Fig. C.5 Example MMFB: Effect of increasing structural stiffness and specific load on bearing stiffness coefficients. Rotor speed of 40 krpm

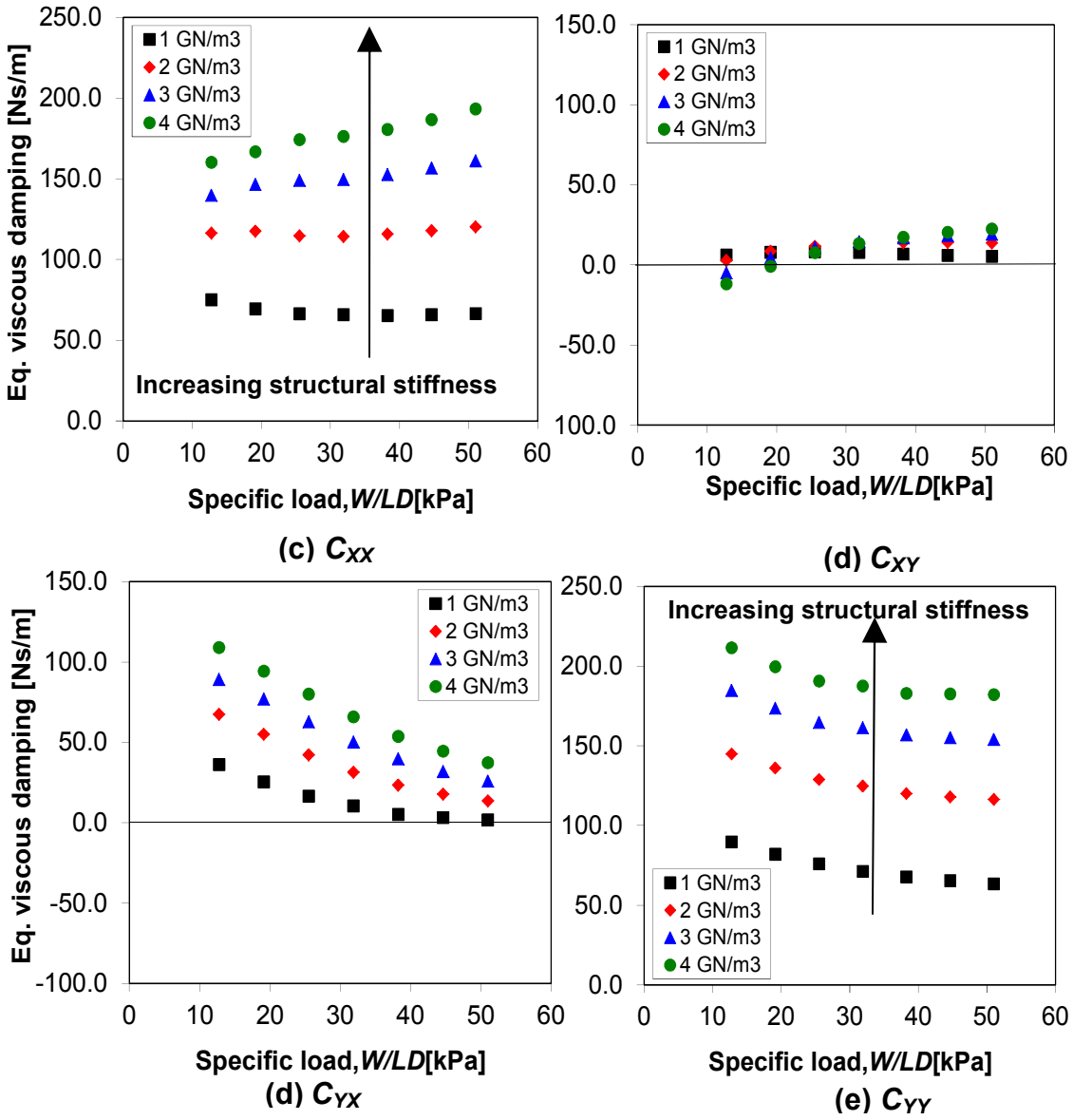

Fig. C.6 Example MMFB: Effect of increasing structural stiffness and specific load on bearing equivalent viscous damping coefficients. Rotor speed of 40 krpm

APPENDIX D. MEASUREMENT OF BEARING DEFLECTION

The appendix presents the bearing deflection measurements for increasing static loads, applied on a test metal mesh foil bearing, *L*=38 mm, *D*=36.5 mm, floating on a journal, of diameter =36.5 mm, spinning to a maximum speed of 60 krpm. Table 2 lists the bearing geometry.

D.1 Experimental Procedure

Figure D.1 shows the schematic view of a turbocharger turbine driven test rig, with a static loading device that applies push and pull loads on a test bearing floating on a spinning journal. The test bearing is softly supported on a squirrel cage like structure. The shop cold air supply to the turbine is manually adjusted to control the shaft spin speed [30]. A simple threaded rod/nut mechanism, along with a plexi-glass block to guide the rod along the vertical direction, applies push or pull loads on the test bearing via a load cell. Two eddy current sensors measure the bearing displacement ($X_{bearing}$) with respect to the rotating journal and the squirrel cage absolute deflection (X_{SqCage}) caused by the applied load W_S.

The squirrel cage stiffness[25] $K_{SqCage} \sim 10$ N/mm. The bearing stiffness $K_{bearing}$ is obtained from the static force balance equation.

$$W_S - K_{SqCage} X_{SqCage} = K_{bearing} X_{bearing} \tag{D.1}$$

D.2 Measurements

Figure D.2 depicts the MMFB deflection ($X_{bearing}$) for rotor at rest and spinning at 40 krpm, 50 krpm, and 60 krpm. Section 3 gives the test bearing specifications and dimensions. The measurements indicate that the bearing stiffness increases with increasing applied loads. The area of the mechanical hysteresis loop indicates the amount of damping in the bearing. The hysteresis loop encloses a smaller area at high rotor speeds compared to that measured with the rotor at rest, indicating a loss of

[25] Estimated using rap tests earlier [26]

damping. Most importantly, for rotor speeds from 40 krpm to 60 krpm, the load versus bearing deflection curve remains fairly similar.

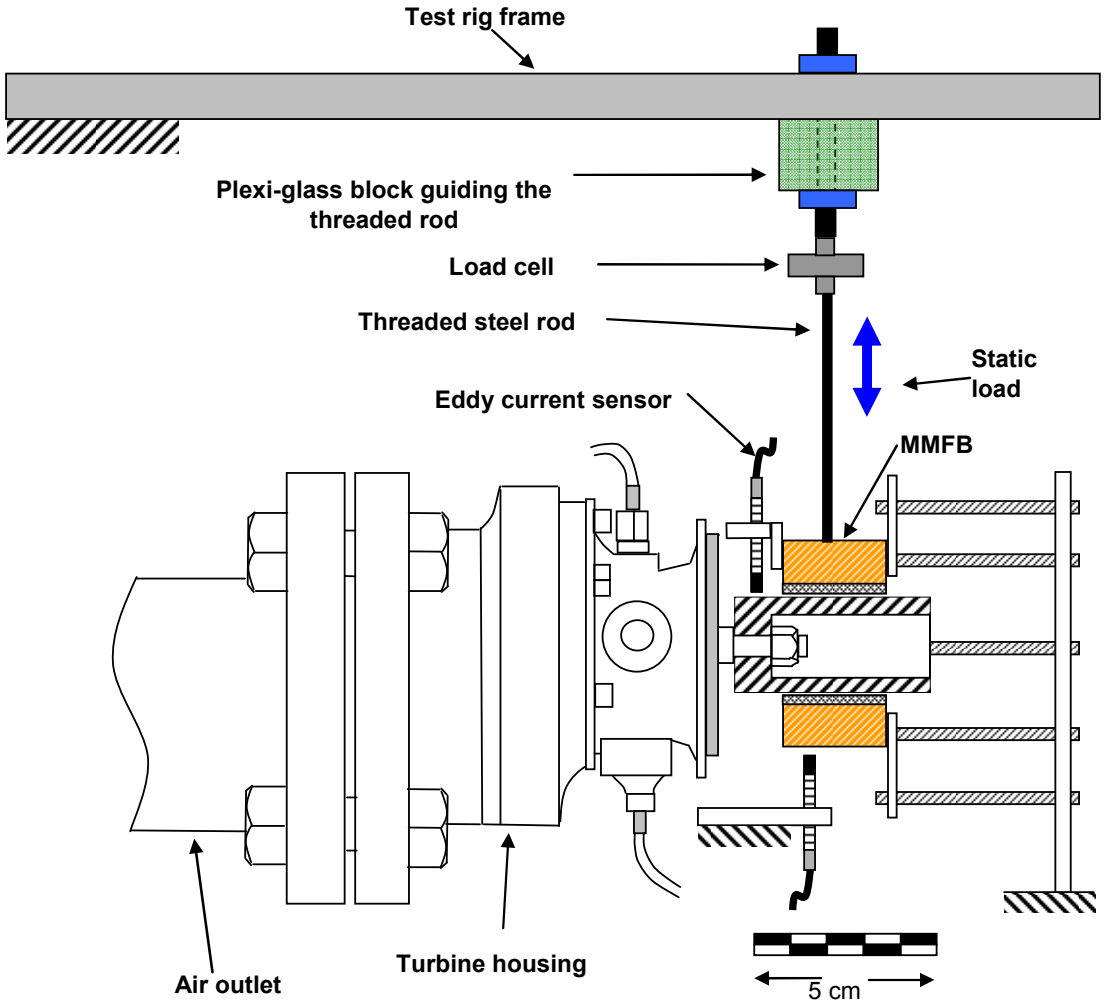

Fig. D.1 Schematic view of test rig configuration for applying static load on test bearing (supported with squirrel cage) with and without journal rotation

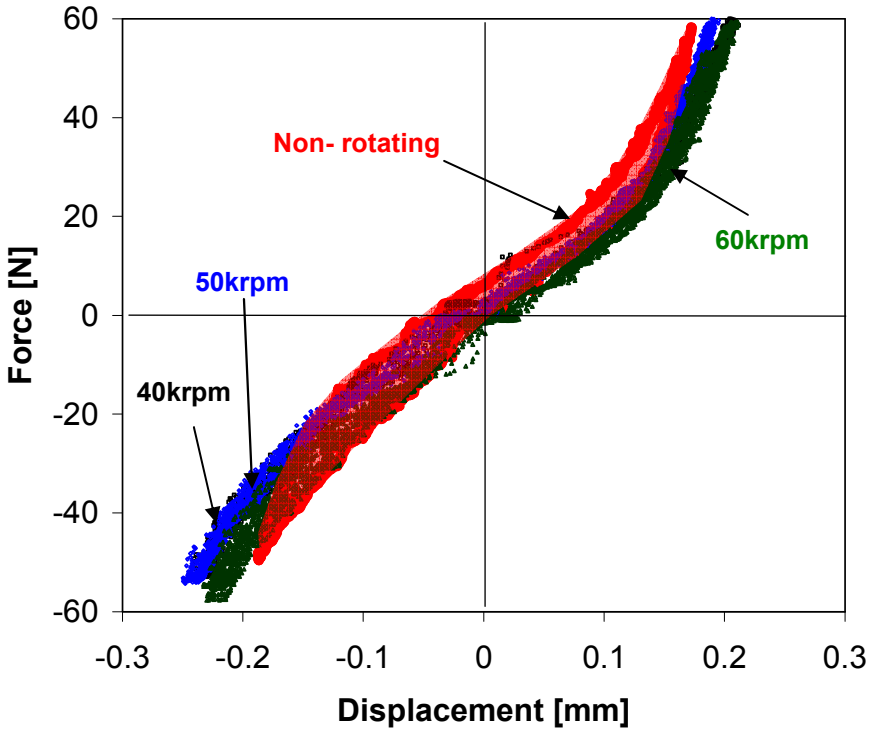

Fig. D.2 Load on bearing ($F\text{-}K_{SqCage}X_{SqCage}$) versus measured MMFB displacement for rotor at rest and spinning at 40 krpm, 50 krpm, and 60 krpm. Three cycles of push and pull loads

APPENDIX E. PREDICTIONS OF MMFB DAMPING FOR VARIOUS STRUCTURAL LOSS FACTORS

This section presents the predicted MMFB damping coefficients for various structural loss factors (γ). The MMFB dimensions and specifications are shown in Table 2. Figures E.1 –E.4 depict the predicted MMFB direct and cross-coupled viscous damping coefficients $C_{\underline{YY}}$, $C_{\underline{XX}}$, $C_{\underline{XY}}$, and $C_{\underline{YX}}$, respectively, for various loss factors for increasing excitation frequencies.

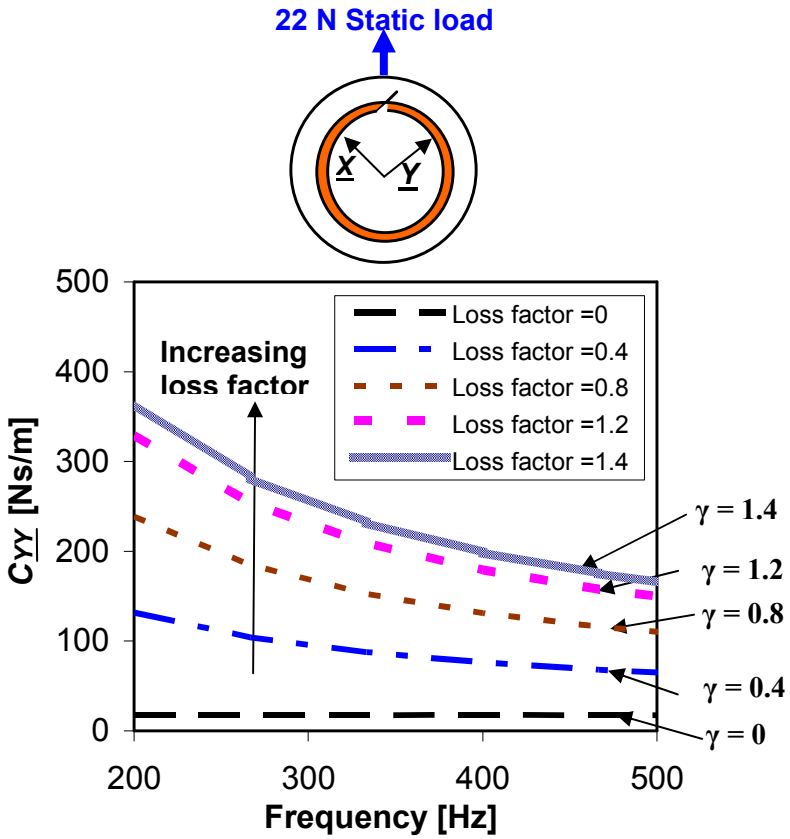

Fig. E.1 Predicted MMFB direct damping coefficient ($C_{\underline{YY}}$) versus frequency for various loss factors. Static load of 22 N along 45º in between $\underline{X}$ and $\underline{Y}$ axes. Rotor speed of 50 krpm (833 Hz)

From the experiments in Section 6, it is clear that the MMFB loss factor varies with frequency. The data below will aid in visualizing the damping coefficients as a function of frequency and loss factor. Note that the experiments in Section 6 show direct damping coefficients increasing with frequency – due mainly to loss factors increasing with frequency. The dynamic elastic modulus of materials increases with frequency [59], thus resulting in an increase in the dissipation of the mechanical strain energy. Recall that both the estimated stiffness and damping coefficients increase with frequency.

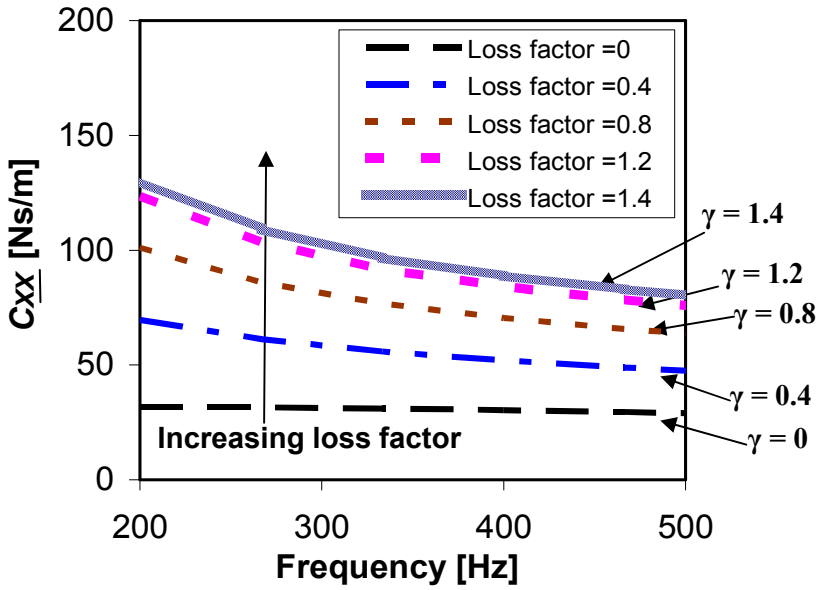

Fig. E.2 Predicted MMFB direct damping coefficient (C_{XX}) versus frequency for various loss factors. Static load of 22 N along 45º in between *X* and *Y* axes. Rotor speed of 50 krpm (833 Hz)

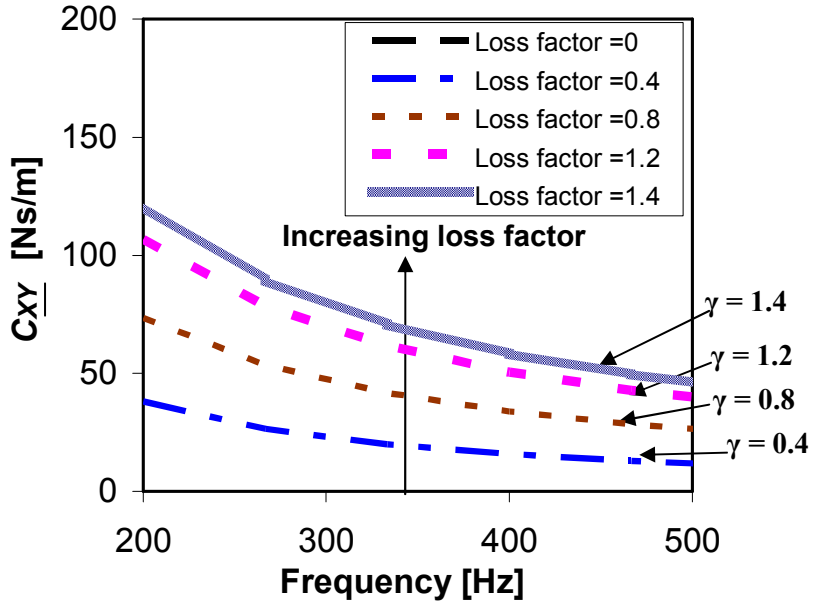

Fig. E.3 Predicted MMFB cross-coupled damping coefficient (C_{XY}) versus frequency for various loss factors. Static load of 22 N along 45º in between *X* and *Y* axes. Rotor speed of 50 krpm (833 Hz)

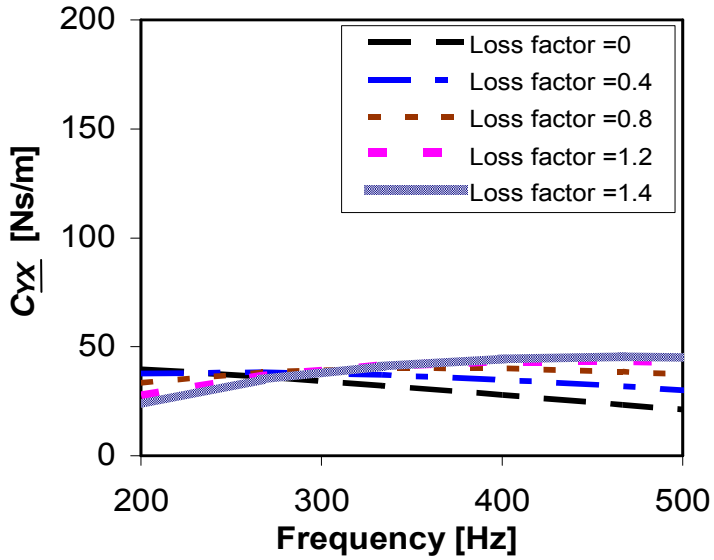

Fig. E.4 Predicted MMFB cross-coupled damping coefficient (C_{YX}) versus frequency for various loss factors. Static load of 22 N along 45º in between *X* and *Y* axes. Rotor speed of 50 krpm (833 Hz)

APPENDIX F. MMFB STIFFNESS AND DAMPING COEFFICIENTS FOR ROTORDYNAMIC RESPONSE PREDICTIONS

Tables F.1 and F.2 present the MMFB synchronous stiffness and damping coefficients, for the rotor free drive end and free end bearings. The force coefficients are used in XLTRC^2 software to predict the rotor response for known imbalance masses. The test rig and bearing details are presented in Section 7. Figure F.1 shows the test bearing coordinate system, with the static load acting along the *Y* direction. Note that the *X*-*Y* directions in Appendix F do not correspond to the coordinate system in Chapter 3.

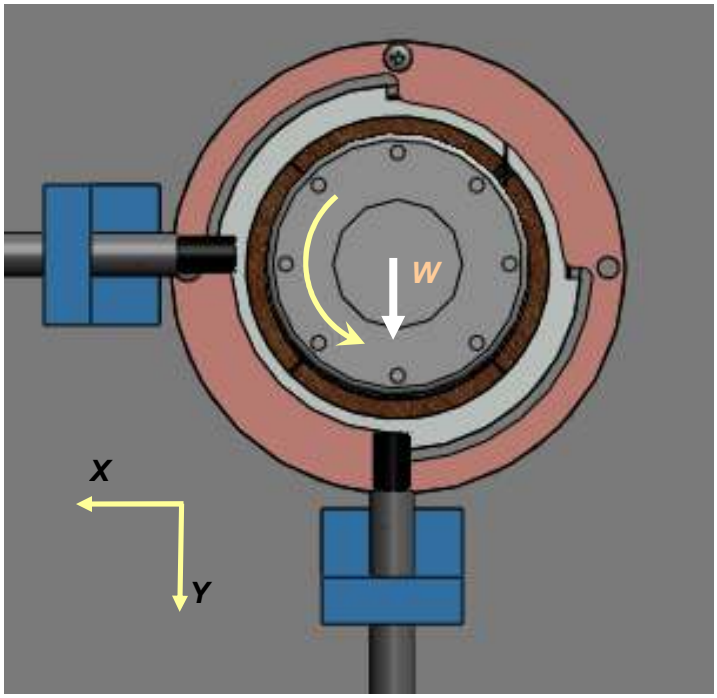

Fig. F.1 Eddy current sensors recording rotor displacement along the *X* and *Y* directions. Load applied along *Y* direction

Table F.1 Predicted MMFB synchronous stiffness and damping coefficients for the DEB carrying 7.39 N load

Speed rpm	K_{XX} N/m	K_{XY} N/m	K_{YX} N/m	K_{YY} N/m	C_{XX} N-s/m	C_{XY} N-s/m	C_{YX} N-s/m	C_{YY} N-s/m
10000	587,000	-19,000	-114,000	598,000	368.9	-192.1	59.6	291.6
15000	691,000	-33,700	-80,800	614,000	272.5	-160	30.7	202.6
20000	767,000	-55,800	-62,100	628,000	211.4	-133.7	15	155.4
25000	837,000	-92,300	-60,800	644,000	169.3	-115.5	4	132.6
30000	891,000	-126,000	-64,000	662,000	139.3	-99.2	-2.2	116.7
35000	936,000	-159,000	-71,400	681,000	117.1	-85.9	-5.9	105.5
40000	971,000	-185,000	-77,100	699,000	100.5	-74.7	-7.8	95.7
45000	1,000,000	-209,000	-84,500	717,000	87.5	-65.6	-8.9	88.2
50000	1,020,000	-229,000	-90,000	733,000	77.2	-58	-9.4	81.3

Table F.2 Predicted MMFB synchronous stiffness and damping coefficients for the FEB carrying 5.74 N load

Speed rpm	K_{XX} N/m	K_{XY} N/m	K_{YX} N/m	K_{YY} N/m	C_{XX} N-s/m	C_{XY} N-s/m	C_{YX} N-s/m	C_{YY} N-s/m
10000	555,000	4,230	-97,700	554,000	385.5	-209.2	75.2	292.5
15000	674,000	-22,600	-64,200	584,000	283.3	-172.1	36.9	206.7
20000	750,000	-44,100	-38,500	603,000	219.8	-138.5	19.4	154.8
25000	823,000	-80,700	-35,500	621,000	176.3	-118	6.1	131
30000	880,000	-114,000	-37,900	640,000	145.5	-100.9	-1.4	114.8
35000	925,000	-143,000	-42,500	659,000	122.8	-87	-5.6	102.5
40000	962,000	-170,000	-48,300	676,000	105.6	-75.8	-8	92.9
45000	1,010,000	-226,000	-84,100	715,000	88	-67.1	-9.4	92.4
50000	1,030,000	-247,000	-91,900	734,000	77.5	-59.1	-9.9	85.5

Figure F.2 depicts the stiffness and damping coefficients for the drive end bearing carrying 7.39 N load. These coefficients are evaluated at frequencies equal to the rotor speed.

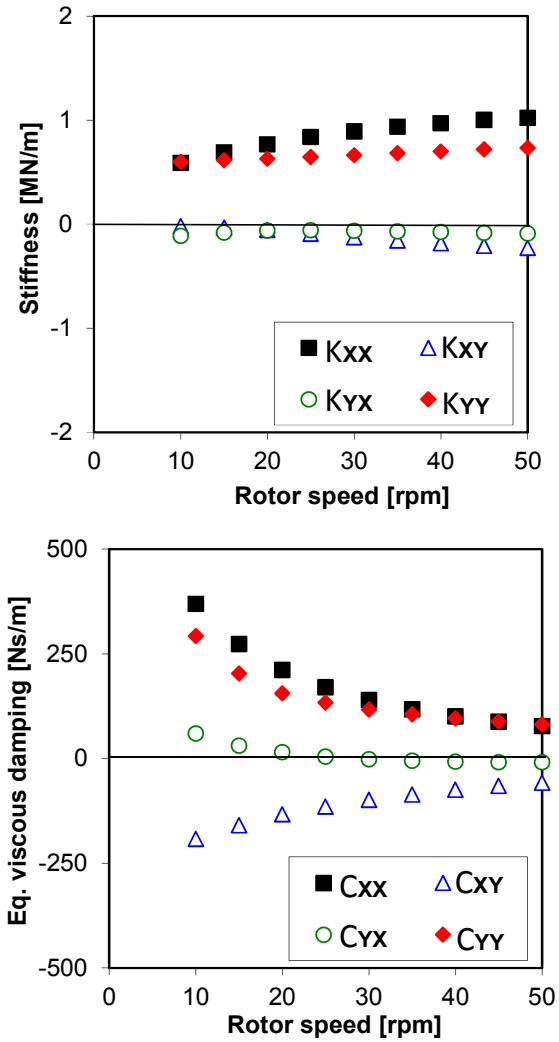

Fig. F.2 Predicted MMFB synchronous stiffness and damping coefficients for the FEB carrying 7.39N load